

2014

VEHICLE TECHNOLOGIES OFFICE

FY 2014 Annual Progress Report - Propulsion Materials

(This page intentionally left blank)

**U.S. Department of Energy
Office of Vehicle Technologies
1000 Independence Avenue S.W.
Washington, DC 20585-0121**

FY 2014

Progress Report for Propulsion Materials

Energy Efficiency and Renewable Energy
Vehicle Technologies Office
Materials Technology

**David Howell Acting Director, Vehicle Technologies Office
Stephen Goguen Acting Program Manager, Materials Technology
Jerry L. Gibbs Technology Manager**

May 2015

Contents

Introduction	1
Project 18516 – Materials for Hybrid and Electric Drive Systems	4
Agreement 23726 – Novel Manufacturing Technologies for High-Power Induction and Permanent Magnet Electric Motors	4
Agreement 26461 – Enabling Materials for High-Temperature Power Electronics	13
Project 18518 – Materials for High-Efficiency Engines	19
Agreement 13329 – Design Optimization of Piezoceramic Multilayer Actuators for Heavy-Duty Diesel Engine Fuel Injectors.....	19
Agreement 17257 – Materials for Advanced Turbocharger Designs	25
Agreement 18571 – Materials Issues Associated with EGR Systems.....	31
Agreement 23284 – Friction Reduction through Surface Modification: Integrated Surface Texturing and Coating	36
Agreement 23425 – Lightweight Heavy-Duty Engine	41
Agreement 23725 – Tailored Materials for Improved Internal Combustion Engine Efficiency.....	46
Agreement 24034 – High-Temperature Aluminum Alloys.....	57
Agreement 26190 – High-Temperature Materials for High-Efficiency Engines.....	69
Project 18519 – Materials for Exhaust and Energy Recovery	74
Agreement 9130 – Development of Materials Analysis Tools for Studying NO _x Adsorber Catalysts (CRADA No. ORNL-02-0659 with Cummins Inc.)	74
Agreement 10461 – Durability of Diesel Particulate Filters (CRADA with Cummins Inc.).....	79
Agreement 26462 – International Energy Agency (IEA IA-AMT) Characterization Methods.....	86
Agreement 26463 – Biofuel Impact on Aftertreatment Devices.....	92
Project 18865 – Application-Specific Materials Simulation, Characterization, and Synthesis . 99	
Agreement 9105 – Characterization of Catalyst Microstructures.....	99
Agreement 26391 – Applied ICME for New Propulsion Materials.....	105
Project 21656 – Cast Alloys for Engines	115
Agreement 26021 – Development of Advanced High-Strength Cast Alloys for Heavy-Duty Engines.....	115
Agreement 26473 – Computational Design and Development of a New, Lightweight Cast Alloy for Advanced Cylinder Heads in High-Efficiency, Light-Duty Engines.....	126
Agreement 27382 – ICME Guided Development of Advanced Cast Aluminum Alloys for Automotive Engine Applications.....	137
Agreement 27387 – ANL: Alloy Development for Rotating Components	145
Agreement 27860 – Development of High-Performance Cast Crankshafts	152
Agreement 27926 – High-Performance Cast Aluminum Alloys for Next Generation Passenger Vehicle Engines (Project Number CEVT211)	162

(This page intentionally left blank)

Introduction

Propulsion Materials Research and Development: Enabling Materials Technologies to Meet Vehicle Technologies Office Goals

The Department of Energy's Vehicle Technologies Office (VTO) is pleased to introduce the *FY 2014 Annual Progress Report for the Propulsion Materials Research and Development Program*. Together with Department of Energy national laboratories and in partnership with universities and private industry across the United States, the Propulsion Materials Program continues to invest in research and development (R&D) that provide enabling materials technologies for fuel-efficient and environmentally friendly commercial and passenger vehicles.

This introduction summarizes the objectives and progress of the program in Fiscal Year 2014. The Propulsion Materials Program actively supports the energy security and reduction of greenhouse emissions goals of VTO by investigating and identifying the materials properties that are most essential for continued development of cost-effective, highly efficient, and environmentally friendly next-generation heavy and light-duty powertrains. The technical approaches available to enhance propulsion systems focus on improvements in both vehicle efficiency and fuel substitution, both of which must overcome the performance limitations of the materials currently in use. Propulsion Materials Program activities work with national laboratories, industry experts, and VTO powertrain systems (e.g., Advanced Combustion Engines [ACE], Advanced Power Electronics and Electrical Machines [APEEM], and fuels) teams to develop strategies that overcome materials limitations in future powertrain performance. The technical maturity of the portfolio of funded projects ranges from basic science to subsystem prototype validation.

Propulsion Materials Program activities are structured to serve as an enabling partner and supporter of the following VTO R&D activities:

- Hybrid and vehicle systems
- Energy storage
- APEEM
- ACE
- Fuels and lubricants

Projects within a Propulsion Materials Program activity address materials concerns that directly impact critical technology barriers within each of the above programs, including barriers that impact fuel efficiency, thermal management, emissions reduction, improved reliability, and reduced manufacturing costs. The program engages only the barriers that result from material property limitations and represent fundamental, high-risk materials issues.

Enabling Advanced Technologies

A Propulsion Materials Program activity focuses on key technical deficiencies in materials performance that limit the expanded capabilities of advanced combustion engines, electric-drive systems, and fuels and lubricants. It provides materials R&D expertise and advanced materials testing and development that support the goals of combustion, hybrid, and power electronics development. The program provides enabling materials support for combustion, hybrid, and power electronics development, including the following:

- Materials for high-efficiency combustion strategies such as homogenous-charge compression ignition.
- Materials for 55% thermal efficiency for heavy-duty diesel engines.
- Materials technologies for effective reduction of tailpipe emissions, including diesel particulate filters, low-temperature catalyst development, characterization and testing, and exhaust gas recirculation coolers.
- Materials technologies for electric and hybrid-electric vehicles, including thermal management of advanced power electronics materials and reducing dependence on rare earth elements in electric motors.
- Materials for alternate-fuels, including engine and exhaust aftertreatment materials compatibility and corrosion in biofuels.
- Support for the Materials Genome Initiative by evaluating existing computational tools and identifying gaps necessary for seamless integration across multiple length scales. Projects in this portfolio are validating the performance of existing tools, identifying gaps, and developing a suite of new materials with improved properties for engine applications.

The program supports these core technology areas by providing materials expertise, testing capabilities, computational expertise, and technical solutions for materials problems. The component development, materials processing, and characterization that the program provides are enablers of the successful development of efficient, durable, and emissions-compliant engines.

Program Organization

The Propulsion Materials Program consists of the following five R&D projects, which support VTO propulsion technologies. Each project consists of several R&D agreements.

1. Materials for Electric and Hybrid Drive Systems
 - Develop materials appropriate for automotive power electronics, electric motors, and other electric and hybrid system applications.
2. Materials for High-Efficiency Engines
 - Develop materials for next-generation, high-efficiency engines and address anticipated issues with engine cylinder block, head, crankshafts, pistons, valves and valve train, fuel injectors, turbochargers, and exhaust gas recirculation systems.
3. Materials for Control of Exhaust Gases and Energy Recovery Systems
 - Develop materials for exhaust aftertreatment and waste heat recovery applications.
4. Cast Alloys for Engines (group of competitively awarded industry-led projects)
 - Develop a suite of new, high-performance, low-cost cast alloys using an integrated computational materials engineering approach, targeting lightweight aluminum alloys for light-duty engines, high-strength cast ferrous alloys for heavy-duty engines, and high-performance cast steel alloys for high-performance crank shafts.

5. Materials by Design (Application-Specific Materials Simulation, Characterization, and Synthesis)

- Adopt computational materials design, including an atomic-scale characterization protocol to develop advanced materials for NOx catalysts, cast engine components, and electric motors and providing a pathway to transition Basic Energy Science research to practical applications.

R&D projects are evaluated annually using strategic objectives. Activities are evaluated based on their relevance to VTO objectives, the supported team's (i.e., ACE, APEEM, and fuels) assessment of the work, and the strength of industrial support for the activity. In order to meet future efficiency improvement targets, new projects and areas of research will be identified by assessments of VTO stretch objectives and resultant demands for increased material performance.

Stephen Goguen
Acting Program Manager, Materials Technology
Vehicle Technologies Office
Energy Efficiency and Renewable Energy

Jerry L. Gibbs
Technology Manager
Vehicle Technologies Office
Energy Efficiency and Renewable Energy

Project 18516 – Materials for Hybrid and Electric Drive Systems

Agreement 23726 – Novel Manufacturing Technologies for High-Power Induction and Permanent Magnet Electric Motors

Glenn J. Grant

Pacific Northwest National Laboratory

902 Battelle Boulevard, K2-03

Richland, WA 99356

Phone (509) 375-6890; fax (509) 375-4448; email: glenn.grant@pnnl.gov

Blair E. Carlson

General Motors Research and Development

30500 Mound Road

Warren, MI 48090

Phone (586) 864-7698; email: blair.carlson@gm.com

DOE Technology Manager: Jerry L. Gibbs

Phone (202) 586-1182; fax: (202) 586-1600; e-mail: jerry.gibbs@ee.doe.gov

Field Technical Manager: Yuri Hovanski

Phone (509) 375-2620; fax: (509) 375-2186; e-mail: yuri.hovanski@pnnl.gov

Contractor: Pacific Northwest National Laboratory, Richland, Washington

Prime Contract No.: DE-AC05-76RL01830

Objectives

- To apply novel solid-state joining and fabrication technologies to develop and deploy high-power induction and permanent magnet rotors and stators that are lighter weight, have better cooling, and are a lower cost to manufacture.
- To apply solid-state processing techniques to improve performance of a low-cost, soft, magnetic material used in the rotors of high-power induction motors.

Approach

- Develop solid-state joining techniques and manufacturing processes that will increase the efficiency of electric motors through lightweighting; improvements in electric and magnetic properties; and improvements in assembly-space efficiency, packaging, and cost.
- Develop the friction-stir welding (FSW) process parameters and evaluate proper tool materials and techniques to produce defect-free FSW in copper alloys specified by project partners.
- Develop a fundamental understanding of solid-state joints between copper materials and between dissimilar copper/aluminum materials. This fundamental knowledge is expected to lead to strategies and techniques that will be used to produce a joining process with low thermal input and low distortion of adjacent parts and to produce joints with a high degree of structural integrity and with high thermal and electrical continuity.
- Gain fundamental information to develop techniques for manufacturing copper and aluminum rotor and stator assemblies for high-power induction and permanent magnet motor systems. Industry collaborators will test and evaluate joined or processed components to demonstrate efficiency benefits and commercial applications.

- Transfer performance data and manufacturing technology to industry through a cooperative research and development agreement with General Motors (GM), ensuring a clear path to commercialization.

Accomplishments

- Demonstrated the software to produce a temperature-controlled weld in copper that can hold weld temperature to within $\pm 5^{\circ}\text{C}$ during the weld.
- Demonstrated a friction-processed region in low-cost, electric, steel-laminate material and characterized the microstructure and grain size of the processed zone.
- Demonstrated a welding strategy that eliminates the exit hole left by the tool pin in the copper end plate. The leading candidate is the ramp or wedge-extract concept. Tested the viability of this concept through experimental weld trials.
- Constructing a stationary shouldered tool assembly and demonstrating that defect-free welds can be made within 4 mm of the weld fixture wall, minimizing material wastage and part deformation.
- Completing full-sized weld-defect and exit-hole-free rotor-cage assemblies and submitting to GM for electrical efficiency testing.

Future Direction

- Use new solid-state joining and processing technologies to increase performance and lower manufacturing cost in alignment with the goals of the U.S. Department of Energy's program on Advanced Power Electronics and Electrical Motors.
 - Fundamental information gained will be used to develop techniques to manufacture copper and aluminum rotor and stator assemblies for high-power induction and permanent magnet motor systems
-

Introduction

This project aims to use novel solid-state joining and fabrication technologies to develop and deploy high-power induction and permanent magnet rotors and stators that are lighter weight, have better cooling, and are a lower cost to manufacture. Barriers to achieving these objectives focus on the manufacturability of novel rotor designs. The project team will apply FSW to join copper subassemblies and copper/aluminum joints to eventually produce prototype lightweight, high-efficiency rotor assemblies. Fundamental work tasks will first focus on copper/copper FSW and dissimilar copper/aluminum FSW joints. Later tasks will involve full-rotor assembly and testing by GM. In addition, the project will apply solid-state processing techniques to improve the performance of a low-cost soft magnetic material used in the rotors of high-power induction motors. GM will provide the motor design and Pacific Northwest National Laboratory (PNNL) will employ a novel method to fabricate the ferrous-based laminates specific to the GM motor design. The PNNL-developed method is based on nanoscale powder synthesis and friction extrusion/consolidation. This new fabrication process may allow for fewer energy-intensive processing steps to reach the microstructure and laminate thicknesses required for a high-performance soft magnetic material at a lower manufacturing cost. The project is a cost-shared cooperative research and development agreement between PNNL and GM.

Background

New manufacturing techniques can cause step changes in the overall cost of manufactured assemblies if the new technique creates a fundamental shift in the way a subsystem is constructed. For example, an electric motor has numerous components that are sensitive to high temperature. Fusion welding, which requires very high temperature to melt the materials being joined, cannot be accomplished directly adjacent to heat-sensitive parts such as sensitive electronics, wiring and insulation, or where coated laminates or substrates are located nearby. This restriction might require the part to

be assembled through a much more complicated multistep process. If another joining technology were available that did not heat the part, then the multistep assembly could be avoided, saving cost.

One example of a joining technology that could satisfy the need for lower adjacent part temperatures is FSW. Previous work by PNNL and others demonstrated that FSW can be made in copper alloys with excellent mechanical, electrical, and thermo-mechanical performance. FSW has a particular advantage in welding copper due to the wide range of weld-specific energy levels that can be applied by the process. Conventional fusion welding must deliver a high level of energy to melt the copper on each side of the joint line. In many applications, the high part temperatures during fusion welding can lead to distortion or overheated adjacent parts. FSW may provide a lower-heat-input joining technique in these special applications, where adjacent parts in the assembly can be damaged.

In addition, the next generation of rotor designs may be copper/aluminum hybrids or have aluminum components to reduce the rotating mass; therefore, joints may be needed between copper and aluminum. Solid-state joining techniques like FSW are logical to develop for specialized dissimilar joints like these that cannot be fusion welded due to the radically different melt temperatures of the components.

Approach

The project will develop the FSW process parameters and evaluate proper tool materials and techniques to produce defect-free friction-stir welds in copper alloys specified by project partners. In addition, the project team will develop statistical confidence around the manufacturing process used to fabricate high-power, induction-motor rotor assemblies (Figure 1) by applying a set of mechanical test methods and procedures to evaluate process robustness. The project team will also investigate the application of FSW to other joining issues around electric drive systems, including dissimilar joining between aluminum/copper and potentially

aluminum/aluminum joints in specific configurations.

Finally, to address the overarching goal of improved energy efficiency of the induction motor design, the project team will apply solid-state processing techniques to fabricate a low-cost soft magnetic material with unique properties that has the potential to display high magnetic flux density (B) and low iron loss (W). Amorphous iron-based metal and alloys offer excellent soft magnetic properties. Literature reports that the material could reduce the core losses of motors by more than 70% and that the efficiency of an induction motor with amorphous iron core could easily reach 80%. However, the production cost of an amorphous iron core is high. Specifically, the thickness of amorphous iron sheet cannot exceed $25\ \mu\text{m}$ because of the requirement for ultra-fast quenching. In this task, we will focus on developing a cost-effective method to produce soft iron alloy sheet with magnetic properties comparable to those of the amorphous iron alloy and with thickness greater than $100\ \mu\text{m}$. This method is based on a modified friction consolidation and extrusion method, where the material is subjected to high strain under a hydrostatic state of stress. This solid-state process has shown the ability to produce ultra-fine grain size in bulk solids.

This project will be divided into three primary task areas: Task 1 will focus on solid-state joining of copper materials used in the rotor assemblies of high-power induction motors. Task 2 will focus on dissimilar material joining, primarily copper to aluminum with an emphasis on components and assembly performance improvement. Task 3 will develop a unique solid-state process to create appropriate microstructures and magnetic performance in bulk soft magnetic materials that may be able to improve on the efficiency of stack laminates in the rotor assembly.

The induction motor rotor represents an excellent example of a multi-material assembly that may be manufactured more efficiently and at a lower cost if new manufacturing techniques could be developed. This project is investigating

using solid-state welding (i.e., FSW) to assemble this component.



Figure 1. Rotor concepts fabricated with FSW.

The primary scope of Task 1 is to develop a weld process to join the copper end cap to the shorting bars that traverse the soft magnetic core of the rotor. These bars carry current up and down the rotor between the end caps to produce the magnetic moment that drives the rotor. The joint has several important characteristics. It needs strength because it will be subjected to high tensional and cantilever loads when the rotor is moving at high revolutions per minute; it needs to have optimum electrical conductivity for high efficiency; and during the joining operation, it cannot get hot enough for the underlying electric steel laminates to melt their polymeric insulating coatings. Figure 2 shows a schematic of a rotor and a photo of a rotor end cap in place on the shorting bars just prior to joining.

Maximum electrical continuity is one of the key factors in rotor efficiency and lightweighting. The joint must be designed for the highest electrical cross section at the minimum weight penalty. The thickness of the heavy copper end cap is a key variable to optimize. The minimum end cap thickness is desirable for weight savings, yet the highest electrical cross section is desirable for current flow. This requires the joined region to have the largest possible area between the end cap and the shorting bar. Figure 3 shows the challenge schematically.

The joined area intersecting the end cap and shorting bar must have maximum width and appropriate depth. The better the electrical continuity and current flow in this area, the thinner the end cap and the greater the weight savings. Much of the work during Fiscal Year

(FY) 2014 was directed at creating a FSW joint that satisfies these demands. The joined area is a function of tool design, tool materials, process parameters, and boundary conditions during welding.

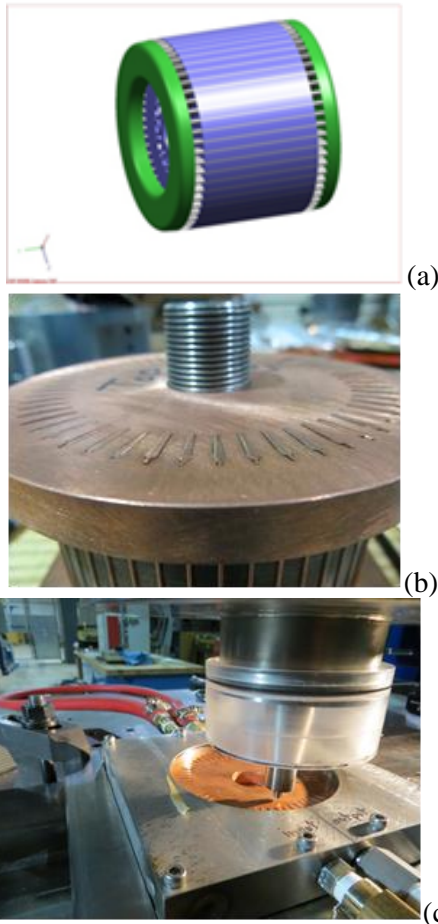


Figure 2. (a) Rotor schematic, (b) copper end ends prior to joining, and (c) friction-stir tool and rotor in fixture prior to welding.



Figure 3. Schematic of the end cap/shorting bar joined area.

Results

During FY 2014, experimental weld trials focused on solving several issues for practical commercialization of the FSW process on a copper-based induction rotor. These problems included weld process refinements to cure part deformation and weld defects seen in some process conditions and developing a strategy for handling the exit hole formed at the end of a weld path after withdrawing the tool from the rotor end cap.

Weld Refinements, Defects, and Process Control

The team completed FSW trials on both linear welds on the copper plate and on two-dimensional circular configurations. Welds were developed for both monolithic materials and for plates that have cutouts for copper bars running the length of the rotors.

Several challenges emerged involving control of the process and weld quality. A circular weld involves returning to the beginning of the weld start area and, in some cases, over running an area previously welded. This creates an ever-changing set of boundary conditions, including a temperature field that changes throughout the weld.

Figure 4 shows a plot of tool temperature versus time taken during the course of a circular weld. The plot shows a continuously increasing temperature during welding. The lack of stability of the tool (and thus weld) temperature can create a wide range of defects, including excess flash and loss of material (see Figure 5).

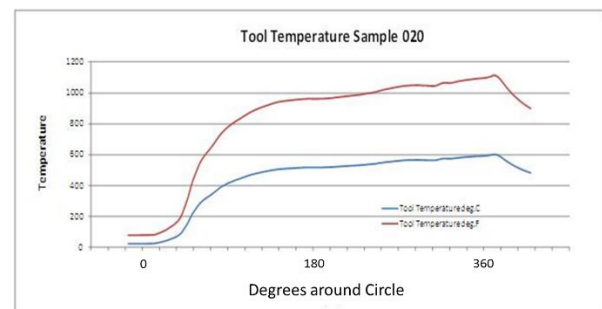


Figure 4. Tool temperature versus time during a circular weld.

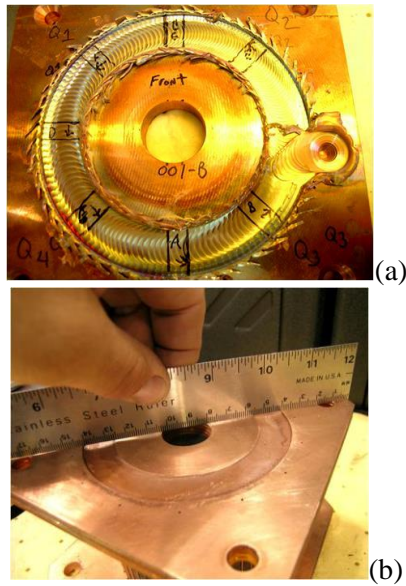


Figure 5. Circular weld run too hot showing (a) excessive flash and loss of material and (b) excessive distortion.

Loss of weld material leads to internal defects and loss of electrical continuity in the joint, a particularly important property that must be maintained in an end-cap weld. To compensate for a weld that is too hot, the process parameters can be set to generate less heat in the process. However, if the parameters are set too low, this can lead to defects that are usually manifested by voids developed in the weld direction (Figure 6).



Figure 6. Surface-breaching void defect due to weld parameters that did not deliver enough weld energy for a consolidated joint.

During FY 2014, the project further developed an adaptive power control system. To adapt to changing temperature boundary conditions, the weld parameters are allowed to change through a torque and power-based

feedback system. This system controls power and tool temperature through a feedback nested-loop controller and can make high-speed adjustments to power to keep tool temperatures within a set range. The system, once fully developed, is expected to solve several of the current challenges to maintaining welds of consistent quality.

Strategies for Mitigating the Exit Hole

Another challenge to commercial implementation concerns a feature of FSW joining, whereby a void is left at the end of the weld run as the tool is extracted from the weld. This is not a problem for a typical weld where the weld can be finished on a run-off tab or in some structurally insignificant area of the part. However, for a circular weld, the weld exit occurs in the welded area and a large void in the part is not acceptable. During FY 2014, the following two concepts for dealing with the exit hole were tested:

6. Utilization of a “ramp” exit
7. Plugging the exit hole with a secondary operation – a solid-state, friction-taper, stud-plug weld.

Exit Ramp

An exit ramp is a wedge-shaped block of material placed on the part surface just before the end of the weld. As the tool travels along the surface, it encounters the ramp and welds up the ramp to a predetermined stop point. As it does this, the pin engages less and less of the original surface until it is completely above the surface and fully engaged only in the ramp material. The ramp serves as a sacrificial material to be removed later.

Two different control mechanisms were utilized to operate the machine to make the tool go up the ramp: (1) position control, in which the slope of the ramp is programmed into the machine, and (2) load control, in which the machine is commanded to maintain a particular force as the tool traverses up the ramp. This command forces the machine to raise the tool in response to increasing loads up the ramp.

The position-control test showed significantly better results than the load-control

test. During the analysis of the weld cross sections along the traverse direction, no defects were introduced inside the nugget where the tool crossed the interface between the ramp and the plate (Figure 7).

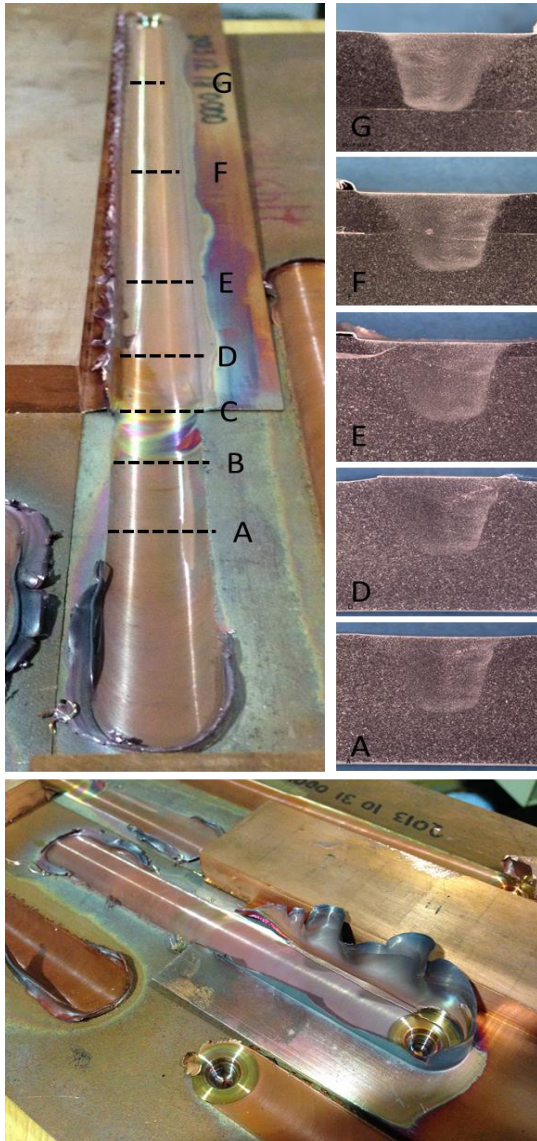


Figure 7. Position-controlled (top) and load-controlled ramp weld (bottom).

During the load-controlled test, the ramp material softened and became incapable of sustaining the load while the tool was traversing.

However, the ramp exit is a complex strategy to implement in a manufacturing environment because, in the case of the rotor, the ramp needs to be semicircular and needs to be placed automatically on the weld area after

the weld has started. The setup requires a complex set of automatic fixtures and actuators.

Friction Taper Stud Welding

Friction taper stud welding consists of rotating a consumable tool concentrically in a hole, while applying a downward load to continuously generate a localized plasticized layer. The plasticized material develops at a rate faster than the axial feed rate of the consumable tool; therefore, the frictional rubbing surface rises up along the length of the tool, giving a dynamically recrystallized interface layer that forms the weld. The concept is to use this process after the weld is finished as a secondary process for closing the exit hole. The plug welding option may be easier to apply in an industrial setting because the FSW and the plug welding are done on the same machine without removing the part from the fixture. This option may be better than the wedge-extract option due to the complex fixturing required by the wedge system.

During FY 2014, the project designed and tested a wide range of tapered plugs. The criterion for a good plug weld is 100% density with no volumetric defects. This requires that the shape of the plug is appropriate for the shape of the FSW tool exit hole. Also, there is a complex relationship between the process parameters and how the plug deforms as it fills the hole. Figure 8 shows the main design variables: the shank, the shoulder, the neck, the cone, and the tip. The tip is designed to facilitate heating up and deformation of the plug in the bottom of the hole and is the first point of contact of the tool. The cone approximates the shape of the hole. The neck is where the plug breaks once the weld is done. The shoulder should assist in forging down the welded material. The shank should be able to withstand and transfer the torque during the entire process.

Figure 9a shows the dimensions of the current stud designs that have produced the best densification of the cross section. As seen in the weld cross section, some voids are still present and additional efforts in tool design and process parameters are ongoing to get a better consolidation in this region.

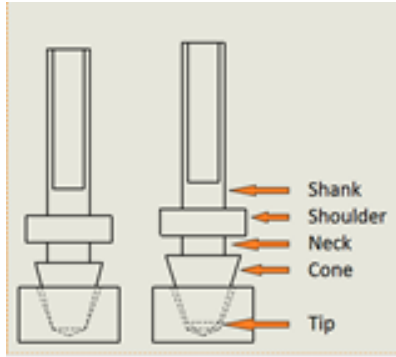


Figure 8. Taper plug terminology.

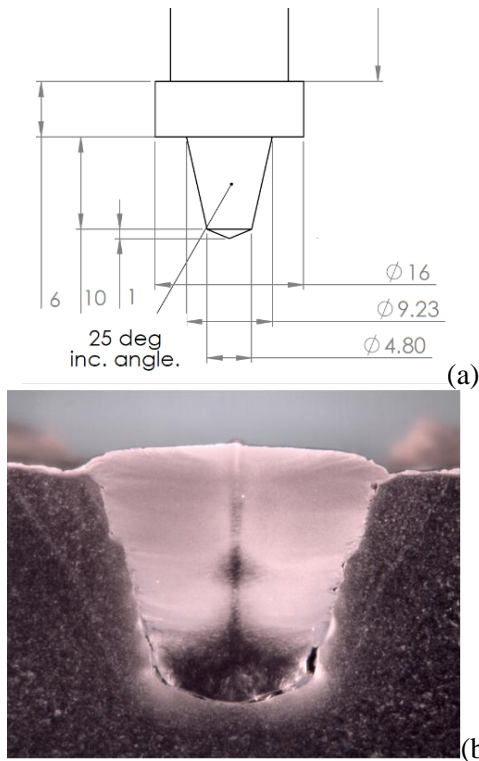


Figure 9. (a) Example of current taper plug dimensions and (b) cross section of taper plug weld showing some lack of fill near the base.

The current experimental efforts are directed at two different plug-welding techniques. The first is focused on optimizing the processing parameters and tool designs for performing the plug weld directly into the exit hole. The objective is to eliminate volumetric defects that can be observed in Figure 9 in the hole/plug interface, particularly in the bottom. This type of defect is commonly ascribed in the literature to low forging force. The second focus of experimental trials involves eliminating the

imperfections of the current exit hole by drilling/machining, followed by plug welding on a more uniform tapered hole. For this, the project designed the two different plug geometries shown in Figure 10.

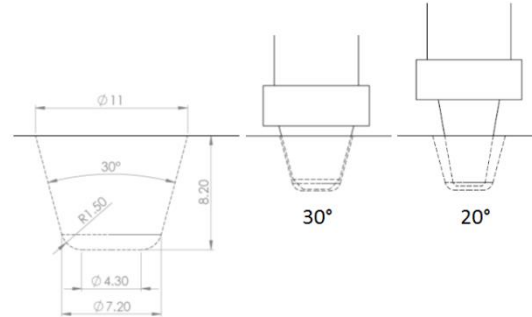


Figure 10. The final geometry of the drilled hole on the left followed by two tool designs for this scenario.

Conclusions

Motor designs, like all complex assemblies, are a compromise between performance and cost (i.e., cost of materials and of manufacturing). New manufacturing processes can be critical in this balance because they can enable lower-cost materials and introduce a lower-cost manufacturing process. In many cases, the new manufacturing process may even directly increase the efficiency of the part by producing an assembly that displays better thermal, mechanical, or electric/magnetic properties. This project will use new solid-state joining and processing technologies to increase performance and lower manufacturing cost in alignment with the goals of the U.S. Department of Energy's (DOE) program on Advanced Power Electronics and Electrical Motors (Figure 11).

Specifically, the project will develop the fundamental understanding of solid-state joints between copper materials and between copper-aluminum dissimilar joints, so they can be achieved with low thermal input, low distortion of adjacent parts, a high degree of structural integrity, and a high degree of thermal and electrical continuity. The fundamental information gained will be used to develop techniques to manufacture copper and aluminum rotor and stator assemblies for high-power induction and permanent magnet motor systems.

Industry collaborators will evaluate joined or processed components to demonstrate efficiency

benefits and commercial applications.

► This Project:

- Will develop a lower cost manufacturing technique to fabricate rotors and stators

- Will develop fabrication techniques that will allow multi-material designs for weight and cost savings

- Will explore a new manufacturing process to fabricate soft magnetic materials for rotor and stator laminates.

Maps to:

Advanced Power Electronics and Electrical Motors Area

Research Focus Areas (Reduce cost and maintain performance)	
Permanent Magnet (PM) Motors	<ul style="list-style-type: none"> ❑ Reduce cost by 75% - required to meet 2020 target ❑ Motor design optimization may reduce cost by 25% to 40%.
Magnet Materials	<ul style="list-style-type: none"> ❑ Magnet material costs are 50% of 2015 target and 75% of 2020 target ❑ Reducing PM cost and increasing temperature capability could reduce motor cost by 5% to 15%
Non-PM Motors	<p>Non-PM motor technology yields the greatest opportunity for motor and system cost reduction:</p> <ul style="list-style-type: none"> ❑ Could reduce motor cost by 30% ❑ Eliminating boost converter (required for IPM machines due to back emf) saves 20% in PE cost ❑ Optimized power factors of non-PM machines can result in up to 15% PE cost savings
New Materials	<ul style="list-style-type: none"> ❑ New materials for laminations, cores, etc. could save 20% of motor cost

ORNL/TM-2011/73, Final Report on Assessment of Motor Technologies for Traction Drives of Hybrid and Electric Vehicles, by R. R. Fessler published March 10, 2011.

Figure 11. Project objectives mapped to the U.S. DOE’s goals and targets for the Advanced Power Electronics and Electrical Motors Area.

Project 18516 – Materials for Hybrid and Electric Drive Systems

Agreement 26461 – Enabling Materials for High-Temperature Power Electronics

Andrew A. Wereszczak* and Zhenxian Liang†

*Materials Science and Technology Division

†Electrical and Electronics Systems Research Division

Oak Ridge National Laboratory

P.O. Box 2008, MS 6068, Building 4515

Oak Ridge, TN 37831-6068

Phone (865) 576-1169; fax (865) 574-6098; email: wereszczakaa@ornl.gov

DOE Technology Manager: Jerry L. Gibbs

Phone (202) 586-1182; fax: (202) 586-1600; e-mail: jerry.gibbs@ee.doe.gov

Field Technical Manager: J. Allen Haynes

Phone (865) 576-2894; fax: (865) 574-4913; e-mail: haynesa@ornl.gov

Contractor: Oak Ridge National Laboratory, Oak Ridge, Tennessee

Prime Contract No.: DE-AC05-00OR22725

Objectives

- Develop and incorporate innovative and cost-effective materials that are to be used within power electronic modules (PEMs) that improve lifetime by 10 times over current state-of-the-art PEMs, while providing sustained operation to at least a 180°C junction temperature.
- Evaluate and enhance materials that would reliably bond constituents within PEMs, promote more efficient thermal transfer among them, and fulfill those characteristics while functioning at 180°C or higher.

Approach

- Demonstrate efficacy of bonding wide band gap (WBG) die to copper cladded substrate using silver sintering interconnection.
- Measure thermal properties of high-temperature-capable perfluoropolymers for power electronic modules (PEM) use.
- Compare shear strength responses of Ag and Au-plating on direct-bonded copper (DBC) substrates.
- Submit article to the Institute of Electrical and Electronics Engineers conference on silver sintering.

Accomplishments

- Developed test coupons to study the effects of residual stress in sintered silver interconnects.
- Co-developed (with the National Renewable Energy Laboratory) fatigue model for delamination of sintered silver interconnects.
- Published an article on sintered silver processing strategies.
- Submitted invention disclosure on sintered silver pad shape to mitigate stress concentrations in sintered silver interconnects.

Future Direction

- Complete processing of DBC sandwiches, coefficient of thermal expansion (CTE)-mismatched disk specimens, and their mechanical and thermal-cycling testing.
 - Correlate delamination response of interconnects in CTE-mismatched specimens with V-K analysis.
-

Introduction

The Vehicle Technology Program's Advanced Power Electronics and Electric Motors Program has expressed emphasis on cost-reducing research targets, challenges, and areas. These include high-temperature components, packaging, and reliability for long-term transformation technologies and thermal management technologies to reduce volume and enhance thermal reliability. The technical goals of this project directly strike at that emphasis.

PEMs are subjected to high service temperatures that require efficient and sustained thermal management so they can reliably perform during a 15-year lifetime. Higher-temperature capability also is now of greater interest, with the increased desire to use and exploit wide WBG semiconductor technology and its attributes. The achievement of increased reliability and temperature capability, with concomitant decreases in size, weight, and cost, will occur when the following four aspects are addressed in parallel:

- *Increase strain tolerance among and between PEM constituents.* PEMs are comprised of many different material constituents, with each serving a specific electrical function. Those dissimilar materials will impose residual strains on each other during service that can cause inter and intra-constituent mechanical failures (resulting in loss of electrical function of the entire PEM) if those strains are sufficiently high. Those strains are amplified as PEM service temperature increases. An increase in the inter-bonding strain tolerance, or strength, between constituents will improve overall PEM reliability.
- *Reduce imposed strain on PEM constituents.* This is accomplished through improved thermal management of the constituents and their simpler architectural design. This includes using more thermally conductive materials, where allowed, and reducing the complexity of the PEM's interior architecture to position the semiconductor closer to the heat sink. A reduction in the imposed strain, no matter the means, among the PEM constituents, will improve overall PEM reliability.
- *Increase temperature capability of constituents.* As WBG semiconductors are integrated more frequently into PEMs, the temperature capability of the rest of the PEM constituents must also increase. This is because the temperature capability of the entire PEM is only as high as that of the lowest temperature-capable constituent. PEM constituents consist of polymers, metals, semiconductors, and ceramics; therefore, consideration of higher temperature-capable polymers must occur to increase the temperature capability of the entire PEM.
- *Reduce or sustain cost while satisfying the other three aspects.* This perhaps is the greatest challenge. However, careful and innovative materials science and engineering can indeed accomplish this. Such innovation can result via use of unconventional, yet mature, materials that are used in other (non-electrical) applications.

This project model for achieving improved reliability, smaller size, and higher-temperature capability of PEMs is best achieved through a marriage of electronic package engineering and materials science and engineering. This will be accomplished through a collaboration of the Vehicle Technology Program's Propulsion Materials and Advanced Power Electronic and Electric Motors Programs, and the testing of surrogate specimens (see Figure 1) that facilitate characterizations of plating and interconnect materials. Collaboration with the National Renewable Energy Laboratory will occur, pending programmatic authorization on their size. Additionally, input from the USCAR Electrical and Electronic Technical Team will contribute to this project's path.

Results

Four efforts comprised the Fiscal Year (FY) 2014 effort.

Sinter-Silver Interconnection of WBG Die

Silicon carbide WBG semiconductor dies were bonded to silver-plated DBC substrates using sinterable silver paste. Examples of bonded dies are shown in Figure 1. Their surface character is shown in Figures 2 and 3. A commercially available sinterable paste was used to bond integrated gate bipolar transducers and diodes at elevated temperature with pressure assistance. Polished cross-sections of the bonded joint showed that a consistently good joint was produced.

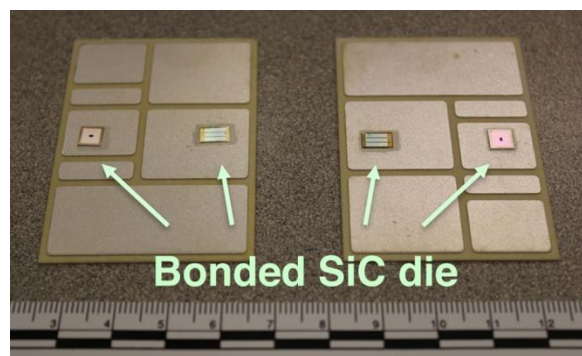


Figure 1. Silicon carbide diodes (far left and far right) and MOSFETs (inner left and inner right) silver-sintered onto a DBC substrate.

MgO-Filled Perfluoropolymers

The consideration of a high-temperature-capable, thermally conductive molding compound occurred. A perfluoropolymer was chosen for the matrix material, owing to its high-temperature capability. MgO filler was chosen because of the past demonstration of it increasing the thermal conductivity of epoxy. Processed billets are shown in Figure 4.

Properties were measured (see Table 1), but processing complications associated with the perfluoropolymer and its bonding to the filler were identified using the specimens shown in Figure 5. While the MgO filler increased the thermal conductivity, this material system needs additional development in order to confidently exploit its potential.

Silver Sintering and Platings

The study of the comparison and effect of plating material and printing method (i.e., screen and stencil printing) on interconnect shear

strength is underway. An illustration of this and the examples of to-be-tested processed test coupons are shown in Figures 6 and 7. Unfortunately, the work was delayed for months because of laboratory equipment movement. Processing of test coupons has neared completion now; shear testing and performance interpretation will begin and end early in the first quarter of FY 2015.

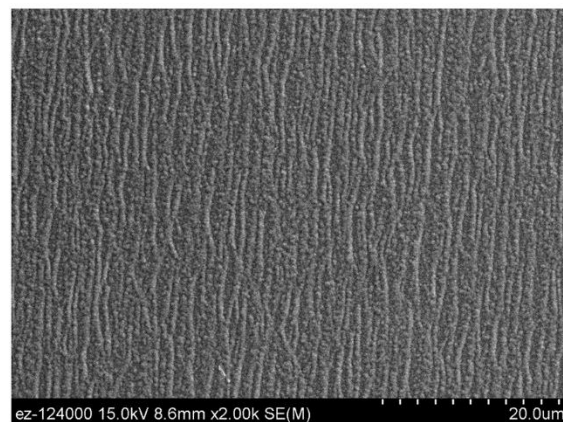
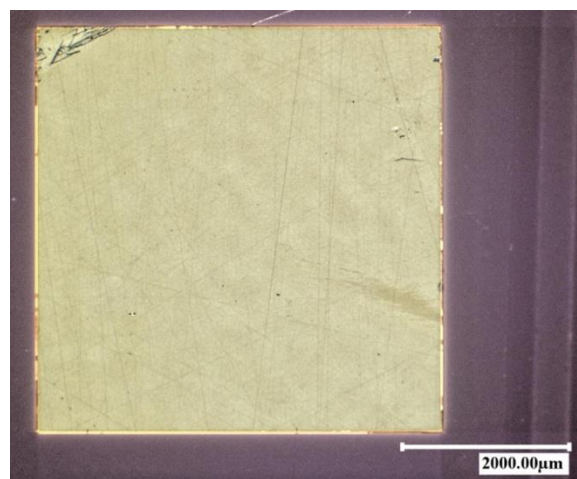


Figure 2. Low (top) and high (bottom) magnification images of the silicon carbide diode surface that was silver-sinter interconnected to the DBC substrate shown in Figure 1.

Article on Silver Sintering

A journal article was written that overviews Oak Ridge National Laboratory's silver sintering work from the last couple of years (its reference: A. A. Wereszczak, Z. Liang, M. K. Ferber, and L. D. Marlino, 2014, "Uniqueness and Challenges of Sintered Silver as a Bonded

Interface Material,” in press, *Journal of Microelectronics and Electronic Packaging*).

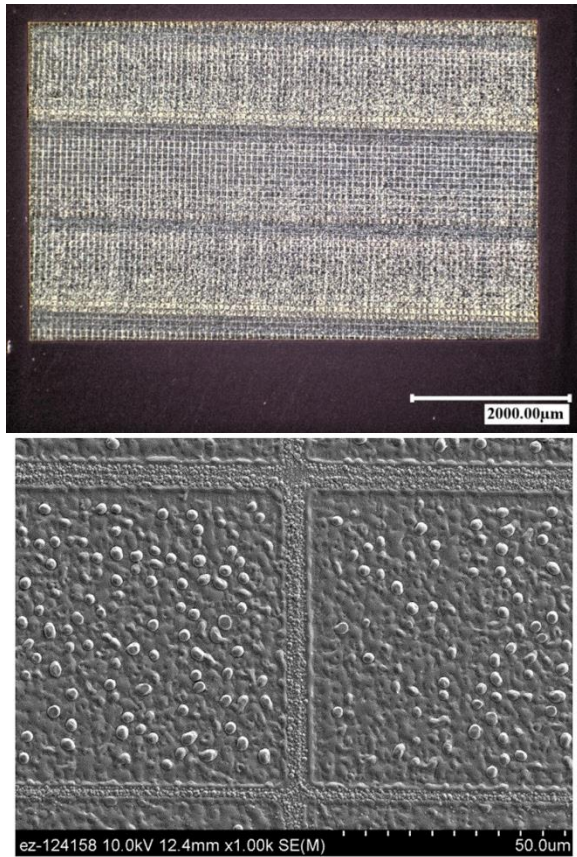


Figure 3. Low (top) and high (bottom) magnification images of the silicon carbide MOSFET surface that was silver-sinter interconnected to the DBC substrate shown in Figure 1.

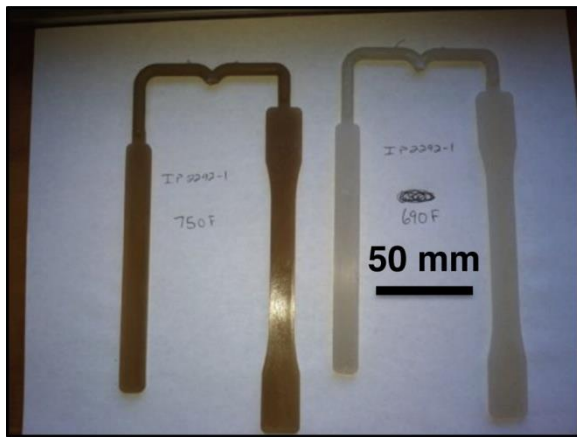


Figure 4. Billets of MgO-filled perfluoropolymer.

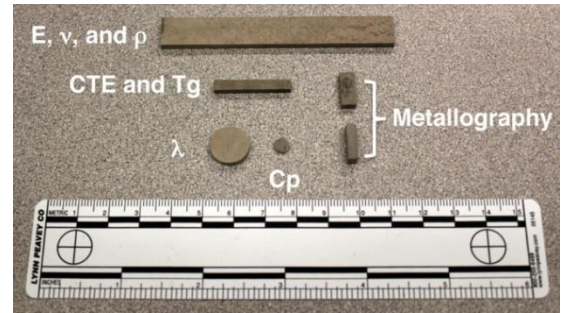


Figure 5. Harvested test coupons from MgO-filled perfluoropolymer billets.

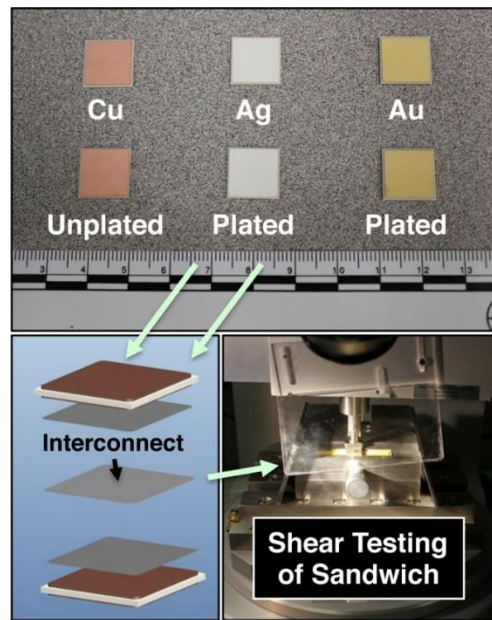


Figure 6. DBC substrates, sandwiching, and shear-strength testing.



Figure 7. Processed DBC sandwiches ready for shear-strength-testing. The effects of plating (silver versus gold) and printing method (screen versus stencil) on shear strength are under evaluation.

Table 1. Properties of the MgO-perfluoropolymer composites (silane-coated MgO) compared with base polymer.

Property	1	5	6	7
Wt. % ECA 3000	100	39.5	45.5	51.5
Wt. % MgO	0	60	54	48
Wt. % Silane treatment	0	0.5	0.5	0.5
Density (g/cc)	2.12	2.65	2.60	2.54
Vol. % ECA 3000	100	64	67	71
Vol. % MgO	0	36	33	29
Thermal diffusivity at 25°C (mm ² /s)	*	0.36	0.43	0.33
Heat capacity at 25°C (J/kg·K)	1010	914	957	998
Thermal conductivity at 25°C (W/mK)	0.4 **	0.9	1	0.8
T _g (°C)	-190	>200	>200	>200
Average CTE (ppm/°C)	162	85	95	108
Elastic modulus through 0.5% strain (GPa)	0.31	*	0.70	0.70

Conclusions

The bonding of a WBG die to copper-cladded substrate using a silver-sintering interconnection was demonstrated. A commercially available sinterable paste was used to bond integrated gate bipolar transducers and diodes at elevated temperature with pressure assistance. Consistently good joints were produced.

A candidate high temperature-capable, thermally conductive molding compound was considered. Processing complications associated with the perfluoropolymer and its bonding to the MgO filler were identified. This system needs additional development in order to confidently exploit its potential.

The evaluation of the shear strength responses of Ag and Au-plating on DBC substrates was initiated. Processing of test coupons has neared completion now; shear testing and performance interpretation will end early in the first quarter of FY 2014.

An article reviewing silver sintering was submitted to an Institute of Electrical and Electronics Engineers journal: A. A. Wereszczak, Z. Liang, M. K. Ferber, and L. D. Marlino, 2014, "Uniqueness and Challenges of Sintered Silver as a Bonded Interface Material," in press, *Journal of Microelectronics and Electronic Packaging*.

Publications

- A. A. Wereszczak, 2014, "Improved Sintered Silver Joints via Controlled Topography of Electronic Packaging Subcomponents," U.S. Patent 8,822,036 B1, 02 September 2014.
- R. Wiles and A. A. Wereszczak, 2014, "Motor Size Reduction via use of Novel Phase Change Materials," Invention Disclosure Number 201403317, DOE S-124,932, 15 April 2014.
- A. A. Wereszczak, 2014, "Hybrid-Filled Epoxy Molding Compositions," U.S. Patent Application No. 14/180,633, 14 February 2014.
- A. A. Wereszczak, D. J. DeVoto, and P. P. Paret, 2013, "Perimetric Structure for Improved Reliability in Electronic Device Interconnection," Invention Disclosure Number 201303197, DOE S-124,788, October 2013.
- A. A. Wereszczak, Z. Liang, M. K. Ferber, and L. D. Marlino, 2014, "Uniqueness and Challenges of Sintered Silver as a Bonded Interface Material," in press, *Journal of Microelectronics and Electronic Packaging*.
- A. A. Wereszczak, Z. Liang, M. K. Ferber, and L. D. Marlino, 2014, "Uniqueness and Challenges of Sintered Silver as a Bonded Interface Material," Paper WA23, pp. 178-187 in *Proceedings of the IMAPS HiTEC 2014*, Albuquerque, NM.
- D. Devoto, P. Paret, and A. A. Wereszczak, 2014, "Stress Intensity of Delamination in a Sintered-Silver Interconnection," Paper WA26, pp. 190-197 in *Proceedings of the IMAPS HiTEC 2014*, Albuquerque, NM.
- A. A. Wereszczak, T. G. Morrissey, C. Volante, P. Farris, Jr., R. Groele, R. H. Wiles, and H. Wang, 2013, "Thermally Conductive MgO-Filled Epoxy Molding Compounds," *IEEE Transactions on Components, Packaging and Manufacturing Technology* 12(3):1994-2005.

Project 18518 – Materials for High-Efficiency Engines

Agreement 13329 – Design Optimization of Piezoceramic Multilayer Actuators for Heavy-Duty Diesel Engine Fuel Injectors

Hong Wang, Hua-Tay Lin, and Andrew A. Wereszczak

Materials and Technology Division

Oak Ridge National Laboratory

PO Box 2008, MS 6069

Oak Ridge, TN 37831-6068

Phone (865) 574-5601; fax (865) 574-6098; email: wangh@ornl.gov

DOE Technology Manager: Jerry L. Gibbs

Phone (202) 586-1182; fax: (202) 586-1600; e-mail: jerry.gibbs@ee.doe.gov

Technical Advisor: J. Allen Haynes

Phone (865) 576-2894; fax: (865) 574-4913; e-mail: haynesa@ornl.gov

Contractor: Oak Ridge National Laboratory, Oak Ridge, Tennessee

Prime Contract No.: DE-AC05-00OR22725

Objectives

- Apply established structural ceramic probabilistic design and reliability analysis to piezoelectric multilayer actuators (PMLAs).
- Generate the required micromechanical property data on lead zirconate titanate (PZT) piezoceramics and macro-mechanical property data on PMLAs for input into the design and reliability analysis of the latter.
- Identify minimum mechanical performance requirements for fuel injector PMLAs.
- Adapt these strategies to improve reliability of PMLAs that are candidates for use in diesel engine fuel injectors.

Approach

- Evaluate PMLA reliability under representative service conditions.
- Link constituent piezoceramic micromechanical and PMLA macro-mechanical responses.

Accomplishments

- Experimental study on the down-selected piezo stacks for heavy-duty diesel engine fuel injector continued on the 10-layer plate specimens extracted from the prototype stacks.
- Piezodilatometer was upgraded to include temperature capability and cycle testing on the 10-layer plate specimen conducted in temperature environment.
- The effect of humidity and a temperature environment on the mechanical strength of PZT was studied by using a ball-on-ring setup.

Future Direction

- Investigate the fatigue responses of PZT stacks in a high-electrical-field cycle test in a specified temperature environment.
 - Study the effect of long-term exposure to humidity and temperature (i.e., 80% RH, 85°C or equivalent) on the mechanical strength of down-selected PZT ceramics.
-

Introduction

The use of PMLAs as diesel fuel injectors has the potential to reduce injector response time, provide greater precision and control of the fuel injection event, and reduce energy consumption. PMLA (or piezo-stack) fuel injectors contain a solid-state ceramic actuator that converts electric energy into linear motion, precisely controlling the needle's opening and closing. This capability results in an engine with outstanding performance, improved fuel economy, low noise, and low emissions. Though their use is very attractive for the reasons mentioned, uncertainty continues as to how reliable piezo-actuated fuel injectors will be in the challenging environment of a heavy vehicle diesel engine. Though piezoelectric actuation is the obvious primary function of PZT ceramic PMLAs for fuel injectors, their reliability may be a performance and life limiter because the PZT ceramic within them is brittle, lacks high strength, and may exhibit fatigue susceptibility. That brittleness and relatively low strength can be overcome with a proper probabilistic component design methodology.

This project undertakes the reliability characterization of candidate PMLAs used in these fuel injectors and the piezoceramics used in the PMLAs. Testing and characterization of the piezo stacks and piezoceramics have continued based on recommendations from Cummins Inc.

Results

Characterization of Piezoelectric Multilayer Actuators

The objective of this work is to develop an experimental approach to conducting accelerated electric fatigue testing and, at the same time, characterizing the fatigue responses and lifetime of down-selected piezo stacks. The database and understandings developed in this study can be applied by end users in optimizations of the design and deployment of piezo stacks in a heavy-duty fuel injection system.

The down-selected piezo stack (manufactured by EPCOS) for a heavy-duty engine fuel injector has dimensions of $12 \times 12 \times 54$ mm. The rated capacitance is $16.15 \mu\text{F}$.

Testing of stacks of this size presents a substantial challenge to electronic systems. To address this issue, low-profile stacks with a relatively low capacitance or 10 and 20-layer plates extracted from prototype stacks were used in cyclic fatigue tests. The prototype stacks generally were provided without any encapsulation and the partial discharge would be induced near the surface of stacks during cycling should the test be carried out in open air. The testing of the extracted specimens was conducted by using a piezodilatometer system developed at Oak Ridge National Laboratory. The piezodilatometer system is equipped with electronic liquid (FC-40) to control the partial discharge.

The piezodilatometer was upgraded in the reporting period to include temperature capability. Immersion heating was proposed, in which the specimen was heated by a hot electronic liquid. An MTO-110/120 E1 immersion heater (Omega, Stamford, CT) was installed in the tank of the piezodilatometer, along with temperature control (see Figure 1).



Figure 1. An immersion heater (MTO-110/120 E1) is installed in the tank of piezodilatometer that can heat the electronic liquid to a target temperature.

The 10 and 20-layer plates were provided by Cummins, Inc. The cycle test followed the procedures described previously in Zeng et al. (2013). The unipolar sine wave with peak levels $3.0/0.0$ kV/mm at 100 Hz was used in cycling. The cycle test stopped when the accumulated cycles reached 10^8 or breakdown occurred. The measurement for piezoelectric response involved a 0.1-Hz triangle wave with amplitudes of

1.5/0.0 and 3.0/0.0 kV/mm, and the measurement for dielectric response consisted of a 50-Hz sine wave with the same amplitudes. Testing of 10-layer specimens was conducted in the reporting period. Preliminary testing in an elevated temperature environment was also conducted on a 10-layer specimen.

Two 10-layer specimens were found to have had dielectric breakdown in poling. For those that sustained poling, one (P1002) has completed 10^8 cycles, whilst two (P1007, P1009) did not reach the target number of cycles due to dielectric breakdown. The fatigue responses of the PZT stacks in terms of piezoelectric coefficient d_{31} , piezoelectric loss angle δ_{p31} , dielectric coefficient ϵ_{33} , and dielectric loss angle δ_{33} are given in Figures 2 and 3, respectively. The pre-fatigue coefficients of the specimens apparently fall within the range of published data (Zeng et al. 2013, Wang et al. 2010, Noliac Group 2013). The results demonstrated that the integrity of specimens as a piezo stack had been maintained, even though the specimens were extracted from prototype stacks but not delivered as a standard product.

There was a certain effect of measurement field level on the measurement results. Under a higher measurement field, a smaller value of piezoelectric or dielectric coefficients was usually observed. This was mainly because of the saturated polarization and suppressed domain switching from dc bias, which became stronger with an increasing measurement field (Wang et al. 2014). Given a measurement field, the absolute value of d_{31} and ϵ_{33} exhibited a substantial reduction after about 10^6 cycles. On the other hand, no clearly defined variation trend was observed for the loss angles during fatigue testing. Overall, the fatigue-induced degradation in 10-layer specimens, especially of piezoelectric coefficient, was lower than that in 20-layer specimens. The cyclic fatigue testing at 50°C was conducted on a 10-layer specimen (P1010) with the cycle number over 4×10^7 . The online monitoring of dielectric response was enabled. The variations of ϵ_{33} are presented in Figure 4 for the specimens tested at both room temperature and 50°C .

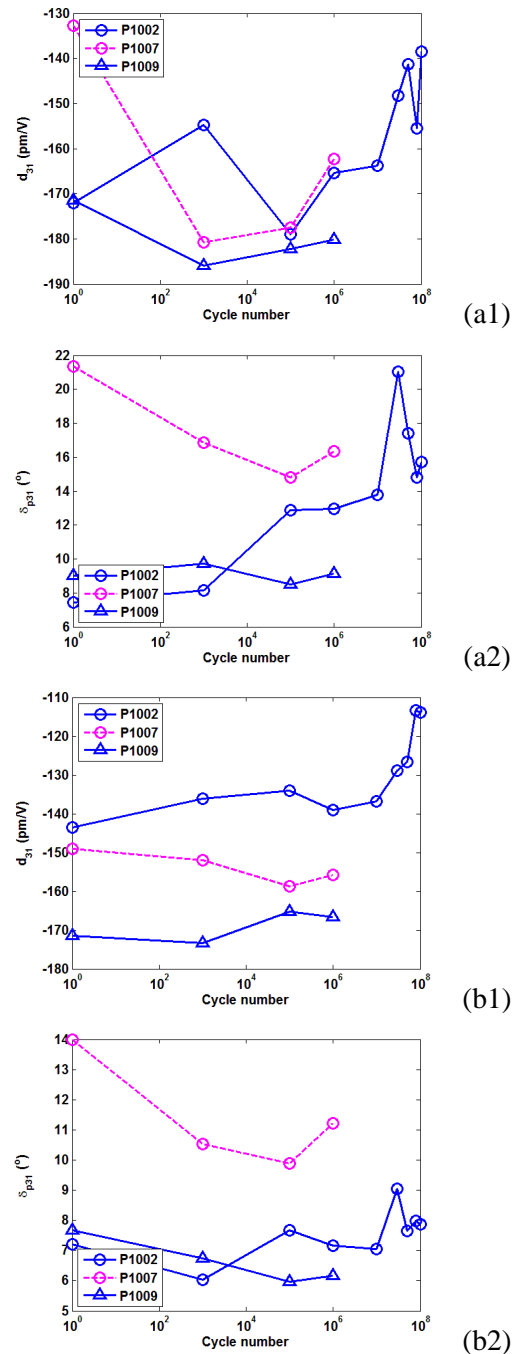


Figure 2. Variation of piezoelectric coefficients d_{31} and piezoelectric loss angle δ_{p31} as a function of cycle number measured at (a) 1.5 kV/mm and (b) 3.0 kV/mm for 10-layer specimens.

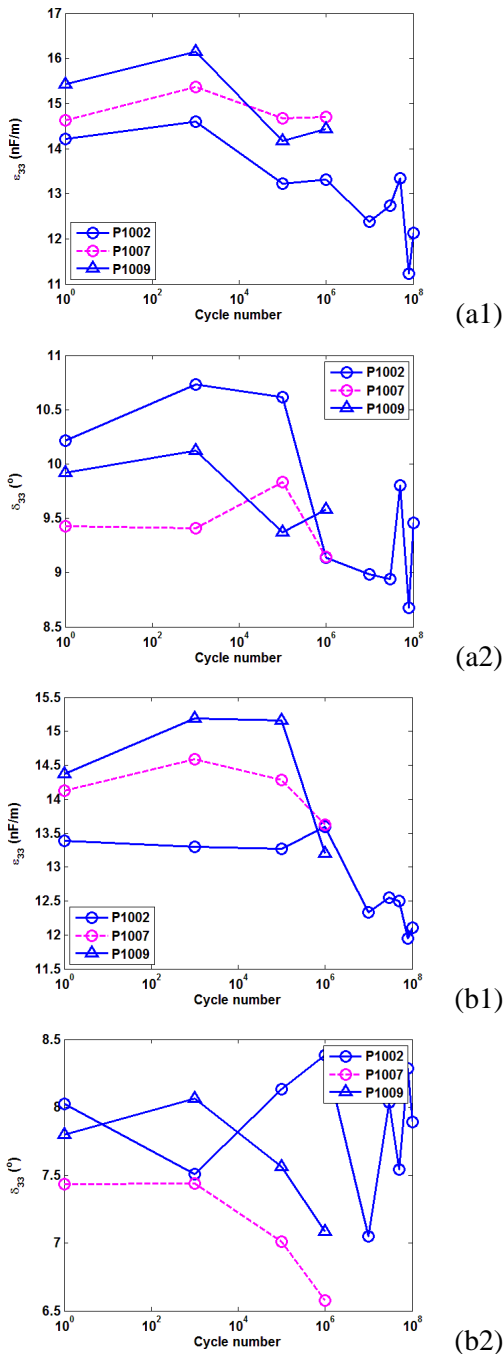


Figure 3. Variation of dielectric coefficients ϵ_{33} and piezoelectric loss angle δ_{33} as a function of cycle number measured at (a) 1.5 kV/mm and (b) 3.0 kV/mm for 10-layer specimens.

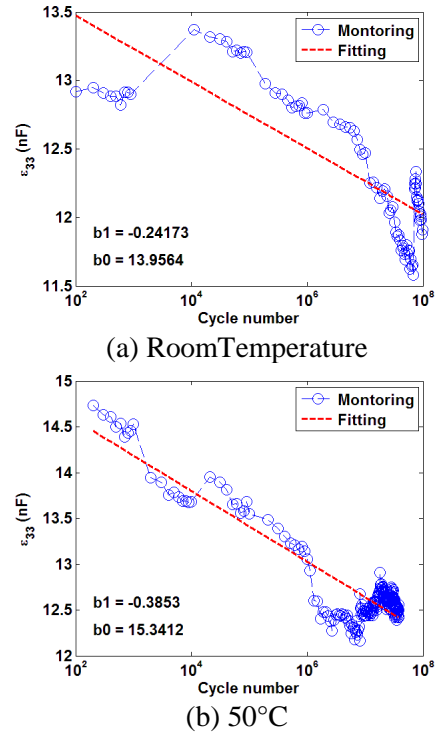


Figure 4. Online-monitoring-based dielectric coefficients ϵ_{33} as a function of cycle number for 10-layer specimens tested in various testing temperature conditions.

The curve fitting was based on: $\epsilon_{33} = b_0 + b_1 \cdot \log(N)$, where N is the number of cycles (Wang et al. 2014) and the fitting results are given in the plots as well. While the initial level of specimens was a little different for the two specimens, the fatigue rate (absolute value of b_1) of the specimen tested at 50°C was shown clearly to be higher than that at room temperature. The result is preliminary, but it signifies the effect that temperature may have on the fatigue response of the PZT stack, which needs to be investigated further.

Optical microscopy revealed that the failure of specimens was generally related to burning resulting from partial discharge or delamination. The image in Figure 5 illustrates a part of the burning zone taking place around one corner of a 10-layer specimen.

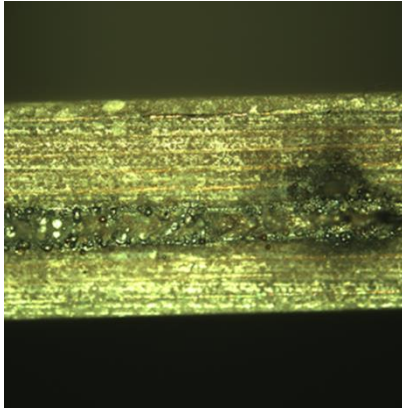


Figure 5. A part of an extended burned zone observed on the non-termination side of a failed 10-layer specimen.

Characterization of Piezoceramics

The objective of this work is to study the effect of humidity-temperature environment on the mechanical strength of PZT. As mentioned in the previous reports, because the single-layer PZT required for this task is not available, testing of PZT for the EPCOS stacks has been directed to test the subunits or extracted 10-layer plate specimens. The testing of the 10-layer specimens also provides an opportunity to examine the interaction between individual PZT layers, which cannot be achieved through use of the single-layer specimen.

At first, the 10-layer specimens were treated in an environment close to that of PZT stacks in an HDD engine fuel injection system. The controlled environment (i.e., 79.27% R.H. at 80°C) was obtained by heating a saturated KBr solution in a vacuum oven (Fisher 281). Twelve 10-layer PZT specimens ($12 \times 12 \times 0.74$ mm) supplied by Cummins were placed within the container and were treated for 30 days.

The 12 treated PZT plate specimens were then tested, along with 20 as-received specimens by using a ball-on-ring setup. A load ball of $\phi 6.35$ mm and a supporting ring of $\phi 9.10$ mm were used. The ball-on-ring testing was conducted under displacement control at a rate of 0.02 mm/s. The results showed that no significant difference was observed in mechanical strengths between the as-received and the treated. The confidence rings (i.e., curves of estimated characteristic strength versus

Weibull modulus at 95% confidence level) of the two data sets overlapped to a great extent (see Figure 6). The result corresponds to that obtained on other commercial PZT (PSI 5A4E) specimens. In that experimental study, the single-layer PZT specimens were treated in 85% R.H. at room temperature for more than 5 months and no significant change was seen on flexural strength after the treatment. However, it should be stressed that the combined humidity and temperature exposure of 10-layer specimens in this study is quite limited and performance of PZT stacks in a much longer term or equivalent lifetime is needed.

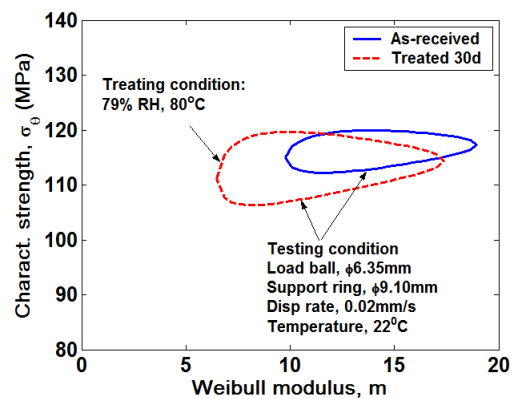


Figure 6. Confidence rings (at 95%) of flexural strength for 12 treated and 20 as-received 10-layer specimens. The results are based on ball-on-ring testing.

Conclusions

An experimental study on the down-selected piezo stacks for heavy-duty diesel engine fuel injector continued by using low-profile stacks, mainly 10-layer plate specimens extracted from the prototype stacks.

- The unipolar high-field cyclic testing showed that the fatigue-induced reduction in piezoelectric and dielectric coefficients became substantial when the cycle number was near and over 10^6 .
- A number of failures, mainly due to dielectric breakdown, occurred in the extracted 10-layer specimens during poling or cycling. Burning and delamination were observed on the sides of specimens. The role

of structural damage in the dielectric breakdown remains to be investigated.

The piezodilatometer was upgraded with elevated temperature capability by using immersion heating. The cyclic fatigue testing of the 10-layer specimen was conducted at 50°C, with an accumulated number of cycles over 4×10^7 .

- Under the same cycle testing condition (3.0/0.0 kV/mm, 100 Hz), the specimen cycled at 50°C exhibited a much higher fatigue rate than that at room temperature.

The effect of combined temperature and humidity environment on mechanical strength of PZT was studied by pre-treating the specimens in a controlled environment provided by a heated KBr solution. The 10-layer specimens were treated and tested by using a ball-on-ring mechanical testing setup.

- After the 30-day exposure to 79.27% R.H. 80°C environment, the mechanical strength of the treated specimens did not show any statistically significant difference compared to that of untreated specimens.

Future Work

Discussion was initiated with Cummins regarding future work after the U.S. Department of Energy Cooperative Research and Development Agreement concluded in October 2014. The following topics will be the focus of potential collaborations with Cummins:

- The mechanical strength of down-selected PZT or PZT stacks exposed to long-term high temperatures and humidity needs to be investigated. The mechanical behavior of PZT stacks under short-term high temperature and humidity (30 days) was studied. However, the mechanical reliability of PZT stacks under long-term exposure to temperature and humidity experienced by piezo fuel injectors has not been studied yet.
- Piezoelectric and dielectric fatigue responses of PZT stacks need to be investigated under a high-temperature environment. The temperature environment enhanced the bias electrical field of bulk PZT and introduced the increased asymmetry of strain in the

bipolar measurement (Glaum et al. 2011). The cycle test at 50°C in this project revealed that the response of a PZT multilayer actuator at temperature environment was different than bulk PZT to a certain extent. The temperature response of PMLA or down-selected PZT stacks needs to be studied systematically.

References

- Glaum, J., T. Granzow, L. A. Schmitt, H.-J. Kleebe, and J. Rödel, 2011, "Temperature and driving field dependence of fatigue processes in PZT bulk ceramics," *Acta Materialia*, 59, 6083–6092.
- Noliac Group, 2013, "Piezo Ceramics," <http://www.noliac.com>, accessed October 12, 2013.
- Wang, H., T. A. Cooper, H.-T. Lin, and A. A. Wereszczak, 2010, "Fatigue responses of lead zirconate titanate stacks under semi-bipolar electric cycling with mechanical preload," *J. Appl. Phys.*, 108, 084107.
- Wang, H., S.-M. Lee, J. L. Wang, and H.-T. Lin, 2014, "Fatigue of extracted lead zirconate titanate multilayer actuators under unipolar high field electric cycling," *Journal of Applied Physics*, submitted 2014.
- Zeng, F. W., H. Wang, and H.-T. Lin, 2013, "Fatigue and failure responses of lead zirconate titanate multilayer actuator under unipolar high-field electric cycling," *J. of Appl. Phys.*, 114, 024101.

Publications and Presentations

- Wang, H., S.-M. Lee, J. L. Wang, and H.-T. Lin, 2014, "Fatigue of extracted lead zirconate titanate multilayer actuators under unipolar high field electric cycling," *Journal of Applied Physics*, submitted 2014.

Project 18518 – Materials for High-Efficiency Engines

Agreement 17257 – Materials for Advanced Turbocharger Designs

Philip J. Maziasz

Materials Science and Technology Division

Oak Ridge National Laboratory

PO Box 2008, MS 6115

Oak Ridge, TN 37831-6068

Phone (865) 574-5082; fax (865) 574-7659; email: maziaszpj@ornl.gov

DOE Technology Manager: Jerry L. Gibbs

Phone (202) 586-1182; fax: (202) 586-1600; e-mail: jerry.gibbs@ee.doe.gov

Technical Advisor: J. Allen Haynes

Phone (865) 576-2894; fax: (865) 574-4913; e-mail: haynesa@ornl.gov

Contractor: Oak Ridge National Laboratory, Oak Ridge, Tennessee

Prime Contract No.: DE-AC05-00OR22725

Objectives

- Cooperative Research and Development Agreement (CRADA) NFE-08-01671 – Provide critical test data for new, improved materials that enable the design of advanced turbochargers with upgraded performance, durability and reliability.
- Cast CF8C-Plus steel is good for turbocharger housings for diesel engines (750 to 800°C), but better alloys must be developed for automotive turbocharger housings for gasoline engines, which push temperatures to 950 to 1000°C.

Approach

- Honeywell provides input on the acceptability of alloy properties, particularly for automotive gasoline engine turbocharger applications.
- Honeywell and the U.S. Department of Energy expressed an interest in cast stainless steels with more strength above 800°C than CF8C-Plus steel; therefore, this year Oak Ridge National Laboratory (ORNL) has tested modified CF8C-Plus Cu/W alloys and procured CN12-Plus steel from the foundry for testing at 1000°C and above.

Accomplishments

- Testing of CF8C-Plus in a real diesel exhaust environment was found to be much less oxidizing at 800°C than testing in air +10% water vapor.
- Modified CF8C-Plus Cu/W steels with more Cr and Ni added were found to have much better oxidation resistance after 5,000 hours in air +10% water vapor at 800°C, with similar creep-rupture resistance to standard CF8C-Plus steel.
- Oxidation testing at 1000°C in air with 1-hour cycles severely oxidized the standard and modified CF8C-Plus steels after 100 hours, but showed good behavior of the HK30Nb and HP40Nb alloys, which contain 25% Cr.

Future Direction

- ORNL will procure CN12-Plus stainless steel from the foundry with 25%Cr and C+N = 0.8 for oxidation and creep-rupture testing at 1000°C and above for automotive turbocharger and exhaust manifold applications.
 - ORNL will begin development of Al-modified CN12-Plus steels for better oxidation resistance at 1000°C and above for automotive turbocharger applications and for variable nozzle/vane advanced turbochargers.
-

Introduction

This ORNL CRADA project with Honeywell, NFE-08-01671, was initially set up to address the temperature and lifetime limitations of various components for both the turbine and compressor portions of the turbocharger system. However, during the last 2-year extension, the focus became the turbocharger housing and upgrades from cast irons to cast austenitic stainless steels such as CF8C-Plus steel. Turbochargers are a particularly attractive way to boost the power and increase fuel efficiency of automotive gasoline engines; therefore, the focus became materials capable of sustained operation at 950 to 1000°C. This year, that requirement made it necessary to consider cast austenitic stainless steels with more temperature capability, such as the modified CF8C-Plus Cu/W steels with more Cr and Ni added and CN12-Plus steel, with 25%Cr and a higher combination of C and N. This will also require oxidation and creep-rupture testing at 1000°C or higher. The CRADA was scheduled to end at the close of Fiscal Year (FY) 2014, but a 2-month, no-cost extension enabled it until December 2014.

Results

Oxidation Testing in a Real Diesel Exhaust Environment

In FY 2014, several exhaust component materials were tested in a real diesel exhaust environment at 800°C by using a specially modified diesel gen-set at the NTRC. As shown in Figure 1, the real diesel exhaust environment is much less corrosive, because it is reducing rather than oxidizing relative to the very aggressive oxidizing environment of air +10% water vapor. After only 100 hours, there is over an order of magnitude less oxidation of the cast iron, CF8C-Plus steel and the HK30 alloy compared to similar laboratory testing in air plus water vapor. CF8C-Plus steel is more oxidation resistant than cast iron (SiMo), but is less oxidation resistant than the HK30 alloy because the latter has 25%Cr, while the CF8C-Plus steel has about 19.5% Cr. Future testing will be for longer times in a new diesel gen set rig.

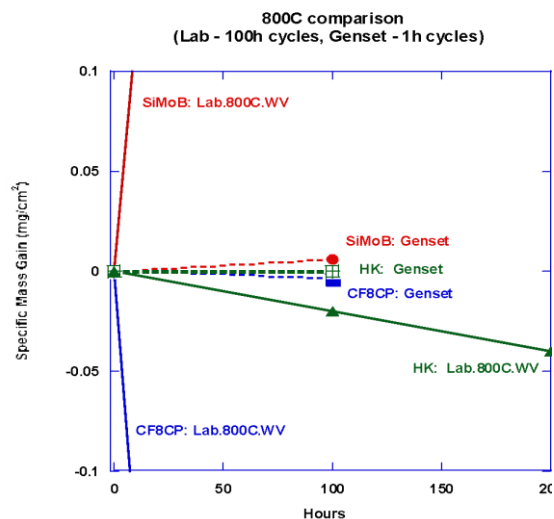


Figure 1. Graph of mass-loss versus time for oxidation testing in an exhaust environment in a specially adapted diesel gen set at 800°C, and for oxidation testing in a laboratory environment with air +10% water vapor. The materials tested include SiMo cast iron, CF8C-Plus cast austenitic stainless steel, and HK30 cast austenitic stainless alloy.

Modified CF8C-Plus Cu/W Steels with More Cr and Ni – Oxidation and Creep-Rupture Testing

Modified heats of CF8C-Plus Cu/W with more Cr and Ni were cast into keel bars by Stainless Foundry and Engineering (Milwaukee, Wisconsin). Three heats, one with the standard 19.5Cr/12.5Ni and two modified heats with 21Cr/15Ni and 22Cr/17.5Ni, were made and tested for oxidation and creep-rupture resistance. The oxidation test was a fairly standard 5,000-hour test at 800°C in air +10% water vapor, with 100-hour cycling to accommodate weight measurements. The results are shown in Figure 2. Standard CF8C (cast 347H steel) and CF8C-Plus undergo severe weight loss due to thick oxide scale formation followed by spallation; testing was stopped at less than 1,000 hours. CF8C-Plus Cu/W performed better and the two modified heats were even more oxidation resistant, with the 22Cr/17.5Ni steel showing the best results after 5,000 hours.

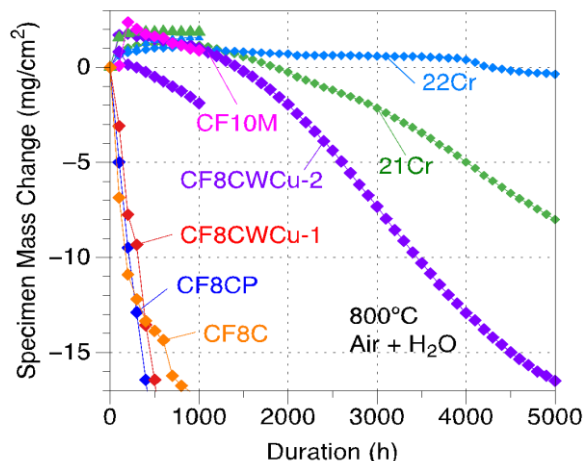


Figure 2. A plot of specimen mass change versus oxidation test duration (h) for several different cast austenitic stainless steels tested at 800°C in air +10% water vapor, with 100 cycles in between weight measurements. Alloys include CF8C, CF8C-Plus (CF8CP), CF8C-Plus Cu/W (CF8CWCu-1 and -2), CF10M (cast 316H), CF8C-Plus Cu/W-21Cr/15Ni (21Cr), and CF8C-Plus Cu/W – 22Cr/17.5Ni (22Cr) steels.

Another measure of goodness for the modified CF8C-Plus Cu/W steels is their creep-rupture resistance and tensile properties at 700 to 1000°C. Figure 3 shows creep-rupture life for various CF8C-Plus steels tested in air at 800°C/75 MPa. Standard CF8C-Plus Cu/W has almost twice the rupture life of the standard CF8C-Plus steel, and the two modified steels with more Cr and Ni have rupture lives comparable to the standard CF8C-Plus steel. Creep testing at 800°C/100 MPa is underway for the standard and modified CF8C-Plus steels, as is tensile testing at 700 to 1000°C. These data will be finished in the first quarter of FY 2015. If we combine the creep and oxidation data, the best combination of creep-rupture resistance and oxidation resistance at 800°C is found in the modified CF8C-Plus Cu/W steel with 22Cr and 17.5Ni.

CN12-Plus Steel and Creep and Oxidation Testing at 1000°C and Above for Automotive Gasoline Engine Exhaust Applications

Turbochargers and exhaust manifolds for automotive gasoline engines must withstand

much higher temperatures than for diesel engine applications, with maximum metal temperatures of 950 to 1000°C. Therefore, cast austenitic stainless steels must have temperature capability of and durability at 1000 to 1100°C for such applications. Standard CF8C-Plus steel has been shown in commercial applications to have capability and durability for the Caterpillar Regeneration System at 900°C for up to 8 years on the road, but properties at higher temperatures must be demonstrated. For this year’s creep-rupture testing of standard CF8C-Plus steel, the modified CF8C-Plus Cu/W steels with more Cr and Ni and HK30Nb (25%Cr) began at 1000°C and 25 MPa, and severe oxidation testing at 1000°C in air with 1-hour cycling was conducted to simulate automotive stop and start operation. The creep-rupture testing is still in progress, but the results of the oxidation testing at 1000°C are show in Figure 4.

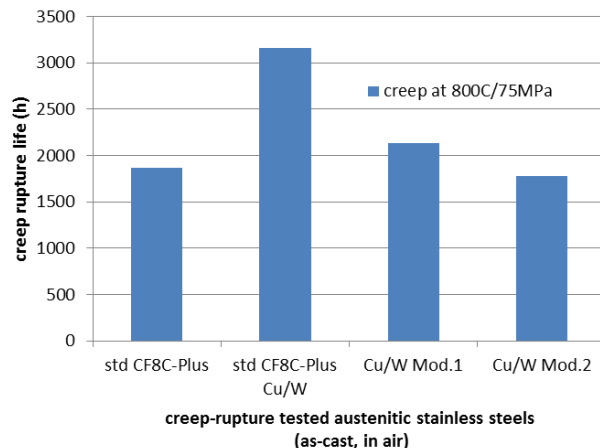


Figure 3. Histogram of creep rupture life for various cast CF8C-Plus steels tested at 800°C/75 MPa in air. Alloys include standard CF8C-Plus, standard CF8C-Plus Cu/W, and two modified CF8C-Plus Cu/W steels with 21Cr/15Ni (mod.1) and 22Cr/17.5Ni (mod. 2).

Oxidation testing at 1000°C severely degrades the CF8C-Plus type steels in less than 100 hours, although the CF8C-Plus Cu/W with 22Cr/17.5Ni shows the best behavior and seems to saturate like HK30Nb does. The HP40Nb and Ni-based CW6MC show no degradation, but this is only 100-hour test in dry air; therefore, their behavior for longer times or in air +10% water

vapor should be measured as well. However, the relative behavior of the modified CF8C-Plus steels and the better behavior of the HK30Nb and HP40Nb, both with 25Cr, argues for benefits of more Cr in these Fe-based steels and alloys. These HK and HP alloys are 2 to 3 times more expensive than CF8C-Plus steel, a negative consideration for automotive applications.

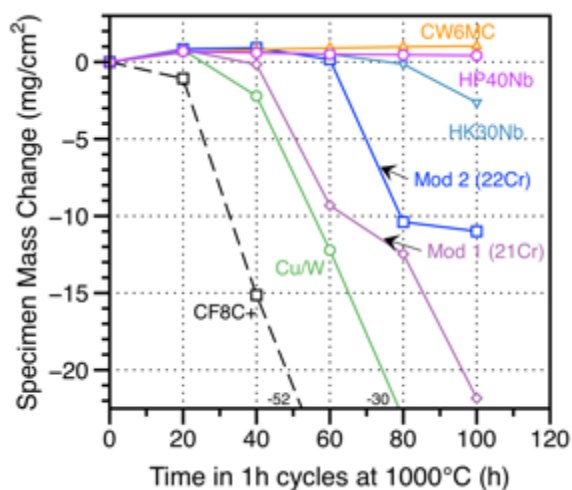


Figure 4. Plot of mass change versus time for oxidation testing in air at 1000°C and 1-hour cycle time for various cast stainless steels, alloys, and Ni-based alloys. Alloys include standard CF8C-Plus steel (CF8C+), standard CF8C-Plus Cu/W (Cu/W), modified CF8C-Plus Cu/W steels with 21Cr/15Ni (mod. 1) and 22Cr/17.5Ni (mod. 2), HK30Nb (25Cr/20Ni) alloy, HP40Nb (25Cr/35Ni) alloy, and CW6MC Ni-based alloy (cast version of alloy 625) with 21Cr.

Finally, the need for more oxidation resistance and creep strength at 1000°C and above created the opportunity to consider the cast CN12-Plus austenitic stainless steel also developed by ORNL and Caterpillar in 1999 through 2002 in the same project that developed CF8C-Plus steel. CN12 was a cast steel with a high sulfur level to provide the brittle MnS phase for enhanced machinability that was developed in an earlier project involving Ford, Caterpillar, and ORNL. CN12-Plus was developed by adding more Mn, eliminating the S, and adjusting the other elements to provide a stable austenitic parent phase strengthened by carbides and nitrides. CN12-Plus was patented

in 2007 (U.S. Patent 7,255,755), and creep-rupture data at 850°C/110 MPa show improvement relative to the standard CN12 steel in Figure 5. CN12-Plus has 25Cr/16Ni, and has more tensile and creep strength than CF8C-Plus steel because it has C+N=0.8 instead of 0.35 to 0.40 found in the latter. CN12-Plus should be stronger than HK30Nb and HP40Nb, both of which have 0.3C and 0.4C and no N, respectively, and cost much less as well. CN12-Plus heats of steel were ordered from Stainless Foundry and Engineering this quarter, and should be delivered to ORNL for testing to begin next quarter (FY 2015).

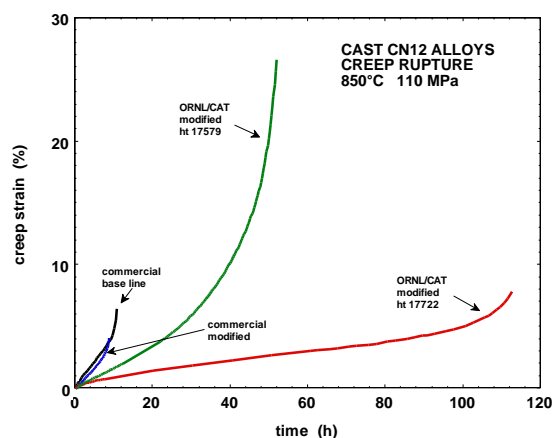


Figure 5. Plot of creep strain versus time for creep-rupture testing of several cast CN12-type austenitic stainless steels at 850°C/110 MPa in air. The alloys include two ORNL/CAT heats of CN12-Plus steels (modified heat 17722 and 17678) and two commercial heats, one standard and one modified, but both containing high S (0.15%).

Conclusions

Oxidation testing of CF8C-Plus steel in a modified diesel gen-set at 800°C showed very little oxidation after 100 hours and orders of magnitude less than shown during laboratory testing at the same temperature in air +10% water vapor.

Standard CF8C-Plus steel shows very poor oxidation resistance at 800°C in air +10% water vapor, while CF8C-Plus Cu/W and modified CF8C-Plus Cu/W steels 21Cr/15Ni and 22Cr/17.5Ni show much better oxidation resistance. CF8C-Plus Cu/W with 22Cr/17.5Ni

has the best combination of creep and oxidation resistance.

Oxidation and creep testing at 1000°C and above for automotive gasoline engine turbocharger housings and exhaust show severe degradation of CF8C-Plus and modified alloys. New CN12-Plus steels with 25Cr, 16Nim and

C+N=0.8 show great potential for having better oxidation and creep resistance at these conditions and costing less than HK30Nb. Test bars of CN12-Plus have been ordered from the foundry and will be delivered and tested at ORNL next quarter.

Project 18518 – Materials for High-Efficiency Engines

Agreement 18571 – Materials Issues Associated with EGR Systems

M. J. Lance

Ceramic Science and Technology Group

Oak Ridge National Laboratory

P.O. Box 2008, MS 6068, Building 4515

Oak Ridge, TN 37831-6068

Phone (865) 241-4536; fax (865) 574-6098; email: lancem@ornl.gov

DOE Technology Manager: Jerry L. Gibbs

Phone (202) 586-1182; fax: (202) 586-1600; e-mail: jerry.gibbs@ee.doe.gov

Technical Advisor: J. Allen Haynes

Phone (865) 576-2894; fax: (865) 574-4913; e-mail: haynesa@ornl.gov

Contractor: Oak Ridge National Laboratory, Oak Ridge, Tennessee

Prime Contract No.: DE-AC05-00OR22725

Objectives

- Provide information to industry specialists about fouling deposit properties to enable improved models and potential design improvements to reduce fouling and its impact on the performance of exhaust gas recirculation (EGR) coolers.
- Develop a protocol for refreshing the EGR cooler during use or during service.

Approach

- Assemble EGR engineers from member companies of the Diesel Crosscut Team to serve as an advisory board for this project.
- Measure permeability of deposit to hydrocarbons to better understand changes to the deposit properties during operation.
- Attempt to densify the deposit through water condensation.

Accomplishments

- Published two Society of Automotive Engineers (SAE) papers: one on neutron tomography of EGR deposits and another on the analysis of lacquer-like deposits that form during EGR cooler plugging.
- Developed testing system for measuring deposit densification while aged under conditions similar to those in diesel engine exhaust.
- Measured deposit densification upon cooling, but observed no change following the introduction of water into the chamber for a light-duty deposit.

Future Direction

- Investigate the influence that cooler geometry has on deposit formation through collaboration with Modine and John Deere. Deposit thickness may be measured with neutron tomography using $GdCl_3$ as a contrast agent (pending approval of a High-Flux Isotope Reactor proposal).
 - Measure heavy-duty deposit density changes caused by temperature and water condensation under controlled conditions.
-

Introduction

High-pressure EGR is the primary nitrous oxide reduction technology used by the diesel industry. Exhaust gas is directed through a heat exchanger (or EGR cooler) where the EGR stream is cooled before being directed back into the engine intake. Inclusion of exhaust in the incoming charge reduces the combustion temperature and oxygen content, thereby reducing the oxidation of N_2 . The EGR stream is also laden with particulate matter and hydrocarbons (HC) which, when directed through the EGR cooler, cause deposits to form through thermophoresis and condensation, respectively. Under some combustion and EGR cooler conditions, high concentrations of HCs in the exhaust gas may accelerate the rate of deposition, causing plugging of the EGR cooler channels. These conditions may occur, for example, during regeneration of diesel particulate filters. As EGR utilization continues to be expanded to new operating regimes, EGR fractions are likely to increase and the coolant used to cool the EGR stream will likely decrease in temperature. These trends may exacerbate the EGR cooler plugging.

In February 2009, a team consisting of engineers responsible for EGR systems was assembled from nine diesel engine manufacturers: Caterpillar, Cummins, Detroit Diesel, Ford, GM, John Deere, Navistar, DAF Trucks, Volvo/Mack, and one heat exchanger supplier, Modine. They were asked, "What is the biggest problem facing EGR cooling systems?" and the clear winner was fouling. Over the course of this project, the EGR team has been notified of results generated and have contributed coolers for forensic analysis. To date, studies of EGR fouling have focused mainly on the cause of stabilized effectiveness loss, whereby low-HC deposits form but rapidly reach a plateau in thickness (Lepperhoff and Houben 1993, Lance et al. 2013, Sluder et al. 2013, Abarham et al. 2013, Warey et al. 2012, Warey et al. 2013, Bika et al. 2013). More recently, researchers have focused on removing deposits by purposely condensing water within the EGR cooler during use (Warey et al. 2013, Warey et al. 2014). This work has shown that large amounts of condensed water may flush the

deposit out of the EGR cooler, with results dependent on the surface chemistry of the deposits. The approach taken here is to take advantage of the high porosity of the deposit (i.e., greater than 98%) and use small amounts of water condensate to collapse the deposit microstructure, thereby densifying it and improving its thermal conductivity. The objective is to understand what exhaust conditions improve the effectiveness of a model deposit in order to provide a protocol for refreshing EGR coolers during use that the whole industry can use on their platforms. This will be done by tracking surface deformations, while aging in a heating stage using digital image correlation (DIC). In addition, an attempt was made to measure the permeability of the deposit using porous aluminum tubes.

Results

Deposit Densification by Water Condensation

Deposits were previously formed on square cross-section tubes at the Fuels, Engines, and Emissions Research Center under two conditions that simulate heavy-duty and light-duty operation. The light-duty deposit shown in Figure 1 was used in this study. The deposit was about 99% porous and was run at high HC levels (i.e., about 200 ppm).

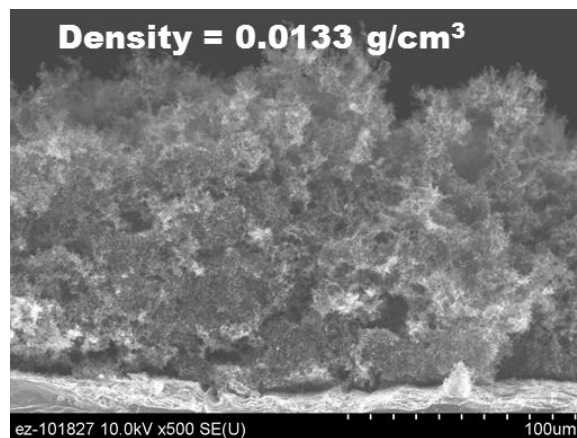


Figure 1. Cross section of the light-duty deposit used in this study.

A number of experimental issues needed to be resolved in order to track the change in density of the deposit during exposure to simulated diesel exhaust. First, the heating stage

was calibrated with a metal tab harvested from an uncoated model cooler tube using a thermocouple. As shown in Figure 2, the surface of the metal tab was slightly lower than the heater surface, presumably due to an air gap between the heater and the tab. In order to mitigate this effect, conductive silver paste was placed between the tab and the heater. This improved the heat transfer only slightly, while causing the glass slide that separates the heating stage from ambient air to cloud due to outgassing. Based on these results, the silver paste was deemed unnecessary.

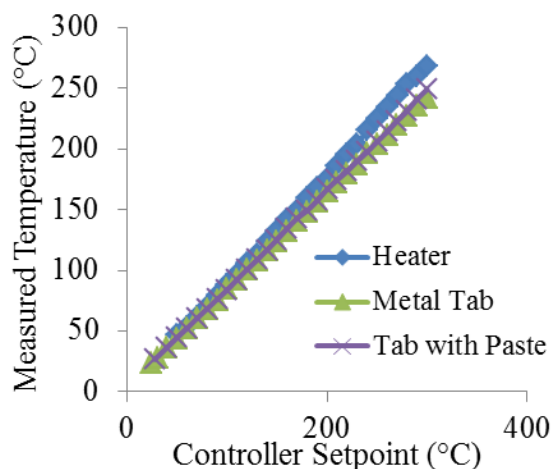


Figure 2. Temperature calibration curves measured on the heating stage.

The software package Vic-2D was used to measure small deformations through the DIC technique. This approach requires a surface that displays a random fine-grained variation in contrast or a speckle pattern, which it uses to track deformations by comparing subsequent images collected from the surface. The approach typically used is to coat the surface with a paint that produces a random speckle pattern. Because of the powder-like properties of the sample deposits, a speckle pattern could not be applied to the surface without affecting the deposit structure and properties. Nonetheless, the innate porosity of the deposit provided a speckle pattern adequate for DIC measurements.

The technique was first calibrated using a metal substrate that was coated with a well-defined speckle pattern (see Figure 3). Using a coefficient of thermal expansion of

16×10^{-6} for 316 stainless steel, the surface at 300°C should strain 4000 microstrain. The Vic-2D software measured a surface microstrain of 4125 when heated to this temperature, confirming that the technique works with this heating stage on a model substrate. The resolution was about 50 microstrain.

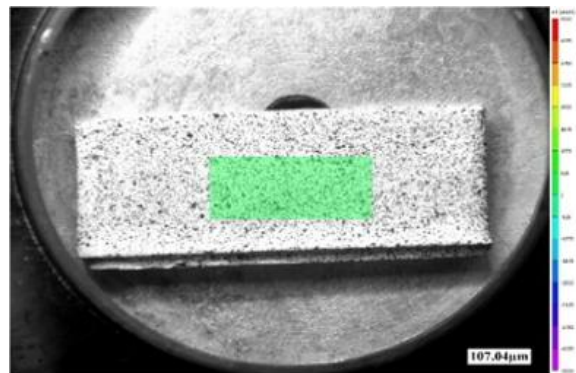


Figure 3. Metal tab coated with paint to provide a speckle pattern for DIC measurements. The green region was the area used to measure surface strain versus temperature.

Various parameters within the Vic-2D DIC software were adjusted to better suit the deposit speckle pattern. It was discovered that the convergence of the software algorithm was enhanced with an increase in subset size, which is the largest number of pixels used to track surface strain between pictures. In addition, step size was evaluated and found to have little relation to a change in error. Finally, a high-magnification (i.e., 100 to 1,000x) Keyence microscope lens was selected and used at low magnifications in order to increase the depth-of-field of the images, thereby improving the natural speckle pattern of the deposit surface.

Following establishment of the technique and calibration of both the heating stage and the Vic-2D software, surface strains of model light-duty deposits were measured while immersed in N_2 saturated with water at room temperature. In order to promote water condensation, the deposit was cooled to 0, -10 , and -20°C and the surface strain measured. The sample was first treated to dry N_2 for 1 hour and then N_2 saturated with water was flowed over the deposit for 1 hour, followed by an additional hour in dry N_2 . Figure 4 shows that the deposit is

shrinking when cooled; however, the presence of water in the chamber does not appear to change the rate of surface shrinkage. This suggests that the light-duty deposit surface is too hydrophobic due to adsorbed HC to allow for water condensate to form. This result is supported by Warey et al. (2014), who found less water condensation on HC-rich deposits. Future measurements will focus on the heavy-duty deposit, which was produced with very low HC levels and, therefore, should be more susceptible to water condensation.

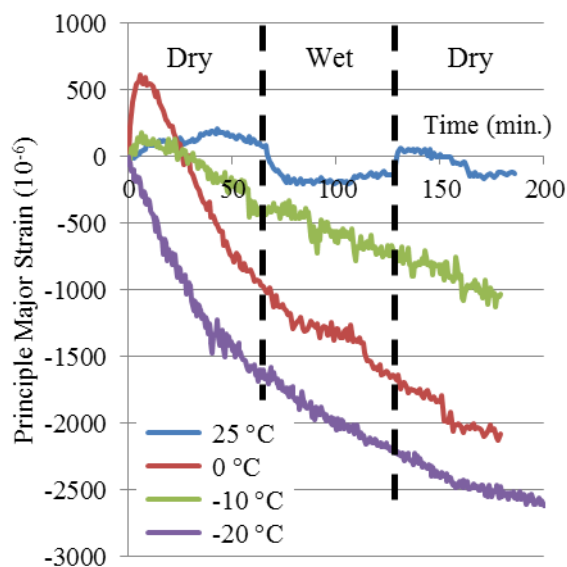


Figure 4. Deposit deformation with water condensation.

Deposit Permeability

Porous aluminum tubes were created and the baseline permeability was measured. An attempt was made to foul the tubes using the Ford 6.4L engine; however, there were mechanical problems with the engine. Because the engine is no longer being used at the Fuels, Engines, and Emissions Research Center and the dyno-cell space is required for other projects, it was decided to not try to repair the engine.

In lieu of permeability testing, detailed microscopy of previously formed deposits using different hydrocarbon levels was performed to ascertain the presence of hydrocarbons at the interface and, from that, the permeability of the deposit to hydrocarbons. Higher HC levels in the exhaust gas up to 250 ppm resulted in deposit

HC adjacent to the metal substrate indicative of diffusion of HC during operation (see Figure 5). This shows that HC may diffuse through the deposit during operation and condense on colder layers near the metal substrate.

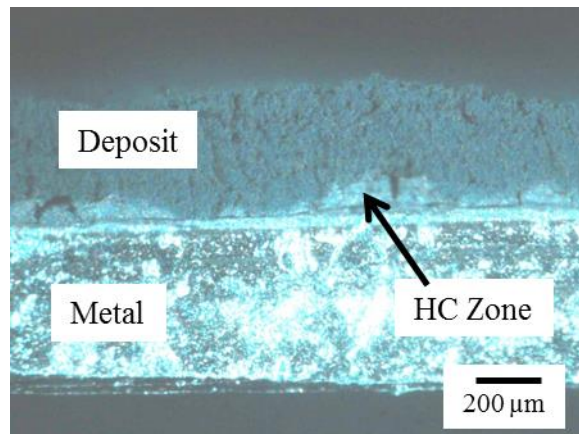


Figure 5. Deposit cross section showing evidence of HC condensation at the metal-deposit interface.

Milestones

Milestone	Completion Date
Deposit densification; establish DIC methodology.	December 2013
Measure deposit density changes caused by temperature and water condensation under controlled conditions.	September 2014
Manufacture porous aluminum tubes and foul them using our tube sampling system and Ford 6.4L engine at NTRC.	June 2014
Measure permeability of the deposit using at least two different gases (air and cetane).	September 2014
SAE paper on neutron imaging of EGR cooler deposits.	April 2014
SAE paper on lacquer-like deposits.	April 2014
Submit annual report.	November 2013
Present progress at annual merit review.	June 2014

Conclusions

A fouled tube was milled open and heated using a high-temperature stage and the surface was imaged using a Keyence digital microscope and optical profiler. The collected images were then inputted into the VIC-2D software, which tracks small changes in surface displacement. The deposit density versus temperature in water-condensing conditions was measured. The heating stage was calibrated using an IR camera and a thermocouple; the optimal imaging parameters using the Keyence microscopy were verified; and the DIC was performed on substrate and deposit. However, the deposit is shrinking when cooled; the presence of water in the chamber does not accelerate the densification process for the light-duty deposit.

References

- Abarham, M., P. Zamankhan, J. W. Hoard, D. Styles, et al., 2013, "CFD analysis of particle transport in axi-symmetric tube flows under the influence of thermophoretic force," *International Journal of Heat and Mass Transfer* 61:94-105, doi:[10.1016/j.ijheatmasstransfer.2013.01.071](https://doi.org/10.1016/j.ijheatmasstransfer.2013.01.071).
- Bika, A. S., A. Waley, P. Szymkowicz, S. Balestrino, et al., 2013, "An Investigation of Diesel EGR Cooler Fouling and Effectiveness Recovery," SAE Technical Paper 2013-01-0533, doi:[10.4271/2013-01-0533](https://doi.org/10.4271/2013-01-0533).
- Lance, M. J., J. M. E. Storey, C. S. Sluder, H. Meyer, et al., 2013, "Microstructural Analysis of Deposits on Heavy-Duty EGR Coolers," SAE Technical Paper 2013-01-1288, doi:[10.4271/2013-01-1288](https://doi.org/10.4271/2013-01-1288).
- Lepperhoff, G. and M. Houben, 1993, "Mechanisms of Deposit Formation in Internal Combustion Engines and Heat Exchangers," SAE Technical Paper 931032, doi:[10.4271/931032](https://doi.org/10.4271/931032).
- Sluder, C. S., J. Storey, M. J. Lance, and T. Barone, 2013, "Removal of EGR Cooler Deposit Material by Flow-Induced Shear," *SAE Int. J. Engines* 6(2):999-1008, doi:[10.4271/2013-01-1292](https://doi.org/10.4271/2013-01-1292).
- Waley, A., S. Balestrino, P. Szymkowicz, and M. R. Malayeri, 2012, "A One-Dimensional Model for Particulate Deposition and Hydrocarbon Condensation in Exhaust Gas Recirculation Coolers," *Aerosol Science and Technology* 46(2):198-213, doi:[10.1080/02786826.2011.617400](https://doi.org/10.1080/02786826.2011.617400).
- Waley, A., A. S. Bika, D. Long, S. Balestrino et al., 2013, "Influence of water vapor condensation on exhaust gas recirculation cooler fouling," *International Journal of Heat and Mass Transfer* 65:807-816, doi:[10.1016/j.ijheatmasstransfer.2013.06.063](https://doi.org/10.1016/j.ijheatmasstransfer.2013.06.063).
- Waley, A., A. S. Bika, A. Vassallo, S. Balestrino, et al., 2014, "Combination of Pre-EGR Cooler Oxidation Catalyst and Water Vapor Condensation to Mitigate Fouling," *SAE Int. J. Engines* 7(1).

Publications and Presentations

- Lance, M. J., H. Bilheux, J.-C. Bilheux, S. Voisin, et al., 2014, "Neutron Tomography of Exhaust Gas Recirculation Cooler Deposits," SAE Technical Paper 2014-01-0628, doi:[10.4271/2014-01-0628](https://doi.org/10.4271/2014-01-0628).
- Lance, M. J., J. Storey, S. Lewis, and C. S. Sluder, 2014, "Analysis of Lacquer Deposits and Plugging Found in Field-Tested EGR Coolers," SAE Technical Paper 2014-01-0629, doi:[10.4271/2014-01-0629](https://doi.org/10.4271/2014-01-0629).
- Lance, M. J., H. Bilheux, J.-C. Bilheux, S. Voisin, et al., 2014, "Neutron Tomography of Exhaust Gas Recirculation Cooler Deposits," at *2014 SAE World Congress*, Detroit, MI.
- Lance, M. J., J. Storey, S. Lewis, and C. S. Sluder, 2014., "Analysis of Lacquer Deposits and Plugging Found in Field-Tested EGR Coolers," at *2014 SAE World Congress*, Detroit, MI.
- Sluder, C. S., J. M. E. Storey, and M. J. Lance, 2014, "Effectiveness Stabilization and Plugging in EGR Cooler Fouling," SAE Technical Paper 2014-01-0640, doi:[10.4271/2014-01-0640](https://doi.org/10.4271/2014-01-0640).

Project 18518 – Materials for High-Efficiency Engines

Agreement 23284 – Friction Reduction through Surface Modification: Integrated Surface Texturing and Coating

Peter J. Blau (retired), Jun Qu, Yan Zhou, and Kevin Cooley

Oak Ridge National Laboratory

PO Box 2008, MS 6063

Oak Ridge, TN 37831-6068

Phone (865) 574-5377; fax (865) 574-4913; email: qujn@ornl.gov

DOE Technology Manager: Jerry L. Gibbs

Phone (202) 586-1182; fax: (202) 586-1600; e-mail: jerry.gibbs@ee.doe.gov

Technical Advisor: J. Allen Haynes

Phone (865) 576-2894; fax: (865) 574-4913; e-mail: haynesa@ornl.gov

Contractor: Oak Ridge National Laboratory, Oak Ridge, Tennessee

Prime Contract No.: DE-AC05-00OR22725

Objectives

- To develop and compare surface engineering methods for applying friction-reducing micro-scale patterns (textures) to the sliding surfaces of diesel engine components.
- To demonstrate the frictional benefits of applying surface texturing to curved surfaces such as those on piston rings, cam lobes, and connecting rod bearings.

Approach

- Fabricate and optimize integrated surface texture designs on diesel engine piston rings and curved surfaces that simulate cam lobes and connecting rod bearing inserts.
- Investigate surface texturing using compression texturing and explore methods of preserving textures by using wear-resistant coatings.
- Test for efficacy in friction reduction using laboratory tests.

Accomplishments

- Identified a wear-resistant thin coating for textured bronze bearing surfaces (Milestone 1).
- Obtained friction test specimens of textured and coated specimens (Milestone 1).
- Completed friction tests of textured and coated surfaces in low-viscosity engine oils (Milestone 3).

Future Direction

- Combining advanced surface engineering and lubrication technologies for synergistic effects on friction reduction and wear control.
-

Introduction

The U.S. Department of Energy has focused research and development efforts on achieving a 50% increase in freight efficiency (measured in ton miles per gallon) for heavy vehicles. This multi-pronged approach includes a reduction in parasitic engine and drivetrain losses, novel waste heat recovery systems, and the use of lightweight materials. In a heavy-duty diesel engine, 10 to 15% of energy is lost to parasitic friction.

The objective of this project is to improve the fuel efficiency of diesel-powered vehicles by reducing the friction between contacting surfaces in the engine via a combination of surface texturing and coating technology. The ultimate goals are reducing boundary and mixed friction, allowing the use of lower-viscosity engine oils to reduce hydrodynamic drag, and mitigating higher peak-cylinder-pressure-induced thinner oil film.

Proper surface texturing/dimpling may alter the flow and film thickness of lubricating fluids locally and across the contact region, change the bearing pressure distribution, serve as channels to supply lubricant to a surface, and trap debris that would otherwise become embedded or abrade the surfaces.

Target components include piston rings, connecting rod end bearings/bushings, and cam followers. This study focuses on developing surface engineering techniques for connecting rod bronze end bearings.

Approach

Three methods of creating textures on bronze bearing surfaces have been developed and evaluated at Oak Ridge National Laboratory (summarized in Table 1). The micro and ball-indentation arrays are no longer in focus because of their non-favorable results in friction behavior and limitation in scale production. The wire mesh compression has been identified as a feasible texturing process for bronze surfaces, with 20 to 40% friction reduction as demonstrated in bench tests. Finer textures

showed more favorable results (see Figure 1). On the other hand, wear and sometimes scuffing failure is inevitable for the relatively soft bronze surface in mixed and boundary lubrication. A wear-resistant coating, diamond-like-carbon (a-C:H DLC), was identified and applied onto the wire mesh compressed surface to prevent the textures from excessive wear.

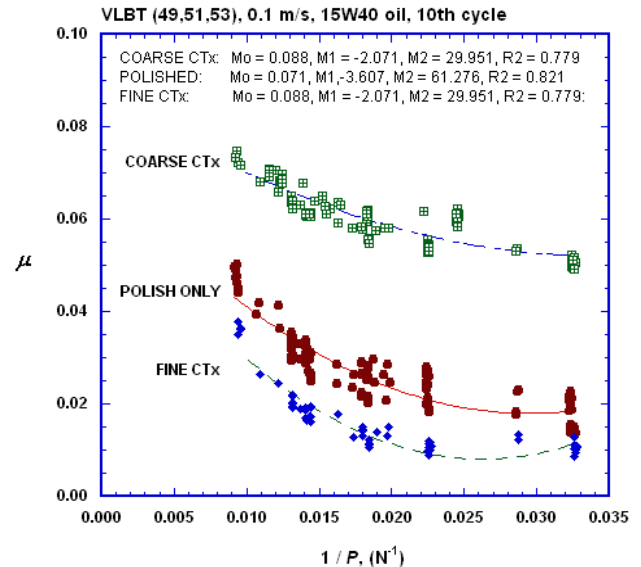


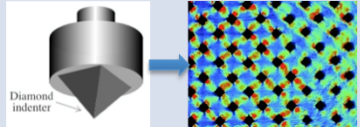
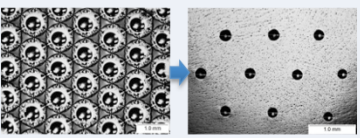
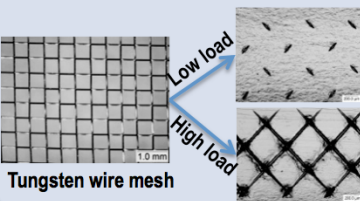
Figure 1. Texture by a 50 x 50 mesh had friction reduction; however, texture by a 20 x 20 mesh behaved worse than non-textured.

Progress During Fiscal Year 2014

Because the surface texture created by a 50 x 50 mesh outperformed that by a 20 x 20 mesh, even finer meshes (e.g., 100 x 100 and 140 x 140) were acquired and used in producing textures in Fiscal Year 2014. Figure 2 shows selected tungsten wire meshes and textures they produced. Multiple compressions were applied for higher dimple densities: 90 and 45 degrees for 100 x 100 mesh and 90, 45, and 0 degrees for 140 x 140 mesh. All compressed surfaces were re-polished using 600-grit silicon-carbide abrasive paper to remove the rim of dimples.

A DLC coating was superimposed on the compression-textured bronze surface by Northeast Coating Technologies. The coating exhibited strong binding to the metal substrate and excellent wear resistance.

Table 1. Summary of methods used at Oak Ridge National Laboratory in producing surface textures on bronze bearings.

Method	Observations	Status
Micro-indentation array 	Friction results not encouraging – edge issues, area fraction too small, and depth-area ratio too high. (<i>time consuming</i>)	No longer a focus of the work
Ball indentation array 	Demonstrated feasibility, but area fraction too low and shapes limited	No longer a focus of the work
Wire mesh compression 	Combinations of grooves and dimples with size control to some extent, encouraging friction results, but wear removing the texture.	Combining with diamond-like-carbon (DLC) coating to address the wear issue and potentially synergistic effects on friction reduction.

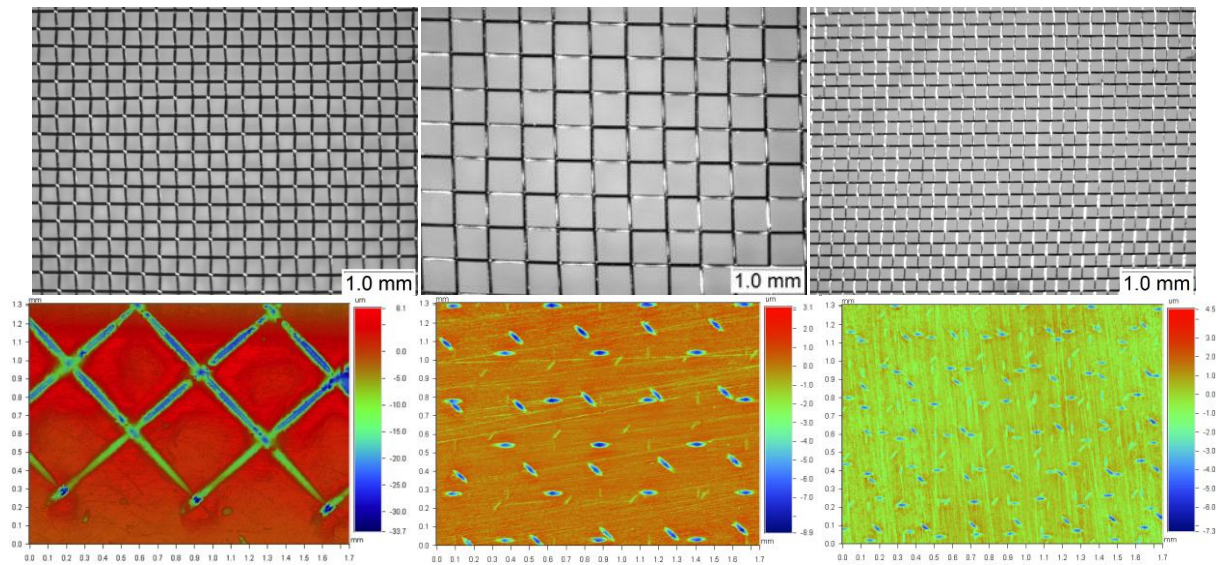


Figure 2. Top (left-to-right): tungsten wire meshes of 50 x 50 (0.002-in. wire diameter), 100 x 100 (0.001-in. wire diameter), and 140 x 140 (0.0007-in. wire diameter); bottom (left-to-right): surface textures created by the 50 x 50, 100 x100, and 140 x 140 meshes, respectively.

Table 2. Text matrix and key observations.

Tribometer	Configuration	Sample surface	Notes
Variable Load/Speed Bearing Tester (VLBT)	Cylinder (steel)-on-flat (sample)	Non-CTx bronze CTx 100 bronze Non-CTx DLC CTx 100/140 DLC	DLC surface effectively protected the CTx texture, but the friction benefits were hardly observed due to the relatively small contact area. Selected results are shown in Figure 4a.
	Cylinder (steel)-on-curved (sample)	Non-CTx bronze CTx 100 DLC	The most successful test configuration with significant friction and wear reduction demonstrated on the DLC-coated CTx-textured surface. See results in Figure 4b. (Drawback: samples were somewhat difficult to make.)
Pin-on-Disc (POD)	Ring (sample)-on-disc (steel)	Non-CTx DLC CTx 100 DLC	Friction could be quantified because the current load cell is not sensitive enough.
	Flat pin (steel)-on-disc (sample)	Non-CTx bronze CTx 100/140 bronze Non-CTx DLC CTx 100/140 DLC	Because the dimples were in intermittent contact, no sustainable local EHD lift was generated, thus no friction reduction. In fact, the rougher CTx surfaces increased the friction due to higher roughness (Figure 4c).
	Flat pin (sample)-on-disc (steel)	Non-CTx DLC CTx 100 DLC	The trial of switching the counterparts in POD was not successful. Unwanted vibration led to high friction in the entire range of testing speeds (Figure 4d).

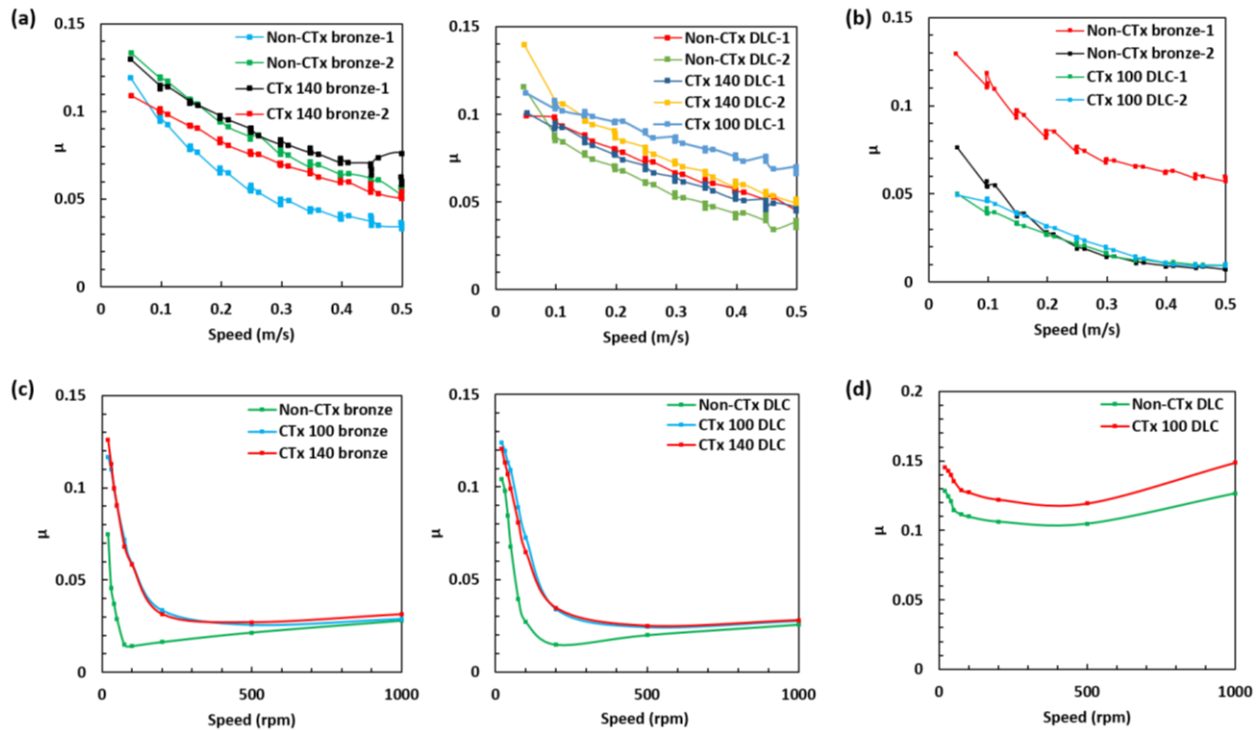


Figure 4. Stribeck friction curves generated in tests of (a) VLBT cylinder (steel)-on-flat (sample), (b) VLBT cylinder (steel)-on-curved (sample), (c) POD flat pin (steel)-on-disc (sample), and (d) flat pin (sample)-on-disc (steel).

Friction and wear reductions were observed in bench testing. Figure 3a compares the friction behavior of uncoated bronze surfaces against a CTx+DLC surface in Society of Automotive Engineers 0W-30 engine oil. Tests were conducted using a Stribeck curve scan under a constant load of 100 N and various sliding speed from 0.5 to 0.05 m/s. Poor repeatability was seen on uncoated bronze due to wear (see Figure 3b). In contrast, consistently lower friction was observed for the DLC-coated textured surface (Figure 3a) with no measurable wear (Figure 3c).

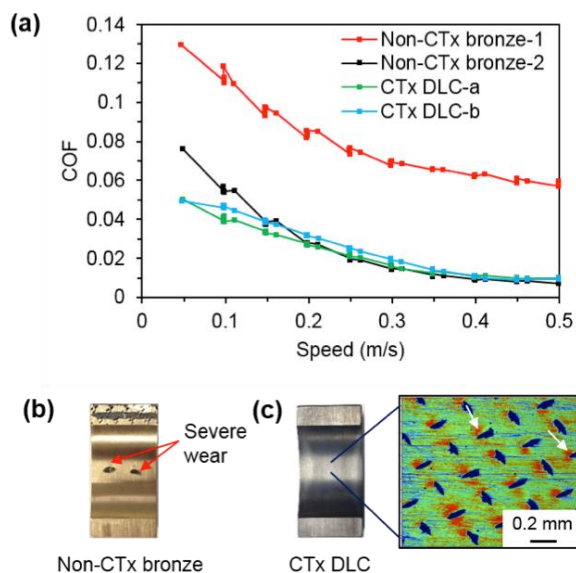


Figure 3. (a) Friction behavior; (b) post-testing image shows worn spots on uncoated bronze; (c) no detectable wear on DLC-coated surface and the texture was well preserved.

Table 2 summarizes the test matrix and key observations for the non-textured, textured, coated, and textured+coated surfaces against a steel counterface in a low-viscosity Society of Automotive Engineers 0W-30 engine oil. Stribeck curve friction tests were carried out on the VLBT, as well as a POD system under a series of loads and speeds. All VLBT tests were carried out under a 100 N load and all POD tests were conducted at 10 N. In any case, the DLC coating exhibited strong binding to the substrate and excellent wear resistance.

Friction results are shown in Figure 4. The effects of surface textures are highly dependent

on the test configuration and parameters and could be either beneficial (i.e., micro-elastohydrodynamic lift) or detrimental (i.e., higher effective roughness) on friction behavior.

Future Work (if Funding Available)

Combining advanced surface engineering and lubrication technologies for synergistic effects on friction reduction and wear control.

Compositions of alloys will be modified based on the observed trends in the oxidation resistance of the alloys **and** strength properties measured in the new alloy heats.

Conclusions

The feasibility of using a wear-resistant DLC coating to protect the compression-produced textures on soft bronze bearing surfaces has been successfully demonstrated.

Finer textures have been created by using 100 x 100 and 140 x 140 wire meshes with multiple compressions.

A test matrix using five different test configurations has been carried out to evaluate the effects of the coated textures.

Results suggest that effects of surface textures are highly dependent on the test configuration and parameters and could be either beneficial (i.e., micro-elastohydrodynamic lift) or detrimental (i.e., higher effective roughness) on friction behavior.

Overall findings and data from this multi-year project will be summarized in a final report.

Publications and Presentations

Blau, P. J., K. M. Cooley, and D. L. Erdman, "Effects of Indentation and Compression Texturing on the Lubricated Friction of Non-Ferrous Surfaces under Spectrum Loading," *STLE 69th Annual Meeting & Exhibition*, Orlando, May 18-22, 2014.

Blau, P. J., K. M. Cooley, and Jun Qu, "Friction Reduction Through Surface Modification," *2014 DOE Vehicle Technologies Program Annual Merit Review*, D.C., June 19, 2014.

Project 18518 – Materials for High-Efficiency Engines

Agreement 23425 – Lightweight Heavy-Duty Engine

G. Muralidharan, Amit Shyam, Michael P. Brady, and T. R Watkins

Materials Science and Technology Division

Oak Ridge National Laboratory

1 Bethel Valley Road

Oak Ridge, TN 37934

Phone (865) 574-4281; fax (865) 574-4357; email: muralidhargn@ornl.gov

Roger England

Cummins Technical Center

1900 McKinley Avenue

Columbus, IN 47201

Phone (812) 377-3135; email: roger.d.england@cummins.com

DOE Technology Manager: Jerry L. Gibbs

Phone (202) 586-1182; fax: (202) 586-1600; e-mail: jerry.gibbs@ee.doe.gov

Technical Advisor: J. Allen Haynes

Phone (865) 576-2894; fax: (865) 574-4913; e-mail: haynesa@ornl.gov

Contractor: Oak Ridge National Laboratory, Oak Ridge, Tennessee

Prime Contract No.: DE-AC05-00OR22725

Objectives

- The primary focus of this project is to develop/identify alternate materials for heavy-duty diesel engine exhaust manifolds and pistons that would enable improvements in high-temperature capabilities of these components, facilitating improvements in brake thermal efficiency (BTE) and power density.

Approach

- Evaluation of component design, materials, and manufacturing process for selected components with impact on engine BTE.
- Evaluation of alternate materials, materials testing, and component design modification.
- Prototype component fabrication and testing.

Accomplishments

- One candidate alloy, CF8C+, has been down-selected for fabrication of the first prototype exhaust manifold.
- Redesign of prototype exhaust manifold for new alloy has been completed.
- Issues with the use of multi-material pistons have been evaluated.

Future Direction

- Cast prototype exhaust manifold using down-selected alloy and perform evaluation of materials properties and engine test manifold.
 - Evaluate thermal-physical properties and reliability of new multi-material, substrate-coating combinations for piston.
-

Introduction

This project with Cummins supports the development of next generation heavy-duty diesel engines that can achieve a 50% or better BTE. The fuel efficiency roadmap for the 50% BTE engine considers six main areas for efficiency improvement in the baseline engine, several of which involve making more efficient use of thermal energy (i.e., heat) in the engine. Increased operating temperatures and improved thermal management are expected to enable significant increases in *power density*, thus resulting in greater power output for the same sized engine or engine downsizing (or light weighting) for the same power output. However, it is becoming apparent that several key components will be exposed to temperatures beyond the capabilities of current engine and exhaust materials, requiring the availability of the next generation of high-temperature materials to allow the engine to reach the efficiency, commercially viable durability, and emission targets. Because of the different combinations of property requirements, new materials technologies specific to the targeted engine components are needed to enable operation in the higher-temperature environment.

A detailed analysis of the development of the high-efficiency engine being envisioned by Cummins showed that a higher-temperature capability in the exhaust system has significant impact on technologies that improve BTE by waste heat recovery from exhaust gases. In addition, an increase in the temperature capability of piston materials also had a positive influence on the efficiency of the next generation diesel engines. Because the current materials (i.e., high SiMo cast irons in exhaust manifolds and 4140 steel in pistons) are already operating near the limits of their temperature and strength capabilities, it has been determined that new materials with the right combination of properties are required for these components. Replacement of current materials with materials that have a higher strength and oxidation resistance at higher temperature also allows redesign of components to have thinner walls for the same stress levels, thus facilitating light weighting and increased power density. It is

anticipated that critical technologies (such as waste heat recovery) will not only demand the availability of improved materials to achieve the efficiency targets for the SuperTruck program in short-term engine efficiency measurements, but will continue to drive the development of advanced materials that would enable the manufacture of a durable, commercially viable high-thermal efficiency engine. Table 1 shows the key properties that were initially identified by the team to be of interest for the two components. These properties will be used for initial screening of new materials for this application and to define the initial test matrix.

Table 1. Components down-selected and the critical materials properties of interest.

Component	Critical material properties of interest
Exhaust Manifold	Constrained thermal fatigue strength, elevated temperature strength, high-temperature fatigue strength, creep strength, oxidation resistance, thermal expansion coefficient, specific heat, density, elastic modulus, thermal conductivity, microstructural stability at high temperatures, and the ability to be cast into complex shapes.
Piston	Constrained thermal fatigue strength, high-temperature strength, high-temperature fatigue strength, thermal conductivity, density, specific heat, and oxidation resistance

Results

Exhaust Manifolds

Several new classes of materials have been identified as alternatives to the high SiMo cast irons currently used in exhaust manifolds. The following are the three major classes of materials:

1. D5S-austenitic nodular cast iron
2. Cast austenitic stainless steels (chromia-forming)

3. Alumina-forming, cast austenitic stainless steels.

Table 2 shows some example candidates of cast austenitic stainless steels being considered for this application. The “ORNL” in parenthesis shows that a particular class of alloy was developed at Oak Ridge National Laboratory (ORNL).

Two major properties were considered as key for prolonged exhaust manifold life: (1) resistance to constrained thermal fatigue and (2) oxidation resistance. As an initial evaluation of their potential to perform adequately in an exhaust manifold application, constrained thermal fatigue tests and oxidation resistance were evaluated for the baseline high SiMo cast iron and other candidate alloys, including D5S, Cast CF8C+, TMA[®]4705, and TMA[®]6301. In addition, thermo-physical properties (such as thermal conductivity, thermal expansion coefficients, and elastic moduli) were evaluated for selected candidate alloys for incorporation into finite element models.

Exhaust manifold alloys: Constrained thermal fatigue testing and oxidation testing were used to down-select the most promising candidate alloys. As reported previously, in the present investigation, thermal cycling was conducted from a maximum temperature of 800°C for temperature ranges (ΔT) ranging from 300 to 500°C. Heating/cooling rates of 1°C/second were employed in the reported tests with a feedback loop temperature controller.

Oxidation tests were conducted by exposing specimens to an environment consisting of air + 10 vol. % H₂O. Mass changes were measured by removing the specimens after exposure to 100-hour cycles at 650, 700, 750, and 800°C. In general, cast austenitic stainless steels such as CF8C+, HK(25Cr-20Ni), TMA 4705, TMA 6301 (25Cr-35Ni), and HP (25Cr-35Ni) have good oxidation resistance compared to the SiMo cast iron and D5S. Although CF8C+ shows Fe-oxide formation at 700 to 800°C, it has good thermal fatigue resistance. Because it offers a

good compromise between properties and cost, it was down-selected for initial trial castings of the exhaust manifold.

Figure 1 shows the yield strength of CF8C+ in comparison with high SiMo cast iron and HK. Note that CF8C+ has a higher yield strength than high SiMo cast iron at higher temperatures (it is better than that of HK at all temperatures). This can be favorable in high-temperature exhaust manifolds, because this can help in decreasing the tendency for localized yielding in local hotspots. It should also be noted that ORNL’s new alloy cast AFA alloy shows yield strength greater than cast iron at all temperatures. Because of the difference in thermo-physical properties, a new prototype exhaust manifold design has been completed and will be cast with CF8C+ as part of the project in Fiscal Year 2015.

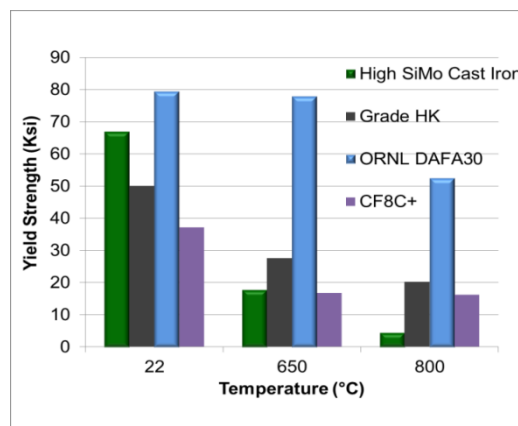


Figure 1. CF8C+ has higher yield strength than SiMo cast iron at higher temperatures.

Piston Materials: Figure 2 shows the effect of piston thermal conductivity on the BTE. Note that decreasing the piston thermal conductivity can increase the BTE by up to 1.3%. One method to decrease the thermal conductivity of pistons is to coat the pistons with a low thermal conductivity metallic alloy.

Table 2. Compositions of cast austenitic stainless steels being evaluated for application in exhaust manifolds.

Alloy	Type of Alloy	Fe	Cr	Ni	Mn	Mo	Nb	W	Si	C	Remarks
High SiMo Cast Iron	Nodular ferritic cast iron	Bal.			0.3	0.6			4.0	3.45	Baseline alloys
D5S	Nodular austenitic cast iron	Bal.	2	35	0.5				5	1.9	High-performance cast iron
Cast CF8C+ (ORNL)	Cast Austenitic	Bal.	19	12.5	4.0	0.3	0.8	0	0.5	0.1	0.25N
TMA [®] 4705 (ORNL) Typical	Cast austenitic	Bal.	26	23.5	0.6	0.47	0.35	0.28	1.33	0.6	Centrifugal casting data only
TMA [®] 6301 (ORNL) Typical	Cast austenitic	Bal.	24	34.2	1.0	0.02	0.41	0.35	1.22	0.43	Centrifugal casting data only
Cast AFA (ORNL) Typical	Alumina-forming cast austenitic	Bal.	14	25	2	2	1	1	1	0.45	Vacuum casting data only, Al 3.5 C:0.2-0.5

In Fiscal Year 2013, it was demonstrated that a 4140 steel substrate could be coated with a low thermal conductivity coating. Figure 3 shows the effect of an alloy 625 coating on the thermal diffusivity of the composite. A 25% decrease in thermal diffusivity was observed at room temperature, with the effect of the coating decreasing gradually at higher temperatures. At about 300°C, there was very little effect of the coating on the thermal diffusivity of the composite, with the effective thermal diffusivity approaching that of the matrix.

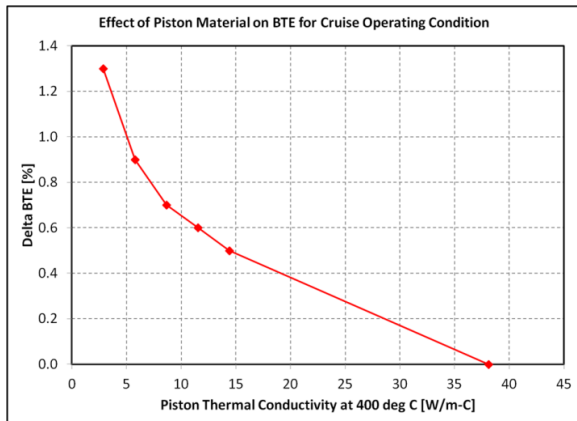


Figure 2. Modeling predicts a significant increase in BTE using pistons with low thermal conductivity.

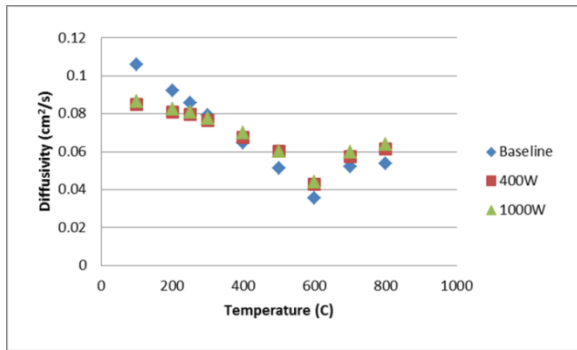


Figure 3. Effect of alloy 625 coating on the thermal diffusivity of the 4140-based composite

Figure 4 shows the effect of a multi-layered coating on the thermal diffusivity of an alternate substrate. Note that in this case, the diffusivity of the coated substrate is significantly lower than that of the matrix and is maintained to temperatures as high as 600°C. This work was completed as part of a milestone on this project in Fiscal Year 2014. Further work will be performed on evaluating the properties of multi-layered coatings on steel substrates in Fiscal Year 2015.

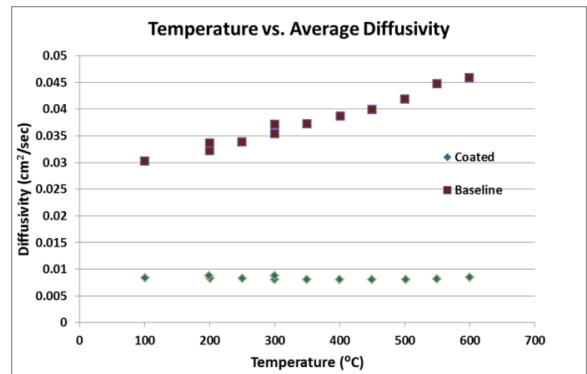


Figure 4. Effect of multi-layered coating on the thermal diffusivity.

Conclusions

Based on the evaluation of thermophysical properties, mechanical properties, oxidation, and cost factors, CF8C+ was down-selected for fabrication of a prototype exhaust manifold.

Multi-layered composite coatings have proven to be effective in reducing thermal diffusivities of substrates relevant to pistons.

Project 18518 – Materials for High-Efficiency Engines

Agreement 23725 – Tailored Materials for Improved Internal Combustion Engine Efficiency

Glenn J. Grant

Pacific Northwest National Laboratory

902 Battelle Boulevard, K2-03

Richland, WA 99352

Phone (509) 375-6890; fax (509) 375-4448; email: glenn.grant@pnnl.gov

Blair E. Carlson

General Motors Research and Development

30500 Mound Road

Warren, MI 48090

Phone (586) 864-7698; email: blair.carlson@gm.com

Rajiv S. Mishra

University of North Texas

1155 Union Circle #305310

Denton, Texas 76203-5017

Phone (940) 565-2316; fax (940) 565-4824; email: rajiv.mishra@unt.edu

DOE Technology Manager: Jerry L. Gibbs

Phone (202) 586-1182; fax: (202) 586-1600; e-mail: jerry.gibbs@ee.doe.gov

Field Technical Manager: Yuri Hovanski

Phone (509) 375-2620; fax: (509) 375-2186; e-mail: yuri.hovanski@pnnl.gov

Contractor: Pacific Northwest National Laboratory, Richland, Washington

Prime Contract No.: DE-AC05-75RL01830

Objectives

- To develop a friction-stir process (FSP) to tailor the properties of conventional, low-cost engine materials (i.e., cast iron, alloy steels, and aluminum alloys) with the goal of increasing their high-temperature performance, durability, and thermal properties.
- To deploy FSP components to enable energy-efficient combustion strategies, especially those that will require higher peak combustion pressure or higher-temperature operation, where component durability is the primary barrier to using the energy-efficient combustion strategy.

Approach

- Develop surface-modification techniques, modified materials, and components. This project is a collaboration with General Motors and with General Motors providing in-kind and materials (i.e., aluminum castings, cylinder heads, engine components, and testing).
- The project is primarily investigating FSP, a new technology that can produce functionally graded surfaces with unique and tailored properties that will allow propulsion materials to withstand higher temperatures and pressures without appreciably losing strength, hot hardness, or wear resistance, and exhibit improved resistance to thermal fatigue.

- Industry collaborators will evaluate and test FSP-treated components to demonstrate efficiency benefits and potential commercial applications.

Accomplishments

- Demonstrated property improvements from FSP that can reach the following metrics established by the project team: minimum two-fold improvement in fatigue life and 20% improvement in average failure stress level at N cycles. Completed and exceeded with an order-of-magnitude improvement in fatigue life (Fiscal Year [FY] 2014).
- Developed the FSP process, tools, and control necessary to produce defect-free FSP regions in a cast steel typically used in crankshaft applications and characterized microstructure (FY 2014).
- Documented the differences in thermal (creep) fatigue performance at elevated temperature between coarse-grained microstructures and fine-grained microstructures and demonstrated that FSP-aluminum head-material coupons can maintain creep performance at elevated temperature and achieve a minimum improvement of 10% over as-cast materials (FY 2014).

Future Direction

- Additional testing at higher temperature to determine if creep mechanisms ever enter into consideration to determine if there is a preferred FSP microstructure for creep-fatigue.
 - Apply FSP to a prototypic cylinder head and test the durability performance through a thermal stress test designed by General Motors.
 - Complete FSP fatigue testing on rotating beam fatigue specimens with and without simulated oil holes and apply the process to a subscale prototypic crankshaft for instrumented testing.
-

Introduction

This project aims to improve the durability and thermal properties of conventional, low-cost materials so they can withstand the increased level of mechanical performance required in new combustion strategies such as homogenous charge compression ignition (HCCI), low-temperature combustion, and other conditions where higher peak combustion pressures (PCPs) are anticipated. HCCI, premixed charge compression ignition, low-temperature combustion, and other strategies can produce higher specific power (SP) levels that can allow engine downsizing and decreased fuel consumption, but increases in PCP are often a result. A barrier to fully realizing these energy-efficient strategies can be the engine component materials themselves. Increasing the durability of engine components can increase the operational envelopes of the engine, allowing designers of the combustion process to access areas of engine control, where increased SP and low emission levels are found, but high PCPs can create reliability problems.

This project supports the U.S. Department of Energy goals for increased fuel and thermal efficiency in both light and heavy-duty engines by developing and deploying FSP, a new surface-modification technology shown to significantly improve the strength and durability of current engine materials. This project will experimentally develop FSP required to engineer the surface of propulsion materials for improved properties and fabricate prototype parts that will be tested in-engine by project partners. The microstructural modification created by FSP is expected to lead to a set of materials with enhanced surface properties that can handle increased combustion pressures, resulting in improved engine efficiency.

Background

In the history of the inception of internal combustion engines, SP output has risen steadily. SP is correlated with efficiency and is the combined effect of better optimization of

combustion, fuels, engine materials and design, reduction in parasitic losses, and improved heat management. Figure 1 shows a steady increase in SP from 1970 to 2001. After 2001, SP levels dropped due to emission and after-treatment devices and controls mandated by federal legislation (primarily increased exhaust-gas recirculation rates and particulate filters). The drop in SP from 2001 to about 2003 would have been even greater were it not for significant advances (e.g., in-engine management, computer control, and higher injection pressures) made during this period to compensate for the power losses. However, around 2003, a different restriction on the optimization of the combustion process was beginning to force diminishing returns. The restriction is illustrated in Figure 1 as the PCP plot.

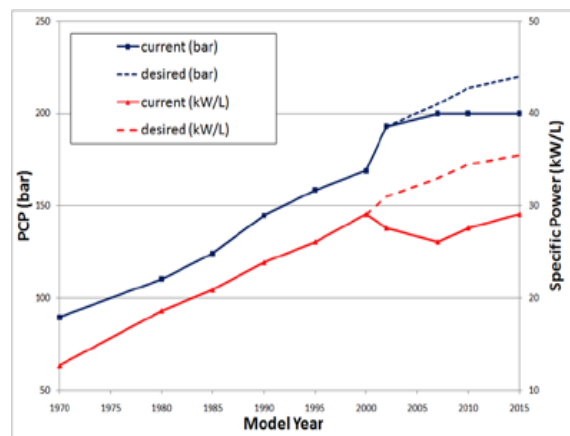


Figure 1. Plot showing the increase in SP and PCP for typical heavy-duty diesel engines from 1970 to 2003 (projected until 2015). (Figure from the Southwest Research Institute <http://www.swri.org/3pubs/brochure/d03/DieselCylHeadDev/DieselCylHeadDev.pdf>.)

Since 2003, PCP has leveled at around 190 to 200 bar. Above this level, conventional engine materials will be beyond strength and fatigue limits.^a To further increase efficiency, either unconventional, expensive materials (i.e., Ni alloys, Ti, CGI, micro-alloyed steels) must be used or conventional materials must be modified in a way that increases their durability. New

diesel engines (i.e., light duty, high speed) achieve SP levels above 75 kW/L in turbocharged and intercooled configurations.

^a Figure 1 represents data primarily from medium-duty to heavy-duty diesel engines. Production automotive

energy-efficient combustion strategies, especially HCCI, will potentially increase PCP above 220 bar. Accordingly, materials must be improved to enable this process.

One of the major challenges for conventional materials under increasing peak pressure environments is resistance to thermal-fatigue failure. 2 shows typical examples of thermal fatigue along the bowl rim of a piston. Pistons and cylinder heads are particularly vulnerable to this failure mode because of the cyclic nature of the loading and temperature changes in the combustion chamber.

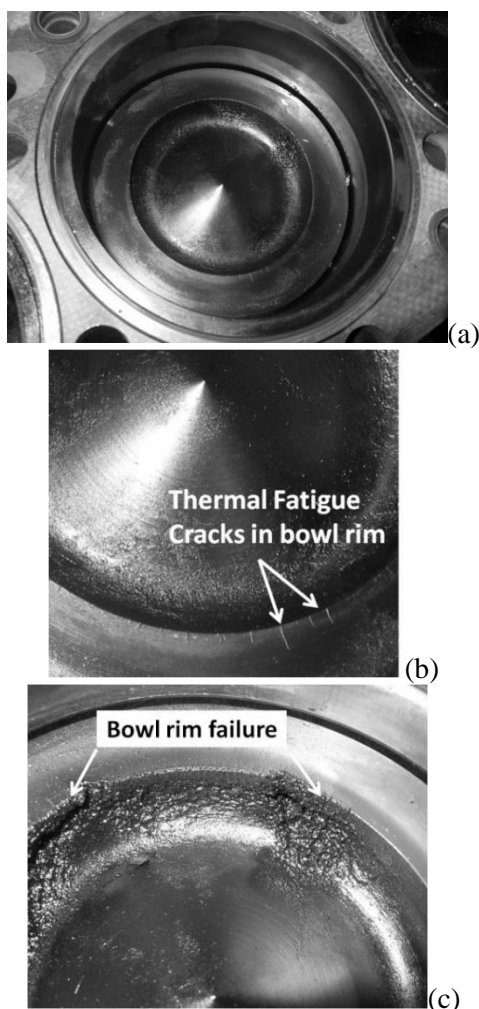


Figure 2. (a) Piston in bore, (b) cracks on inside edges of bowl rim, and (c) bowl rim failure.

Rather than substitute a potentially high-cost, high-temperature, monolithic material, one low-cost strategy to enable higher PCP involves using techniques to improve the

thermal-fatigue performance of current materials. In the case of thermal fatigue in the bowl rim area, the technique need only be applied to the narrow area around the bowl rim itself because failures of this area drive overall material selection.

FSP is a new technology that can be used to create engineered regions on selective areas of a part. In recent years, Pacific Northwest National Laboratory developed techniques and tools that allow FSP to be accomplished in steel, cast iron, and aluminum. The process can be selectively applied to the surface of a material and it alters the microstructure by the severe plastic deformation that occurs in the processed zone.

Approach

The current project will develop the FSP process on both aluminum and steel coupons, produce mechanical property test results that show improved properties that are critical to improved durability, then apply the FSP process on three prototypical engine part applications and subject those parts to in-engine or other relevant testing. The applications will emphasize internal engine components that are expected to have limited durability at very high peak cylinder pressures or high load-rise times during engine operation. These components will have FSP selectively applied to the regions of the part where durability issues are either found or anticipated. Example components will be a cylinder head, a block application, and a crankshaft.

A number of different localized material durability issues that limit highly efficient engine design have been identified and include resistance to thermal fatigue, improved hot strength, improved resistance to erosive or adhesive wear in piston ring grooves, and improved performance and strength in aluminum blocks and cylinder heads of small displacement turbo-gas and turbo-diesel engine materials.

The project will develop and use FSP to produce surface-modified regions on parts composed of conventional engine materials. This work includes the following:

- Developing the FSP manufacturing parameters and selecting and evaluating

proper tool materials and techniques to produce defect-free FSP regions.

- Conducting coupon-level testing and evaluating thermal and mechanical properties. If performance metrics are met for sample materials enhanced by FSP, additional research will include development and demonstration of the appropriate method to apply this process to the two-dimensional and three-dimensional (3D) geometry of the selected parts.
- Once process schedules are established, prototype parts will be fabricated to specifications provided by project partners and relevant part testing will be completed (i.e., in-engine or other tests specified by partners).
- Dividing project tasks by part or application as listed below. The physical parts to be tested are expected to define several primary tasks surrounding the development of FSP for that part and the actual test runs in realistic environments.

Task 1: Cylinder head thermal-fatigue life improvement.

Subtask 1a – Chill casting of A356 plate stock for experimental trials.

Subtask 1b – FSP trials for thermal-aging studies.

Subtask 1c – FSP trials for stable microstructure (resistance to abnormal grain growth [AGG]).

Subtask 1d – Room temperature fatigue studies on FSP coupons (miniature fatigue testing).

Subtask 1e – Elevated temperature fatigue testing on FSP coupons.

Subtask 1f – Translating the process to a 3D part and producing a processed region on an actual head or head analog.

Subtask 1g – Operating-temperature, cylinder head thermal-shock testing (General Motors).

Task 2: Block and head-casting FSP to close near surface porosity for improved strength and durability.

Subtask 2a – FSP trials on block materials in plate form for thermal-aging studies.

Subtask 2b – FSP trials for stable microstructure (resistance to AGG).

Subtask 2c – Room temperature fatigue studies on FSP coupons (miniature fatigue testing).

Subtask 2d – Translating the process to a 3D part and producing a processed region for microstructural examination and testing.

Task 3: Oil hole fatigue performance improvement on rotating shafts.

Subtask 3a – FSP trials on steel alloy plate for process parameter development.

Subtask 3b – Mechanical and toughness testing of FSP coupons.

Subtask 3c – Room temperature fatigue studies on FSP coupons (e.g., rotating beam fatigue).

Subtask 3d – Translating the process to a 3D part and producing a processed region on an actual rotating shaft assembly.

Subtask 3e – In-engine, or other appropriate, testing.

Technology Transfer Path

Technology transfer both during and at the end of this project will be directly through the project participant General Motors, who will implement the technology.

Results and Discussion

During FY 2014, work focused primarily on the following areas:

- Room-temperature and elevated-temperature fatigue testing of FSP A356 alloy (head and block analog).
- FSP parameter development on a crankshaft steel alloy (typical microalloyed crank steel).

Elevated Temperature Fatigue Properties of A356 Alloy in a FSP Condition

FSP leads to significant microstructural refinement (e.g., eutectic Si particle and grain size), removal of casting porosity, and

breakdown of dendritic structure in any cast Al-Si alloys. During previous years, this microstructure produced significantly improved fatigue performance at room temperature. However, engine components are subjected to temperatures ranging from below 100°C in areas near the coolant to temperatures over 250°C in areas near the valves in the head. The concern for a FSP microstructure is whether the refined grains benefit durability as temperature increases. In addition, some FSP microstructures can undergo excessive grain coarsening (i.e., AGG) when exposed to elevated temperatures. Much of the focus in FY 2014 was to experimentally determine the fatigue performance of these different microstructures to ensure our excellent room temperature results translated to real engine conditions

During FY 2013, the occurrence of AGG in FSP parts was shown to be linked to the process parameters used (e.g., tool RPM, tool travel speed, etc.). During FY 2014, fatigue properties at elevated temperatures were determined as a function of microstructure (i.e., coarse grain [AGG] versus fine grain [non-AGG]). Our previous study identified two separate process parameters: one process condition creates a very coarse-grain microstructure after post-weld heat treatment (PWHT), while the other process condition keeps the weld nugget grains small even after PWHT.

Fatigue properties were determined by conducting bending fatigue tests. Because the FSP zone is relatively small, the project employed miniature fatigue testing. Figure 3 shows the fatigue specimen geometry and the specimen orientation with respect to the process zone.

The fatigue behavior at room temperature is shown in Figure 4. Three microstructural conditions are reported (i.e., (1) cast + T6, (2) FSP + aged, and (3) FSP + AGG + aged). More than one order of magnitude enhancement in fatigue life resulted from FSP. The cast material used in the current investigation is Sr modified; therefore, it has very fine eutectic Si particles and a highly refined secondary dendrite arm spacing. This microstructure is already quite good in fatigue in the as-cast state. However, the

beneficial aspect of FSP can still be observed, even over this optimized cast microstructure, indicating performance gains can be made without introducing a new high-performance bulk alloy.

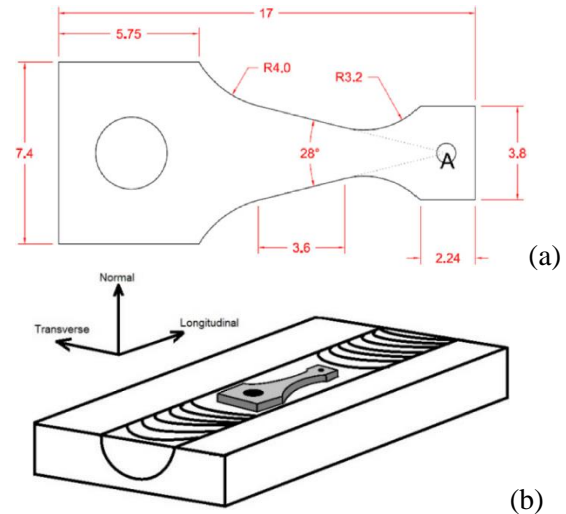


Figure 3. (a) Geometry of miniature bending fatigue sample (dimensions in mm) and (b) specimen orientation.

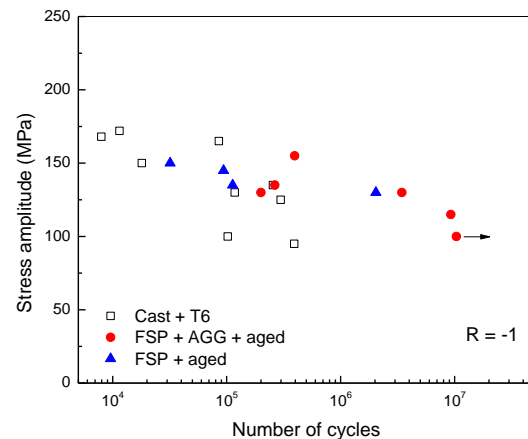


Figure 4. S-N plot at room temperature, FSP versus cast condition.

The project determined fatigue behavior at elevated temperature by immersing the sample and test fixture in an oil bath during the test. The existing miniature testing set-up (Figure 5[a]) was modified to include a hot oil bath system (Figure 5[b]), which was maintained at the test temperature. Tests were conducted at 150 and 200°C.

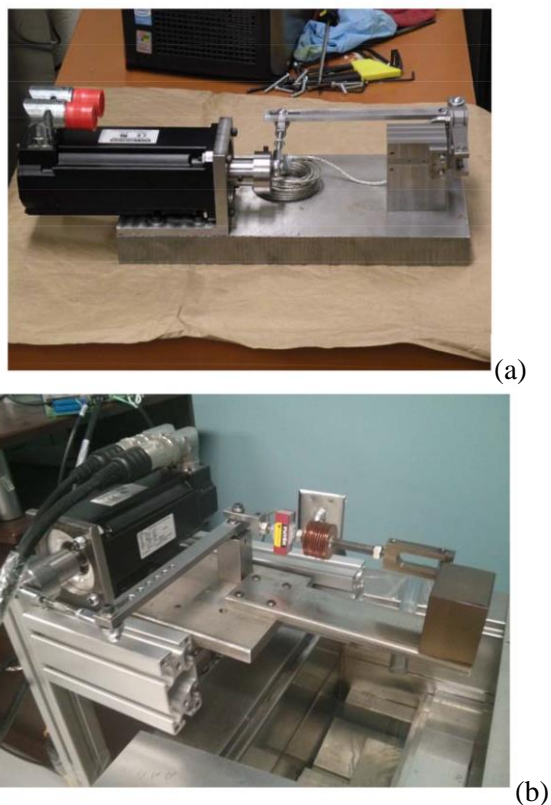


Figure 5. (a) Miniature bending fatigue test set-up; (b) An oil bath used to carry out the elevated-temperature fatigue tests.

The S-N plot for fatigue tests done at 150°C is shown in Figure 6. This plot shows three populations of samples representing different microstructures: (1) the as-cast + T6 condition, (2) the FSP + aged condition, which is an FSP material so that it does not show AGG upon PWHT (or at elevated engine temperature), and (3) FSP/AGG + aged, which is an FSP material so that it exhibits extreme grain growth during PWHT (or at engine temperature). As the plot shows, the beneficial aspect of FSP can be realized for both the non-AGG and for the AGG microstructures at elevated temperature. Formation of coarse-grain structure through AGG demonstrated no detrimental effect on the fatigue performance in FSP condition.

The A356 original cast microstructure consists of primary α -Al dendrites and refined eutectic Si particles at inter-dendritic regions. The alloy also contains a small amount of Mg that forms the strengthening Mg_2Si precipitates during aging treatment. When exposed to 150°C,

those precipitates grow, normally causing a decrease in strength at elevated temperature. In addition, the plates were chill cast and, as a result, the dendrite sizes were small as well. Overall, the cast microstructure at 150°C comprises small primary Al cells, refined Si particles, and coarsened Mg_2Si particles.

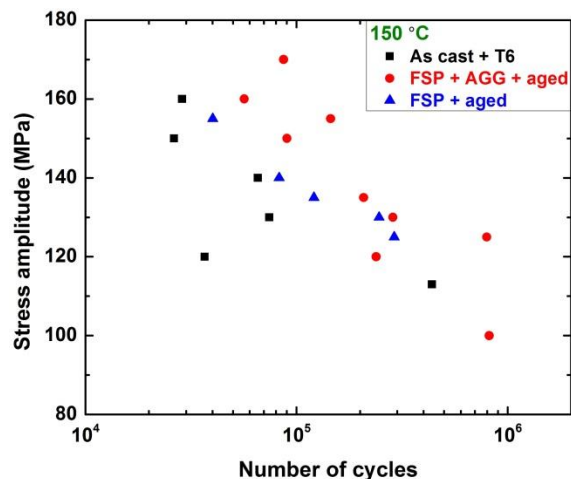


Figure 6. S-N plot at 150°C, cast versus FSP condition.

In comparison, the FSP/AGG microstructure comprises very large grains; uniformly distributed, refined Si particles; and coarsened Mg_2Si precipitates. Our continued observation of better fatigue performance, especially at higher stress levels in FSP condition over cast condition indicates that the occurrence of AGG may not be detrimental to fatigue behavior at elevated temperature. It is generally believed that a microstructure with refined grain size would fare better in a fatigue-dominated environment against a coarse-grain microstructure. The reverse is true for a creep-dominated environment. However, the present results show that the coarse-grain microstructure is showing better fatigue performance both at room temperature and at elevated temperatures.

At elevated temperature, yield strength differs in the three microstructural conditions. To remove this effect from the data presentation, the results were re-plotted on a normalized plot of the applied stress divided by the UTS of the respective class of microstructure. The results are shown in Figure 7(a) and Figure 7(b). The

results indicate that the beneficial aspect of FSP is more prominent at room temperature than it is at elevated temperature, but the FSP material is still significantly better in fatigue.

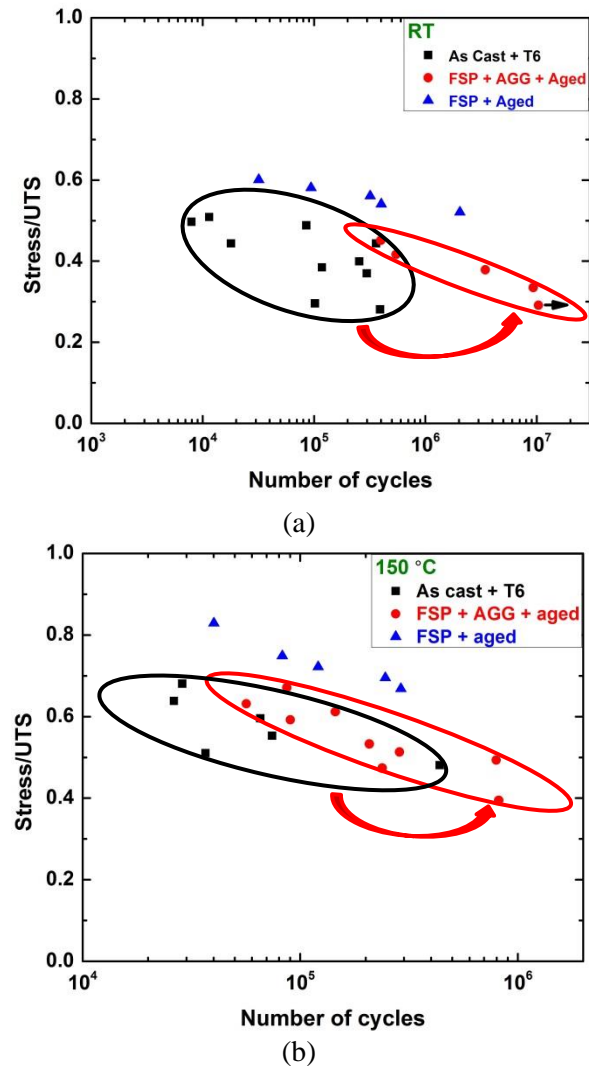


Figure 7. Comparison of S-N behavior as a function of temperature, (a) room temperature and (b) 150°C.

Fatigue testing was also conducted at 200°C (Figure 8). There does not appear to be any significant difference in fatigue behavior between 150 and 200°C. It is possible that recovery of the microstructure is taking place through dislocation annihilation because of the higher temperature of testing. As a result, less defect accumulation occurred over time. Softer material at higher temperature may also promote

crack sintering/welding, resulting in a significant reduction in the rate of crack propagation.

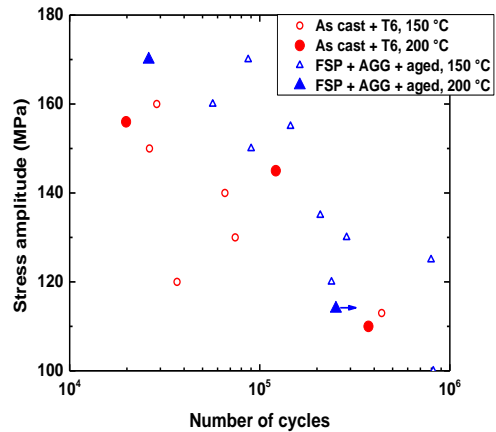


Figure 8. S-N plot at 200°C, cast versus FSP condition.

The project conducted detailed fractography to understand the crack initiation and propagation mechanism. Crack propagation behavior is found to change as a function of temperature. At room temperature, cracks are trans-granular, whereas at elevated temperature, inter-granular cracks are more prominent. Persistent slip bands (PSB), a common feature of fatigue failure, have also been identified. The PSB spacing gets coarser with increases in test temperature. Figure 9 shows the fractographs.

FSP of Crankshaft Grade Steel

Fatigue-crack initiation and subsequent failure around oil holes in a rotating crankshaft is one of the possible failure modes of crankshafts subjected to high mechanical loading from high power-density engines. FSP may help in mitigating such early fatigue problems by removing the potential crack-starting features (notches) from the microstructure.

During FY 2014, the project attempted FSP of a typical crankshaft grade steel. The steel used in this study is SAE 1538MV. This is a micro-alloyed, medium carbon steel. A micrograph of the parent material is shown in Figure 10. The microstructure consists of ferrite and pearlite, and the volume fraction of pearlite is about 50%.

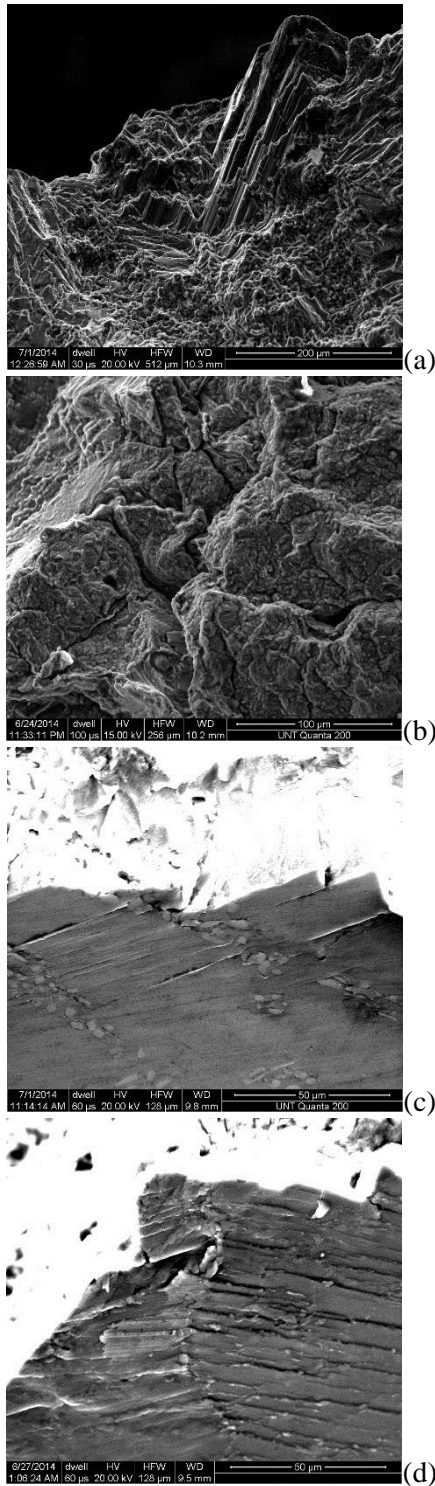


Figure 9. Fractographs of failed specimens: (a) trans-granular fracture seen at room temperature, (b) inter-granular fracture at 150°C, (c) fine PSB spacing at room temperature, and (d) coarse PSB spacing at 150°C.



Figure 10. Microstructure of the parent material, 1538-MV micro-alloyed steel. Presence of ferrite and pearlite phases is evident.

Additionally, stringer-like MnS inclusions can be seen uniformly dispersed through the matrix. Upon heating, the matrix transforms into austenite. The Ac1 and Ac3 temperatures were determined to be about 730 and 820°C.

A preliminary FSP trial on this grade of steel using a composite PCBN tool has been completed. The preliminary weld trial was carried out to evaluate the types of phases that would form in the weld nugget as the steel cools down to room temperature. A low magnification representative image of the weld nugget in transverse cross-section is shown in Figure 11(a). A basin-shaped nugget and a prominent heat-affected zone around the nugget are clearly visible. Upon closer examination, the heat-affected zone reveals existence of various austenite transformation products. Inside the nugget, the presence of martensite and widmanstätten ferrite can be seen near the weld top and middle region (Figure 11[b]). Toward the bottom of the weld nugget, the presence of bainite (acicular ferrite) is observed (Figure 11[c]). This indicates that during the welding process, the parent material transformed into austenite with the passage of the weld tool.

At present, only the fatigue properties of the parent material are determined. The test method used for the crankshaft FSP tasks is rotary beam fatigue testing at room temperature. Prior to fatigue testing, quasi-static tensile testing of the parent material was done at the 1E-2 strain rate. The yield strength of the parent material was

about 520 MPa, and the percent elongation to failure was about 5%. Tensile properties are summarized in Figure 12.

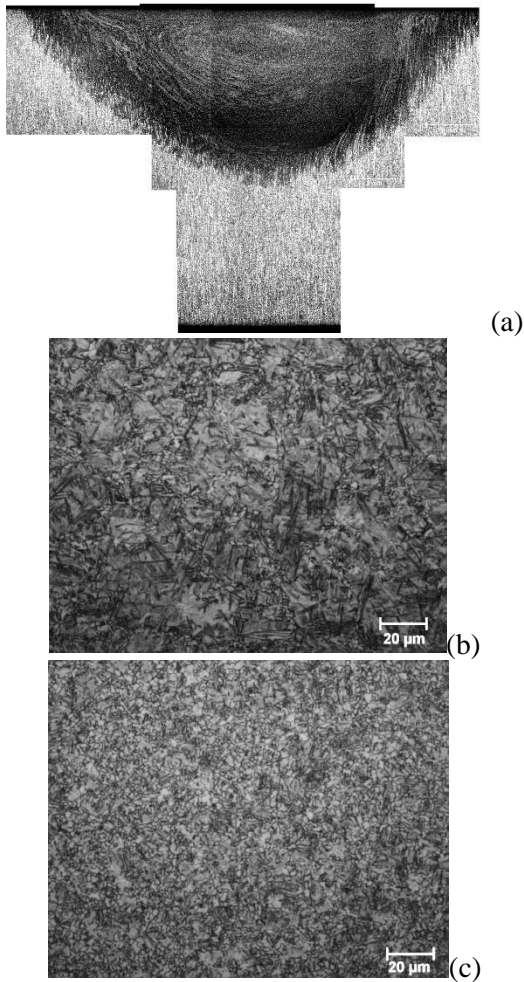


Figure 11. FSP of 1538-MV steel using a composite polycrystalline cubic boron nitride tool for a (a) weld nugget cross-section, (b) martensitic structure near the weld top surface, and (c) acicular ferritic structure near the weld bottom.

The fatigue tests were carried out at room temperature at a 100-Hz frequency and at a load ratio of $R = -1$. S-N behavior of the parent material is shown in Figure 13. No failure was observed whenever the applied stress was below about 300 MPa; therefore, this is the endurance limit for this grade of steel.

Fractographs of the failed specimens indicated crack initiation from the surface. The fractograph shown in Figure 14(a) corresponds

to 209,000 cycles to failure at 317-MPa stress. This fatigue fracture surface appearance is representative of low nominal stress and low stress concentration. The crack initiation site is highlighted. Crack propagation plays a major role during fatigue failure for this grade of steel, as noted from the image. Presence of dimple/microvoid features, which signifies final ductile failure by overload, was noted at a diametrically opposite direction to crack initiation site. An example of ductile rupture pattern is shown in Figure 14(b).

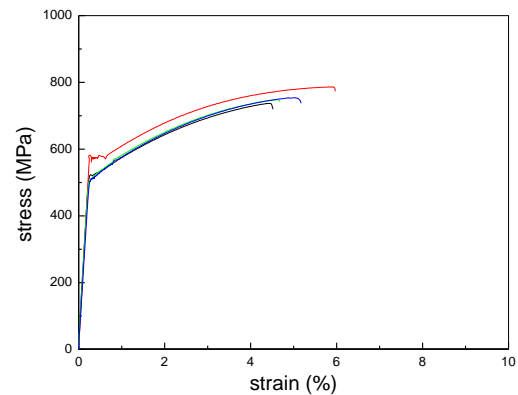


Figure 12. Stress-strain curves of Society of Automotive Engineers 1538-MV steel.

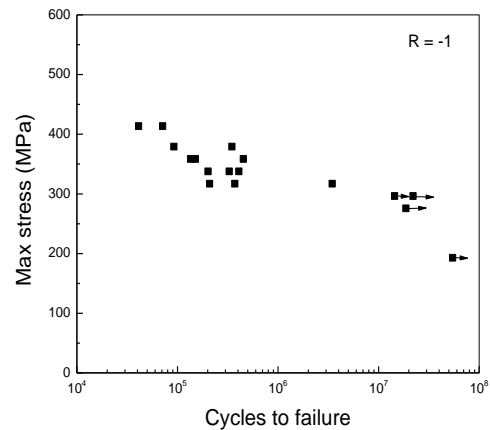


Figure 13. S-N plot of Society of Automotive Engineers 1538-MV steel at room temperature.

Conclusions

The goal of this project is to use FSP to develop components that enable energy-efficient combustion strategies, especially strategies that

require higher PCP or higher-temperature operation. FSP produces selected, graded structures that have shown increased strength and durability in fatigue. Surface modification through FSP may address some emerging material problems seen in very high combustion pressure systems (e.g., HCCI engines).

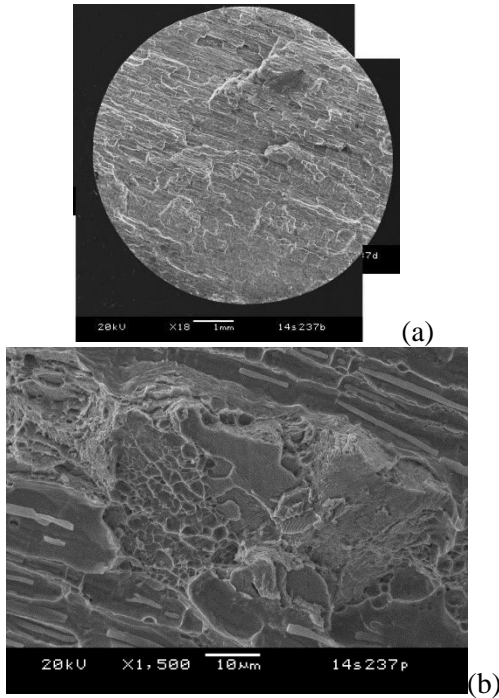


Figure 14. Fractograph of the parent material (Society of Automotive Engineers 1538-MV steel), (a) low-magnification image, (b) ductile rupture pattern seen at overload area.

FY 2014 accomplishments show that FSP processing can improve the fatigue performance of conventional engine alloys even at elevated temperatures. The excessive grain growth in aluminum materials processed under some FSP conditions appears to have no effect on the fatigue behavior at a higher temperature. Additional testing at higher temperature in FY 2015 will determine if creep mechanisms ever enter into consideration for these applications and, if so, is there a preferred FSP microstructure for creep-fatigue. In addition, the project will apply FSP to a prototypic cylinder head and test the durability performance through a thermal stress test designed by General Motors.

Preliminary work has begun to investigate the effect of FSP on crankshaft-grade steel. The fatigue properties of the parent material were established, and some initial weld studies have been carried out. In FY 2015, the project will complete FSP fatigue testing on rotating beam fatigue specimens with and without simulated oil holes and apply the process to a subscale prototypic crankshaft for instrumented testing.

Project 18518 – High-Strength and High-Temperature Materials for Heavy Duty Engines

Agreement 24034 – High-Temperature Aluminum Alloys

Stan G. Pitman

Energy Materials Group

Pacific Northwest National Laboratory

P.O. Box 999, MS K2-03

Richland, WA 99352

Phone (509) 371-6746; fax (509) 375-4448; email: stan.pitman@pnnl.gov

Howard Savage

Cummins, Inc.

Phone (812) 377-5998; email: howard.savage@cummins.com

DOE Technology Manager: Jerry L. Gibbs

Phone (202) 586-1182; fax: (202) 586-1600; e-mail: jerry.gibbs@ee.doe.gov

Field Technical Manager: Yuri Hovanski

Phone (509) 375-2940; fax: (509) 375-4448; e-mail: yuri.hovanski@pnnl.gov

Contractor: Pacific Northwest National Laboratory, Richland, Washington

Prime Contract No.: DE-AC05-76RL01830

Objectives

- To develop aluminum alloys in laboratory-scale processing, which have high strength at elevated temperatures (300 MPa tensile strength at 300°C). This objective is being approached using melt-spinning processes to produce flake and consolidating the flake by extrusion.
- To produce high-strength aluminum alloys in commercial-scale processes using industrial suppliers for the melt-spinning and consolidation processes.
- To produce forgings that will be evaluated for a commercial application requiring high-temperature strength.

Approach

- Produce the rapidly solidified alloy compositions using the Pacific Northwest National Laboratory (PNNL) pilot flake system. Consolidate flake materials via extrusion using laboratory-scale extrusion tooling at PNNL.
- Measure elevated temperature mechanical properties and compare to the mechanical properties of the baseline materials.
- Produce larger quantities of flake via Transmet (under subcontract to PNNL) using the production melt-spinning system.
- Consolidate the production flake by degassing, canning, and hot isostatic pressing, followed by extrusion.
- Test full-scale components using the appropriate test system at Cummins, Inc.
- Perform engine testing at Cummins, Inc. if the component test is successful.

Accomplishments

- Evaluated potential high-temperature, high-strength aluminum alloy systems that can be produced by rapid solidification (RS) and subsequently processed via extrusion or forging.
- Feedstock melting methods were developed, which resulted in production of the aluminum-iron-manganese (AFM)-11 alloy that has a tensile strength exceeding the target value of 250 MPa.
- Developed a more detailed understanding of microstructural evolution of the AFM-11 alloy during processing and identified potential scale-up issues.

Future Direction

- Perform fatigue tests, if warranted, by evaluation of mechanical properties and understand the service life potential of the AFM-11 alloy
-

Introduction

Aluminum alloys that possess strengths approaching 300 MPa at 300°C have been produced in small quantities by numerous mechanical attrition (MA) methods. Although MA can produce unique combinations of properties, MA processing approaches have not been able to meet the requirements for low-cost, high-volume production. The purpose of this project is to demonstrate that MA-type alloys can be produced with adequate high-temperature mechanical properties through development of a low-cost, high-volume RS production process.

Mechanical attrition aluminum alloys with strengths approaching 300 MPa at 300°C have been produced by adding alloying elements that have very low solubility and that form intermetallic dispersions (e.g., Fe, Ti, Cr, Mn, and Zr) in the aluminum matrix. Milling cycles can require hundreds of hours to adequately homogenize the alloy, which produces a large amount of oxide, limiting production and ductility, respectively. In the past, PNNL has worked with melt-spinning methods to produce alloys by RS using a process that produces a low-surface-area particulate (i.e., flake).

The RS flake can be consolidated by elevated-temperature extrusion. This project intends to use the RS flake/extrusion process to produce an aluminum alloy with an increased elevated temperature strength that can be used in diesel engine service environments up to 300°C.

Approach

The approach is to evaluate the feasibility of producing Al-Fe high-temperature alloys by two different rapid solidification methods: melt spinning of flake and rotating cup (shot) processing of powder particles. The two methods are known to have solidification rates that differ by several orders of magnitude, with the RS flake estimated at 10^6 degrees/second cooling rate and the rotating cup particle process at 10^2 degrees/second. The rotating cup RS method was being evaluated in spite of the lower solidification rate, because it is established as one of the high-volume RS processes and because the shot particulate has some advantages in handling and consolidation.

This evaluation has been completed and will be discussed in a subsequent section of this report. The melt-spinning method was chosen for use in the following steps:

4. Produce the rapidly solidified alloy compositions using the PNNL pilot flake system. The PNNL flake melt-spinning machine can produce limited quantities of experimental alloys in the form of rapidly solidified flake. The following subtasks were initiated after producing aluminum flake feedstock by melt spinning:
 - a. Conduct a comprehensive technology review of prior high-temperature and high-strength aluminum alloy development, including alloys developed by Allied Signal and academic institutions.
 - b. Select three alloy compositions: two similar to the early Allied Signal Al-Fe-X compositions and the $\text{Al}_3\text{Fe}_2\text{Cr}_2\text{Ti}$ previously developed by MA.
5. Consolidate flake materials via extrusion using laboratory-scale extrusion tooling at PNNL. Rapidly solidified flake will be consolidated using the canning and indirect extrusion process previously developed by PNNL.
6. Measure elevated temperature mechanical properties and compare to baseline materials. Elevated temperature tensile tests of sample materials will be conducted to establish temperature strength behavior for the materials.
7. Produce larger quantities of flake via Transmet (under subcontract to PNNL) using the production melt-spinning system. The selected alloy composition(s) will be made into master alloy feedstock and provided to Transmet for melt spinning into rapidly solidified feedstock. Quantities of several hundred pounds are anticipated, depending on the alloy systems selected.
8. Consolidate the production flake by degassing, canning, and hot isostatic pressing, followed by extrusion. Larger billet diameters will be used, and processing

will simulate anticipated full-scale production methods.

9. Test full-scale components using the appropriate test system at Cummins, Inc. Cummins, Inc. will select components that will benefit from the high-temperature aluminum properties and process the materials supplied by PNNL into full-scale test components.
10. Perform engine testing at Cummins, Inc. if the component test is successful. Established rig testing will be conducted to establish performance and mass reduction benefits.

The primary deliverables from the project will be as follows:

- Development and production of high-temperature aluminum alloys by rapid solidification
- Characterization of the RS alloys and baseline materials for elevated temperature fatigue strength
- Cost analysis of the process to produce full-scale extrusions
- Full-scale component testing to validate performance of the alloys.

Results and Discussion

Work on this project began in May 2011, conducted under a Cooperative Research and Development Agreement between Cummins, Inc. and PNNL. The first phase of the effort focused on identification of candidate aluminum alloy systems that can provide higher strengths (300 MPa) at elevated temperatures of approximately 300°C and on evaluation of two methods for producing RS feedstock: melt spinning of flake and rotating cup processing of powder particles. The work with melt spinning is described here, with a discussion of melt spinning relative to rotating cup processing following.

A series of five alloy compositions were evaluated, along with two different consolidation and extrusion processes. All alloys contain iron (Fe) as a key alloy addition, along with smaller additions of silicon, Ti-Cr-V, and manganese. With the exception of silicon, alloy

additions were chosen for their low solubility in aluminum and ability to form stable second-phase particles. Evaluated alloy compositions are listed in Table 1. The first two alloys contain Si and V, while the aluminum-iron-chrome/titanium (AFCT) alloy contains a lower level of Fe, combined with higher weight percentages of Cr and Ti. The AFM alloy was developed at PNNL in earlier work.

The first three alloys previously have been produced in small quantities and tensile tested at a range of temperatures. Tensile strengths for these alloys at 300°C have been reported in the 250 to 300-MPa range, close to or meeting the property goals.

The processing steps that were selected for this project include induction melting to produce suitable feedstock alloys that approximate the compositions of the alloys listed in Table 1, analysis of actual compositions and the alloy melting characteristics, induction remelting of the alloys, and melt spinning to produce RS flake materials for subsequent processing. Figure 1 shows the RS flake material and the melt-spinning equipment used to produce it.

The second focus of the project was development of laboratory-scale extrusion tooling to be used in consolidation and extrusion of the RS flake to produce a wrought-extruded rod. The extruded rod material provides sufficient material for machining of tensile specimens for room temperature and elevated temperature (i.e., 300°C) tensile testing. Two processing approaches were developed for preparing the RS flake material for extrusion into the wrought rod product. The first approach involved cold (i.e., room temperature) pressing of the RS flake into an aluminum can, followed by weld sealing the can under vacuum conditions. The sealed can was heated and extruded to the rod product using a 19:1 extrusion ratio. In the second approach, the canned flake was placed in a vacuum hot press at 450°C and pressed to preconsolidate the RS flake to approximately 90% theoretical density. The canned and consolidated billet was then extruded into the rod using the same 19:1 extrusion ratio.

Table 1. Initial high-temperature, high-strength aluminum alloys.

Alloy Designation	Fe	Si	V	Cr	Ti	Mn
Al-12Fe	12.4	2.3	1.2			
Al-8.5Fe	8.5	1.7	1.3			
AFCT	6.0			3.4	3.2	
AFM-11	11.4	1.8	1.6			0.9
AFM-13	13.2	2.6	.50			0.9



Figure 1. (a) Picture of the PNNL flake melt-spinning machine with the front chamber removed; (b) typical RS flake product produced with the melt-spinning equipment; (c) photograph of the canned RS flake billet (top) and the extruded rod.

Figure 1 also shows an example of the canned billet (50-mm diameter) and the resulting extruded rod (11.4-mm diameter).

Following extrusion of the RS flake materials, the extruded rods were cut into lengths and machined into round American Society of Testing Materials subsize tensile specimens with a gage length of 25 mm and a gage diameter of 6.4 mm. Approximately 150 mm of the nose and tail of the extrusion were discarded to minimize non-uniform material. Machined tensile specimens were then tested at room temperature and at an elevated temperature of 300°C. A minimum of three tests were conducted at each temperature. Results of the tensile tests for the various aluminum alloys and heat-treated conditions are shown in Table 2.

The goal of this project is to approach a tensile strength of 300 MPa at 300°C test temperature. As shown in Table 2, the AFM-11 alloy comes closest to meeting that goal. Based on the initial results for the candidate alloys, further processing of the AFCT and AFM-11 alloys has been initiated. These alloys were chosen because they showed the most

pronounced increase in the measured elastic modulus of the tested materials. Initial characterization showed that all compositions exhibited refined grain size (less than 1 μm), along with an extensive distribution of submicron secondary phase particles. Both the AL-8.5Fe and the AFM alloy have areas of larger, less dense secondary particles, indicating some phase growth during processing. Figure 2 shows low-magnification micrographs of these three extruded aluminum alloys.

In addition to the elevated-temperature strength goal, high-temperature (300°C) fatigue life is an important material property for heavy-duty engine applications. To meet these project goals, two different processing techniques (i.e., melt spinning and rotating cup processing) were tested for their ability to elevate mechanical properties beyond that of the extruded values (Table 2). Rapid solidification techniques are well known for their ability to improve mechanical properties such as wear resistance, thermal expansion, and high-temperature strength of microcrystalline aluminum, all of which are ideal properties for applications such as engine components.

Table 2. Room and elevated-temperature tensile test results for candidate high-temperature extruded aluminum alloys.

Alloy Designation	Extrusion Temperature (°C)	Elastic Modulus (GPa)	Elastic Modulus (GPa) 300°C	Tensile Yield Strength (MPa)	Tensile Yield Strength (MPa) 300°C	Ultimate Tensile Strength (MPa)	Failure Strain (%)	Failure Strain (%) 300°C
Al-8.5Fe - EB	450	83.5	74.5	345.0	210.9	390.4	19.1	25.1
Al-8.5Fe - EB	500	84.2	76.6	331.2	208.2	389.4	18.0	21.7
Al-8.5Fe - HP	500	86.9	71.8	338.1	204.2	384.9	18.3	18.4
AFCT - HP	500	95.9	80.7	400.2	226.7	448.6	12.2	18.8
AFM-11-HP	500	96.0	91.1	427.8	256.8	493.6	7.2	17.0

EB = vacuum electron beam welded can without hot press

HP = vacuum hot-pressed billet. Failure strains measured using an extensometer. Notes: Yield strength and ultimate strength are the same at the 300°C test temperature. Extension at failure calculated from gage section measurements.

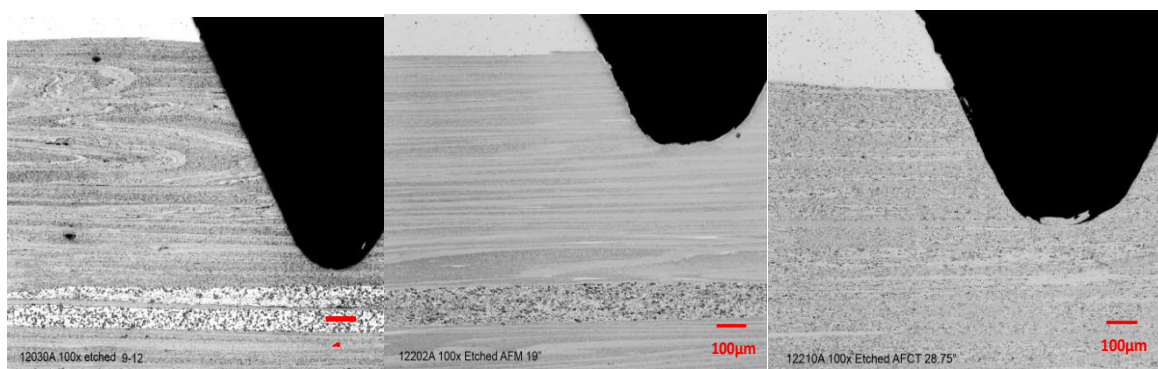


Figure 2. Low-magnification micrographs of extruded aluminum alloys: (left) AL-8.5Fe, (center) AFM-11, and (right) AFCT. Specimens are from the thread ends of actual tensile specimens as indicated by the black thread contour. The white upper material is the 6061 aluminum can used for extrusion.

Discussion of Melt Spinning Relative to Rotating Cup Processing for Processing of Al-Fe High-Temperature Alloys

Processing of Al-Fe series high-temperature alloys was conducted by two different RS methods: melt spinning of flake and rotating cup processing of powder particles. The two methods are known to have solidification rates that differ by several orders of magnitude, with the RS flake estimated at 10^6 degrees/second cooling rate and the rotating cup particle process at 10^2 degrees/second. Two high-temperature aluminum alloys (AFCT and AFM-11) were processed by melt spinning and, subsequently, consolidated into billets and extruded to make a round rod product, as described previously.

The same two alloys were then processed by Transmet Corporation (Columbus, Ohio) using their rotating cup RS shot process. PNNL

supplied induction-melted ingots of the two alloy compositions to Transmet, who then processed them into RS shot samples. After receiving the shot samples and performing optical metallography of the materials, the shot-processed alloys were canned, cold compacted, and consolidated using the same vacuum hot-press parameters. Several consolidated billets were then extruded using the same temperatures and extrusion parameters used for the RS flake materials. As with the RS flake extrusions, a minimum of three tensile specimens were tested at room temperature and 300°C to measure the tensile properties of the RS shot materials. Tensile test results are summarized in Table 3.

Tensile test results show that the flake material has significantly higher tensile strengths when compared to the extruded shot material.

Table 3. Tensile test results for extruded RS flake and rotating cup shot material, alloys AFCT and AFM-11.

Alloy Designation	Test Temperature (°C)	Yield Strength (MPa)	Ultimate Tensile Strength (MPa)	Failure Strain (%)
AFCT flake	room	400.2	448.6	12.2
AFCT shot	room	169.0	215.3	4.9
AFM-11 flake	room	427.8	493.6	7.2
AFM-11 shot	room	287.0	411.2	1.8
AFCT flake	300°C	(1)	226.7	18.8
AFCT shot	300°C	(1)	91.8	2.9
AFM-11 flake	300°C	(1)	256.8	17.0
AFM-11 shot	300°C	(1)	185.6	5.8

(1) Yield and tensile strength were equal at 300°C test temperature

The extruded flake materials also display relatively high elongations to failure, which would indicate good consolidation during extrusion and a stable, refined microstructure.

A key goal for Fiscal Year (FY) 2014 was to downselect to one alloy system. Because tensile data and optical microscopy indicated that the AFM-11 alloy was the ideal candidate for optimization, detailed metallographic examinations of the flake and shot materials were performed at various stages during processing.

Rapid Solidified Flake and Shots

In the RS flake process, the spinning copper wheel has a special knurled pattern of lines running in the direction of rotation and perpendicular to the rotation direction. This surface pattern produces discontinuous flakes that are approximately 1 mm x 1 mm square, with a thickness of 35 to 55 μm , depending on the operating parameters and materials. This ensures very high through-thickness cooling rates for the flake, while the comparatively large length and width of the solidified flake reduces the surface area and oxygen content. A micrograph of the Al-Fe RS flake is shown in Figure 3.

Nanocrystalline (possibly amorphous) regions are present near the wheel side of the flake. The thickness of these regions is variable, which is not surprising considering the large thermal gradients required to produce such a

structure coupled with the surface variation (knurled pattern) on the spinning copper wheel. Aside from the nanocrystalline area, another dispersed phase appears from the Al matrix in the form of bright circular regions (Figure 3). The size of this phase increases as distance from the wheel is increased, corresponding to slower cooling. Microstructural variation in the AFM-11 room temperature flake material is shown in Figure 4.

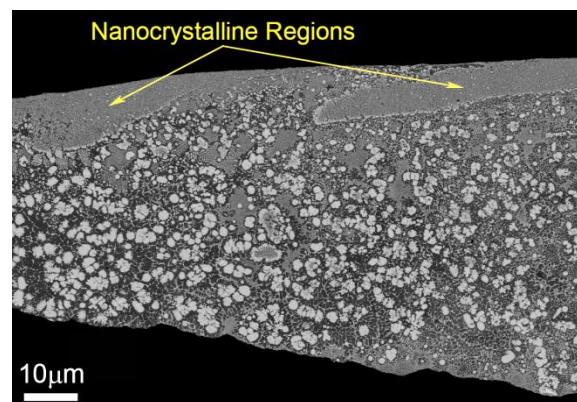


Figure 3. AFM-11 flake material showing the formation of nanocrystalline or amorphous regions near the wheel side.

Four distinct phase morphologies were observed in the room temperature flake material and were compared with variations seen in the shot material (Figure 5). The shape of shot is similar to a water droplet with elongation in the direction of the centrifugal force. Two key differences exist between the flake and shot microstructures. The nanocrystalline/amorphous

layer is not present in the shot material and the length scale of phases in the shot material is much larger than that of the flake.

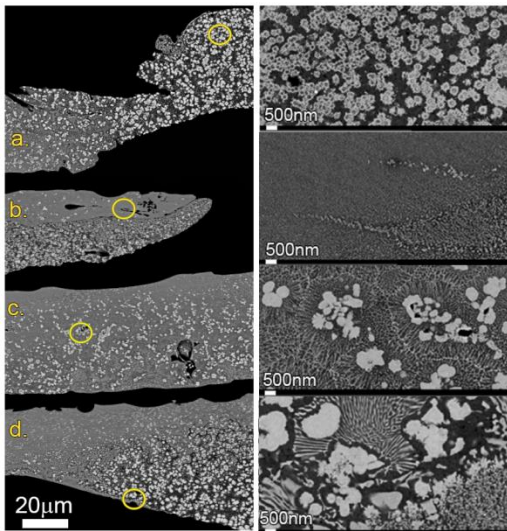


Figure 4. Microstructural variance in the room temperature flake material: a) rings, b) amorphous /nanocrystalline regions, c) dendritic-cellular network, d) lamella/eutectic phase.

As an example, dendritic branching in the flake material was on the order of 10 to 50 nm, whereas branching in the shot material was 0.5 to 1.5 μm . The larger microstructural features of the shot material can be easily understood as due to the slower cooling rates associated with this processing method. The refined microstructures of the flake material and increased surface area lead to a higher density of grain boundaries and likely account for the elevated strength of the flake material shown in Table 3. Also shown in Table 4 was a significant drop in the ultimate tensile strength of the AFM flake materials at elevated temperature (i.e., 300°C). For these reasons, microstructural evolution of the flake material was investigated at two heat-treated conditions: 10 hours at 450°C and 10 hours at 450°C followed by an additional 3 hours at 500°C. Because of the morphological variability that was seen in these materials (Figure 4), comparison to illustrate a direct causal relationship between each stage of the heat treatment and its structural effect is difficult. However, the 10-hr/450°C + 3-hr/500°C heat treatment did result in precipitation of a needle-like phase (Figure 6) that was not seen in any of the other AFM-11 flake or shot materials.

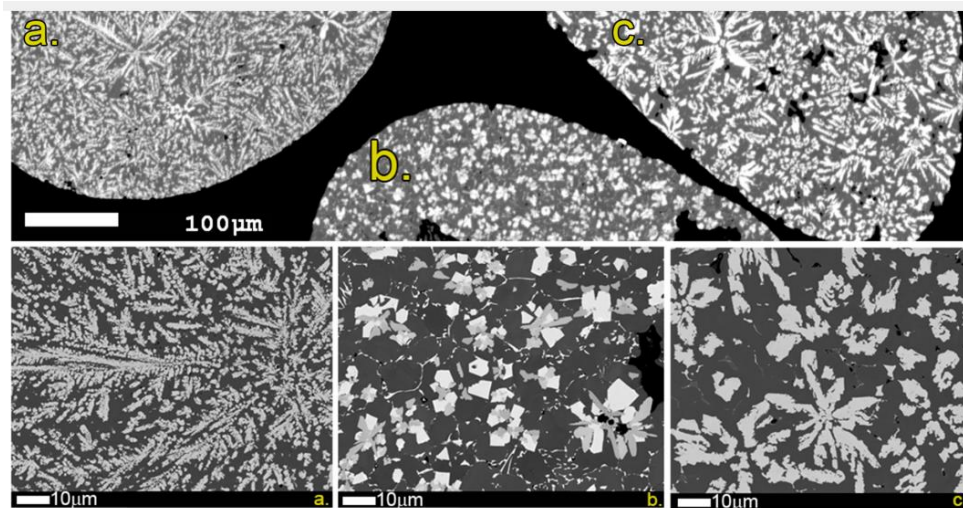


Figure 5. Microstructural features seen in the room temperature shot material: a) dendrites, b) angular precipitates in a cellular structure, and c) rosettes.

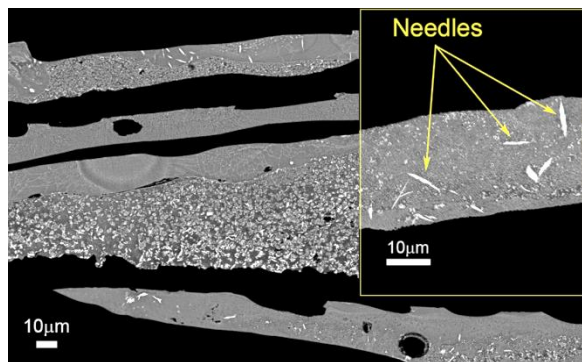


Figure 6. Formation of a needle-like phase in the AFM-11 alloy as a result of the 10-hr/450°C + 3-hr/500°C heat treatment.

Microscopy information to this point has indicated that new phases form at elevated temperatures. Because the AFM-11 alloy was developed at PNNL, it is difficult to predict what phases could be formed at specific temperatures because there is no time-temperature-transformation curve available for this material. However, literature on Al-Fe-(V and Si) alloys among others has shown the formation of very similar phase morphologies. Energy dispersive spectroscopy (EDS) results coupled with this information have proven to be a very valuable tool. EDS was performed on all of the phases shown in Figures 3 through 6 to identify compositional information; however, phases discussed below are only those measured from the flake material (Figure 7).

Compositional information for the phases identified above is shown in Table 4. Because of the high cooling rates associated with RS methods, the nanocrystalline/amorphous phase is likely a non-equilibrium microstructure. Heat treating has the potential to result in the nucleation of an equilibrium phase from this non-equilibrium region. The formation of the needle-like phase in the heat-treated specimen is believed to be precipitation of an intermetallic compound, which could lead to a decrease in strength.

Microstructural Analysis of Extruded and Forged Flake Material

The extruded and forged flake material was evaluated for formation of the needle-like intermetallic and is shown in Figure 8.

Extrusion of the consolidated flake material resulted in the formation of a banded structure, aligned with the extrusion direction. Dark regions were identified as pure, crystalline Al with a grain size on the order of 1 to 5 microns. The Al-rich banding and overall structure was not significantly altered by forging. Iron-rich phases were identified solely from compositional information extracted using EDS. Confirmation of phase identification will be performed using transmission electron microscopy. The AFM-11 alloy chemistry coupled with processing methods, which can produce metastable intermetallics, amorphous and quasicrystalline regions, or mixtures of them, requires a more detailed approach to phase identification beyond chemical assay alone.

Technology Transfer and Conclusions

By participating in this Cooperative Research and Development Agreement, Cummins, Inc. will benefit by applying new technology to improve the high-temperature performance and life of engine combustion components, air-handling systems, and emission-control components. In addition, Cummins, Inc. benefits by coupling its own engineering production experience and knowhow with the scientific expertise and technical capabilities of PNNL staff and U.S. Department of Energy laboratories to solve relevant problems that benefit the industry and achieve U.S. Department of Energy fuel economy goals.

The early phase of this project has evaluated potential high-temperature, high-strength aluminum alloy systems that can be produced by RS and subsequently processed via extrusion or forging. A group of five candidate alloys were selected for processing and characterization. Feedstock melting methods were developed, which resulted in production of the AFM-11 alloy that has a tensile strength exceeding the target value of 250 MPa. The focus of FY 2014 was centered on developing a more detailed understanding of microstructural evolution of the AFM-11 alloy during processing and on identifying potential scale-up issues. FY 2015 goals will be to perform fatigue tests, if warranted, by evaluation of mechanical

properties, and understand the service life potential of the AFM-11 alloy.

Table 4. EDS compositions from point areas identified in Figure 7.

AFM-11			Mass Percent				
Region	Color	Morphology	Al	Fe	Si	V	Mn
1	Gray	Nanocrystalline	83.2	12.6	1.8	1.4	1.0
2	White	Circular	77.5	17.0	2.1	2.0	1.4
3	Dark	Matrix	90.3	7.2	1.2	0.8	0.5
4	Lt. Gray	Mottled	81.3	14.3	1.8	1.6	1.1
5	Gray	Agglomerate	82.8	13.0	1.8	1.4	1.0
6,7,8,9	white	Needles	71.6	25.5	1.2	0.9	0.9
10,11	Gray	Nanocrystalline	85.4	10.5	1.7	1.5	1.1
12	Dark	Matrix	89.1	8.2	1.0	0.9	0.8
13	Lt. Gray	Mottled	78.3	16.5	2.1	1.8	1.3

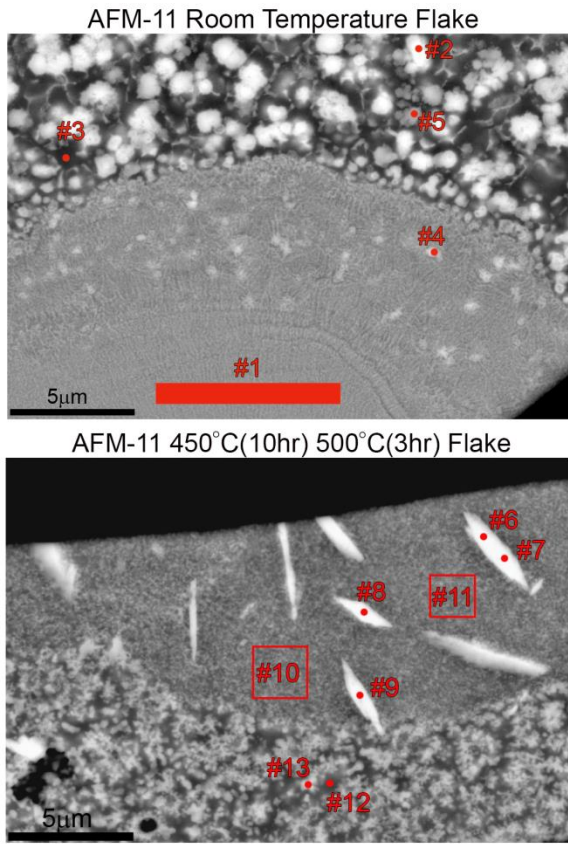


Figure 7. AFM-11 flake material in the room temperature condition (top) and heat-treated condition (bottom). Red points and highlighted regions indicate areas where compositions were recorded.

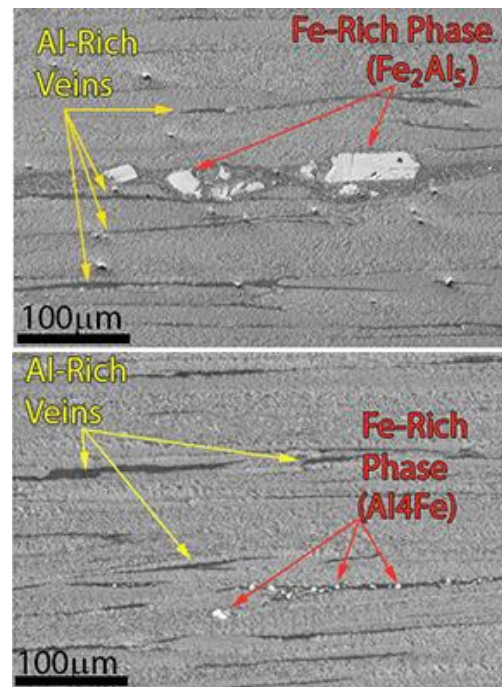


Figure 8. Extruded (top) and forged (bottom) AFM-11 microstructure in the extrusion direction. Needle-like phase was not observed.

Project 18518 – Materials for High-Efficiency Engines

Agreement 26190 – High-Temperature Materials for High-Efficiency Engines

G. Muralidharan and B. Pint

Materials Science and Technology Division

Oak Ridge National Laboratory

1 Bethel Valley Road

Oak Ridge, TN 37831-6068

Phone (865) 574-4281; fax (865) 574-4357; email: muralidhargn@ornl.gov

DOE Technology Manager: Jerry L. Gibbs

Phone (202) 586-1182; fax: (202) 586-1600; e-mail: jerry.gibbs@ee.doe.gov

Technical Advisor: J. Allen Haynes

Phone (865) 576-2894; fax: (865) 574-4913; e-mail: haynesa@ornl.gov

Contractor: Oak Ridge National Laboratory, Oak Ridge, Tennessee

Prime Contract No.: DE-AC05-00OR22725

Objectives

- Identify and catalog the materials property requirements for exhaust valves in next generation high-efficiency engines.
- Evaluate mechanical properties and oxidation resistance of leading existing Ni-based alloys candidates and alternate materials with the capability to operate at 950°C.
- Adopt Integrated Computational Materials Engineering-based techniques to develop alternate lower cost Ni-based alloys for exhaust valve applications at temperatures up to 950°C.

Approach

- Mechanical property requirements for operation at 950°C will be defined and the microstructure required to achieve these properties will be identified.
- Oxidation tests will be performed to understand composition effects on oxidation behavior and establish limits of critical elements.
- A synergistic computational modeling and experimental evaluation approach that was followed in the design of new alloys for exhaust valve applications up to 870°C will be refined and used to identify promising compositions for service at 950°C.
- Trial heats of new compositions will be prepared, properties measured, and compositions refined in an iterative manner.

Accomplishments

- Cyclic oxidation behavior of several Ni-based alloys has been characterized at 900°C in air with 10% water vapor for times up to 500 hours to understand the effect of composition.
- A target microstructure has been identified for improved high-temperature strength.

Future Direction

- Develop new development alloys with targeted microstructure for improved high-temperature strength.
 - Evaluate alloying element additions to improve high-temperature oxidation resistance.
-

Introduction

Improving the engine efficiencies of passenger and commercial vehicles is a major goal of the Vehicle Technologies Program, and propulsion materials play a significant role in achieving this objective. One of the important strategies to achieving the goals of improving engine thermal efficiency is by advancing technologies that increase engine combustion efficiency such as lean-burn operation (i.e., high-efficiency clean combustion), high levels of exhaust gas recirculation, turbocharging, variable valve actuation, and/or variable compression ratios. One of the barriers to achieving increased efficiency is the need to simultaneously reduce pollutant formation, achievable through high-efficiency combustion technologies. One potential method for achieving improved engine efficiency while reducing emissions is through retaining more heat in the exhaust gas.

Strategies for retaining more heat in the exhaust naturally result in increased exhaust gas temperatures, thus increasing the operational temperature requirements of components in the exhaust gas path, including exhaust valves. It has been projected that exhaust gas temperatures would increase from a current value of 760°C to values of at least 870°C and very likely reaching up to 1000°C in the long-term. Availability of materials with adequate high-temperature mechanical properties and oxidation resistance to enable the projected engine operating parameters, without exceeding the cost constraints is a barrier to adoption of new high-efficiency technologies. The objective of this project is to address the needs of cost-effective materials for exhaust valves for operation up to 950°C.

A recently concluded project successfully addressed development of new lower-cost alloys for use in exhaust valves at temperatures up to 870°C through a “materials-by-design” approach. “Materials-by-design” is a concept that encompasses a collection of materials-related techniques, including modeling, correlation, and materials modification. The premise behind materials-by-

design is that mechanical properties are correlated to microstructure and phase chemistry. The phase composition and microstructure can be achieved through thermodynamic equilibrium or through non-equilibrium techniques such as quenching, rapid casting solidification, or mechanical working. These characteristics can then be correlated to desired mechanical properties through computational equilibrium thermodynamics or through a variety of correlation techniques. The correlations allow untested compositions or treatments to be computationally modeled so that desired trends can be rapidly established. Small heats of targeted materials can then be processed to confirm the modeled properties and to broaden the correlation database. Figure 1 captures the concepts in this approach.

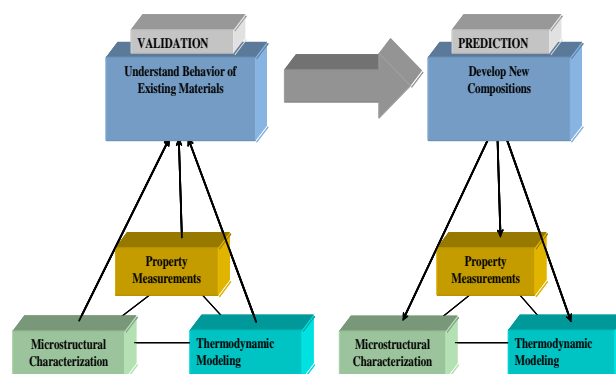


Figure 1. Overall approach for materials-by-design.

Exhaust valves currently used at temperatures up to about 760°C are fabricated using Ni-based alloys such as alloy 751. Other high-performance, Ni-based alloys primarily developed for aerospace applications have the potential to operate at temperatures of 950°C with desired strength and oxidation resistance but may be expensive for automotive applications. Therefore, new alloys with appropriate strength and oxidation resistance may have to be specifically developed for the operating characteristics and lifetime expectations for automotive valves.

In an earlier study on automotive valves for performance at 870°C, a “materials-by-design” approach consisting of synergistic computational

and experimental aspects was used to develop cost-effective, Ni-based alloys for use at this temperature. High-temperature fatigue strength was identified as a critical factor in determining the performance of these alloys in the valve application. An understanding of the strengthening mechanisms in existing commercial alloys was required to use the computational modeling approach to developing materials with improved properties and lower cost. A range of Ni-based alloys with potentially varying weight fractions (or volume fractions) of γ' were identified in efforts to correlate the fatigue properties with the microstructure of the alloys. The selection of nine commercial Ni-based alloys included Alloy 751, Waspaloy, Udimet 520, and Udimet 720 with Ni+Co contents ranging from 66 to 76 wt. %. To obtain initial information on the microstructures of these alloys at equilibrium, thermodynamic calculations have been carried out. Comparison of the results of the calculations showed that all alloys have a matrix of γ with the major strengthening phase as γ' . One or more carbide phases (such as $M_{23}C_6$, MC, and M_7C_3) may also be present in different alloys. The primary difference between the microstructures of the various alloys was the weight percent of the γ' phase at a given temperature and the highest temperature at which the γ' phase is stable in the different alloys. Because the size of the strengthening precipitates is also critical, it was anticipated that the kinetics of coarsening this phase would also be influential in long-term performance of the alloys in this application.

Using the microstructures of these alloys as a guide, computational thermodynamics was used to design new alloys with a microstructure similar to the commercial alloys in an effort to obtain materials with desirable properties. In contrast to the commercially available alloys with Ni+Co contents greater than 66 wt%, the Ni+Co content in these newly identified candidate alloys was lower than 50 wt. % (Ni being replaced with other elements such as Fe), with the potential to achieve comparable properties. The lower Ni content implies that the alloys would be of lower cost, with the potential to achieve targeted fatigue life.

Based on the results of this computational alloy design process, small batches of the new lower-Ni candidate alloys were cast. The alloys were then homogenized and rolled at high temperatures. Small tensile specimens were machined from these alloys and tensile tests were conducted *in-situ* at 870°C. Based on the results of the tensile tests, several of the candidate alloys from the newly developed suite of promising compositions with Ni+Co contents lower than 50 wt. % were down-selected for preparation of larger sized heats. These were cast under inert gas cover and then mechanically processed into plates for further machining. High-temperature fatigue tests were performed on the down-selected alloys. New alloys with fatigue lives of 100 million cycles at stresses of 25 to 30 Ksi at 870°C were identified, and two invention disclosures have been filed.

The purpose of this project is to extend this successful approach to the identification/development of materials for exhaust valves that could operate at temperatures up to 950°C. In addition to high-temperature mechanical properties (i.e., creep and fatigue), oxidation resistance is expected to play a role in determining the lifetime of exhaust valves at higher temperatures and will be considered in identification/development of new materials for exhaust valves. As part of this project, the required materials properties will be identified, baseline material properties will be evaluated, and development of new materials will be targeted to achieve required properties at low cost. Initial work will be focused on Ni-based alloys but if properties and cost targets cannot be met, intermetallics will be considered as an alternate option.

Results

In an effort to understand the mechanical properties and oxidation resistance of candidate Ni-based alloys, high-temperature tensile testing and oxidation testing was initiated on selected commercial and newly developed Ni-based alloys. To understand the effect of composition on the oxidation resistance of Ni-based valve alloys, oxidation resistance of various alloys were evaluated in air +10% water vapor environment at 900°C. It should be noted that

this test may be harsher than the conditions experienced by exhaust valves and is used only as a guidance to the trends. Figure 2 shows the specific mass change in several development alloys fabricated in the laboratory scale, which were observed to have improved mechanical properties at 870°C. Also shown in the plot are the specific mass changes for the higher Ni-baseline alloy 751 and 31V currently used in exhaust valves for exposure times up to 500 hours. The dotted line shows the preferred oxidation performance. As observed in the figure, development alloys show greater mass losses after about 300 cycles of exposure at 900°C when compared to the commercial alloys.

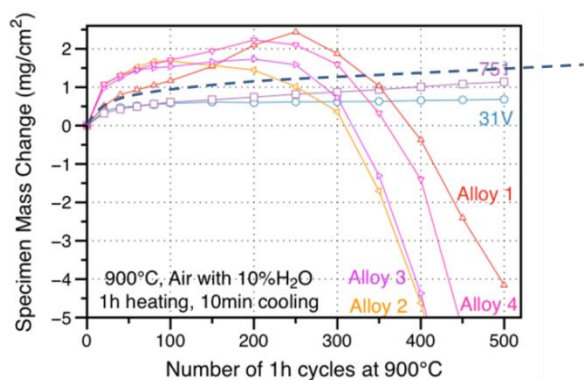


Figure 2. Specific mass change (mass change/unit area) measured in several developmental alloys and baseline alloy 751.

Several factors may be responsible for the difference in oxidation properties. One factor that is likely to cause this difference is the inherent differences in the compositions and the microstructures of the alloys. New alloys with distinctly different compositions have been designed, fabricated, and tested to understand the role of composition on oxidation resistance. The second factor that may be responsible for this difference is the minor impurities in the alloys. To understand if minor impurities are responsible for the differences in oxidation resistance, two alloys have been prepared using commercial-scale vacuum processing by a commercial Ni-based alloy producer and will be evaluated for their oxidation resistance. This data will be compared with data from laboratory-scale heats.

Figure 3 shows the effect of modified alloying element additions on the oxidation behavior of alloys tested at 900°C. The understanding developed on the effect of alloying elements on oxidation behavior of these alloys will be used in further design of alloys.

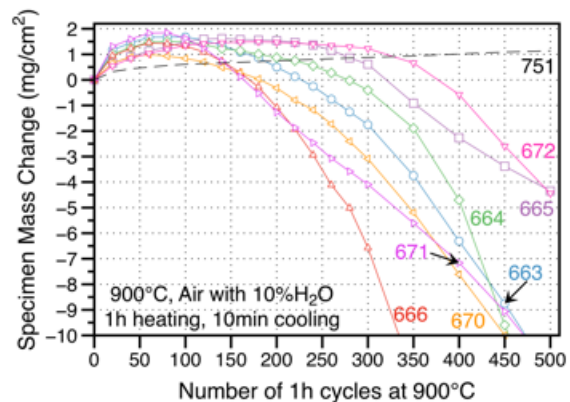


Figure 3. Specific mass change (mass change/unit area) measured in several new developmental alloys and baseline alloy 751.

Figure 4 shows the effect of temperature on the yield strength of alloy 751, alloy 520, and Oak Ridge National Laboratory (ORNL) alloy 3. Alloy 751 and alloy 520 have about 70 wt. % Ni, while ORNL alloy 3 has less than 60 wt. % Ni. Alloy 520 has strength properties much better than that of alloy 751, meaning it is a target alloy for this research project. Note that at 950°C, alloy 3 has yield strength better than that of alloy 751 and is lower than that of alloy 520.

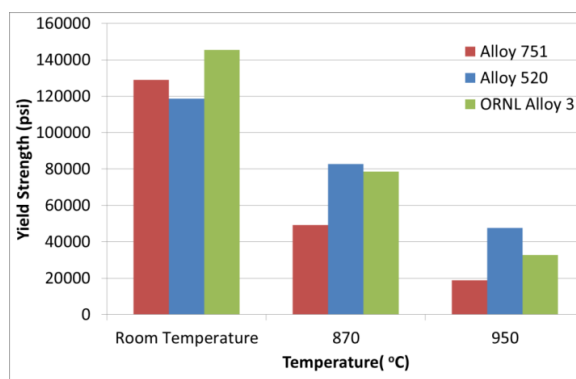


Figure 4. Yield strengths of commercial alloys 751, 520, and ORNL developmental alloy 3 as a function of temperature.

Figure 5 shows the amount of strengthening phase calculated to be present in the three alloys

at these temperatures. Note that the amount of strengthening phase present in alloy 520 is larger than that of ORNL alloy 3 at 950°C and hence has been identified as the target microstructure for the new alloys. Yield strength values of new alloys shown in Figure 3 fabricated this year confirm this observation, indicating the completion of a milestone. New alloys will be designed and developed in the following year based on these conclusions.

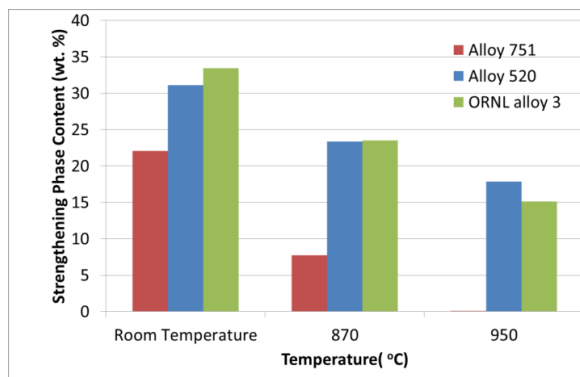


Figure 5. Strengthening phase content of commercial alloys 751 and 520 and ORNL developmental alloy 3 as a function of temperature.

Compositions of alloys will be modified based on observed trends in the oxidation resistance of the alloys and strength properties measured in the new alloy heats.

Conclusions

Development of exhaust valve materials for use at temperatures up to 950°C has been initiated. This project will adopt a synergistic approach that uses an experimental and computational methodology to develop cost-effective exhaust valve alloys for use at 950°C. Oxidation tests in air +10% water vapor have demonstrated the effect of composition on oxidation resistance at 900°C. Target microstructures for improving strength at temperatures up to 950°C have been identified. Further work will use computational methodologies to identify alloys with the required combination of oxidation resistance, high-temperature tensile, and fatigue properties.

Patents

Two patents were filed for new lower-cost, high-temperature valve alloys.

Project 18519 – Materials for Exhaust and Energy Recovery

Agreement 9130 – Development of Materials Analysis Tools for Studying NO_x Adsorber Catalysts (CRADA No. ORNL-02-0659 with Cummins Inc.)

Thomas Watkins, Larry Allard, and Michael Lance

Oak Ridge National Laboratory

P.O. Box 2008

Oak Ridge, TN 37831-6064

Phone (865) 387-6742; fax (865) 574-4913; e-mail: watkinstr@ornl.gov

Krishna Kamasamudram and Aleksey Yezerets

Cummins Inc.

1900 McKinley Avenue, MC 50197

Columbus, IN 47201

Phone (812) 377-4935; fax (812) 377-7226; e-mail: Krishna.Kamasamudram@Cummins.com

DOE Technology Manager: Jerry L. Gibbs

Phone (202) 586-1182; fax: (202) 586-1600; e-mail: jerry.gibbs@ee.doe.gov

Technical Advisor: J. Allen Haynes

Phone (865) 576-2894; fax: (865) 574-4913; e-mail: haynesa@ornl.gov

Contractor: Oak Ridge National Laboratory, Oak Ridge, Tennessee

Prime Contract No.: DE-AC05-00OR22725

Objectives

- The objective of this effort is to produce a quantitative understanding of the process/product interdependence leading to catalyst systems with improved final product quality, resulting in diesel emission levels that meet the prevailing emission requirements.

Approach

- Characterize lab-engine tested samples with x-ray diffraction (XRD), spectroscopy, and microscopy. Correlate findings with Cummins data and experience.

Accomplishments

- Discovered in one of the Cu-Chabazite formulations from the overlapping NH₃ release and oxidation functions, the built-in ammonia oxidation (AMOX) function has the potential to significantly reduce NH₃ slip from the selective catalytic reduction (SCR) catalyst. Characterization by *in situ* XRD, electron microscopy, and Raman spectroscopy at Oak Ridge National Laboratory (ORNL) indicated that upon hydrothermal aging, the zeolite structure changes and the Cu species sinter, which reduces the extent of the desirable overlap between the NH₃ release and oxidation activity.

Future Direction

- The Cooperative Research and Development Agreement (CRADA) was complete September 30, 2014. This project has provided the fundamental insights needed now and for future aftertreatment technologies that might result in improved aftertreatment strategies and fuel-efficient and cost-effective aftertreatment technologies.
-

Introduction

Commercial, off-the-shelf aftertreatment technologies are now available to meet the 2010 U.S. Environmental Protection Agency emission requirements for diesel exhaust (40 CFR 86). However, the performance of these technologies and their integration with engine control systems needs optimization. In particular, the catalytic materials can change or age with exposure to high temperatures and engine exhaust conditions. Consequently, Cummins Inc. is working to understand the basic science necessary to effectively utilize these catalyst systems. ORNL is assisting with the materials characterization effort. This report will focus on the study of materials used in ammonia oxidation.

Ammonia-containing compounds may be added to diesel exhaust to reduce NO_x to N_2 , as in SCR. The reductant reduces NO_x to H_2O and N_2 (Chorkendorff and Niemantsverdriet 2003). Excess ammonia is often needed, resulting in NH_3 escaping or “slip.” This slip is a potential concern for sociability and environmental reasons. Although not regulated, proactive steps are taken to mitigate even small amounts of ammonia slip by employing a selective oxidation catalyst.

Oxidation catalysts are usually present in after-treatment systems to oxidize ammonia that is not being oxidized upstream by SCR catalysts. These oxidation catalysts ensure that ammonia slip to ambient is minimal and are referred to by several names: AMO_x catalysts, selective catalytic oxidation (SCO) catalysts, or ammonia slip catalysts (ASC). Candidate catalysts typically have a two-layer structure: the top is a zeolite-based catalyst and the bottom is alumina-supported metal or alumina-supported metal oxide catalysts. Hydrothermal conditions, temperature, and water content strongly influence the functioning of these catalysts by changing or “aging” the catalytic materials. These changes and their impact on performance are not well understood.

Goals, Barriers, Relevance, and Integration

In the study area of Vehicle Technology’s Materials Technology subprogram, the Propulsion Materials Technology activity provides materials research and development expertise to enable advanced materials and supports the goals of several Vehicle Technology subprograms (EERE 2010). Within the Advanced Combustion Engine research and development activity, one primary research and development direction is to develop aftertreatment technologies integrated with combustion strategies for emissions compliance and minimization of an efficiency penalty (EERE 2010). Correspondingly, one *goal* is to, by 2015, improve the fuel economy of light-duty gasoline vehicles by 25% and light-duty diesel vehicles by 40%, compared to the baseline 2009 gasoline vehicle.

In support of these goals, this project addresses four *barriers* (EERE 2010) related to emission control: (1) lack of cost-effective emission control, (2) durability, (3) cost (e.g., precious metal content), and (4) improving market perception. This project is *relevant* to this goal because as the understanding of material aging underlying the AMO_x catalyst performance degradation increases, efficient and durable AMO_x with higher nitrous oxide (NO_x) conversion efficiencies can be attained. This minimizes constraints on engine-out NO_x emissions and allows engines to be tuned for optimal fuel efficiency, cost, and durability.

This project supports clean diesel, which increases acceptance by the public. Larger acceptance, in turn, results in larger percentages of conversion to diesel, resulting in reduction in petroleum usage/dependency on foreign oil. Similarly, this project also addresses three *barriers* (EERE 2010) related to the Propulsion Materials Technology activity itself: (1) changing internal combustion engine combustion regimes, (2) long lead times for materials commercialization, and (3) costly precious metal content. This project is *integrated* within the Vehicle Technologies Program as it utilizes the characterization tools acquired and

maintained by the High Temperature Materials Laboratory Program.

Approach

The main focus of the CRADA in Fiscal Year 2012 was to continue characterization of a practically relevant zeolite AMOx catalyst, which was subjected to hydrothermal aging for lifetime prediction model input. The technical approach will be as before: experimentally characterize materials supplied by Cummins from all stages of the catalyst's lifecycle (i.e., fresh, de-greened, aged, regenerated, on-engine, and off-engine). The crystal structure, morphology, phase distribution, particle size, and surface species of catalytically active materials supplied by Cummins were characterized using transmission electron microscopy, XRD, and Raman spectroscopy. Ultimately, an understanding of the thermal and hydrothermal aging processes and other degradation mechanisms is sought throughout the lifecycle of the catalytic material.

Results

The Fiscal Year 2014 milestones were (1) quantify phases present in the as-received and hydrothermally treated Cu-zeolite catalyst and quantify the impact of hydrothermal aging temperature, time, and spatial distribution of copper species in the Cu-zeolite and platinum crystallite size and its distribution; (2) correlate the fundamental degradation mechanisms identified by ORNL through the above milestones with activity and selectivity in ammonia oxidation (evaluated at Cummins) on select hydrothermally treated ammonia oxidation catalysts.

XRD patterns were collected *in situ*, while the Cu-Chabazite AMOx zeolite catalyst was hydrothermally aged in simulated air with 2 volume percent water at 550, 600, 650, 700, 750, 800, 850, and 900 °C at 4 hours per temperature. In between these hydrothermal aging temperatures, the catalyst powder was cooled to 500°C and the XRD pattern was taken to eliminate any influence of adsorbed water. The XRD diffraction patterns of the Cu-Chabazite zeolite powders show the structure shrinking and degrading as a function of hydrothermal aging

temperature (Milestone1). The changes in lattice parameters were anisotropic (see Figure 1).

While dealumination of zeolite was expected to decrease the cell parameters, the anisotropic changes indicate a potential reorganization of species inside the chabazite crystal. A Cu species distribution in small pore zeolite crystallite has not been attempted before (see Figure 2). The Cu atoms are surprisingly uniformly distributed in the as-received, Chabazite crystallite (Milestone 1); this characterization technique is under further development. Thin sections of hydrothermally aged (i.e., 4 hours of hydrotreatment at 850°C) Chabazite zeolite were prepared by appropriately embedding the powder and slicing via ultramicrotomy to make electron-transparent thin sections. The cube-shaped chabazite crystals (2 to 5 μm on a side) typically fracture into lamellar shards that are elongated normal to the slicing direction.

Figure 3 shows a dark-field/bright-field pair of such a slice. Care was taken to minimize the electron beam dose on any area being imaged (e.g., no high-magnification images were recorded initially). The fine bright spots seen in this interior area of the crystal are Cu-containing particles, as determined by energy-dispersive spectroscopy (not shown here). The bright field image still shows crystal lattice fringes, as seen in the upper right inset and also shown by the diffractogram of the central area of the image. The retention of lattice (in the easily beam-damaged zeolite) illustrates the minimal dose used and confirms the presence of the Cu (CuOx presumed likely) nanoparticles in the hydrotreated sample. No platinum was detected (i.e., less than 0.1 wt%).

Figure 4 shows the Raman spectra collected from the Cu-Chabazite zeolite powders hydrothermally aged at 550 and 900°C. Both spectra show the characteristic band from the chabazite structure at 475 cm⁻¹. Neither spectra show lower frequency bands that have been correlated to Cu-O-Cu vibrations (Guo et al. 2013). This shows that following hydrothermal aging, the Cu is still present in the zeolite structure and no Cu-O-Cu species have formed above the detection limit of the technique.

NH₃ temperature-programmed desorption and oxidation experiments at Cummins (see Figure 5) show that the overlapping NH₃ release (i.e., solid curves) and oxidation (i.e., curves with circular points) functions discovered in one of the Cu-chabazite formulations can significantly reduce NH₃ slip from the SCR catalyst (a built-in AMOx function). This feature is not universal to all Cu-chabazite zeolite formulations. The changes in Cu-chabazite zeolite catalyst functions upon hydrothermal treatment (i.e., black curves), reduce the extent of the desirable overlap between the NH₃ release and oxidation activity and alter the distribution of NH₃ between the two sites within the zeolite structure. XRD clearly shows the crystal structure changing (Milestone 2). Hydrothermal treatment leads to an increase in the weak storage sites at the expense of the strong storage sites and a decrease in NH₃ oxidation activity due to re-distribution and sintering of redox sites.

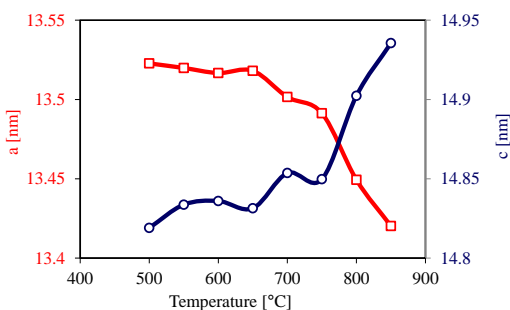


Figure 1. The Cu-Chabazite zeolite lattice parameters as a function of hydrothermal aging temperature.

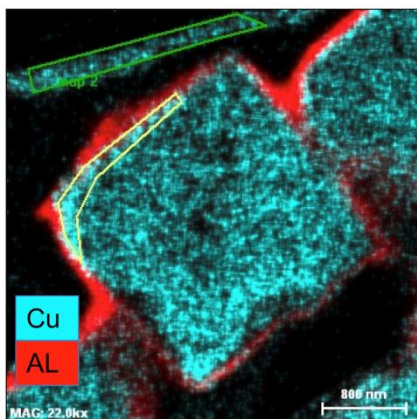


Figure 2. An elemental map of an as-received Chabazite zeolite crystallite.

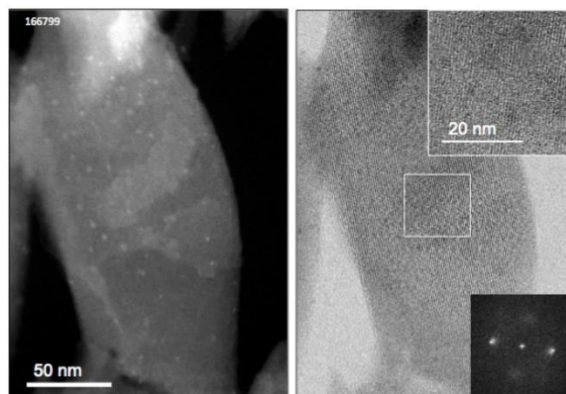


Figure 3. A dark-field/bright-field pair of images from a hydrothermally treated Cu-Chabazite zeolite crystallite.

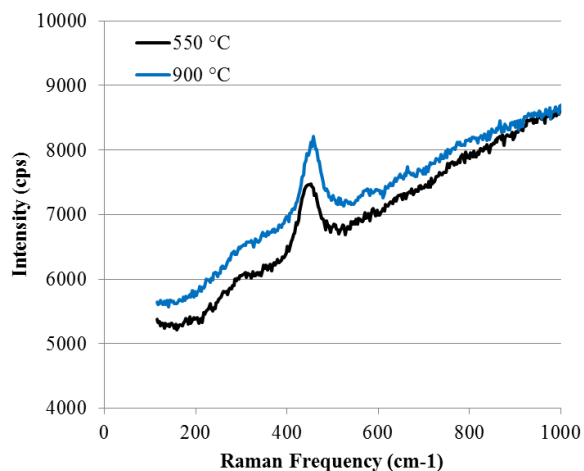


Figure 4. Raman spectra of Cu-zeolite aged at 550 and 900°C.

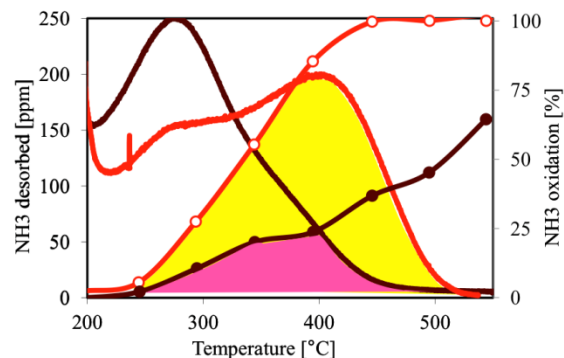


Figure 5. NH₃ release (solid curves) and oxidation (curves with circular points) as a function of temperature and condition from one of the Cu-Chabazite formulations.

Summary

The overlapping NH₃ release and oxidation functions, discovered in one of the Cu-Chabazite formulations, can significantly reduce NH₃ slip from the SCR catalyst (built-in AMO_x function). Two distinct NH₃ storage sites are present in this Cu-Chabazite formulation, which is not universal to all Cu-Chabazite formulations. Changes in Cu-zeolite catalyst functions with hydrothermal treatment reduces the extent of the desirable overlap between the NH₃ release and oxidation activity, meaning hydrothermal treatment leads to an increase in the weak storage sites at the expense of the strong storage sites and a decrease in NH₃ oxidation activity due to re-distribution and sintering of redox sites.

Characterization by *in situ* XRD, electron microscopy, and other techniques at ORNL indicated that upon hydrothermal aging, anisotropic changes occur due to potential reorganization of species inside the zeolite crystallite and an increase in the concentration of reduced copper species concentration and sintering of copper species to form copper agglomerates that can be correlated to reactor studies.

This project is providing the fundamental insights needed now and for future aftertreatment technologies that might result in improved aftertreatment strategies and fuel-efficient and cost-effective aftertreatment technologies.

Presentation

Watkins, T. R., L. F. Allard, M. J. Lance, K. Kamasamudram, and A. Yezerets, 2014, "Catalyst Characterization," presented at the *DOE 2014 Vehicle Technologies Annual Merit Review and Peer Evaluation Meeting*, Washington, D.C., June 20, 2014.

Publication

Kamasamudram, K., A. Kumar, J. Luo, N. Currier, A. Yezerets, T. Watkins, and L. Allard, 2014, "New Insights into the Unique Operation of Small Pore Cu-Zeolite SCR Catalyst: Overlapping NH₃ Desorption and Oxidation Characteristics for Minimizing Undesired Products," SAE Technical Paper 2014-01-1542, 2014, doi:10.4271/2014-01-1542.

References

- 40 CFR 86, July 1, 2010 Edition, *U.S. Code of Federal Regulations*, pp. 144-722.
- Chorkendorff, I. and J. W. Niemantsverdriet, 2003, "Concepts of Modern Catalysis and Kinetics," Wiley-VCH Verlag GmbH & Co. KGaA, Weinheim, pp. 395-400.
- EERE, 2010, "Multi-Year Program Plan 2011-2015," Vehicle Technologies Program, EERE, DOE, December 2010, pp. 2.3-1, 2; 2.5-8. (http://www1.eere.energy.gov/vehiclesandfuels/resources/fcvt_plans_road_maps.html).
- Guo, Q. et al., 2013, *ChemCatChem*, 6(2), 634-639, doi: 10.1002/cctc.201300775.

Project 18519 – Materials for Exhaust and Energy Recovery

Agreement 10461 – Durability of Diesel Particulate Filters (CRADA with Cummins Inc.)

Thomas R. Watkins, Amit Shyam, and Ryan Cooper
Oak Ridge National Laboratory
P.O. Box 2008, MS 6064
Oak Ridge, TN 37831-6064
Phone (865) 387-6472; fax (865) 574-3940; email: watkinstr@ornl.gov

Randall J. Stafford
Cummins Inc.
1900 McKinley Avenue, MC 50183
Columbus, IN 47201
Phone (812) 377-3279; fax (812) 377-7050; email: randy.j.stafford@cummins.com

DOE Technology Manager: Jerry L. Gibbs
Phone (202) 586-1182; fax: (202) 586-1600; e-mail: jerry.gibbs@ee.doe.gov
Technical Advisor: J. Allen Haynes
Phone (865) 576-2894; fax: (865) 574-4913; e-mail: haynesa@ornl.gov

Contractor: Oak Ridge National Laboratory, Oak Ridge, Tennessee
Prime Contract No.: DE-AC05-00OR22725

Objectives

- To identify and implement test techniques to characterize the physical and mechanical properties of ceramic substrates used as diesel particulate filters (DPFs).
- To identify the mechanisms responsible for the progressive thermo-mechanical degradation and resultant fracture of DPFs.
- To develop analyses and provide data for simulation tools for predicting the long-term reliability and durability for DPFs under engine operating conditions.

Approach

- Application of advanced characterization techniques to DPF ceramic substrates.
- Refinement of DPF service lifetime prediction models based on characterization of field-returned filters.

Accomplishments

- Determined that the Young's moduli of cordierite, aluminum titanate, and silicon carbide DPF materials perpendicular to extrusion direction.
- Fracture toughness of cordierite under uniaxial tension has preliminary results.

Future Direction

- Initiate model development and new testing methodologies for fracture toughness/fracture energy of the highly porous materials.
- Complete determination of strength, fracture toughness, density/porosity/microstructure, and thermal expansion as a function of time at elevated temperatures for a fourth alternate substrate material.

Introduction

The U.S. Environmental Protection Agency regulates the emissions of nitrogen oxides (NO_x) and particulate matter (PM) from diesel engines. Stringent regulations on PM went into effect in 2007. Many technologies exist that are designed to reduce emissions from diesel engines. Prominent among the technologies for PM control are DPFs. A DPF is often a ceramic device that collects PM in the exhaust stream. The high-temperature nature of the ceramic withstands the heat of the exhaust and allows heating to break down (or oxidize) the particles inside. DPFs reduce emissions of PM, hydrocarbons, and CO by 60 to 90%.

Most DPFs consist of a ceramic honeycomb with hundreds of cell passages partitioned by walls (Figure 1). Each cell passage has a square cell opening at one end and a plug at the other end; therefore, the cell passages are alternately closed at each end. The so-called checkerboard plugging structure forces the exhaust gases through the porous, thin ceramic honeycomb walls. When the gases carrying the PM flow through the fine pores of the walls, the PM is filtered out. High porosity values in the range of 40 to 70% heighten filtration efficiency to more than 90% and reduce gas-flow resistance.

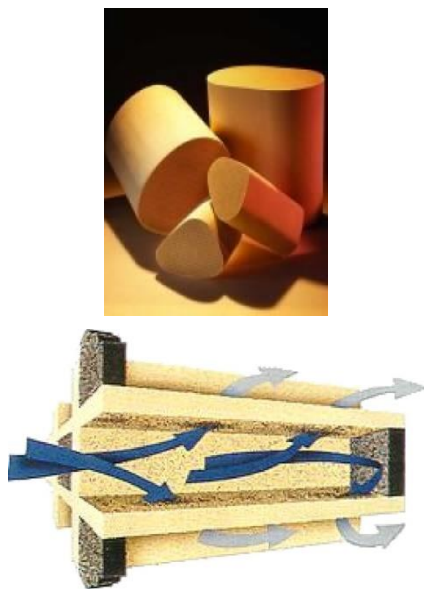


Figure 1. Top: image of cordierite-based DPFs; bottom: SCHEMATIC of exhaust flow through a DPF.

The process of diesel PM collection is continuous while the engine is operating. The particles are collected on the ceramic walls and, as a result, the backpressure of the system increases. The back pressure is reduced by oxidizing the trapped PM, aided by a catalytic reaction using exhaust gas heat at 400°C or more, into CO₂ and water vapor. This process, called regeneration, results in a cleaner filter. The regeneration process is dependent on exhaust temperature, oxygen, NO_x content, time, and PM levels.

The key to successful application of DPFs is to reliably regenerate the filter (e.g., to clean up the PM that the filter continues to trap or collect). Traditionally, combustion of soot is done in an oxygen atmosphere (i.e., air). In air, the soot will oxidize at about 500°C and up. However, this is not a typical operating temperature for diesel engine exhaust. Therefore, to oxidize soot in air, an active system (i.e., one that increases the temperature of the exhaust using some external heat source) is required. However, if an active system is not carefully controlled or, if too much PM collects on the filter walls, the filters can experience an “uncontrolled regeneration,” wherein the temperature increases to 600°C or more, resulting in damage to the filter element.

The objective of this project is to identify and implement test techniques to characterize the physical and mechanical properties of ceramic substrates used as DPFs, to identify the mechanisms responsible for the progressive thermo-mechanical degradation and resultant fracture of DPFs, and to develop analyses and provide data for simulation tools for predicting the long-term reliability and durability for DPFs under engine operating conditions, particularly through the regeneration cycle.

Goals, Barriers, Relevance, and Integration (EERE 2010)

This work is in the study area of Vehicle Technology’s Materials Technology-Propulsion Materials Technology and addresses the goal of, by 2015, develop materials that reduce the fuel economy penalty of particle filter regeneration by at least 25% relative to the 2008 baseline. This project addresses the following three

barriers within Materials Technology, Propulsion Materials: (1) changing internal combustion engine combustion regimes, (2) long lead times for materials commercialization, and (3) cost. It also addresses the following four barriers within Advanced Combustion Engine, Research and Development-Combustion and Emission Control Research and Development: (1) lack of cost-effective emission control, (2) lack of modeling capability for combustion and emission control, (3) durability, and (4) cost.

This project is as relevant to the goal and barriers as the thrust is to characterize the material properties and improve the durability and lifetime prediction, resulting in the lowest overall cost, while preventing emission release in service. This is achieved by understanding the relationships of the material properties for the filter substrates by characterizing the porosity, strength, elastic modulus, thermal conductivity, and thermal expansion, leading to improved regeneration strategies and fuel efficiency. This project supports clean diesel, which increases acceptance by the public by reducing unsightly diesel exhaust plumes. Larger acceptance, in turn, results in larger percentages of conversion to diesel, resulting in reduction in petroleum usage/dependency on foreign oil (Hansen 2013, Ulrich 2013).

This project is integrated within the Vehicle Technologies Program because DPF substrate materials are used in both DPF and catalyst systems and because it utilizes many of the characterization tools acquired and formerly maintained by the High-Temperature Materials Laboratory Program.

Approach

The design process for making DPFs that are durable and reliable includes a complex materials property optimization and selection process (Adler 2005). For example, the porosity of DPFs, which allows the removal of PM from the exhaust gas stream, has a deleterious effect on their mechanical and fracture strength. However, a higher porosity decreases the engine backpressure and increases the efficiency of the diesel engine. Designing mechanically reliable DPFs is important because these components will experience demanding thermo-mechanical

conditions during service. These include, for example, thermal shock resulting from rapid heating/cooling and thermal stresses that arise from temperature gradients.

Techniques for assessing the elastic and fracture properties of virgin or unexposed DPF substrates have been identified, implemented, and reported earlier (Vehicle Technologies Program 2013). The test techniques were applied to rank the suitability of common candidate substrates for application in DPFs. The developed test techniques were applied to characterize DPFs returned from field service. The material properties responsible for the thermal shock resistance and mechanical property degradation in the various stages of the bathtub curve were determined. These properties include thermal expansion, thermal conductivity, heat capacity, density, porosity, elastic properties, strength, fracture toughness, and environmentally assisted crack growth at ambient and elevated temperatures in air and in relevant environments.

In turn, the information generated has been input into predictive models. These service life predictions are based on a combination of experimentally determined strength data, stress analyses of the component using a finite-element analysis, and selection of appropriate failure criteria. The durability (i.e., service life) of the component can also be predicted using this framework by considering the elastic behavior as a function of load.

Results

Work was initiated on a fourth alternate substrate material, a zeolite. This material is quite challenging given its very thin wall thickness, 0.2 mm, and its compliant nature. Attempts to measure its dynamic and static fatigue response were unsuccessful with current techniques because the material simply crushed under small loads. After the key staff member in charge of this milestone retired, subsequent consultations with Cummins resulted in Milestone 1 being replaced with the following: initiate the determination of the Young's moduli of cordierite, aluminum titanate-based, and silicon-silicon carbide DPF materials perpendicular to the extrusion direction. This

was completed (see Table 1, which compares previously measured mechanical properties to the perpendicular mechanical properties). Samples were fabricated with the gage length running perpendicular to the extrusion direction. In the microtensile setup, samples were loaded until failure. Digital image correlation (DIC) was used to measure the strain in the sample. A measurable difference in Young’s moduli was observed in all three materials.

Table 1. Comparison of the average Young’s modulus and maximum stress measured perpendicular and parallel to the extrusion direction (i.e. 90 and 0 degrees, respectively). The 90-degree measurements are the result of 10 uniaxial tension measurements for cordierite, silicon carbide, and aluminum titanate-based materials. The 0-degree measurements were previously published in (Pandey et al. 2014) and are shown for comparison. The values in [] are the standard deviation.

	E (GPa) at 90°	Max stress (MPa) at 90°	E (GPa) at 0°	Max stress (MPa) at 0°
Cordierite	6.7 ±[1.3]	2.7 ±[0.62]	10 ±[0.11]	2.9 ±[0.1]
Silicon carbide	11.1 ±[0.9]	5.3 ±[0.98]	15 ±[0.19]	6.2 ±[0.5]
Aluminum titanate	0.6 ±[0.13]	0.76 ±[0.09]	0.9 ±[0.3]	0.9 ±[0.15]

Further uniaxial testing was undertaken to investigate the strain distribution during loading. The DIC strain measurement provides a measurement of strain across the entire gage section of the specimen. Initial tests confirmed that no strain concentrations occurred due to mounting. Further inspection revealed local strain variations within the gage section of aluminum titanate (see Figure 1D through G). These preliminary results could help to explain the nonlinear mechanical response of porous microcracked ceramics. The nonlinear stress-strain curve of aluminum titanate is shown in Figure 1A. Traditional engineering materials exhibit very uniform strains across the gage section while experiencing elastic deformations. In Figure 1D, we see that even under very small loads, the strain varies within the gage section.

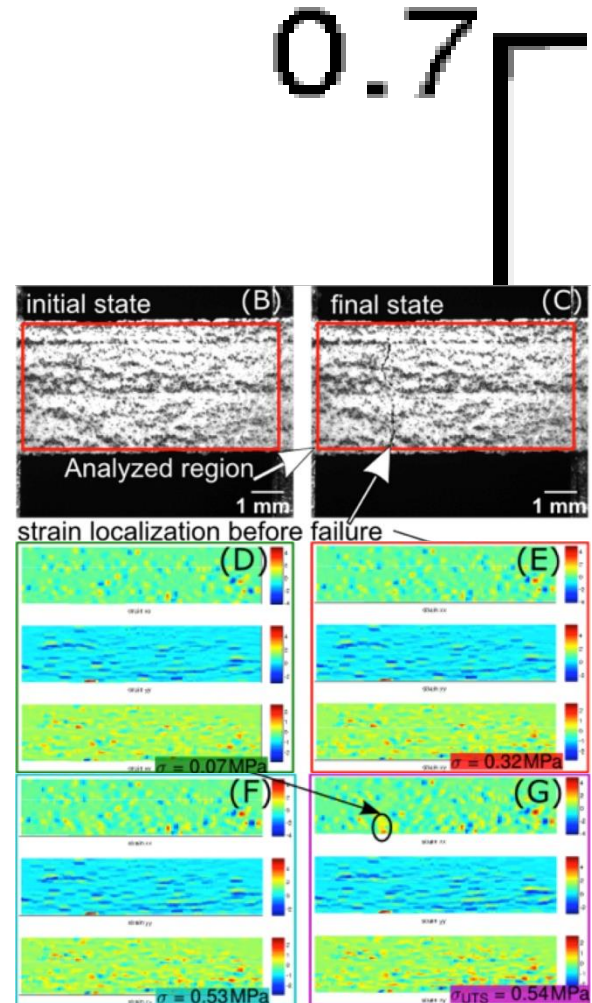


Figure 1. (A) The applied stress as a function of the average strain. Depicted above is the strain distribution (D-E) of aluminum titanate as measured with DIC, pictured before and after loading (B) and (C), respectively. (D-G) show the local strain variations in the direction of loading (top), perpendicular to loading (i.e., Poisson contraction [middle] and in-plane shear strain [bottom] for four applied loads: 0.07, 0.32, 0.53, 0.54 MPa in D, E, F, and G, respectively). No strain concentrations due to grips are detected, but local variations in the strain distribution are quite noticeable. The extreme localization occurs just before failure in (G), which is highlighted by the black oval.

Preliminary results from development of a single edge-notched beam in tension have been measured in cordierite. Specimens were notched using a steel razor and mounted on the microtensile setup. Initial specimens were loaded with a constant displacement rate of 100 $\mu\text{m/s}$. At this loading rate, cracks propagated faster than the camera's collection rate of 5 Hz. The average stress of failure for these notched specimens was determined to be 3.2 MPa, with a standard deviation of 0.6 MPa. A notched sample was then loaded to 60% of the load at fracture and held at a constant displacement. The resulting strain evolution provided insights into the slow crack growth of the specimen.

The strain concentration around the notched region is shown in Figure 2 after the displacement was held constant (top) and just before fracture (bottom). Estimating the crack length before total failure to be 2.8 mm and total width of the sample being 3.64 mm, we estimate the fracture toughness to be 1.6 $\text{MPa}\sqrt{\text{m}}$.

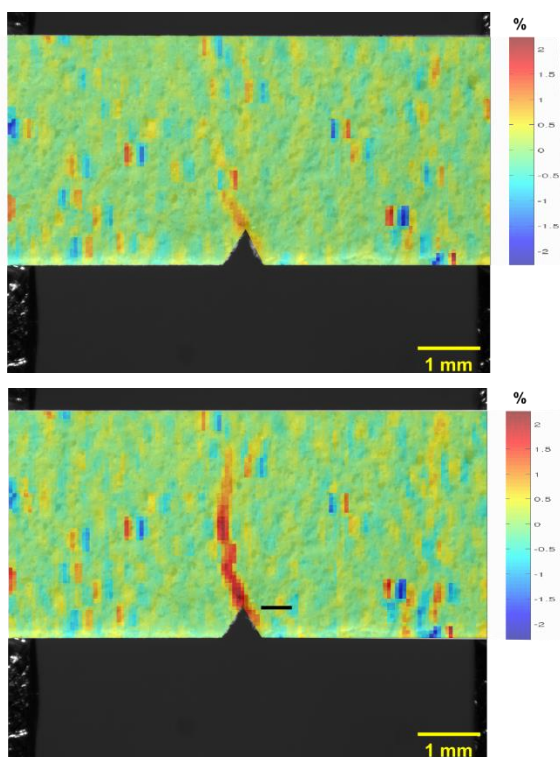


Figure 2. Top: the strain along the direction of loading (left to right), with strain distribution after the sample was loaded to 2.1 MPa and displacement was held constant. Bottom: the

strain distribution just before failure when the stress had decreased to 1.8 MPa due to crack growth. The strain concentration due to crack length is estimated based on the strain localization measured by DIC.

Milestone 2 has also been completed, initiating various characterizations of the zeolite material. The average strength of the zeolite-based sample was measured in four point flexure and found to be 3.1 and 0.6 MPa parallel and perpendicular to the extrusion direction, respectively. The material is 58% porous and contains two phases: (1) CoAPSO-44, which is quite similar to Chabazite and (2) Al_2O_3 , as determined using x-ray diffraction (see Figure 3). A preliminary fracture toughness value of 0.08 $\text{MPa}\sqrt{\text{m}}$ was obtained using the double torsion technique.

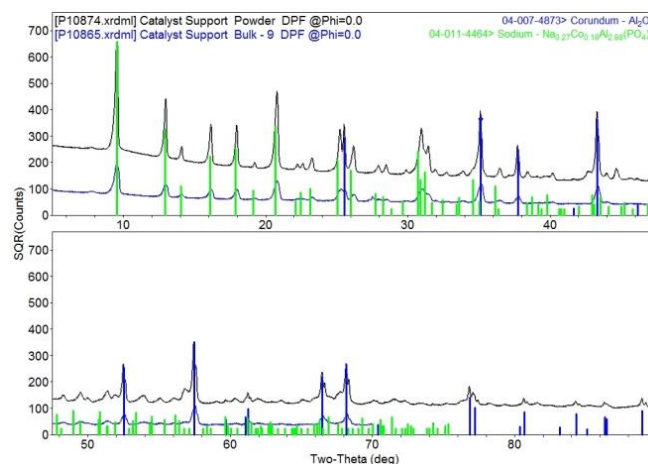


Figure 3. Two x-ray diffraction patterns of the solid and powder forms of the zeolite support.

Summary

A uniaxial microtensile setup, coupled with DIC, was used to measure anisotropy in mechanical properties in diesel particulate fuel filter materials and to initiate development of a second methodology to measure the fracture toughness of porous ceramics in pure tension. Computational researchers will be able to implement the anisotropic elastic constants into current models for better lifetime prediction of long-term reliability and durability of diesel particulate filters. The single edge-notched beam in tension affords the opportunity to investigate fracture toughness without complications due to

complex stress states, as in the case of 3-point and 4-point bend experiments. An investigation of the mechanical properties of a next-generation filter material, zeolite, has been initiated. Further testing on current DPF materials will continue to gain further insights into their complex mechanical behavior.

Presentation

Watkins, T. R., A. Shyam, H. T. Lin, A. Pandey, and R. Stafford, 2014, "Durability of Diesel Engine Particulate Filters," presented at the *DOE 2014 Vehicle Technologies Annual Merit Review and Peer Evaluation Meeting*, Washington, D.C., June 20, 2014.

Publication

Pandey, A., A. Shyam, T. R. Watkins, E. Lara-Curzio, R. J. Stafford, and K. J. Hemker, 2014, "The Uniaxial Tensile Response of Porous and Microcracked Ceramic Materials," *J. Am. Ceram. Soc.* 97(3): 899–906.

References

EERE, 2010, "Multi-Year Program Plan 2011-2015," Vehicle Technologies Program, EERE, DOE, December 2010, pp. 2.3-4; 2.5-7, 8. (www1.eere.energy.gov/vehiclesandfuels/resources/fcvt_plans_road_maps.html).

Hansen, S., 2013, "U.S. Clean Diesel Auto Sales Increase 41% in August 2013, Hybrid Sales Jump 38%," Diesel Technology Forum, www.dieselforum.org/index.cfm?objectid=4FD0F215-1A56-11E3-95AC000C296BA163 (September 11, 2013).

Ulrich, L., 2013, "Fossil-Fuel Mileage Champ," *New York Times*, www.nytimes.com/2013/07/21/automobiles/autoreviews/fossil-fuel-mileage-champ.html?_r=0&pagewanted=all (July 19, 2013).

Adler, J., 2005, "Ceramic Diesel Particulate Filters," *International Journal of Applied Ceramic Technology*, 2(6): 429-39.

Vehicle Technologies Program, 2013, *Propulsion Materials Annual Progress Reports*, Vehicle Technologies Program, U.S. DOE, Energy Efficiency and Renewable Energy, Office of Vehicle Technologies, www.ornl.gov/sci/propulsionmaterials/Reports.html.

Pandey, A. A. Shyam, T. R. Watkins, E. Lara-Curzio, R. J. Stafford, and K. J. Hemker, 2014, "The Uniaxial Tensile Response of Porous and Microcracked Ceramic Materials," *J. Am. Ceram. Soc.* 97(3): 899–906.

Project 18519 – Materials for Exhaust and Energy Recovery

Agreement 26462 – International Energy Agency (IEA IA-AMT) Characterization Methods

Hsin Wang

Materials Science and Technology Division

Oak Ridge National Laboratory

1 Bethel Valley Road

Oak Ridge, TN 37831

Phone (865) 576-5074; fax (865) 574-3940; email: wangh2@ornl.gov

DOE Technology Manager: Jerry L. Gibbs

Phone (202) 586-1182; fax: (202) 586-1600; e-mail: jerry.gibbs@ee.doe.gov

Technical Advisor: J. Allen Haynes

Phone (865) 576-2894; fax: (865) 574-4913; e-mail: haynesa@ornl.gov

Contractor: Oak Ridge National Laboratory, Oak Ridge, Tennessee

Prime Contract No.: DE-AC05-00OR22725

Objectives

- Leading a thermoelectric materials annex for the International Energy Agency Advanced Materials for Transportation (IEA-AMT), with the focus on evaluating transport properties measurement methods and developing standard testing procedures to evaluate the figure of merit, ZT.
- Developing measurement standards of bulk thermoelectric devices for vehicle waste heat recovery application in the temperature range of 300 to 800K.

Approach

- Focus is on bulk thermoelectrics for vehicle waste heat recovery application in the temperature range of 300 to 800K.
- The IEA-AMT annex is also planning to evaluate the measurement reliability of low-dimensional materials.
- Understand non-structural changes in catalyst under operating conditions and correlating the changes to performance.

Accomplishments

- Third international round-robin of n-type half heusler material was completed with 12 participating laboratories in six IEA-AMT member countries.
- International survey of thermoelectric module efficiency testing method was completed and published.
- Review of the measurement reliability of low-dimensional thermoelectric was carried out between Oak Ridge National Laboratory (ORNL) and KRISS of Korea.
- The annex results were reported to the executive committee in Hong Kong (December 2013) and Lanzhou (June 2014).

Future Direction

- Finish reporting and publication of round-robin results.
 - Explore the possibility of expanding the IEA-AMT results into International Standards Organization standards.
 - Organize international testing efforts on efficiency of thermoelectric modules.
-

Introduction

Thermoelectrics are a class of materials that capture waste heat from engine operations and can contribute significantly to the energy efficiency of cars and trucks. Current thermoelectric materials are widely used in refrigeration and wine coolers due to their low efficiency. For engine waste heat recovery, a much higher efficiency material is needed. Current literature contains many thermoelectric materials with higher efficiencies; however, verification of such claims is hindered by wide variation in the measurement techniques. Creation of standard test procedures, coupled with standard reference materials issued by national laboratories, will pave the way for rapid high-efficiency thermoelectric materials. The main objectives of this project are as follows:

- Leading a thermoelectric materials annex for IEA-AMT, with a focus on evaluating transport properties measurement methods and developing standard testing procedures to evaluate the figure of merit, ZT.
- Developing measurement standards of bulk thermoelectric devices for vehicle waste heat recovery application in the temperature range of 300 to 800K.

Approach

After initial round-robin studies on state-of-the-art bismuth telluride materials, the study is focusing on bulk thermoelectrics for vehicle waste heat recovery application in the temperature range of 300 to 800K. In addition to bulk materials, the IEA-AMT annex is also planning to evaluate the measurement reliability of low-dimensional materials. At the device level, energy conversion devices need to be evaluated for conversion efficiency. The lack of standard testing methods and procedures require an international study. These are important steps for bringing advanced materials from research laboratories to scaled-up vehicle applications.

Task 1: International Round-Robin of High-Temperature Bulk Thermoelectric (2014-2015):

Complete reporting to IEA of the third international round-robin testing. Publish the

results to promote standardization of transport property measurements. Explore the possibility of developing the IEA procedures into an International Standards Organization standard.

Task 2: Survey of Low-Dimensional Thermoelectric Materials Characterization (2014-2015):

The IEA annex will organize an international study to evaluate the reliability of the transport properties of low-dimensional materials. Past studies on thin film and nano-wire thermoelectrics will be reviewed and evaluated on measurement technique and data analysis. The potential of low-dimensional materials in applications and materials development will be accessed. The results will be reported to IEA-AMT and the reviews will be published in a research journal.

Task 3: Efficiency Testing of Energy Conversion Devices (2014-2015):

The IEA-AMT Annex VIII will start a new task to conduct a study of the current state-of-the-art methods for determining energy conversion efficiency of thermoelectric devices for vehicle applications. An intentional collaboration will be coordinated by ORNL to assess the efficiency testing system in each participating laboratory and the published results in literature. This is a new IEA-AMT effort to evaluate and standardize efficiency testing methods for advanced vehicle energy conversion materials.

Accomplishments

- Third international round-robin of n-type half heusler material was completed, with 12 participating laboratories in six IEA-AMT member countries. The main testing results are shown in Figure 1.
 - Efforts were made to include more types of techniques. More homemade systems were used, although some laboratories could not measure all properties.
 - Great improvements were made in thermal diffusivity and electrical resistivity measurements.
 - Seebeck coefficient measurements showed a clear difference between the

four-point measurement and two-point measurement methods. This result was not very conclusive in the first two round-robins with bismuth telluride materials because of the temperature range (300 to 450K). At higher temperature, the heat loss due to probe configurations became more important. The IEA-AMT findings are being prepared for publication and will result in future improvement of measurement techniques and analysis.

- Improvement in specific heat measurement was also notable. The measurement of C_p was identified as the major source of error for ZT in previous work. With the new IEA-AMT procedures, the experimental scatter was much smaller in the third round-robin testing.
- An international survey of the thermoelectric module efficiency testing method was completed and published. As shown in Figure 2, several testing setups at key laboratories have similar concepts.

However, there are major differences in approaches and detailed design:

- Heat flow method: General Motors Research and Development (commercial system), Fraunhofer IMP (homemade system), AIST Japan (homemade system).
- Symmetric heat flow system: Marlow Industries (homemade system).
- Harman method: ORNL (commercial system) and Marlow Industries (modified commercial system).

After the survey and taking into account all pros and cons of each system, the annex proposed an ideal system (Figure 3) that would improve test reliability. Preparation of an international round-robin on efficiency testing is underway.

- Review of the measurement reliability of low-dimensional thermoelectric was carried out between ORNL and KRISS of Korea.
- The annex results were reported to the executive committee in Hong Kong (December 2013) and Lanzhou (June 2014).

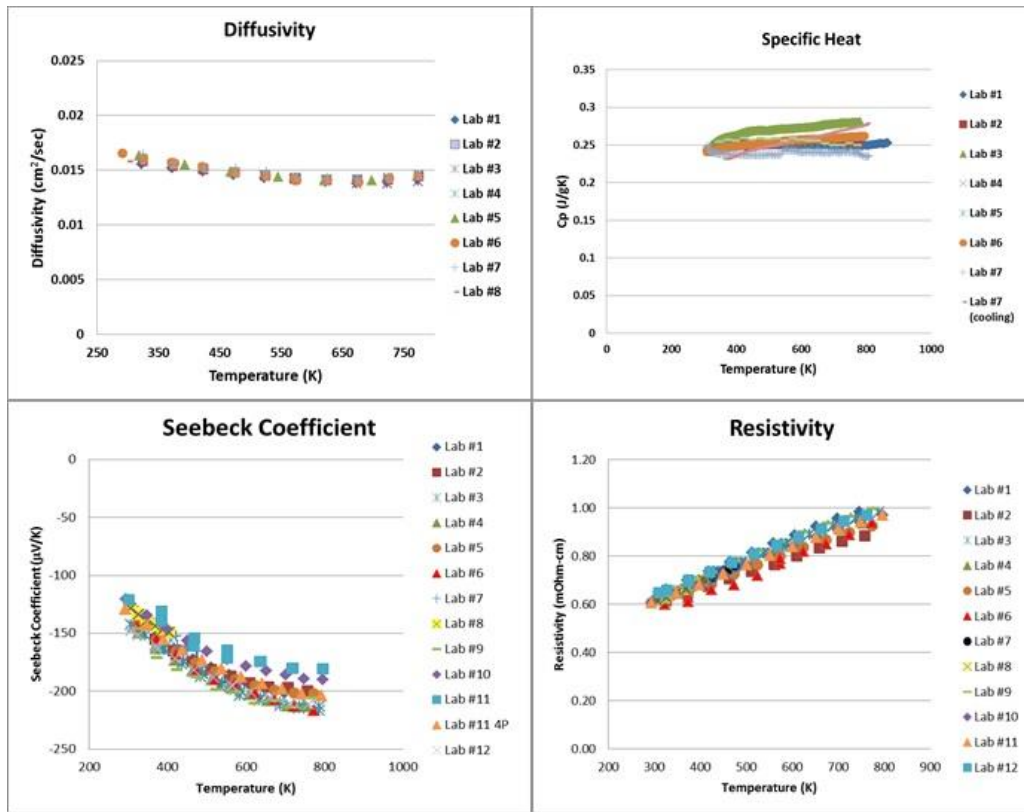


Figure 1. Third international round-robin results on n-type half-heusler.

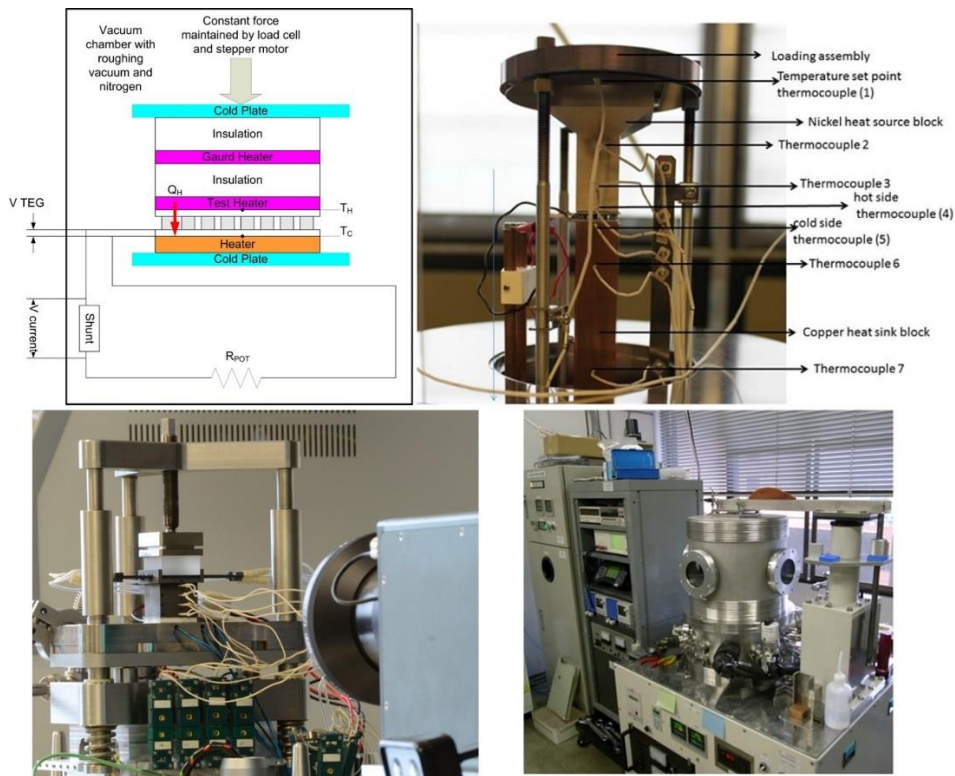


Figure 2. International survey of module efficiency testing was completed.

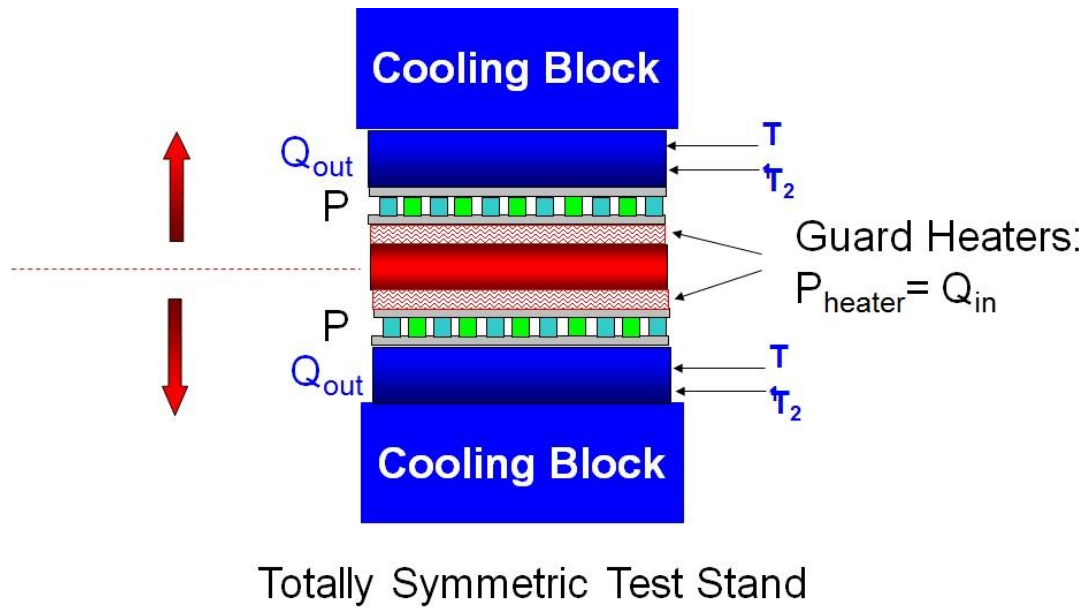


Figure 3. An ideal efficiency test system was proposed after the international survey.

Project 18519 – Materials for Exhaust and Energy Recovery

Agreement 26463 – Biofuel Impact on Aftertreatment Devices

M. J. Lance, T. J. Toops, E. J. Nafziger*, and C. Xie**

Ceramic Science and Technology Group

Oak Ridge National Laboratory

P.O. Box 2008, MS 6068, Building 4515

Oak Ridge, TN 37831-6068

Phone (865) 241-4536; fax (865) 574-6098; email: lancem@ornl.gov

**Fuels, Engines, and Emissions Research Center, ORNL*

DOE Technology Manager: Jerry L. Gibbs

Phone (202) 586-1182; fax: (202) 586-1600; e-mail: jerry.gibbs@ee.doe.gov

Technical Advisor: J. Allen Haynes

Phone (865) 576-2894; fax: (865) 574-4913; e-mail: haynesa@ornl.gov

Contractor: Oak Ridge National Laboratory, Oak Ridge, Tennessee

Prime Contract No.: DE-AC05-00OR22725

Objectives

- Characterize selective catalytic reduction (SCR), diesel oxidation catalyst (DOC), and diesel particulate filter (DPF) devices, following exposure to elevated levels of metal contaminants present in biodiesel, to identify the deactivation and degradation mechanisms that may occur in emissions control devices operated with biodiesel fuel.

Approach

- Use state-of-the-art characterization tools within the High-Temperature Materials Laboratory to analyze degradation mechanisms occurring in emissions control devices that had underwent accelerated aging in biodiesel received from our collaboration with Cummins, the National Renewable Energy Laboratory (NREL), the Manufacturers of Emission Controls Association, and the National Biodiesel Board.
- Establish accelerated aging methodology using the Oak Ridge National Laboratory (ORNL) stationary diesel generator.

Accomplishments

- Determined that doping the B20 with 28 ppm K was too high to use in acceleration studies.
- Determined the extent of Na poisoning of heavy-duty emission control devices following accelerated aging with B20 + 14 ppm Na.
- Purchased and installed a new stationary generator and conducted the first run with doped B20.

Future Direction

- Analysis of heavy-duty emissions control devices aged with B20 + 14 ppm Na will continue with high-resolution electron microscopy of the DOC washcoat and mechanical properties measurements and chemical and microstructural analyses of the DPF.
- Targeted studies of metal impurity poisoning of emissions control devices will be conducted with a stationary generator.

Introduction

To enable renewable fuels to displace petroleum, it is critical to evaluate their compatibility with emissions control devices. Biodiesel fuel is known to contain elevated alkaline (Na and K) and alkaline earth (Ca and Mg) metal levels left over from the processing methods of these fuels. These metallic fuel contaminants are converted to oxides, sulfates, hydroxides, or carbonates in the combustion process to form an inorganic ash that can be deposited onto the exhaust emissions control devices found in modern diesel engines. Alkali metals are well known poisons for catalysts and have been shown to negatively impact the mechanical properties of ceramic substrates (Williams et al. 2011). Furthermore, alkali metal hydroxides such as Na and K are volatilized in the presence of steam; therefore, they can penetrate the catalyst washcoat or substrate.

We are collaborating with Cummins, NREL, the Manufacturers of Emission Controls Association, and the National Biodiesel Board to characterize accelerated biodiesel-aged specimens. The first phase of this research focused on the effect of Na, K, and Ca on heavy-duty catalyst parts referenced to a system aged with undoped ultra-low sulfur diesel (ULSD) (Williams et al. 2011). The aged system did not meet the 0.2 g/bhp-hr NO_x emission standard; however, the results could not be attributed to metal exposure because no Na was observed on catalyst. In addition, the thermal shock resistance of the cordierite DPF declined 69%, following simulated aging to 425,000 miles.

Phase 2 focused on the effect of Na, K, and Ca on light-duty exhaust systems and the determination of an acceptable acceleration level (Williams et al. 2013). Phase 3, discussed below, returns to a heavy-duty system in order to determine if lower metal limits are needed based on issues seen in Phase 1. Using a testing protocol developed at Cummins, full production exhaust systems were aged at NREL, with biodiesel fuel doped with 14 ppm Na in order to

determine if there will be increased degradation of the emissions control devices when operated with 20 vol% biodiesel (B20) compared to ULSD. Samples were characterized using tools and techniques at the High-Temperature Materials Laboratory at ORNL, such as scanning electron microscopy, energy dispersive x-ray spectroscopy, x-ray fluorescence, x-ray diffraction (XRD), Raman spectroscopy, and thermogravimetry.

Long-term, low-cost testing of materials in real diesel engine exhaust was established through a previous annual operating plan at the Fuels, Engines and Emissions Research Center using a stationary diesel generator (genset). A second genset was added this fiscal year, which is better suited for testing conditions necessary for these samples. This genset can be run unattended overnight with different fuels, enabling low-cost testing without the use of an entire test cell and full-scale diesel engine. Accelerated aging with Na doping of biodiesel fuel was conducted in order to further specify the effect of metal impurities on emission control device performance.

The expected benefit of this project is to identify the poisoning mechanisms of alkali metals by tracking local chemical changes in the washcoat or substrate using high-resolution probes (both electron and photon). With this information, we will be able to make recommendations to industry regarding the fuel composition and operating conditions necessary to ensure the same lifetime of emission control devices operated with B20 that they currently have with ULSD.

Results

Aging a full-production exhaust system from a Cummins ISL was conducted at NREL to 435,000 miles simulated in 1,000 hours using B20 + 14ppm Na. Aging was conducted on the Cat C9 test stand. The emissions control devices were positioned with the DOC at the front, followed by the DPF and then the SCR system. Micro-cores were extracted at 0, 280, 553, 756, and 1,001 hours from the front face of both the

DOC and the SCR. The front face of the DOC catalyst brick is shown in Figure 1. A white powder was present within an annulus about 2 in. wide on outer edge of the front face of the DOC. A higher magnification image of the powder is shown in Figure 2. No white powder was observed at the center or at the DOC outlet. The micro-cores that were provided to ORNL were from this outer region and will be discussed below.

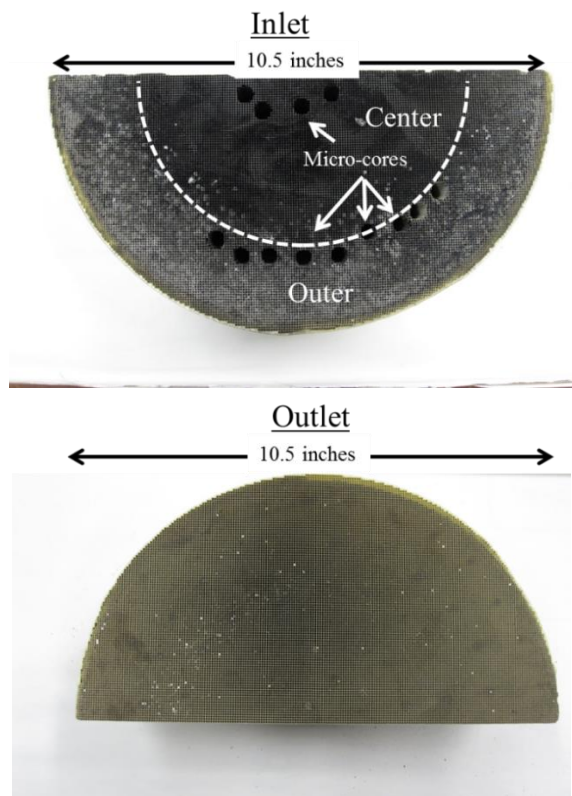


Figure 1. Front face (inlet) and back face (outlet) of the fully-aged DOC. The holes left by the micro-cores that were extracted during testing are visible on the front face.

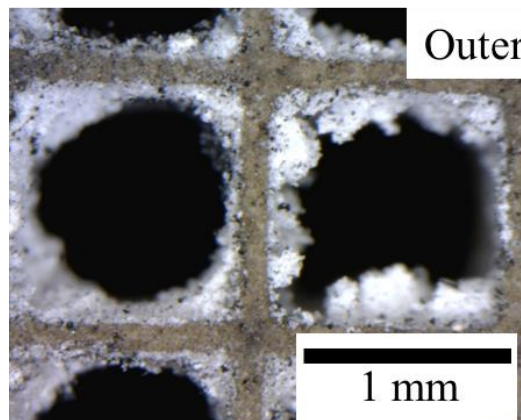


Figure 2. White powder observed at the DOC inlet near the outer edge.

The chemical composition of powder collected from the DOC front face and the DPF was measured using energy dispersive x-ray spectroscopy in scanning electron microscopy and is shown in Figure 3. Na is present in both the DOC powder and in ash collected from the DPF and will come entirely from the dopant in the fuel. P, S, Ca, and Zn are present in oil. S is also in the fuel dopant. Fe is probably from engine wear and Mg, Al, and Si are likely from cordierite.

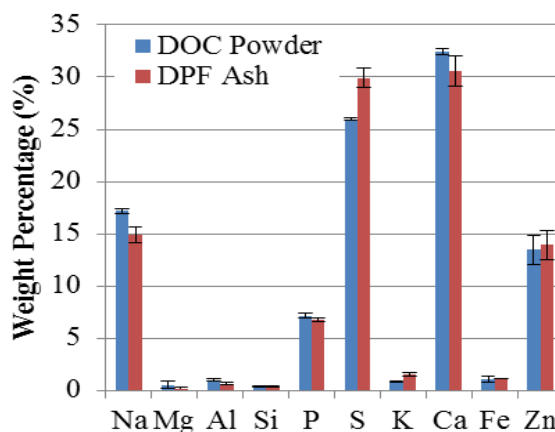


Figure 3. Compositional measurements of the powder in Figure 2 and ash from the DPF.

XRD (Figure 4) and Raman spectroscopy (Figure 5) were collected on powder from the front face of the DOC and revealed the powder to be mostly Na-Ca sulfate. The composition calculated using the XRD pattern is shown in

Table 1. The powder was 71% sulfate, with some phosphate and possibly oxalate species.

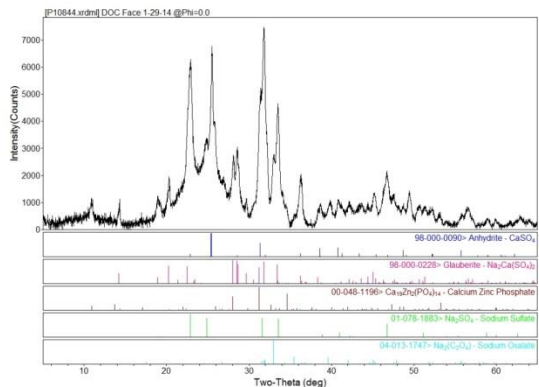


Figure 4. XRD pattern from the powder in Figure 2.

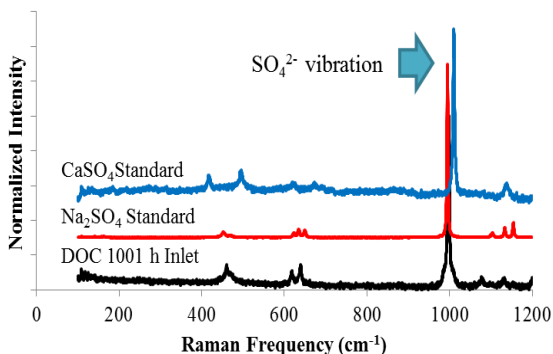


Figure 5. Raman spectra collected from the powder in Figure 2. Reference spectra from Na₂SO₄ and CaSO₄ are also shown.

Table 1: Composition of powder shown in Figure 2.

Compound	Weight Percentage (%)
Na ₂ SO ₄	23
CaSO ₄	16
Na ₂ Ca(SO ₄) ₂	32
Na ₂ C ₂ O ₄	21
Ca ₃ (PO ₄) ₂	8

Optical images collected from four micro-cores harvested from the front face of the DOC are shown in Figure 6. The flow direction is left

to right and the front face of the DOC is at the left side. The white Na-Ca sulfate powder seen in Figure 2 extends only 1 to 2 mm into the DOC brick from the front face. It also appears to increase with exposure time. Because the DOC brick is 102-mm (4 in.) long, the Na-Ca sulfate powder is not expected to have a significant impact on DOC performance.

Elemental maps of Na and S were also collected from the same regions shown in Figure 6 and are shown in Figure 7. These maps confirm that the white powder is predominantly Na₂SO₄ and CaSO₄ (not shown). More importantly, Na and S are detected across the entire washcoat, not just from the white powder region.

Electron probe microanalysis (EPMA) of the DOC was collected on cross sections at 5, 10, 15, and 20 mm from the front face of the DOC. The slice at 5 mm before aging and after aging is shown in Figure 8. Na is present throughout the washcoat, following aging. P, Zn, and Ca on the aged washcoat surface are from the engine oil.

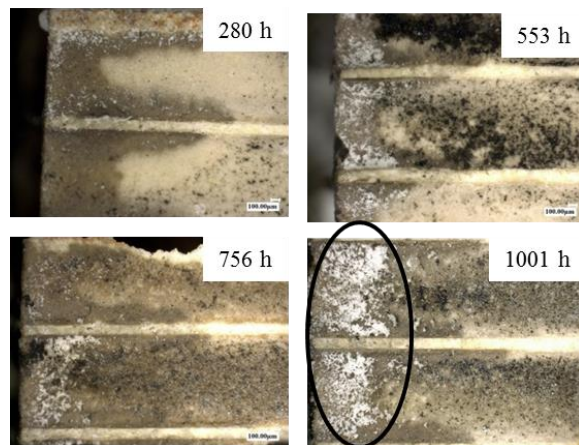


Figure 6. Images of the surface of the four micro-cores extracted from the front face of the DOC during aging. The black circle highlights the white powder seen in Figure 2. Image widths are 5 mm.

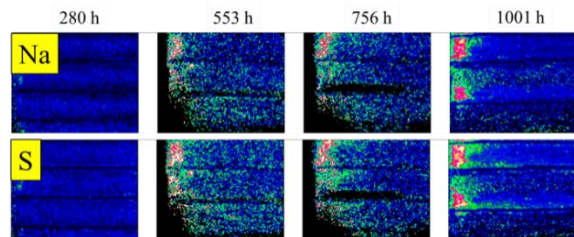


Figure 7. Na and S maps collected from the same regions in Figure 6.

Normalized EPMA maps of Na of the DOC micro-cores at 5 and 20 mm from the front face (Figure 9) show Na present throughout the washcoat following aging. The Na content does not appear to change within the first 20 mm of the sample, suggesting the Na is infusing the entire washcoat across the DOC.

The next device after the DOC is the DPF; however, this filter has yet to arrive from Cummins and no micro-cores were collected due to the need to maintain wall-flow for the filter. Micro-cores were harvested from the SCR device, and EPMA elemental maps collected from cross sections 5 mm from the inlet on an unaged and aged sample are shown in Figure 10.

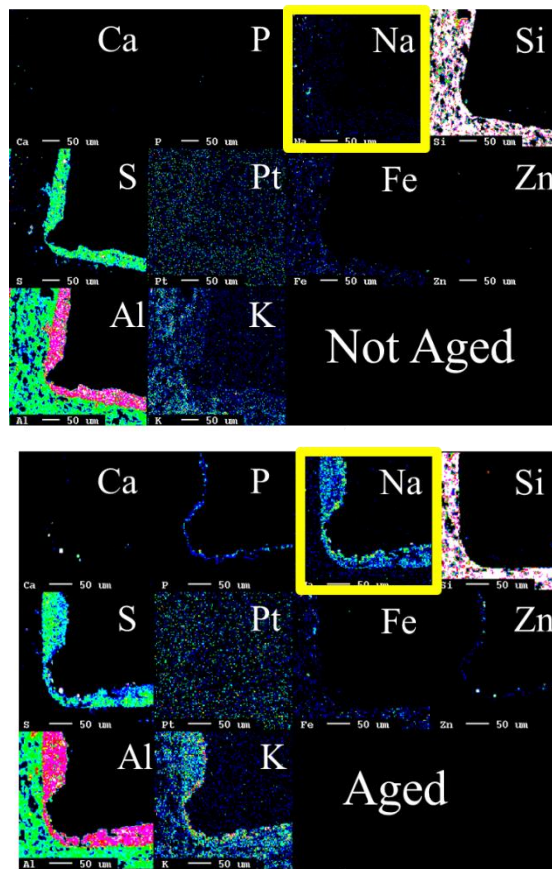


Figure 8. EPMA elemental maps collected on a cross section of the DOC washcoat from a not aged (top) and aged (bottom) sample. The yellow box highlights the change in Na following aging.

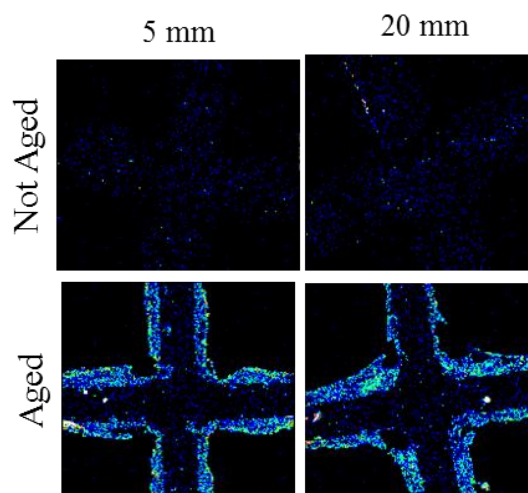


Figure 9. EPMA Na maps of the not aged and aged samples at 5 and 20 mm from the DOC inlet.

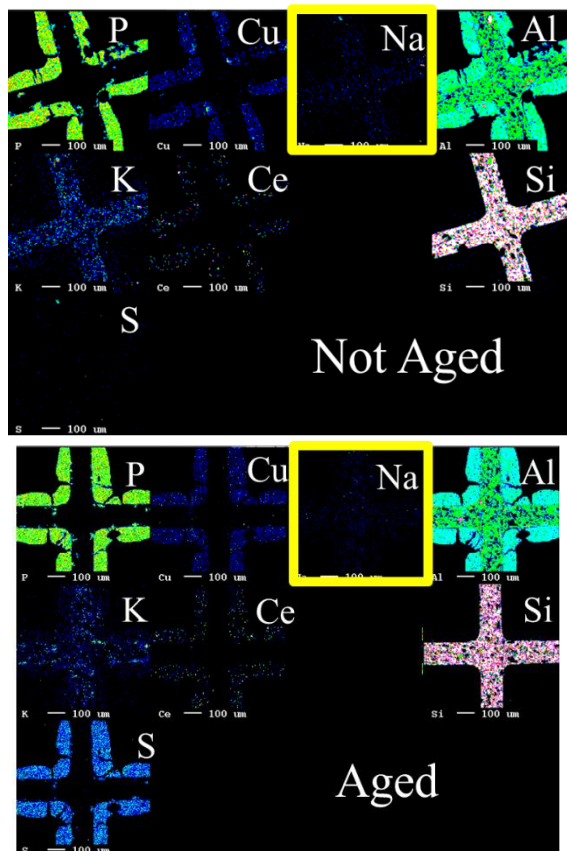


Figure 10. EPMA elemental maps collected on a cross section of the SCR washcoat from a not aged (top) and aged (bottom) sample. The yellow box highlights the change in Na following aging.

The only measureable change is that sulfur in the SCR brick increases following aging. Na was not detected after aging. The limit of detection for EPMA for Na is about 0.1 wt%; therefore, if there is Na present in the SCR, it must be below this level. This shows that the DPF is an effective trap for Na coming from the engine.

Stationary Generator

A Northern Lights 9-kW stationary generator that can run at 1,800 RPM and is Tier 4-compliant was purchased and installed at the Fuels, Engines and Emissions Research Center (see Figure 11). A shake-down and first test of this engine was conducted using Na-doped fuel. The samples from this run will be analyzed to determine if the changes observed in the NREL samples are also

occurring with the genset. This approach will allow us to generate diesel exhaust using different fuels that have been doped with chemicals to increase the Na and K content to match long-term operation with biodiesel fuel without the use of a full dynamometer and engine, which is much more costly.



Figure 11. Northern Lights stationary generator.

Milestones

Milestone	Completion Date
Complete analysis of potassium-aged samples (7, 14, 28 ppm).	December 2013
Identify deactivation mechanism in DOC and SCR devices caused by alkali metal impurities.	September 2014
Reproduce accelerated aging done by NREL using NTRC stationary generator.	June 2014
Use stationary generator to expose fresh emission control systems to targeted dosing set points guided by results from the NREL full-scale aging samples.	September 2014
Submit paper on SCR deactivation.	September 2014
Submit annual report.	November 2013
Present progress at annual merit review.	June 2014

Conclusions

Na is present in two forms in the DOC: First, 1 to 2 mm (out of 102 mm) from the inlet around the outer edge has Na-Ca sulfate powder. This is possibly related to lower temperatures in this region. Na is present throughout the washcoat within the first 20 mm of the inlet.

Na was not detected in the SCR.

These materials characterization results will be compared to emissions testing to better understand the impact of Na on the emissions control devices.

References

- A. Williams et al., 2011, "Impact of Biodiesel Impurities on the Performance and Durability of DOC, DPF and SCR Technologies," *SAE Int. J. Fuels Lubr.* 4(1): 110-124.
- A. Williams et al., 2013, "Impact of Fuel Metal Impurities on the Durability of a Light-Duty

Diesel Aftertreatment System," SAE International.

Publications and Presentations

- A. Williams, R. McCormick, M. Lance, C. Xie et al., 2014, "Effect of Accelerated Aging Rate on the Capture of Fuel-Borne Metal Impurities by Emissions Control Devices," *SAE Int. J. Fuels Lubr.* 7(2), doi:10.4271/2014-01-1500.
- A. Williams, T. J. Toops, and M. Lance, 2013, "Impact of Metal Impurities on Catalyst Durability," *Biodiesel Technical Workshop*, November 5, 2013.
- A. Williams, T. J. Toops, M. Lance, and G. Cavataio, 2014, "Impact of Metal Impurities on Catalyst Durability," *2014 National Biodiesel Conference*, January 23, 2014.

Project 18865 – Application-Specific Materials Simulation, Characterization, and Synthesis

Agreement 9105 – Characterization of Catalyst Microstructures

Dr. Lawrence F. Allard

Oak Ridge National Laboratory

Materials Science and Technology Division

1 Bethel Valley Road

Oak Ridge, TN 37831-6064

Phone (865)607-1144; fax (865) 576-5413; email: narulack@ornl.gov

DOE Technology Manager: Jerry L. Gibbs

Phone (202) 586-1182; fax: (202) 586-1600; e-mail: jerry.gibbs@ee.doe.gov

Field Technical Manager: J. Allen Haynes

Phone (865) 576-2894; fax: (865) 574-4913; e-mail: haynesa@ornl.gov

Contractor: Oak Ridge National Laboratory, Oak Ridge, Tennessee

Prime Contract No.: DE-AC05-00OR22725

Objectives

- Provide unique catalyst characterization capabilities to help meet mandated emission reduction targets for automotive and diesel engines.
- Primary focus is atomic-level aberration-corrected electron microscope (ACEM) coupled with both *in situ* and *ex situ* gas reaction capabilities.
- The real value of our technology is the unsurpassed ability to heat and react catalyst materials under “real world” conditions (e.g., to mimic bench-top reactors) to correlate atomic-level changes in structure/chemistry to observed behavior and performance.

Approach

- Partner with Protochips Co. to expand capabilities for *in situ* reaction studies with a unique gas cell reactor system for the ACEM. Develop a Gen4 gas cell holder design and beta-test the commercial version of the computer-controlled gas manifold system.
- Continue current studies of experimental “self-regenerating catalysts,” based on precious metal/perovskite structure materials, for nitrous oxide reduction applications. Contributed additional imaging in new partnership with University of New Mexico (UNM) colleagues (Datye group) to characterize the regenerability of atomically dispersed Pd on γ -alumina for low-T exhaust treatment catalysis.

Accomplishments

- An extensive suite of calibration experiments with Protochips Inc. to permit accurate control of temperature in the gas cell was successful in determining that temperature versus resistance of the heater membrane yielded a gas composition and temperature-independent control method.
- A full computer-controlled Gen 4 gas cell reactor system was tested at the JEOL factory (Akishima, Japan) to qualify for commercial deployment by that manufacturer. Currently, the qualifying system is in further use at Oak Ridge National Laboratory.

- Work with UNM has showed that the addition of LaO_x to the γ -alumina support helps stabilize the dispersion of single Pd atoms, which leads to low-temperature (i.e., 40°C) onset of catalytic activity in CO oxidation reactions. A paper on this work was published in *Nature Communications* (Peterson et al. 2014).

Future Direction

- Continue new studies with UNM colleagues, focusing on determination of the size and morphology of Pd particles that can be reversibly dispersed to form the isolated single-atom species on γ -alumina. We know that the low-temperature reactivity of Pd can be regenerated through oxidative treatment, but we hypothesize that once bulk PdO forms, we prevent further mobility of the Pd species. Hence, the small clusters that form *in situ* during CO oxidation represent the species that can be redispersed. To conclusively identify the mechanism of redispersion, *in situ* gas-reaction experiments are needed.
 - We also will maintain our close collaboration with colleagues at the University of Michigan, who have recently inaugurated a new 300-kV, double-aberration-corrected transmission electron microscope (TEM)/scanning transmission electron microscope (STEM) (JEOL 3100) that is housed in a special new laboratory and who also have purchased the now-commercial Protochips gas cell system. This will provide the opportunity to compare the results of gas-cell experiments both at 200 and 300-kV operating potential and to determine the benefits of both methods. Work will continue to focus on regenerable precious-metal/perovskite materials for nitrous oxide reduction.
-

Introduction

While we have been testing/using the Gen4 gas cell holder fabricated by Protochips Inc. for well over a year, in November 2013, the holder was married to the new gas manifold system and equipped with electro-mechanical valving capability that permits full control of gas reactions via a special software package also provided by Protochips. Characteristics and testing of the system are described in the results section. Also discussed in this report is the work with UNM on the regenerable PdLa/ γ -alumina single-atom catalyst recently published in *Nature Communications* and, finally, some background on future work with UNM on regenerable catalysts for CO oxidation.

Results

Figure 1 shows the “alpha” commercial gas manifold system and Figure 2 presents the graphical user interface (GUI) for the software developed to run the manifold. This program was debugged and tested for several weeks, prior to crating of the manifold for shipment to Japan to be qualified at the JEOL factory. The basic layout of the system is shown on the GUI; three gases can be supplied to the manifold, two for reaction experiments and, typically, nitrogen as a purge gas. The gases can also be mixed, and stored in two experimental supply tanks. A receiving tank is provided into which gases can flow during flowing gas experiments (if so desired). The backpressure in the receiving tank offers a means for controlling flow rate, as was determined last year during our experiments on the nature of flow in the overall system. Pressures are detected via a series of appropriately placed capacitance manometer (Baratron) gauges and fed to the program during operation.

The ability to run gas reaction experiments via computer control offers a number of major benefits over our original hand-run manifold system. The panel in the upper right quadrant of the GUI directs the operator through a series of steps that allows naming gases, installing a calibration file for temperature control of the heater device, testing the device automatically to ensure it meets specifications and can be run appropriately, automatically running a series of

purge gas steps to prepare for the reaction gas, and setting up experimental conditions (e.g., temperature, flow, pressure, etc.). With our home-built manifold, all of these steps would require careful attention by the operator, but the new system allows, for example, purge steps to be run while the operator is doing other things. The most important benefit of the computer control, however, is continual recording of reaction conditions as displayed in the lower left panel of the GUI. For example, the temperature and pressure are recorded relative to time and can be compared directly to the time-stamped images taken on the ACEM during the experiment. This removes the need for most additional note taking that is subject to operator error while the experiment is underway, thereby providing confidence of a more reliable reaction experiment for subsequent reporting.



Figure 1. “Alpha” version of Protochips commercial gas manifold for computer-controlled operation of a gas reaction holder for the JEOL 2200PS ACEM.

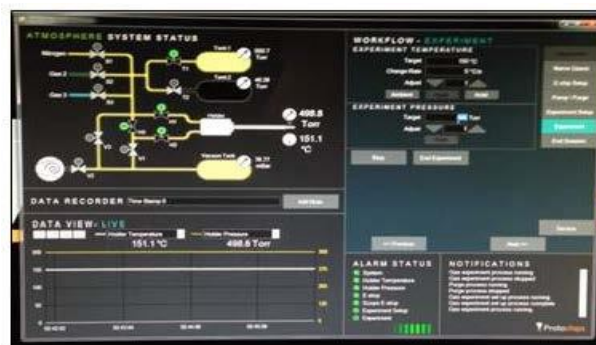


Figure 2. Computer GUI for software to run the gas reaction experiment with full external control (see text for details).

Numerous improvements were suggested as a result of the initial test-out from running the software during actual reaction experiments, leading to an improved version being available during the testing at JEOL. Figure 3 shows Larry Allard operating a JEOL 2100 STEM/TEM instrument at the factory during the March 2014 qualification tests. A major success of the tests was to assure JEOL that a catastrophic failure of a gas cell window and/or heater during a run at atmospheric pressure would not cause any harm to the microscope's electron gun or vacuum system. Purposeful breaking of a window during a test showed that the electron gun would be automatically protected by the present microscope vacuum operation and, ultimately, JEOL/Protochips will provide feedback to the Protochips computer to allow closing of a gas supply to the holder and re-pumping the holder if a window fails.

Further imaging experiments conducted (e.g., on Pt-barium cerate catalysts in work with the University of Michigan) showed conclusively that imaging of crystal lattices at elevated temperatures and pressures up to a full atmosphere is not impeded to any significant extent by the presence of the gas. This can be seen in Figure 4, which shows the barium cerate lattice with a relative vacuum (i.e., 35 Torr) versus high pressure (i.e., 700 Torr) of gas in the cell.



Figure 3. Dr. Larry Allard operating the JEOL 2100 TEM/STEM instrument at the JEOL factory during the qualification test/test out of the Protochips alpha-version commercial gas reactor system.

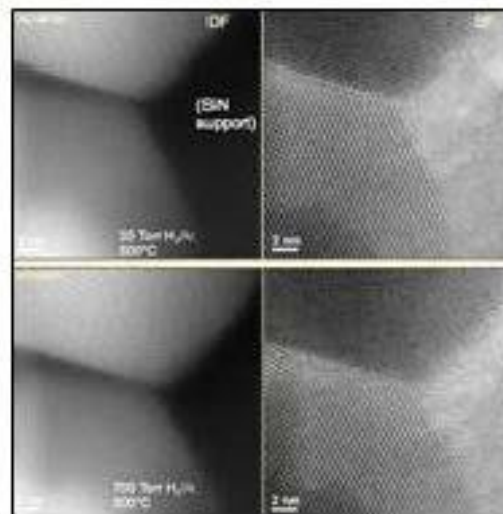


Figure 4. Example of resolution at atomic lattice level at low and high pressure of reducing gas in the reactor; HAADF-BF image pairs, both set at 500°C.

Work with colleague Professor Abhaya Datye at UNM has proved fruitful in the final writing of a major paper showing the potential for regenerability and stability in a single-atom catalyst formulation involving Pd stabilized by lanthana on γ -alumina. The work was selected for publication in *Nature Communications* (Peterson et al. 2014) and has led to future directions for our collaboration. Following from the original work conducted under the auspices of our Energy Efficiency and Renewable Energy agreement, in which our collaboration with Professor Jingyue Liu (Arizona State University) and colleagues in Professor Tao Zhang's group in the Chinese Academy of Sciences showed, for the first time, direct imaging proof of the efficacy of single Pt atoms on FeOx supports to catalyze CO oxidation reactions, Professor Datye has now shown that Pd single atom species stabilized by LaOx on industrially relevant γ -alumina can also catalyze CO oxidation, especially at low temperatures. Figure 5 is a figure from the *Nature Communications* paper that illustrates analysis of the intensities of the heavy metal species on the alumina and the intermingling of La with Pd single atoms, which is then related to catalytic performance.

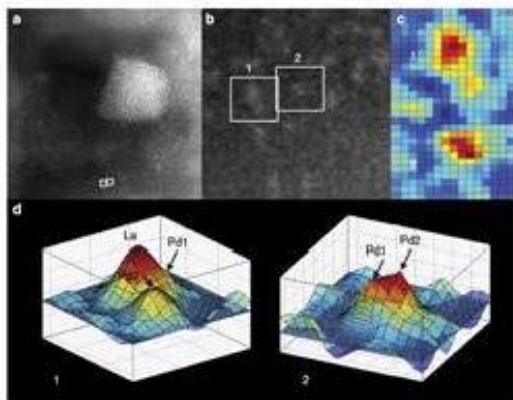


Figure 5. Figure from *Nature Communications* paper showing intermingling of LaOx with single atoms of Pd; catalyst shown to be regenerable and active for CO oxidation with dispersion of catalytic species on industrially relevant γ -alumina (see Peterson et al. [2014] for details).

Future Work

Valuable understanding about the nature of regenerability of heavy metal species on oxide supports will be gained by experiments we will conduct beginning this fall. We want to understand the particle size range where redispersion can be achieved, which will be important for design of catalysts that provide enhanced low-temperature reactivity and are able to be regenerated *in situ* through appropriate redox treatments. The work will involve heating highly dispersed Pd on the SiOx surface of the thin SiN membrane in the Protochips heater under mild reducing conditions to form small clusters and nanoparticles. Calcining *in situ* under oxidizing atmospheres in the gas cell reactor should lead to redispersion. Once larger Pd particles form, they will not redisperse, as seen from our previous work (Figure 6).

Conclusions

Much of the work on our project over the last several years has been devoted to developing the capability to perform gas reaction studies with the full capability for imaging at the atomic level under “real” reaction conditions by using a “closed-cell” gas reactor specimen holder design. With the full

computer-controlled system now commercialized and shown to fulfill all of the original desired capabilities, this work has proven highly successful. Coupled with increasing interest throughout the field in the potential for the “holy grail” of single-atom catalysis to be possible in a number of catalytic systems, we are excited in the possibility of using our *in situ* reaction capabilities to help further this research direction for our VT program.

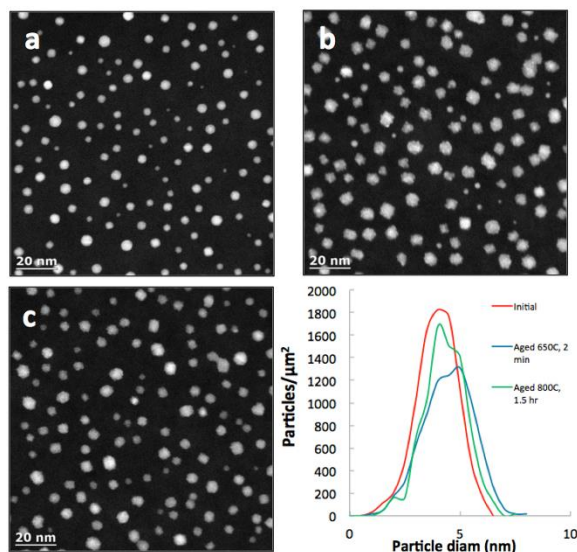


Figure 6. HAADF STEM images of Pd/SiO₂ in its (a) initial state, (b) aged 650°C for 2 minutes, and (c) aged 800°C for 1.5 hours. There is very little sintering, which is evident from the nearly constant number of particles per unit area and from the particle size distributions (bottom right). No loss of metal due to evaporation was detected on these samples.

References

Allard, L. F., W. C. Bigelow, S. Zhang, X. Pan, Z. Wu, S. H. Overbury, W. B. Carpenter, F. S. Walden, R. L. Thomas, D. S. Gardiner, B. W. Jacobs, D. P. Nackashi, and J. Damiano, 2014, “Controlled *In Situ* Gas Reaction Studies of Catalysts at High Temperature and Pressure with Atomic Resolution,” *Microsc. Microanal.* 20 (Suppl 3), 1572-73.

August 7, 2014, Dr. Larry Allard visited Professor Xiaoqing Pan’s group at the University of Michigan to tour the newly opened microscopy building and see the

- recently installed JEOL 300-kV double-corrected cold-field-emission STEM/TEM instrument. Discussed ongoing research and future directions with Professor Pan and group.
- Blom, D. A., T. Vogt, L. F. Allard, and D. J. Buttrey, 2014, "Observation of Sublattice Disorder of the Catalytic Sites in a Complex Mo-V-Nb-Te-O Oxidation Catalyst Using High Temperature STEM Imaging," *Topics in Catalysis* 57(14-16), 1138-1144.
- CNMS Advanced Electron Microscopy Workshop, September 2014: Aberration-Corrected STEM Imaging, Spectroscopy and In Situ Microscopy; "Atomic-Resolution Electron Microscopy at High Temperatures and Pressures, via MEMS-based Closed-Cell Gas Reactor Technology."
- Georgia Tech Workshop to Dedicate Electronics and Nanotechnology Center, May 2014; "A Comparison of Techniques for *In Situ* Gas Reaction Studies in Electron Microscopy."
- Kwak, Ja Hun, Robert Dagle, Gerald C. Tustin, Joseph R. Zoeller, Lawrence F. Allard, and Yong Wang, 2014, "Molecular Active Sites in Heterogeneous Ir-La/C-Catalyzed Carbonylation of Methanol to Acetates," *J. Phys. Chem. Lett.* 5(3), pp 566-572, DOI: 10.1021/jz402728e.
- Liu, Jingyue (Jimmy) and Lawrence F. Allard, 2014, "*In Situ* Investigation of the Carbothermal Reduction of ZnO Nanowires," *Microsc. Microanal.* 20 (Suppl 3), 1554-55.
- Peterson, Eric J., Andrew T. DeLaRiva, Sen Lin, Ryan S. Johnson, Hua Guo, Jeffrey T. Miller, Ja Hun Kwak, Charles H.F. Peden, Boris Kiefer, Lawrence F. Allard, Fabio H. Ribeiro, and Abhaya K. Datye, 2014, "Low-temperature carbon monoxide oxidation catalysed by regenerable atomically dispersed palladium on alumina," *Nature Communications* 5:4885, September 15, 2014; DOI:10.1038/ncomms5885 www.nature.com/naturecommunications.
- Sanchez, Sergio I., Lawrence F. Allard, Wharton Sinkler, and Steven A. Bradley, 2014, "Characterization of Sub-Nanometer Pt Cluster Formation on γ -Al₂O₃ via *Ex Situ* Reductions using MEMS-Based Heating Technology," *Microsc. Microanal.* 20 (Suppl 3), 1656-57.
- Yang, Ming, Lawrence F. Allard, Sungsik Lee, Manos Mavrikakis, and Maria Flytzani-Stephanopoulos, 2014, "Alkali metals stabilized atomic Au- and Pt-OH_x species on L-zeolite and MCM41 catalyze the low-temperature water-gas shift reaction," International Congress on Environmental Catalysis, Asheville, NC, August 2014. *Note: This paper was one of three chosen for a Keynote Address, delivered by Professor Flytzani-Stephanopoulos.*
- Yang, Ming, Yuan Wang, Sha Li, Jeffrey A. Herron, Ye Xu, Manos Mavrikakis, Lawrence F. Allard, Sungsik Lee, Jun Huang, and Maria Flytzani-Stephanopoulos, 2014, "Au-(OH)_x species stabilized by alkali ions catalyze the water-gas shift reaction on zeolites and other inert oxide supports," submitted to *Science*, September 2014.

Project 18865 – Application-Specific Materials Simulation, Characterization, and Synthesis

Agreement 26391 – Applied ICME for New Propulsion Materials

David J. Singh

Materials Science and Technology Division

Oak Ridge National Laboratory

PO Box 2008, MS 6056, Building 4100

Oak Ridge, TN 37831-6068

Phone (865) 241-1944; fax (865) 574-7659; email: singhdj@ornl.gov

DOE Technology Manager: Jerry L. Gibbs

Phone (202) 586-1182; fax: (202) 586-1600; e-mail: jerry.gibbs@ee.doe.gov

Technical Advisor: J. Allen Haynes

Phone (865) 576-2894; fax: (865) 574-4913; e-mail: haynesa@ornl.gov

Contractor: Oak Ridge National Laboratory, Oak Ridge, Tennessee

Prime Contract No.: DE-AC05-00OR22725

Objectives

- Employ an Integrated Computational Materials Engineering (ICME) approach, encompassing close feedback between theory and experiment, to meet several pressing propulsion materials challenges:
 - The need for higher performance piezoelectric materials to be used as actuators in the high-performance fuel injectors necessary to meet future U.S. Department of Energy fuel efficiency targets.
 - The need for high-performance, rare-earth free permanent magnets to be used in technological applications such as hybrid electric vehicles and wind turbines.
 - The need for catalysts capable of attaining light-off and associated high conversion efficiency for criteria pollutants at temperatures well below 250°C.
 - The need for stable, inexpensive, high-performance thermoelectric materials to deploy in vehicular waste heat recovery and cabin climate control applications.
 - The need for stronger engine materials to withstand the higher combustion temperatures and cylinder pressures characteristic of future high-efficiency engines.

Approach

- Perform first principles calculations of the structure and properties of perovskite oxides related to $\text{Pb}(\text{Zr},\text{Ti})\text{O}_3$ (PZT), along with synthesis and characterization of perovskite oxides with feedback between theory and experiment to optimize properties.
- Perform synthesis and magnetic measurements for potential high-performance ferromagnets, including Fe_3P - based, $\text{Co}_{23}\text{Hf}_6$ -based, and related materials, and first principles calculations of magnetization and anisotropy as a function of composition to guide magnet optimization.
- Use an integrated approach with computational modeling and experimental development, design, and testing of new catalyst materials.
- Perform Boltzmann transport calculations of thermoelectric properties.
- Perform theoretical assessment of materials needs for high-performance engines.

Accomplishments

- Found that oxide $(\text{PbZr}_{0.5}\text{Ti}_{0.5}\text{O}_3)_{0.75}(\text{BiZn}_{0.5}\text{Ti}_{0.5}\text{O}_3)_{0.25}$ theoretically is near morphotropic phase boundary with lattice distortion of $c/a=1.08$, substantially larger than c/a value of PZT of approximately 1.025. Sample synthesis initiated.
- Experimental synthesis and study of potential permanent magnet $\text{Fe}_3\text{P}_{1-x}\text{As}_x$. Initial experimental and theoretical results suggest an increased Fe moment with As concentration, but experimental variability precludes definitive conclusion.
- Found that single supported Pt atoms theoretically are catalytically active for NO oxidation. Found that bimetallic CuMn zeolite catalysts experimentally attain higher NO conversion at temperatures under 180°C than Cu zeolite catalysts. Technical reports submitted for publication.
- Found that lead chalcogenide PbS theoretically may show high thermoelectric performance ($ZT \sim 1.7-2$) at temperatures above 1000K, and that this material possesses mechanical properties superior to those of PbTe.
- Found from preliminary engine modeling that current engine materials are not sufficiently robust to withstand stresses in future higher performance engines.

Future Direction

- Continue application of ICME approach to meet needs for improved piezoelectric, magnetic, and catalytic materials.
 - Identification of advanced piezoelectric materials; practical, high-performance, rare earth-free, permanent magnet materials; and durable, low-temperature catalysts.
-

Piezoelectric Materials

Introduction

The advent of advanced combustion techniques, such as those envisioned in the SuperTruck program, has resulted in the need for improved fuel injection control. Such control is essential in order to achieve excellent fuel economy without sacrificing the necessary control of criteria pollutants such as hydrocarbons, carbon monoxide, and oxides of nitrogen. Currently, most high-performance fuel injectors use piezoelectric actuators such as $\text{PbZr}_{0.5}\text{Ti}_{0.5}\text{O}_3$ (PZT).

Piezoelectrics are useful for this purpose because they change their length extremely rapidly upon application of an electric field. This rapid motion allows precise control over the fuel injection process. However, PZT is not sufficiently high performance for the advanced engines under current development. In particular, its tetragonality (a key measure of the distortion producible by electric fields) is only approximately 1.025, limiting its performance. Therefore, we seek a compound with similar characteristics to PZT, but with larger tetragonality.

Piezoelectrics, such as PZT, are typically found near morphotropic phase boundaries (MPB) in a ferroelectric system, where the crystalline structure of a compound changes abruptly as a function of chemical composition. The PZT system, for example (see Figure 1), shows such a boundary very near the 50:50 mixture of Zr and Ti. As might be expected, the sensitivity of the structure to the exact chemical composition near an MPB leads to a great enhancement of piezoelectric properties for materials near this point. However, finding an MPB experimentally is difficult and time consuming, because there is no way of knowing at what composition an MPB, if present, might emerge.

We adopt a theoretical approach, based on first principles density functional theory, combined with experimental synthesis and study. By studying the energies, atomic displacements (relative to symmetric “centered” positions), and ferroelectric polarizations of both

tetragonal and rhombohedral structures (the usual structures on opposite sides of an MPB), we can estimate the potential piezoelectric performance of a material and assess its nearness to an MPB. We are studying the compositions depicted in Figure 2, with an eye toward a possible MPB as indicated in Figure 2.

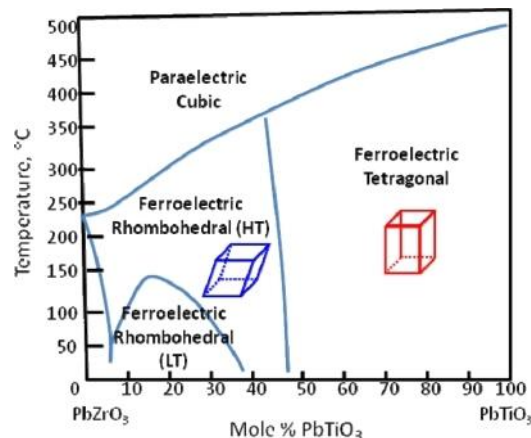


Figure 1. The phase diagram of PZT (from www.openi.nlm.nih.gov). Note the rhombohedral-tetragonal morphotropic phase boundary in the center of the diagram.

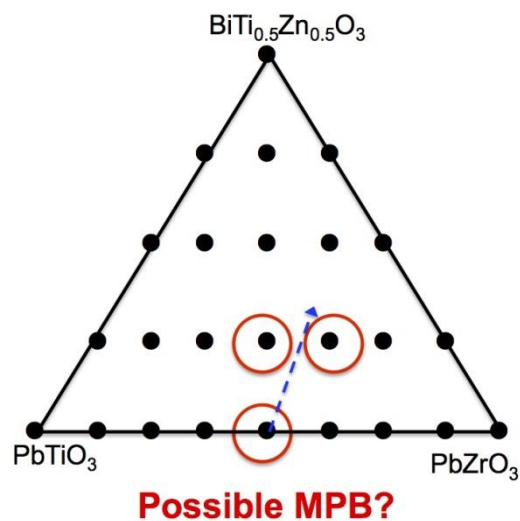


Figure 2. A ternary diagram of the compositions studied theoretically and experimentally, with the potential morphotropic phase boundary indicated.

Results

Figure 3 depicts the primary result of the theoretical effort. We plot the energy of the

oxide composition $(\text{PbZr}_{0.5}\text{Ti}_{0.5}\text{O}_3)_{0.75}(\text{BiZn}_{0.5}\text{Ti}_{0.5}\text{O}_3)_{0.25}$ as a function of c/a ratio. These energies were generated via calculation of the properties of a 40-atom supercell (the minimum size necessary to describe this composition) of the specified c/a ratio. In these calculations, the internal coordinates were allowed to vary in order to minimize the energy, thus generating displacements of the atoms relative to the symmetric positions associated with the parent cubic structure.

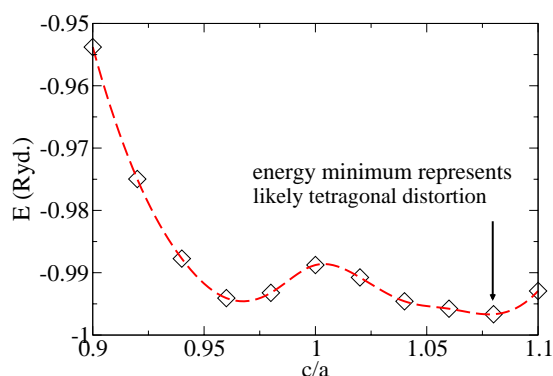


Figure 3: The variation of energy with c/a ratio for the oxide composition $(\text{PbZr}_{0.5}\text{Ti}_{0.5}\text{O}_3)_{0.75}(\text{BiZn}_{0.5}\text{Ti}_{0.5}\text{O}_3)_{0.25}$.

The plot depicts a bifurcated structure, with distinct energy minima near the two c/a ratios 0.97 and 1.08. Ratios less than unity are generally associated with a rhombohedral structure (see Figure 1), while ratios greater than unity are generally associated with a tetragonal structure. Of particular importance is the energy minimum at $c/a=1.08$, which is an absolute minimum over the whole range. This means that an oxide of the stated composition will tend to assume a tetragonal structure with this c/a ratio. This c/a ratio is to be compared to the approximate 1.025 value of the known high-performance piezoelectric PZT. In particular, the larger c/a ratio means that larger ferroelectric polarizations and associated piezoelectric coefficients will likely be associated with this composition. Preliminary calculations on the corresponding oxide $(\text{PbZr}_{0.5}\text{Ti}_{0.5}\text{O}_3)_{0.75}(\text{BiZn}_{0.5}\text{Zr}_{0.5}\text{O}_3)_{0.25}$ indicate a possibility of an energy minimum on the

rhombohedral side, suggestive of an MPB between these two oxide compositions, but these calculations are not yet complete. They will be reported on during Fiscal Year 2015.

On the experimental side, Bismuth substitution in PZT-based piezoelectric ceramics was investigated. The aim of this study is to determine whether the alloys are stable and how the chemical substitution may affect the crystal structure. Alloys of PZT with “ $\text{BiZn}_{0.5}\text{Ti}_{0.5}\text{O}_3$ ” (BZT) and “ $\text{BiZn}_{0.5}\text{Zr}_{0.5}\text{O}_3$ ” (BZZ) were examined. Two samples were synthesized: $\text{PZT}_{0.9}\text{BZT}_{0.1}$ and $\text{PZT}_{0.9}\text{BZZ}_{0.1}$ via solid state reactions starting with binary oxides. Powder diffraction analysis demonstrated that homogeneous alloys can be formed in both systems at the level of substitution studied. In addition, both samples were found to adopt the same tetragonal structure as PZT at room temperature and with a similar level of distortion. With the stability of the alloys demonstrated and the synthesis procedures developed, further studies on additional alloy compositions will determine whether improved piezoelectric performance can be realized using this strategy.

Conclusions

We have theoretically and experimentally studied alloys of PZT with “ $\text{BiZn}_{0.5}\text{Ti}_{0.5}\text{O}_3$ ” (BZT) and “ $\text{BiZn}_{0.5}\text{Zr}_{0.5}\text{O}_3$ ” (BZZ). Theoretical evidence for increased tetragonality in the PZT-BZT alloy is found, suggestive of large ferroelectric polarization, and preliminary calculations on the PZT-BZZ alloy suggest the possibility of an MPB between these two compositions, although these calculations are not yet complete. Experimental work on these alloys found that for small amounts of BZT and BZZ (approximately 10%) both are tetragonal, suggesting that larger concentrations of these alloys may be necessary to find an MPB.

Permanent Magnets

Introduction

Strong permanent magnets (such as $\text{Nd}_2\text{Fe}_{14}\text{B}$ and $\text{Sm}_2\text{Co}_{17}/\text{SmCo}_5$) are used in a number of clean energy applications such as hybrid and battery electric vehicles and wind

turbines. However, the key rare earth elements in these magnets (such as Nd and Sm) are subject to supply disruptions, necessitating the development of new strong permanent magnets without these elements.

Results

Chemical Substitutions in Ferromagnetic Fe_3P

The synthesis and magnetic properties of $\text{Fe}_3\text{P}_{1-x}\text{As}_x$ were studied. We found that this new alloy system is ferromagnetic (see Figure 4), with Curie temperatures near 690 K, like the end member Fe_3P , and nearly independent of x , which could be varied up to about $x = 0.20$. Our theoretical findings indicated that substitution of As for P produces a small increase in the magnetic moment of iron in this system due, in part, to the increase in unit cell volume. Experimental investigations suggest an increase in moment with x , but experimental uncertainties make the small change difficult to verify. No indication of increased magnetic anisotropy was observed with As substitution, suggesting other chemical modifications would be required to significantly enhance the potential for Fe_3P -based permanent magnet materials.

Single Crystal Study of MnBi

Detailed studies of the single crystals of the permanent magnet material MnBi were conducted in collaboration with the Critical Materials Institute. Interest in developing a better understanding of this compound is motivated by a particularly unusual and beneficial magnetic behavior: coercivity that increases strongly with temperature all the way up to the decomposition temperature. Results include new structural information revealed by the first single crystal neutron diffraction measurement on this material. The data show anisotropic vibrations of the Bi atoms, which increase at high temperature, likely related to the unusual thermal expansion and good magnetic performance displayed by MnBi. In addition, crystal structure distortion (see Figure 5) was discovered to occur below about 90 K (i.e., the temperature at which the magnetic moments are known to reorient). The detailed crystallographic results should be useful in future theoretical

studies of this material, and the anisotropic vibrations of the Bi atoms may provide a link between the unusual thermal expansion and unusual magnetic behavior. A report describing our findings has been submitted for publication in *Physical Review B*.

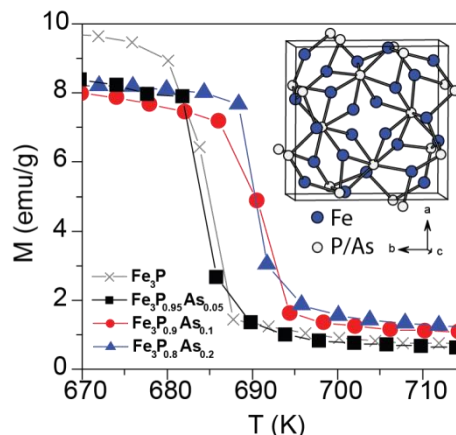


Figure 4. Temperature dependence of magnetization near the Curie temperature in several alloys in the $\text{Fe}_3\text{P}_{1-x}\text{As}_x$ system.

Single Crystal Study of MnBi

Detailed studies of single crystals of the permanent magnet material MnBi were conducted in collaboration with the Critical Materials Institute. Interest in developing a better understanding of this compound is motivated by a particularly unusual and beneficial magnetic behavior: coercivity that increases strongly with temperature all the way up to the decomposition temperature. Results include new structural information revealed by the first single crystal neutron diffraction measurement on this material. The data show anisotropic vibrations of the Bi atoms, which increase at high temperature; this is likely related to the unusual thermal expansion and good magnetic performance displayed by MnBi. In addition, crystal structure distortion (see Figure 5) was discovered to occur below about 90 K, the temperature at which the magnetic moments are known to reorient. The detailed crystallographic results should be useful in future theoretical studies of this material, and the anisotropic vibrations of the Bi atoms may provide a link between the unusual thermal expansion and unusual magnetic behavior. A

report describing our findings has been submitted for publication in *Physical Review B*.

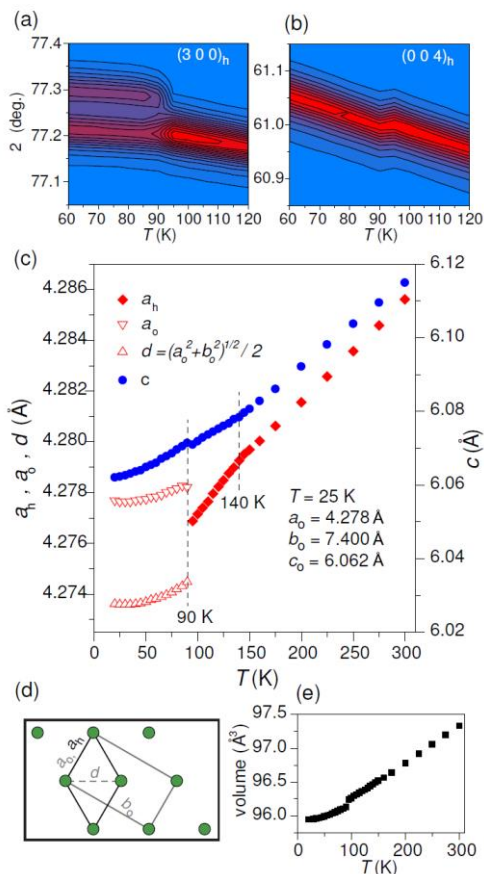


Figure 5. From top: neutron diffraction intensity patterns of the ferromagnet MnBi, showing the hexagonal to orthorhombic transition at which the moments re-orient. Bottom plot shows the relationship of the hexagonal and orthorhombic unit cells and the volume with temperature.

Annealing Effects in $\text{Hf}_2\text{Co}_{11}\text{B}$ Permanent Magnet Alloys

Our study of annealing effects on amorphous $\text{Hf}_2\text{Co}_{11}\text{B}$ melt-spun materials was concluded. Valuable information about the microstructure and chemical phase composition of these complex, rare earth-free permanent magnet materials was revealed by x-ray diffraction, scanning electron microscopy, and magnetic properties measurements. Annealing the ribbons in high magnetic fields was found to significantly accelerate grain growth and produce unique microstructures. This suggests that magnetic field processing may provide a

means to access tailored microstructures for enhanced magnetic properties that may be otherwise unattainable. The findings from this study have been summarized in a report submitted for publication in *the Journal of Applied Physics*.

Neutron Diffraction from the Anisotropic Ferromagnet FePd

FePd is a ferromagnet with high magnetic anisotropy. It would be an attractive permanent magnet material if not for the expense of Pd. There is strong incentive to produce the analogous FeNi compound in bulk form, with the tetragonal and chemically ordered structure adopted by FePd (and FePt and CoPt). However, the kinetics of the Fe-Ni ordering is strongly reduced relative to Fe-Pd or Fe-Pt.

To gain insight into how the phase transformation from the cubic and disordered phase to the tetragonal and ordered phase can be favored, a neutron diffraction study was conducted at the Spallation Neutron Source at Oak Ridge National Laboratory. In this study, powder neutron diffraction data were collected as a function of applied pressure and over a temperature range that spans the order-disorder transition and the Curie temperature of FePd. This compound was chosen because it can easily be prepared in either the ordered or disordered state; therefore, it provides a good model system for studying this transformation. Determining whether pressure favors or disfavors the phase with good magnetic properties will help in designing synthesis strategies for FeNi.

Analysis of the data is still underway and follow-on diffraction studies are planned for the next experiment cycle at the spallation neutron and pressure beamline at the Spallation Neutron Source.

Conclusions

Significant progress has been made in understanding the origin of the increasing coercivity (with increasing temperature) of the ferromagnet MnBi, which may aid in development of future more powerful magnets with this property. Through study of the ferromagnet Hf_2Co_7 , progress has also been made on the new technique or high-magnetic

field processing, which may allow the generation of optimum microstructures for high magnetic performance. Technical reports summarizing these findings have also been submitted for publication. Finally, work has begun on a technique that may aid efforts at synthesis of the ferromagnet tetrataenite FeNi, which is likely to have favorable permanent magnet properties, but currently is only available in meteoritic form.

Catalysis

Introduction

Increasingly, high-efficiency engines are requiring development of new catalytic materials that are capable of achieving high conversion efficiency for criteria pollutants, particularly nitrous oxide (NO_x) (the primary criteria pollutant from diesel engines), at lower exhaust temperatures. Below follows a summary of both theoretical and experimental results in these areas.

Results

Catalyst by Design: First Principles Studies of Supported Catalyst to Guide Low-Temperature Catalytic Activity

We have employed a first principles study of the supported and zeolite catalysts to guide us in the design and synthesis of catalysts that are active at low temperatures. Our focus has been on single-supported atoms, a component of fresh catalysts (diesel oxidation, three-way, and lean NO_x), and low-temperature NH₃-SCR catalysts. The results are summarized in the following paragraphs.

The dependence of NO oxidation on platinum particle size is well known, with NO oxidation diminishing as the platinum particle sizes decrease. Because single supported atoms are the smallest possible clusters, it can be postulated that NO oxidation on such catalysts will be quite ineffective, especially because they are fully oxidized. Despite this concern, our first principles study predicts that NO oxidation on single supported Pt atoms can proceed via a modified L-H mechanism [Figure 6].

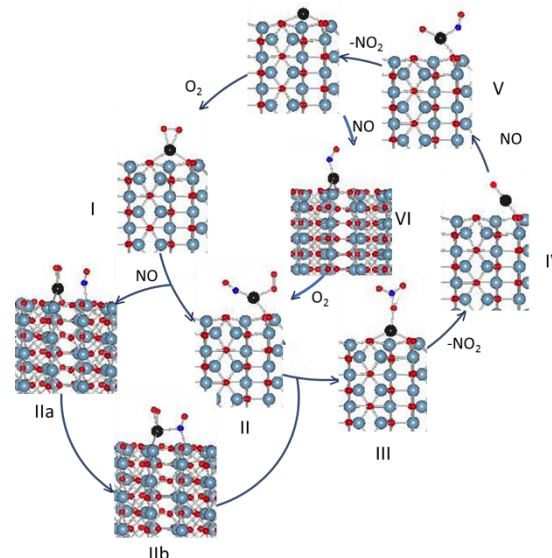


Figure 6. NO oxidation pathway over single supported atoms.

We have found that single supported Pt atoms are indeed catalytically active for NO oxidation and their turnover frequency is comparable to that of fully formed supported Pt particles (Table 1). A manuscript describing this work is in review for publication in *Nature Scientific Reports*. Our modeling study also predicts that supported Pd atoms will be superior to supported Pt atoms for NO oxidation. Work aimed at experimental validation of these predictions is in progress.

Table 1. Turnover frequency of single supported Pt atoms.

Catalyst Samples on θ -alumina	Pt _s (mol)	TOF ($\times 10^4$ / s) [†]		
		265°C	315°C	415°C
Single Pt atoms	$9.232e^{-7}$	1.8	2.7	6.2
Pt rafts (10-20 atoms)	$9.232e^{-7}$	2.0	4.2	7.1
10 nm Pt particles	$9.232e^{-7}$	2.9	4.7	6.6

[†]TOF was calculated based on Pt dispersion [mol NO_x/mol surface Pt (Pt_s)].

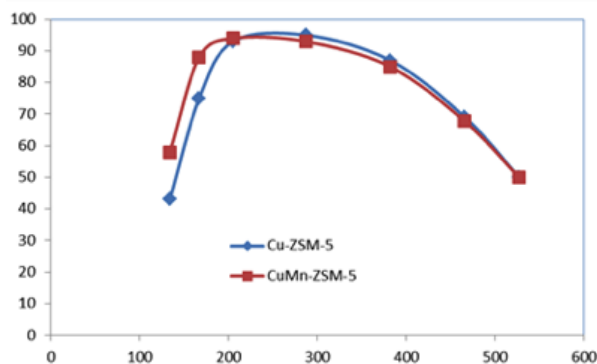
Experimental Work: Heterobimetallic Zeolite Catalysts

We are testing new catalysts for both on-road and off-road conditions and under fast and standard SCR conditions. A new catalyst, CuMn-ZSM-5, was synthesized by incipient wetness of Cu-ZSM-5 and subsequent calcination at 500°C for 4 hours. Importantly, a

comparison of NO_x reduction under off-road conditions of NH₃-SCR (gas hourly space velocity, GHSV of 50K h⁻¹) shows that CuMn-ZSM-5 has higher NO_x conversion activity at 150°C than Cu-ZSM-5, although there is no significant difference above 200°C (Figure 7, left graph). This result is different from that of CuFe-ZSM-5, which showed higher activity at high temperatures. It is likely that the high-temperature activity of CuFe-ZSM-5 is due to the iron component.

Under off-road conditions (Figure 7, right side), the presence of NO₂ has a dramatic impact on NO_x conversion. For example, about 82% of NO_x is reduced when NO and NO₂ are present in equal proportion, but NO_x conversion efficiency drops to about 28% when there is no NO₂. Even a small amount of NO₂ (12.67%) increases the NO_x conversion to 43% at 160°C.

Based on our previous work (Narula et al., *J. Phys. Chem. C*, 2012, 116, 23322), we expect a very similar behavior for NO_x conversion from CuMn-SSZ-13, with the added advantage of hydrothermal durability. We plan to synthesize CuMn-SSZ-13 and test it for NO_x conversion.



Conclusions

From theory, we have found that single supported Pt atoms are indeed catalytically active for NO oxidation and that their turnover frequency is comparable to that of fully formed supported Pt particles (Table 1). We also find from theory that supported Pd atoms will likely be superior to supported Pt atoms for NO oxidation. From our experimental work, we find that bimetallic CuMn zeolite catalysts have higher NO_x conversion than single metallic catalysts in the important temperature range between 150 and 200°C.

Publications and Presentations

Moses-DeBusk, M., M. Yoon, L. Allard, D. Mullins, Z. Wu, X. Yang, G. Veith, G. Stocks, and C. K. Narula, 2013, "CO Oxidation on Supported Single Pt Atoms – Experimental and Ab Initio Density Functional Studies of CO interaction with Pt Atom on θ -Al₂O₃(010) Surface," *J. Am. Chem. Soc.* **135**, 12634-12645.

Narula, C. K., L. F. Allard, G. M. Stocks, and M. M. DeBusk, 2014, "Remarkable NO oxidation on single supported platinum atoms," *Nature Scientific Reports*, (under review).

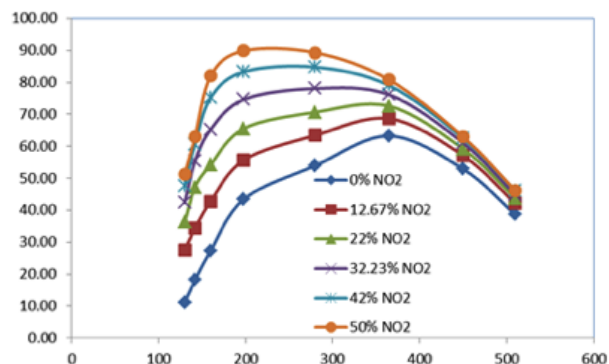


Figure 7. A comparison of CuMn-ZSM-5 with Cu-ZSM-5 (left) and the impact of NO₂ on NO_x conversion under off-road conditions (right).

Thermoelectric Materials

Introduction

The use of thermoelectric devices to convert waste heat in vehicle exhaust to electricity, if sufficiently high performance and low cost, may

offer substantial energy savings. We are developing improved materials using a science-based approach with a primary focus on materials for waste heat recovery. We use materials design strategies based on first principles calculations of electronic, vibrational and transport properties to identify potentially

low-cost, high-performance thermoelectric materials suitable for application in vehicles. We also calculate properties of existing materials as a function of doping and other parameters to obtain information needed for optimization of these materials. Our emphasis is on the thermoelectric figure of merit, ZT , at temperatures relevant to waste heat recovery and materials properties of importance in engineering thermoelectric modules, such as transport anisotropy and mechanical properties.

Results

In a published technical report (Parker and Singh 2014), we have identified lead chalcogenide PbS (a sister material to PbTe) as a material that is expected to show thermoelectric performance (measured as the figure-of-merit ZT) comparable to commercial PbTe at the highest waste heat recovery temperatures. The predicted ZT values are depicted in Figure 8 for both p-type and n-type. The plot depicts ZT values exceeding 1.7 for both p-type and n-type in the temperature range from 1000 to 1200 K, with the highest values potentially above 2. Such high ZT values mean that exhaust waste heat recovery using this material at these temperatures would be particularly efficient. In this work we also found, based on a review and analysis of published experimental data, that the mechanical properties of this material are expected to be much better than PbTe and, in fact, would rival that of the skutterudites (used in the General Motors DOE exhaust waste heat recovery project (American Physical Society News 2014)). This is important because the exhaust waste heat recovery environment is particularly harsh, with substantial thermal and mechanical stresses necessitating the use of mechanically robust materials. Finally, the ability to use both p-type and n-type high-performance legs from this material (unlike the skutterudites) is a substantial advantage for applications because it removes issues of asymmetric thermal expansion.

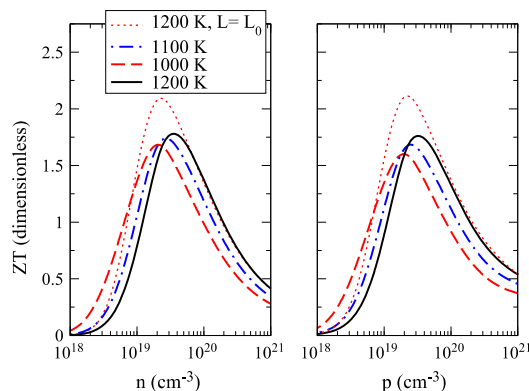


Figure 8. The calculated figure-of-merit of PbS at high temperatures for both n-type (left) and p-type.

Conclusions

We have identified the lead chalcogenide PbS as possessing high ZT values, as high as 1.7 to 2, between temperatures of 1000 and 1200 K for both p-type and n-type doping. We also found that this material has elastic properties far more favorable for applications than PbTe.

Publications and Presentations

American Physical Society News, 2014, "Applied Physics at the APS March Meeting," April 2014, p. 1.

Parker D. and D. J. Singh, 2014, *Solid State Comm.* **182**, 34.

Materials Needs for Ultra-High-Efficiency Heavy-Duty Engine Operation

Introduction

Heavy-duty internal combustion engines for the transportation sector are operating at increasingly high peak cylinder pressures (PCP) to achieve required increases in brake thermal efficiency. Current operating PCPs are 75 to 190 bar PCP, and the next decade could see over 300 bar PCP. Current materials, such as gray cast iron, are not adequate for the higher pressures and temperatures of future higher-efficiency engines. Understanding of near-cylinder stresses and materials properties that are necessary to enable desired engine

efficiency and power densities of future HD engines is lacking.

Numerical simulations offer insight into the cylinder environment at these conditions and can identify design needs and changes more rapidly than via experiment. The current practice of simulation can achieve low or high-dimensional modeling of the combustion environment or the cylinder/engine structure, but a fully coupled, high-dimensional computational fluid dynamics – finite element analysis (CFD-FEA) simulation of combustion, heat transfer, and consequential material temperatures and stresses is a fundamental development need.

Part of this limitation is the time and level of detail required to set up simulations. For FEA particularly, a proper meshing of complex geometries for high-fidelity calculation of materials stresses with conjugate heat-transfer can be very labor-intensive. However, with simplifications, a first-order estimate of future required materials properties can be gauged. This project employs an incremental process for this problem, starting with CFD results as inputs to FEA simulations.

Results

Heat-flux calculations from the CFD simulations were used in the FEA simulations at baseline and elevated pressures. Because of time limitations, the cases were not fully tuned to match available data, but this first-pass evaluation provides valuable insight; future work will match full loads. Figures 9 and 10 show calculated materials stresses in the engine head for the baseline and elevated-pressure cases, respectively. The four circular areas represent the intake and exhaust gas ports. Of particular concern in Figure 10 is the bridge between the exhaust ports (top and right), which see the highest, unacceptable stresses at elevated-pressure operation.

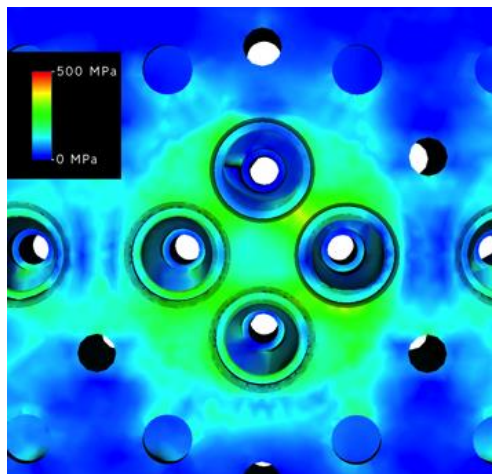


Figure 9. Materials stresses in engine head at baseline-pressure (192 bar) case.

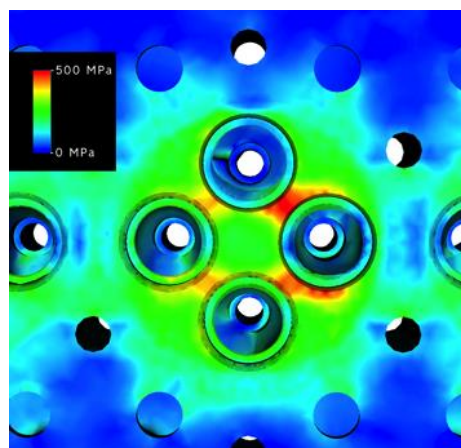


Figure 150. Materials stresses in engine head at elevated-pressure (300 bar) case. Note the high stress (red) between exhaust ports.

Conclusions

Based on yield stress in the first-pass analysis, the current generation of materials will not be sufficient for future generations of heavy-duty internal combustion engines. For a proper evaluation of future materials needs, a fatigue-life basis should be included; this will be the subject of ongoing research.

Project 21656 – Cast Alloys for Engines

Agreement 26021 – Development of Advanced High-Strength Cast Alloys for Heavy-Duty Engines

Richard K. Huff

Caterpillar Inc.

14009 N. Old Galena Road

Mossville, IL 61552-7547

Phone (309) 494-7349; fax (309) 578-2764; email: huffrk@cat.com

DOE Technology Manager: Jerry L. Gibbs

Phone (202) 586-1182; fax: (202) 586-1600; e-mail: jerry.gibbs@ee.doe.gov

Contractor: Caterpillar Inc., Mossville, Illinois

Prime Contract No.: DE-EE0005980

Objectives

- Develop new high-strength ferrous alloys to enable higher cylinder pressures for improved performance and fuel efficiency of heavy-duty engines.
- Provide at least 25% improvement in component strength relative to A842 compacted graphite iron (CGI).
- Identify a pathway to meet incremental cost targets of less than 120% of current A48 cast iron component costs.

Approach

- Use an Integrated Computational Materials Engineering (ICME) approach to computationally engineer new material compositions and manufacturing processes to achieve improved material performance.
- Use a system design approach that is focused on understanding the process-structure-property relationships.
- Focus the material design approach on improving and controlling the solidification nucleation, eutectic solidification growth, austenite decomposition products, and the precipitation of strengthening particles/phases.
- Produce experimental cast heats and conduct Design of Experiments (DoE) using specially designed test castings to produce a range of casting conditions present in the production of actual engine component castings.
- Conduct high-resolution three-dimensional (3D) x-ray tomography to identify and characterize graphite structures and distributions. Use scanning electron microscopy (SEM)/EDX with serial-polishing methods to determine chemical segregation and identify nucleants. Use in-situ x-ray investigations to study phase evolution from melts to understand the nucleation and growth mechanisms.

Accomplishments

- Completed tomographic data collection on several cast irons with various inoculants. Developed procedure for 3D reconstructions of graphite morphology from tomography data.
- Extended eutectic coupled zone model for multi-component alloys with considerations of phase fraction evolution during solidification.

- Identified graphite nucleants using electron microscopy methods (transmission electron microscopy [TEM]/SEM/energy dispersive x-ray spectroscopy [EDS]) and calculated inoculant potencies based on the disregistry of the nucleate and graphite lattices.
- Constructed casting DoE for nano-precipitation strengthening concepts based on sub-scale button results.

Future Direction

- Complete 3D reconstructions of graphite structures in various cast irons and establish correlations between graphite morphology and alloying and inoculant additions.
 - Determine inoculant mechanisms and potency of various compounds for nucleating austenite and graphite using lattice disregistry and interfacial energies calculations.
 - Refine alloy design concepts for enhanced thermal conductivity and strength and continue experimental DoEs.
 - Using high-energy x-rays, investigate phase evolution from iron melts in a time resolved manner.
-

Introduction

Today, customers are demanding heavy-duty engine manufacturers to develop and produce engines with lower weight and improved efficiency to reduce fuel consumption, emissions, and costs associated with vehicle use without sacrificing performance and productivity. Resource limitations leading to rising fuel costs and concern about environmental effects are rapidly increasing the need for these improvements. A significant challenge for heavy-duty engine manufacturers to meet these customer requirements is cost-effective material solutions for engine blocks and heads.

Because of the high number of loading cycles an engine experiences over its life, improving the high-cycle fatigue properties over the current materials is key to improving engine efficiency. Thus, the Department of Energy target fatigue strength of 31 Ksi (214 MPa) will be used as the primary objective. Secondary goals will be to achieve increased yield and tensile strengths in the new alloys. Another important property is thermal conductivity. A high thermal conductivity can lower the thermal gradients in the component and reduce the stress ranges a component must endure. The challenges to meeting these objectives will be the machinability and castability of the material because these will be the primary drivers of production costs.

Current higher strength cast irons are difficult to cast in complex shapes with thin walls, have lower thermal conductivity, and can require expensive heat treatments in addition to the higher casting costs. Over the years, improvements in cast iron materials have largely occurred by accident. The austenite-graphite eutectic solidification is still not completely understood and can be difficult to control in practice. This project aims to fully study the solidification of cast iron materials and use a state-of-the-art integrated computational materials engineering approach to optimize alloy design to improve key properties.

In most alloys, the grain/cell size is an important factor influencing the fatigue strength of the material. This is also the case in cast iron.

Caterpillar has demonstrated a strong correlation between fatigue strength and eutectic cell size. Unique in cast irons is the strong influence of the graphite size and shape on the fatigue performance. This can be understood by the fact that fatigue failures initiate at the graphite structures and propagate through the cells along the flakes. The larger the cell size, the larger the initiation sites and crack propagation paths. The shape of the graphite structures influences the stress field around the graphite. Flake-type graphite acts more like a preexisting crack, while round-shaped graphite lowers the stress concentration and improves fatigue performance. As cracks nucleate and grow, they will eventually have to connect by propagating through the matrix, ultimately leading to a failure. Matrix hardness is a result of the austenite decomposition products and will significantly influence the strength of the different cast iron materials.

The project team is focusing on refining the cell/grain size in the material by optimizing the inoculation and treatment to maximize the number of nuclei during solidification. The project team is concentrating on alloy regimes that result in compacted and spheroidal graphite shapes and maximize the matrix strength. In addition to alloying and inoculation of the iron, novel casting methods can be explored to better control the cooling rates during solidification and the eutectoid transformations. Secondary thermal processing is another approach to modify the austenite decomposition to achieve preferred phases with improved properties or precipitate strengthening particles/phases in the matrix.

Results

Experimental Nucleant Identification

The inoculation process in cast iron can be described as the addition of elements that will form sufficient nucleation sites for the dissolved carbon to precipitate as graphite rather than iron carbides. Currently, the effectiveness of an inoculant is determined by the discrepancy between the inoculant and graphite. A number of new techniques have been explored that will enable a more efficient and comprehensive analysis of the nucleants within cast iron alloys.

The identification of nucleants within graphite particles will be used to further understand the origins of graphite size and morphology via inoculant potency determinations.

Serial sectioning in the focused ion beam SEM was used, with the goal of isolating a nucleant particle in order to better understand its morphology and chemistry. While using deep etching allowed immediate access to the nodule without having to cut through the iron matrix, the graphite particles have a low sputter yield and a consequently low material removal rate, making this a prohibitively time consuming process.

Micro-beam x-ray fluorescence analysis is another technique that was tried to probe the chemical information of the graphite core. The attenuation length for carbon and iron at this energy is about 5 mm and about 20 μm , respectively. This high penetrating depth of synchrotron x-ray enables detection of the elements below the sample surface, eliminating the need for focused ion beam or other sectioning methods. The incident x-ray will energize the electrons in atoms and emit unique fluorescence light for each element present.

Several graphite particles, both nodular (NG) and vermicular graphite, were examined. A Ca-rich core was found in an NG (Figure 1). Further mapping of the area near the center ($10 \mu\text{m} \times 10 \mu\text{m}$ area with a step size of $2 \mu\text{m}$) clearly shows the distribution of the Ca at the center of the NG. The size of the Ca-rich particle is about $4 \mu\text{m}$ in diameter and the size of the NG is about $45 \mu\text{m}$. The result also suggests that the core contains not only Ca, but also a small amount of Fe. Unfortunately, the experimental setup is not sensitive for lighter elements such as Al, Si, S, and Mg. Also, it takes about 8 to 14 hours to scan an $80\text{-}\mu\text{m} \times 60\text{-}\mu\text{m}$ area; thus, it is also not a feasible choice to study CGI.

SEM coupled with EDX is probably the most common way to study the nucleus of graphite in cast iron. The sample is usually sliced mechanically and polished, and the SEM is used to show the morphology of the graphite particle and locate the region of interest. Then the EDX technique steps in to obtain the chemical information of the nucleus. An

example is shown in Figure 2, where the element map indicates the nucleus of the small NG particle is a rare earth sulfide (Ce/La)S.

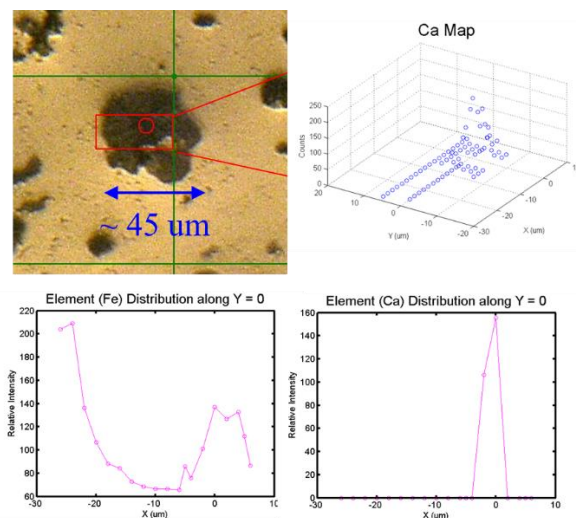


Figure 1. Chemical mapping of NG. The top-left figure shows the measured grid and the top right figure is the corresponding map for Ca (top). The bottom figures are the distribution of Fe and Ca from the edge of the graphite to the core.

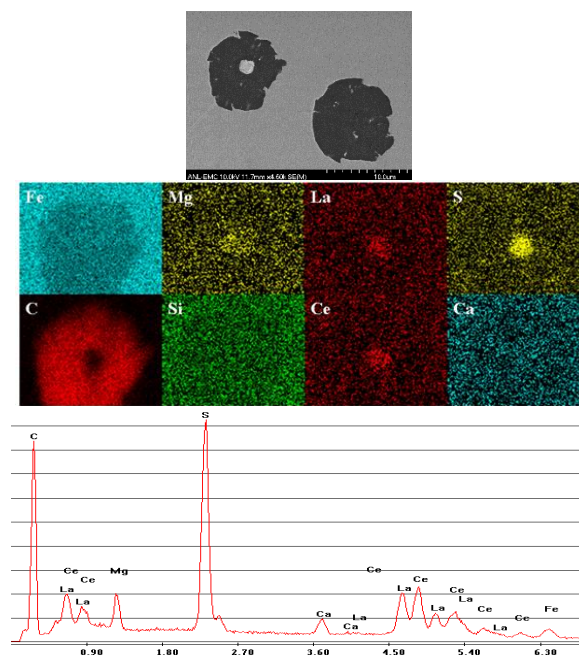


Figure 2. Elements mapping of Type-III NG in a Bi-inoculated sample. The type-III NG has the smallest size among three. Its average diameter is around $10 \mu\text{m}$ and its core contains a high concentration of rear earth elements and sulfur.

These techniques have been successfully used to identify different types of nuclei in various sampled alloys. Generally, nuclei have been characterized by three types in NG particles. The chemical information and the character of these nuclei are summarized in Table 1. More details regarding the analysis of the results can be found in the Fiscal Year (FY) 2014 quarterly reports.

Table 1. Types of nucleus of NG in Bi-inoculated cast iron.

Nucleus Type	Chemistry	Characteristics
Type-I	Mg/Si/Al + S/Ca	Has the largest size, but low sphericity
Type-II	Mg/S + Ca	Has the highest sphericity, and medium size
Type-III	(La,Ce)/S + Mg/S + Ca	Usually small (<10 um in diameter)

The Eutectic Coupled Zone

During the past year, a refined model for the growth of multicomponent eutectics has been developed. For the first time, such a model accounts for the change of phase fractions (austenite, graphite) during solidification of eutectic microstructures at either eutectic or off-eutectic compositions. Details on the derivation of this model for multi-component systems have been reported in the first quarter report for FY 2014. The main equations resulted from the derivation can be summarized as follows:

Growth undercooling:

$$\Delta T = \sum_{j=2}^{N_{elems}} m_{\gamma,j} \left(1 - \frac{1}{\eta_{\gamma} \cdot k_{\gamma,j} \cdot f_{\gamma}^o} \right) \cdot C_j^{\infty} + \frac{K_r^{\gamma,o}}{\lambda} + \left(\frac{K_r^{\gamma'}}{\lambda} - \sum_{j=1}^{N_{elems}} m_{\gamma,j} \cdot H_{o,j} \right) \cdot \Delta f_{\gamma} \tag{1}$$

Average eutectic spacing:

$$\lambda_{av} = f_{\gamma}^o \cdot \sqrt{\frac{K_r^{gr,o} - K_r^{\gamma,o}}{V \cdot P_{\gamma}^o \cdot \sum_{j=1}^{N_{elems}} \frac{m_{gr,j} \cdot A_j}{D_{L,j}}}} \tag{2}$$

where N_{elems} is the number of elements in the chemical composition, C_j^{∞} is the initial

concentration of element j , $m_{\gamma,j}$ and $m_{gr,j}$ are the liquidus slopes of element j for austenite and graphite respectively, $D_{L,j}$ is the liquid diffusion coefficient of element j , f_{γ}^o is the fraction of austenite in eutectic microstructure at the equilibrium eutectic temperature, Δf_{γ} is the change of austenite fraction at solidification temperature, and V is the growth velocity of eutectic microstructure. The other quantities appearing in Equation 1 and 2 are material parameters that were defined in the first quarter report for FY 2014.

The new model was validated by the available literature data for binary Fe-C and ternary Fe-C-0.5wt%Si and as recent experimental measurements performed at the University of Alabama at Birmingham. From the experiments, the observed solidification microstructures and the calculated eutectic spacing (measured L_{exp} and calculated L_{calc}) corresponding to the imposed solidification velocity V are presented in Table 2. For these results, Sample 1 is slightly hyper-eutectic and the others are slightly hypo-eutectic. Strong agreement between measured and calculated eutectic spacing can be observed in this table, thus validating the theoretical model.

Table 2. Growth velocity, average eutectic spacing, and solidification microstructures of samples processed at the University of Alabama at Birmingham.

Sample ID	V ($\mu\text{m/s}$)	L_{exp} (μm)	L_{calc} (μm)	Micro-structure
#1	1.0	31.2	29.20	Austenite dendrites+ eutectic
#2	0.5	54.4	55.63	Eutectic
#3	0.5	47.2	49.19	Eutectic
#4	0.5	47.9	54.20	Eutectic

^a a standard deviation of about 5.6 μm was reported

Influence of Chemical Composition on Eutectic Growth

The eutectic growth model was applied to cast iron alloys of various chemical compositions in order to evaluate the effect of

chemistry on the growth behavior of the alloy. Figure 3 shows the calculated growth velocity as a function of undercooling for two alloys of eutectic chemistry: binary Fe-4.26wt% C and ternary Fe-3.67wt% C-1.9wt% Si. There are two main aspects that can be observed on this figure:

11. The eutectic growth velocity, V , is proportional with the square power of growth undercooling ΔT , *i.e.*:

$$V = \mu \cdot \Delta T^2 \quad (3)$$

where the proportionality factor, μ , is known as the *eutectic growth coefficient*. The growth behavior described by Equation 3 is also one of the results of the classic theory for binary eutectics.

12. A multicomponent eutectic alloy, such as Fe-3.67wt% C-1.9wt% Si, follows the same growth behavior described by Equation 3, but with a growth coefficient μ different from that of a binary alloy. It can be observed on Figure 3 that for this particular ternary alloy, the growth velocity is decreased by Si addition.

Furthermore, if growth of eutectic microstructure is considered for alloys of hypoeutectic compositions, a behavior similar to that described in Figure 3 can be observed (Figure 4). In Figure 4, it is apparent that eutectic microstructures at hypo-eutectic composition grow slower comparing to those of eutectic composition.

A more detailed description of the variation of the growth coefficient μ , and of the eutectic growth velocity, with the chemistry of the alloy, is presented in Figure 5. Once more, it can be observed that μ keeps decreasing as the chemistry (represented by the carbon equivalent, C_{eq}) is more and more hypo-eutectic. Also, the Si additions decrease μ while Mn additions do not seem to have a significant influence on μ . A regression analysis performed on the data presented in Figure 5 shows the following quantitative relationship between μ and the content of alloying elements:

$$\mu = 4.552 \cdot 10^{-8} \cdot \%C + 5.583 \cdot 10^{-9} \cdot \%Si - 1.163 \cdot 10^{-10} \cdot \%Mn - 1.0272 \cdot 10^{-7} \quad (4)$$

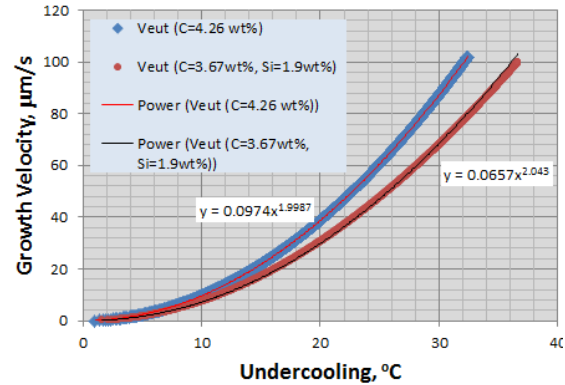


Figure 3. Calculated growth velocity as a function of undercooling for Fe-4.26 wt% C and Fe-3.67 wt% C-1.9wt% Si eutectic alloys.

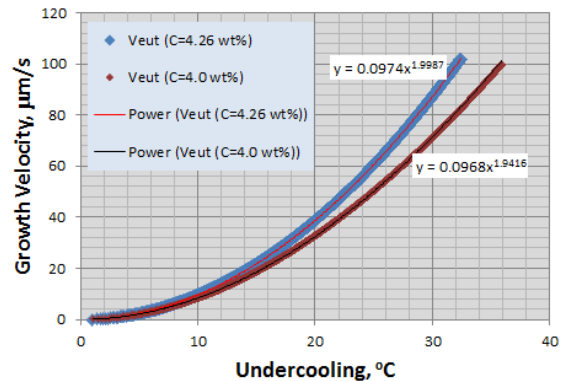


Figure 4. Calculated growth velocity as function of undercooling for eutectic Fe-4.26 wt% C and hypo-eutectic Fe-4.0 wt% C binary alloys.

Chemistry Influence on the Limit of Eutectic Coupled Zone (LECZ)

The currently calculated growth velocity of the LECZ for binary Fe-C alloys is presented in Figure 6. These values were compared with calculations published by Jones and Kurz (JK). The current calculations agree well with those of JK only at the eutectic composition ($C=4.26\%$). At this time, it is thought that the disagreement at off-eutectic compositions arises from the fact that a unique value of the eutectic growth coefficient μ was used by JK, which was the value determined experimentally at eutectic composition. Chemistry-dependent values of μ were used to produce Figure 6.

For a multi-component system of chemistry typical to the commercial gray iron (Fe-C-1.9 wt% Si-0.6 wt% Mn) the calculated LECZ

velocity is presented in Figure 7. At the eutectic composition, which for this alloy is 3.687 wt% C, the calculated LECZ velocity is only 1.6 $\mu\text{m/s}$. This value is much lower than that corresponding to the eutectic Fe-C binary, which was calculated as 6.2 $\mu\text{m/s}$. Thus, it can be concluded that the alloying elements, especially Si, contribute to promoting the dendritic-like growth of the austenite, thus leading to graphite refinement at cooling conditions less severe comparing to the binary Fe-C alloy.

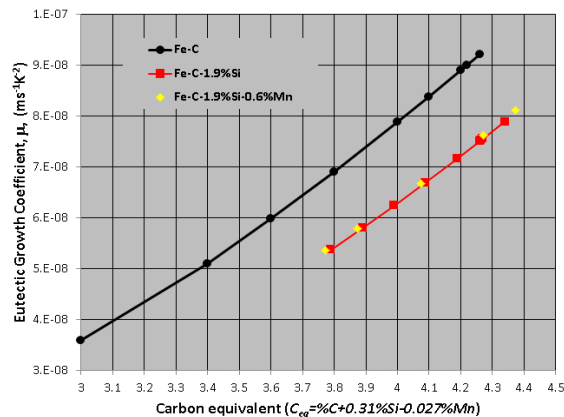


Figure 5. Calculated variation of the eutectic growth coefficient, μ , with the chemistry (carbon equivalent) of cast iron.

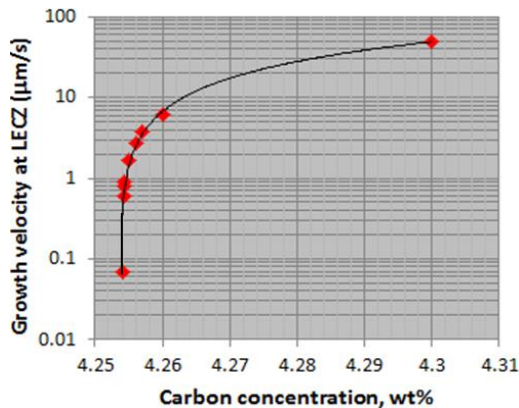


Figure 6. The calculated LECZ velocity for binary Fe-C alloys.

Process-Structure-Property Relationships

The project team is using a system design approach that is focused on identifying and quantifying the process-structure-property relationships in advanced high-strength cast iron

materials. To support this effort, 10 heats of experimental material weighing about 4,000 lb were cast into 36 step block castings (Figure 8). The step blocks provide a range of cooling rates during solidification that are representative of what can be expected in an actual engine component. These castings have generated representative material for three DoEs and three midpoint studies.

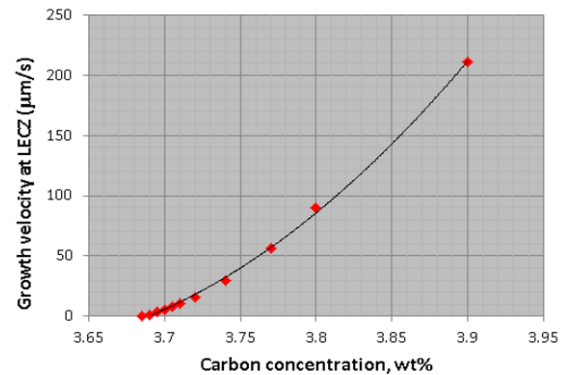


Figure 7. Calculated LECZ growth velocity for the system Fe-C-1.9 wt%Si-0.6 wt%Mn

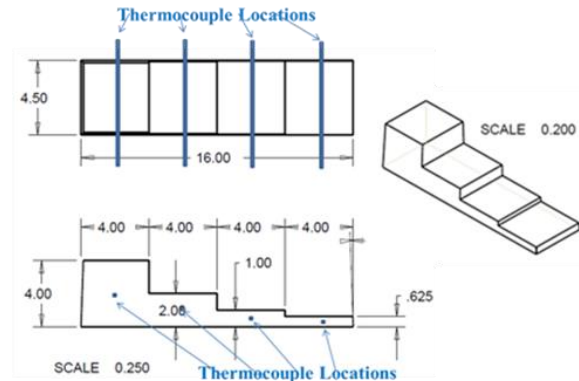


Figure 8. Schematic of step block casting.

An initial DoE1 was created to study the influence of post-inoculant treatment on the final structure of CGI with respect to final nodularity and graphite size or cell size as appropriate. Post-inoculants containing austenite nucleating constituents (labeled “A”) and two different types of graphite nucleating constituents (labeled “G1” and “G2”) were used. One test without a post-inoculant was also tested as a baseline. The results of this test (see Table 3) showed the need for graphite promoting post-inoculation as samples poured without post-inoculant or with

only the austenite inoculant had evidence of carbide formation, which is not desirable for this material. All of the castings were a pearlitic CGI structure.

Table 3. Summary of DoE1 samples collected from Sandwich Trials #8 and #9.

Heat No	Mold No	In-stream inoculant	Graphite	Eutectic carbide	Matrix
8	1	A	CG	Yes	Mostly Pearlite
8	2	G1	CG	No	Mostly Pearlite
8	3	None	CG	Yes	Mostly Pearlite
8	4	A+G1	CG	No	Mostly Pearlite
9	1	A (Duplicate)	CG	Yes	Mostly Pearlite
9	2	G1 (Duplicate)	CG	No	Mostly Pearlite
9	3	A+G2	CG	No	Mostly Pearlite
9	4	G2	CG	No	Mostly Pearlite

Several microstructure characteristics are measured (e.g., the graphite number density is shown in Figure 9) to characterize the structure of each sample. In this case, the step blocks containing the “G2” post-inoculant (i.e., 9.3 and 9.4) have the highest graphite number density. The tensile strengths for the DoE1 samples are shown in Figure 10. The samples with the highest graphite number density do not necessarily exhibit higher strength values. Contrary to NG, where higher nodule counts typically lead to improved properties, in CGI the high graphite density in the two-dimensional (2D) samples may indicate a higher volume fraction of graphite. A higher volume fraction of graphite would lead to reduced mechanical properties. This illustrates the complexity with characterizing the structure using 2D metallography. Many different measurements are still being made to fully characterize the chemistry, structure, and properties for each sample and analyze the relationship to the strength.

A second DoE2 was conducted to explore maximizing the thermal conductivity in very high-strength NG iron. The study was specifically looking to optimize the amount of silicon and various pearlite stabilizers in the alloy. Sample results from the graphite analysis are shown in Figure 11.

As can be expected, the samples with the highest nodule count had the highest nodularity because small nodules have better roundness. The ferrite fraction is shown in Figure 12.

Sample 11.1 has very low alloy levels and both Samples 11.3 and 11.4 had high silicon, which explains the higher percentage of ferrite in these samples.

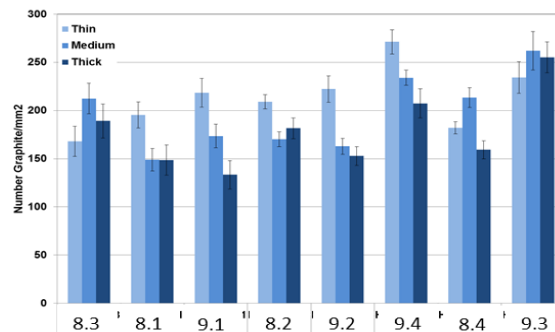


Figure 9. Comparisons of graphite number density for different in-stream post inoculants.

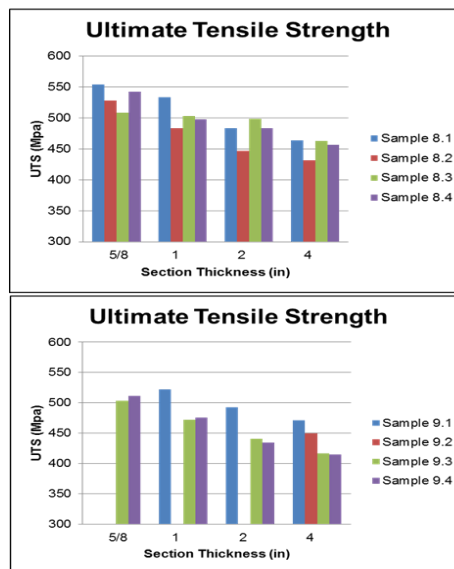


Figure 10. Comparison of ultimate tensile strength for different in-stream post inoculants.

Figure 13 shows the tensile strength for each sample measured in the 5/8-in. and 4-in. thick sections. It should be noted that, while these strengths are very high, these values are still the minimum strength, because there were many thread failures in the tensile specimens. The stress concentration in the threads results in higher stresses in the failure zone than the reported stresses, which were measured in the gage section. Larger thread diameter specimens are being machined to better measure the strength of these alloys.

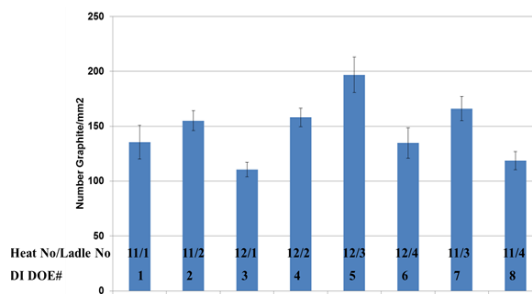


Figure 11. Comparison of graphite nodule count (interface of 0.625-in. and 1-in. sections) for ductile iron with varying alloy content.

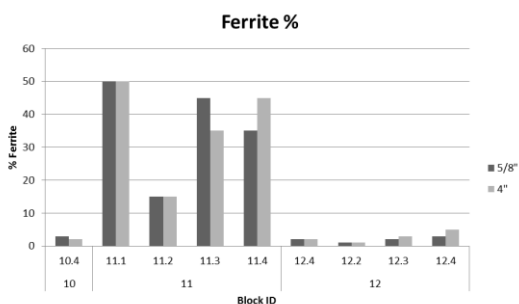


Figure 12. Comparison of the fraction of ferrite for DoE2 samples with varying alloy content.

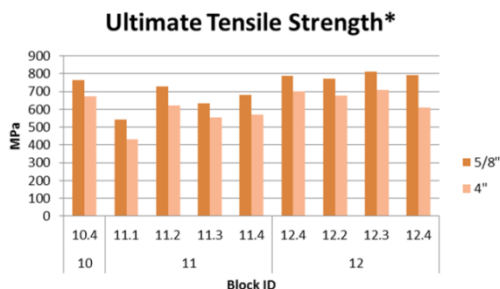


Figure 13. Comparison of the fraction of ferrite for DoE2 samples with varying alloy content.

A midpoint study on the level of magnesium treatment necessary to achieve a CGI structure for alloys with elevated levels of aluminum and sulfur was conducted. The result of this study found a suitable target for the third DoE3, which was run to determine the effect on CGI structures of alloying with aluminum, sulfur, and using various inoculants and different inoculation levels. The aim is to achieve a refined structure by appropriate choice of alloy level and inoculation treatment. These casting are poured and the preliminary analysis

completed. Specimens are now being machined for mechanical testing.

3D X-Ray Tomography

As has been demonstrated, structure characterization with 2D metallography may not be sufficient to reveal the full structure-property relationships. The project team is using the advanced photon source at Argonne National Laboratory to conduct 3D tomography of CGI samples. The goal is to characterize the complex 3D shapes of the graphite and better understand the nucleation and growth of the various graphite structures.

A sample of Caterpillar’s production CGI was characterized to establish a baseline. After tomography measurement, the same sample was mechanically sliced and polished; a distinct feature on the polished surface was then selected under SEM. To further validate that the nondestructive tomography measurement can provide the same information as from metallography, each 2D image from the 3D tomography was reviewed to find the exact same features. The result of the comparison is very encouraging. The SEM image of the feature is shown in the left of Figure 14 and the corresponding 2D tomographic image is shown on the right. The comparison in Figure 14 clearly shows the tomography provides almost identical image as the SEM. There is a NG indicated by red arrow and a bird-like CG circled by the yellow arrow. The image from tomography is slightly blurred due to a lower resolution. Although the expected spatial resolution of the tomography is about 1 μm, the real resolution is estimated around 2 to 4 μm, which is good enough to reveal the graphite morphology with acceptable details in cast iron.

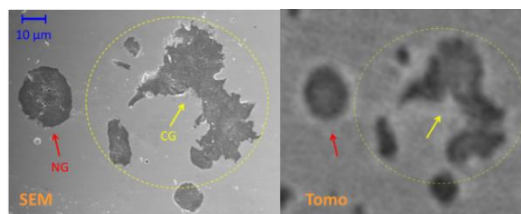


Figure 14. SEM image of a NG and CGI on the mechanical polished surface (right) and the corresponding tomography image of the same

feature inside the material prior to mechanical slicing.

3D models of the particles were built subsequently from a series of 2D images. Figure 15 shows the 3D graphite morphology near the sliced surface (in Figure 14). The graphite structure beneath the polished surface is revealed on the left hand side of Figure 15 and the right-hand side image is the structure that has been removed during mechanical polish. In addition to the shape of the particle, the image shows a dense region inside the core of the NG (red arrow), indicating that there are heavy and non-carbon elements at the core, but the exact chemical information of the core is unknown from the image itself.

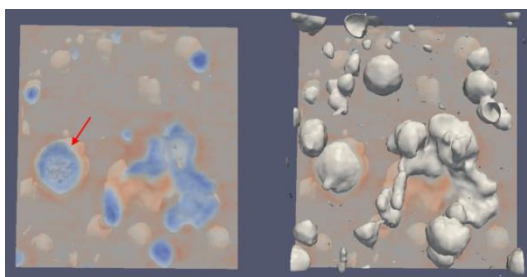


Figure 15. 3D reconstructed model of the NG and CG below (left) and above (right) the 2D section is shown in Figure 16.

The analyzed volume in Figure 15 is roughly $150 \times 150 \times 50 \mu\text{m}^3$, and cannot reveal an entire individual CG structure; therefore, the size of the analyzed area was expanded to $1,002 \times 548 \times 340 \mu\text{m}^3$. Image processing and segmentation techniques were used to separate and isolate each individual particle within the volume, identifying 3,470 particles isolated particles. To have a clearer picture of the CG structure, only the three largest CG particles in this volume and the 3D morphology is presented in Figure 16. It clearly shows the CG tree can span at least $500 \mu\text{m}$. It is not clear how large a CG tree can be at current stage, because size of the volume being analyzed is limited by computing power.

Geometrical analysis was performed on all of the individual 3,470 particles in the analyzed region and the volume, surface area, and sphericity of each individual particle were calculated. The particle distribution as a function

of sphericity and the size distribution of NG are shown in Figure 17. Here, we define NG as a particle with sphericity greater than 0.48. In principle, the sphericity of a perfect sphere is 1.0, the smaller the sphericity, the more deviation the shape of the particle is from a sphere. However, due to the size of the voxel used, the sphericity of even a perfect sphere is only ~ 0.7 . The criterion, 0.48, was determined empirically after manually reviewing several particles in 3D. Based on this value, it was found that greater than 90% of the particles were NG, and most of the NGs are 10 to $20 \mu\text{m}$ in diameter. The statistical analysis of the particles shows the nodularity of this sample is about 30%. It can be seen that 3D analysis is required to determine the correct morphology, connectivity, and distribution of the characteristic features.

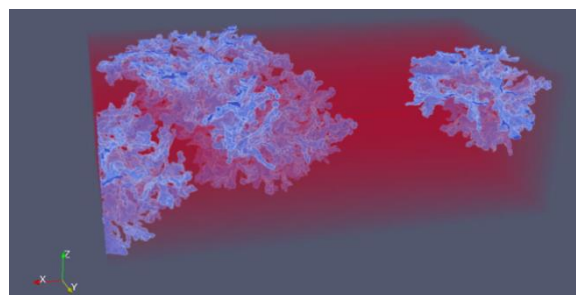


Figure 16. The three largest CGI particles in the analyzed volume. It clearly shows most of the CG has an interconnected tree-like structure that can span millimeters in the matrix.

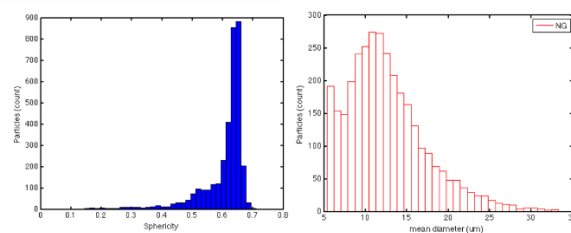


Figure 17. Quantitative analysis of the graphite morphology. The left is the particle distribution as a function of sphericity and the right is the size distribution of NG.

Nanoprecipitation Strengthening

The idea of strengthening the pearlitic iron matrix during post-solidification anneal/stress-relief heat treatments is being explored,

both theoretically and experimentally. Building on the successful use of Cu-rich strengthening phases in high-strength steels, the feasibility of applying Cu-based precipitate strengthening to cast iron is being examined. Strengthening effects of Cu-Mn-Al, Cu₃Al, and Cu-Ni-Al precipitates precipitation have been analyzed in the current year.

Cu-Ni-Al precipitates target the region between the well-known B2 NiAl phase and the Cu₃Al phase. Strengthening responses at temperatures corresponding to typical stress relief treatments were examined as a function of tempering time and temperature in Figure 18, and the nanostructures were examined via atom-probe tomography. The highest hardness peaks were found for the Cu-Ni-Al concept at relevant temperatures.

Current DoEs will expand this to look at strengthening using Cu-Ni-Al precipitates in actual base cast iron compositions and typical casting cooling conditions to investigate the potential effect of ferrite strengthening in mostly pearlitic microstructures. Additional possible precipitate strengthening phases have been identified using high-throughput DFT calculations. These concepts will be evaluated using sub-scale prototype fabrication and hardness testing followed by casting DoEs for successful concepts.

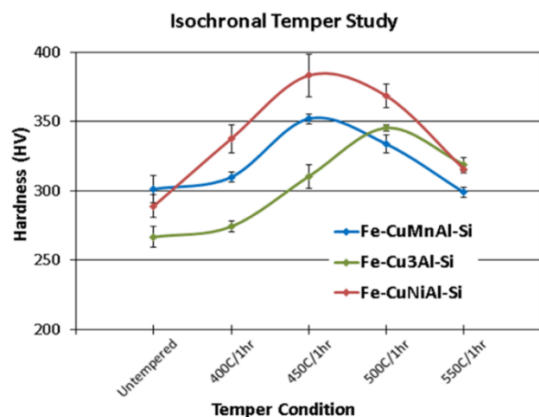


Figure 18. Isochronal temper study of three precipitation concepts at 1-hour aging for each temper condition.

Summary and Next Steps

Identification and classification of graphite and nucleant particles, visualization of complex 3D graphite structures, and the extension of the eutectic growth model have been significant accomplishments in the effort to better understand the solidification of cast iron. The team will continue using advanced modeling and experimental characterization approaches (such as high resolution x-ray tomography) to investigate approaches to control the microstructure and identify high potential candidates for achieving improved properties. In-situ solidification experiments using x-ray tomography and radiography are starting in the first quarter of FY 2015 in an effort to better identify and validate the mechanisms controlling nucleation and growth of the microstructure phases. Casting DoEs will continue to further investigate the high potential alloy candidates.

References

- A. Saha and G. B. Olson, 2007, *J Comput Aided Mater Des* 7(14): 177.
- D. Isheim et.al, 2006, *Acta Mater* 54: 841.
- H. Jones and W. Kurz, 1980, *Metall. Trans. A*, 11A: 1265–73.
- H. Jones and W. Kurz, 1981, *Z. Metallkunde*, 72: 792–797.
- P. Magnin and W. Kurz, 1988, *Metallurgical Transactions A*, 19A:1955–1963.

Project 21656 – Cast Alloys for Engines

Agreement 26473 – Computational Design and Development of a New, Lightweight Cast Alloy for Advanced Cylinder Heads in High-Efficiency, Light-Duty Engines

Mike J. Walker
General Motors Research and Development Center
30500 Mound Road
Warren, MI 48090-9055
Phone (586) 651-3757; email: mike.j.walker@gm.com

Qigui Wang
General Motors Powertrain Division
823 Joslyn Avenue
Pontiac, MI 48340-2925
email: qigui.wang@gm.com

DOE Technology Manager: *Jerry L. Gibbs*
Phone (202) 586-1182; fax: (202) 586-1600; e-mail: jerry.gibbs@ee.doe.gov

Contractor: General Motor, LLC, Michigan
Prime Contract No.: DE-EE0006082

Objectives

- To develop new lightweight alloys that provide a 25% improvement in component strength made with A319 or A356 aluminum and measured using standard materials characterization techniques. Cost targets for components manufactured utilizing the new materials are not to exceed 110% of the baseline alloys.

Approach

- Utilize computational materials engineering tools to accelerate the development of new alloys. Throughout the project a gap analysis will be conducted on the tools to identify future computational needs. All computational methods are being validated through trial castings and experimental methods.

Accomplishments

- Carried out 324 global engine thermal cycle, global engine durability, and fatigue analysis simulations to determine the optimum material properties for high-performance engine heads (Fiscal Year [FY] 2014).
- Defined a ranked set of alloy property requirements based on the above simulations. Ranked properties include castability, thermal conductivity, low and high fatigue strength, tensile strength, yield strength, and plastic elongation. Properties are evaluated at room temperature and at high temperatures up to 300°C (FY 2014).
- Performed 500 precipitate growth simulations of concept alloys in aluminum using PrecipiCalc® software (FY 2014).
- Conducted 5,000 density functional theory (DFT) calculations, including defect energy calculations, interfacial calculations, and enthalpies of formation (FY 2014).

- Performed 600 thermodynamic simulations of phase, Scheil, and equilibrium step diagrams (FY 2014).
- Defined a set of eight alloy concepts for further investigation and refinement based on their ability to meet the set of alloy property requirements (FY 2014).
- Manufactured concept alloy buttons and performed isothermal and isochronal hardness tests (FY 2014).
- Performed both scanning electron microscopy and transmission electron microscopy (TEM) analyses of concept alloy samples for heat treatment procedure and precipitate structure optimization (FY 2014).
- Conducted precipitate atomic structure analysis of some concept alloy samples using local electrode atom probe (LEAP) tomography (FY 2014).
- Carried out mechanical testing of over 450 (72 in 2013 and 378 in 2014) tensile specimens at room and elevated temperatures (FY 2014).

Future Direction

- Create parametric designs of alloys. Parametric designs will introduce elemental modifications to alloy concepts for improvement of thermal, mechanical, and physical properties, as well as castability.
 - Develop final alloy chemistry and process and produce laboratory-scale test casting plates and full-scale head castings. Measure tensile and fatigue properties. Establish chemistry and heat treatment tolerances for the optimal alloy(s).
 - Conduct full recyclability analysis of the optimal alloy(s).
 - Develop alloy and process cost models for full production implementation using the new high-temperature capable aluminum alloy (s).
-

Abstract/Executive Summary

This collaborative project between General Motors, QuesTek Innovations LLC, Northwestern University, Massachusetts Institute of Technology, Camanoe Associates, AFS, and Dr. Fred Major is using Integrated Computational Materials Engineering (ICME) tools, expert knowledge, and experimental validation to accelerate the development of an alloy capable of handling the higher temperatures and pressures used in smaller, more efficient engines.

During FY 2014, General Motors and its partners determined the optimum material properties required for advanced cylinder heads in high-efficiency and light-duty engines. Among many physical and mechanical properties evaluated, thermodynamic conductivity, cyclic hardening coefficient K' , cyclic hardening exponent n' , and low-cycle and high-cycle fatigue strength at 150°C and higher are most important. Using ICME tools, the team has developed eight alloy concepts and their associated heat treatment procedures that may contribute to achieving these properties. To date, two alloy concepts and their variants have been cast, heat-treated, and mechanically tested in tension at room and elevated temperatures. The detailed precipitate structure and thermal kinetic behavior of those concept alloys have been evaluated using LEAP tomography, TEM, and scanning electron microscopy imaging.

Introduction

The U.S. Department of Energy's (DOE) Energy Efficiency and Renewable Energy Program is targeting a 25% lighter powertrain by 2025 and a 40% lighter powertrain by 2050. As a result, the engine power density will be increased significantly. This will result in higher exhaust temperatures and a doubling of the cylinder peak pressures by 2050. To meet these requirements and achieve the stated goals, the properties of state-of-the-art materials (such as cast aluminum alloys) must increase substantially. Historically, it has taken about 10 years to develop and implement a new alloy

and it has taken about 100 years to improve the performance of a material such as cast aluminum by 50%. Thus, traditional methods of experimental trial and error are no longer sufficient. Fortunately, both computational and analytical methods have been vastly improved in the last few decades. ICME and advanced analytical tools (such as focused ion beam microscope, high resolution scanning transmission electron microscope, and LEAP experimental techniques) are now available to accelerate the timeframe to develop new alloys. Combining ICME with expert knowledge from the field and judicious experiments for validation and confirmation is the quickest way to achieve the goals of a new high-temperature capable aluminum alloy for head production.

Approach

State-of-the-art ICME tools (such as first principles calculations, computational thermodynamic and kinetic models, virtual casting modules, and commercially available casting process simulation and structural and durability analysis software) will be used to design a new, lightweight cast-alloy with ideal multi-scale microstructures and minimum tendency for casting defects to achieve the desired high-temperature strength and fatigue performance requirements in complex castings. The *iCMD*[™] platform is used in this project to develop concepts, perform modeling, validating, and progressing to a more refined state. QuesTek's proprietary *iCMD*[™] platform is a core modeling software system that integrates proprietary and commercial mechanistic modeling tools to facilitate rapid design and development of new materials (see Figure 1).

General Motors' Virtual Cast Component Development Program uses an integrated state-of-the-art modeling and simulation methodology for cast aluminum components, starting from computational alloy and casting design through casting and heat treatment process modeling and multi-scale defect and microstructure simulation, and culminating in casting property and durability prediction (see Figure 2).

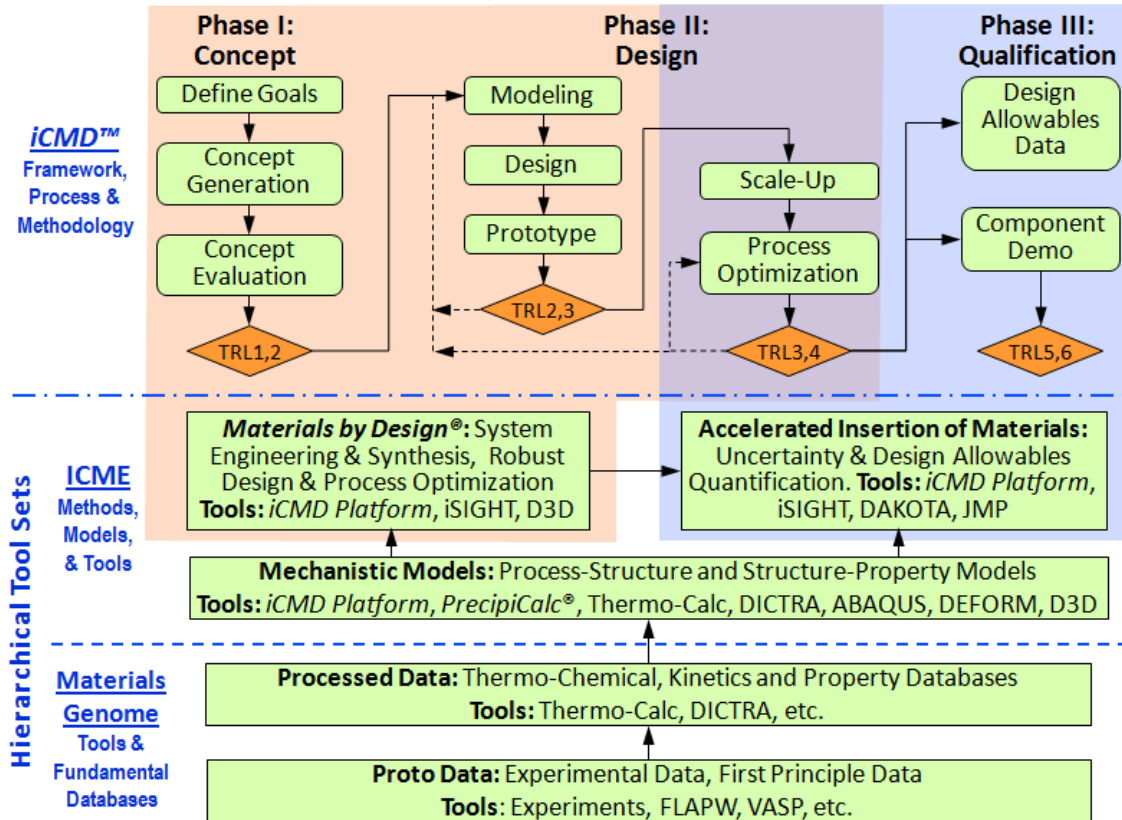


Figure 1. QuesTek’s iCMD and ICME technology.

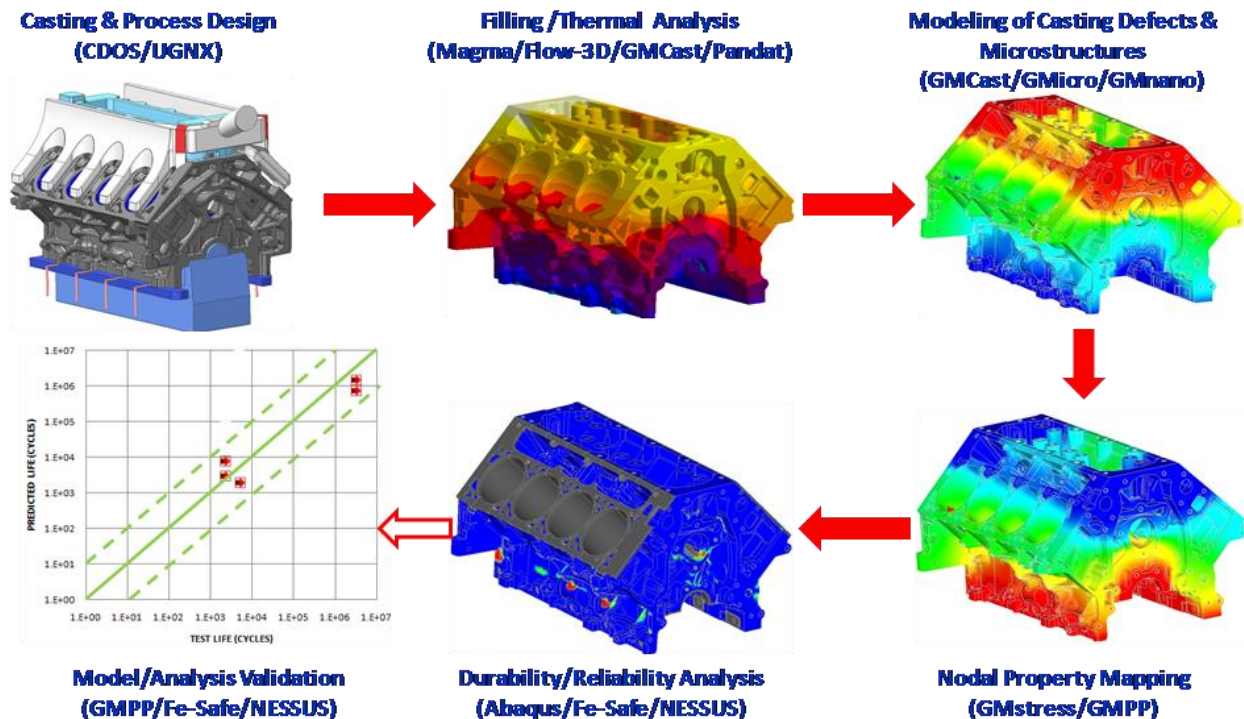


Figure 2. General Motor’s Virtual Cast Component Development modeling and simulation method for cast product property and life prediction.

At the first stage of the project, a material requirement matrix was developed to guide alloy development. The first generation of the matrix was based on property requirements in the original DOE funding opportunity announcement, as well as the best achievable properties of current alloys. Improvements to the matrix were based on a design for six sigma optimization. Initial input variables for the finite element analysis included: coefficient of thermal expansion, thermal conductivity, heat capacity, Young's modulus, and density. These simulations were completed in 2013.

During 2014, a second design for six sigma study looking at nine input variables, including the thermal conductivity, ultimate tensile strength, strength coefficient (K), and the hardening coefficient (n), and low-cycle and high-cycle fatigue strengths at room and elevated temperatures, was completed to establish and identify the importance of room and high-temperature tensile and fatigue properties on engine performance. The analysis looked at temperature in the valve bridge area, deck face flatness (distortion), mean and alternating stresses on the flame, and water jacket sides of the combustion chamber. The simulation analysis looked at both dual overhead cam and overhead valve architectures. In total, 324 global engine thermal cycle, global engine durability, and fatigue analysis simulations were carried out to complete this task.

QuesTek's iCMD and ICME technology was used to develop the alloy concepts. Beginning with expert knowledge and past research as a guide, thermodynamic and kinetic databases were utilized to create the initial alloy concepts. Precipitation modeling was then used to estimate peak strengthening heat treatments for targeted precipitate structures. DFT calculations were used to determine key input parameters beyond the reach of experimental methods. These inputs for thermodynamic and kinetic models include interfacial energies and accompanying changes with solute additions, high-throughput searches of new stable crystal structures, and solute partitioning energies to interfaces and precipitate phases. Once concepts have been created, buttons are cast and analyzed to find the precipitate phase through LEAP or

TEM. Isothermal and isochronal hardness measurements are conducted to establish the long-term stability of precipitates of the various concepts. Isochronal hardness plots are used to find the temperature to achieve peak hardness in an hour and to confirm precipitation. Isothermal hardness plots are utilized to determine time for peak aging and a first look at the strength and long-term stability of a concept.

Data collected from these experiments is also used as input in the strength models for future alloy calculations. Continuing with QuesTek's iCMD and ICME approach, substitutional elements are selected that may reduce the coarsening of the precipitate phase or otherwise enhance the high-temperature mechanical properties of the alloy. Parametric models are created for the alloys using the initial alloy concepts. These parametric models are then used to design prototype alloys that strive to meet the multifaceted criteria of the material requirement matrix. Strength, fatigue resistance, thermal conductivity, and good castability are all necessary to create a viable alloy. At this stage, General Motor's Virtual Cast Component Development Process is used to predict casting defects such as macroporosity, microporosity, hot tears, and overall mechanical performance and product durability.

In conjunction with the modeling approach, chilled plate castings are made for microstructure and mechanical property validation. Castability studies are carried out using fluidity spirals, N-Tek MetalHealth® Fluidity molds, hot tear molds, and Tatur molds. After the parametric model and prototype stage, the alloy and process is scaled up to reflect a real application, in this case a production head. The alloy and process is optimized in terms of alloy elemental tolerances, heat treatment temperatures and times, costs, and recyclability evaluation. In 2014, the goal was to develop the material requirement matrix, the alloy concepts, data generation for these concepts, and concept validation. In addition, some of the first generation alloy designs have been cast into chilled plates for mechanical testing.

Results and Discussion

The results of the design for six sigma analysis create response plots based on the input variables and the simulation carried out. Figure 3 is the response plot for maximum temperature based on the global engine durability analysis. Although not surprising, thermal conductivity is the only variable that significantly impacts the maximum mean temperature of the head in the combustion chamber area. However, it stresses the importance of thermal conductivity in determining head temperature. Furthermore, because of the loss of mechanical properties at the higher temperatures, high thermal conductivity is a critical physical property for making a successful high-temperature cylinder head alloy.

The response plot for maximum mean stress in the global engine thermal cycle analysis is shown in Figure 4.

This plot reveals the importance of having a low cyclic hardening coefficient K' and a high cyclic hardening exponent n' on lowering the mean stresses in the head. These two figures are just examples of the numerous response plots made to evaluate the material properties required for an optimal alloy. All of these plots were thoroughly analyzed to produce the recommended material requirement matrix shown in Figure 5.

A high-throughput DFT search for stable and metastable structures has been completed and possible precipitate strengthening structures were identified. Three additional alloy concepts have been added to the original five defined in 2013. Buttons were cast using these concepts and are currently under evaluation to determine any precipitation formation using atom probe (i.e., LEAP) measurements. Consideration of additional elements to various alloy concepts was researched using DFT simulations. Buttons were cast with compositions, including these elements. These elements may act as slow diffusers and reduce coarsening of the phases as predicted by DFT calculations. The solubilities of these elements in the phases were calculated, along with site preferences. An example of the

calculation is shown in Figures 6a and 6b. The actual element names and phases have not been identified because it is protected information. In Figure 6a the energy to substitute atom "E" into the various sites of the phase was determined. As is seen in the figure, element "E" can substitute for atom B in either of its positions because the partitioning energy is negative. However, as shown in Figure 6b, atom "F" cannot replace any of the other atoms with a net negative partitioning energy and is unlikely. It must be noted that these calculations only give the energy differences between the matrix and the precipitate and do not take into account interfacial interactions (i.e. interfacial strengthening/embrittling energies or interfacial partitioning). Thus, future calculations will consider these effects and initial interfacial crystal cells have been developed for this purpose.

The existence and stability of phases were measured using various microstructural methods, including atom probe tomography and TEM. In Figure 7, alloy button samples were held in a furnace at 200°C for up to 100 hours. At 30 minutes, 5 hours, 24 hours, and 100 hours, a sample was removed each time from the furnace and a LEAP sample was prepared. The growth of the phase is clearly apparent and is a strong indication of the expected deterioration of material properties at high temperature. Analysis of the LEAP data also quantifies the geometrical shape of the precipitate phase. In Figure 8, the aspect ratio of the precipitate phase and the length versus width are plotted. This knowledge is critical to understanding of the evolution of microstructure and to calibration of current strength models for the alloy.

Isochronal plots for various concept alloys are shown in Figure 9. As shown in this plot, peak hardness is achieved at 200°C for all four alloys, which is greater than that of the solution heat treated and quenched samples. This is an indication of precipitate formation. With an increase in aging temperature, peak hardness is already in decline, meaning that the precipitates become coarser and the number density of the precipitates is decreased, as observed by the LEAP data.

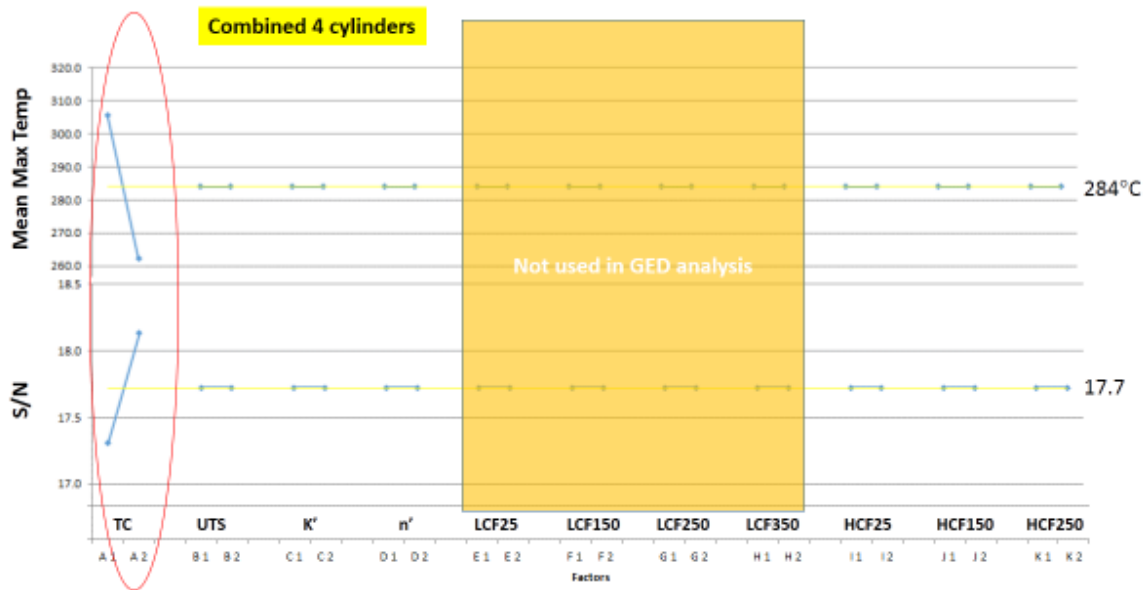


Figure 3. Response plot of maximum temperature in a global engine durability analysis.

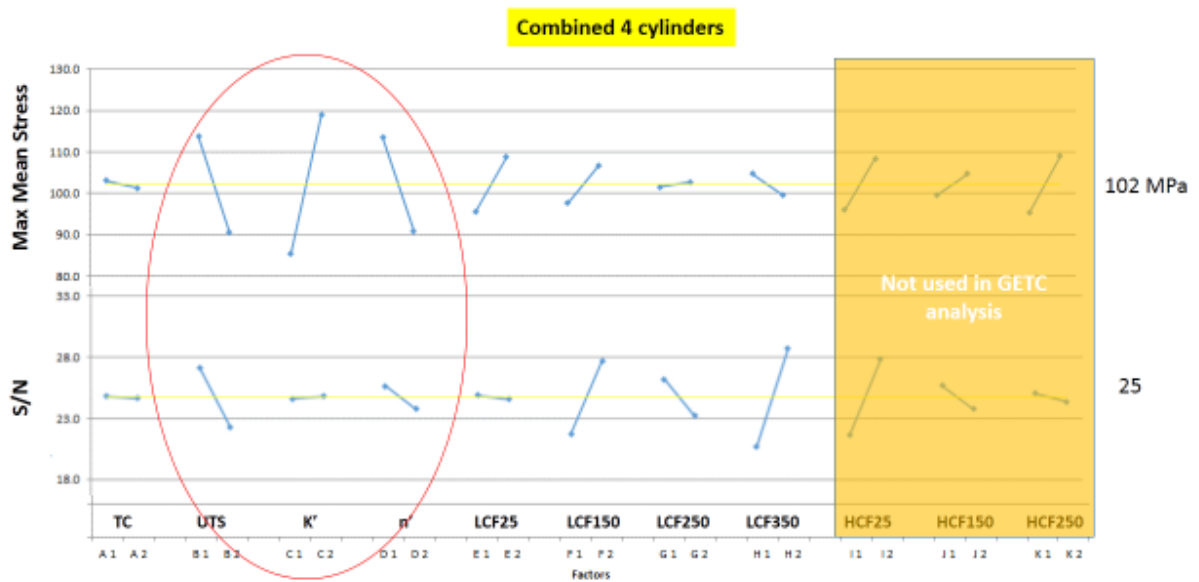


Figure 4. Response plot: maximum mean stress in global engine thermal cycle analysis.

Baseline and Targets for Cast Lightweight Alloy. Alloy Requirement Matrix Final Version					
Property	Temperature	Baseline	Targets		
		DOE Cast Aluminum *	DOE Cast Lightweight Alloy	GM Counter Proposal	Proposal Ranked Importance
Tensile Strength (MPa)	Room Temperature	227.5	275.8	300	19
	150 C	N/A	N/A	280	15
	250 C	51.7	N/A	100	17
	300 C	N/A	65.5	65.5	21
Yield Strength (MPa)	Room Temperature	165.5	206.8	210	13
	150 C	N/A	N/A	200	14
	250 C	34.5	N/A	75	12
	300 C	N/A	44.8	45	20
Plastic Elongation (%)	Room Temperature	3.5	3.5	> 3.5	11
	300 C	N/A	< 20	N/A	22
Fatigue Strength at 10 ⁷ cycles (MPa)	Room Temperature	58.6	75.8	N/A	23
	150 C	N/A	N/A	70	7
	250 C	N/A	N/A	50	9
Fatigue Strength at 10 ⁴ cycles (MPa)	150 C	N/A	N/A	140	8
	250 C	N/A	N/A	60	10
Density (g/cm ³)	Room Temperature	2.7	< 6.4	< 3.0	5
Shear Strength	Room Temperature	179.3	206.8	206.8	24
Thermal Conductivity (mw / mm-C)	150 C	N/A	N/A	202	6
Coefficient of Thermal Expansion (mm / mm-C)	150 C	N/A	N/A	2.20E-05	16
Fluidity (Die Filling Capacity / Spiral Test)		Excellent	Excellent	Same as 319	3
Hot Tearing Resistance		Excellent	Excellent	Same as 319	4
Manufacturing cost including alloy and processing			< 110% Baseline	< 110% Baseline	2
Corrosion resistance				GMW15272 for Underhood Vehicle Requirements (Neutral Salt Spray Testing) Compatibility with alternative fuels	18
Recyclability				Must comply with GMW3059 (GADSL: Global Automotive Declarable Substance List) GMW3116 Recyclability / Recoverability must be considered	1

Figure 5. Material requirement matrix.

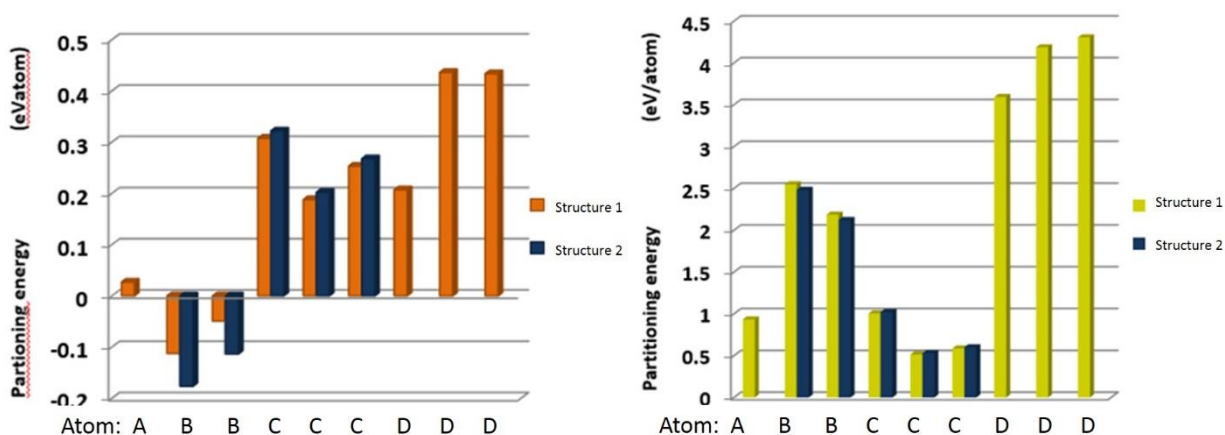


Figure 6. Partition energy of substituting alternative atoms in the precipitate phase: (a) substitution of atom E into precipitate phase and (b) substitution of atom F into precipitate phase.

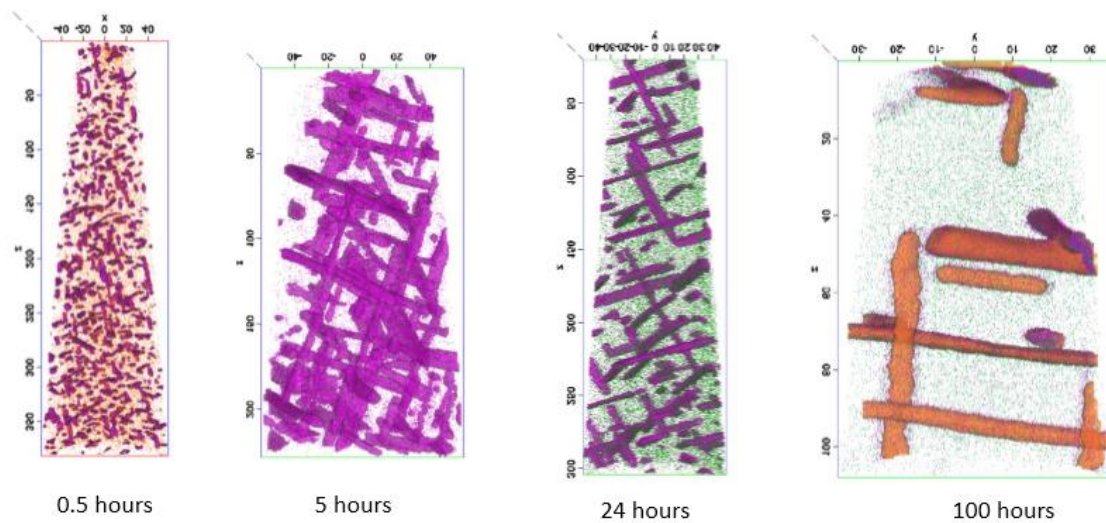


Figure 7. LEAP images of a precipitate phase held at 200°C for an extended period of time.

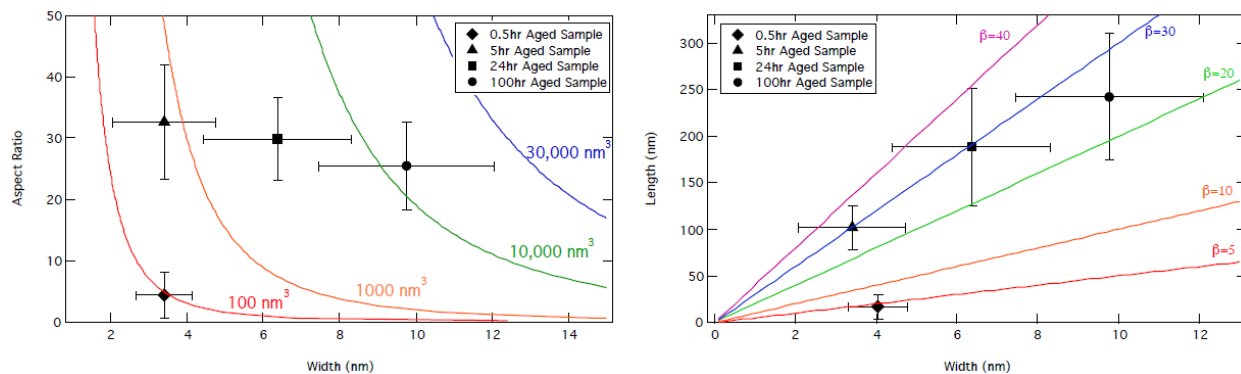


Figure 8. Evolution of the aspect ratio (left) and particle length (right) versus particle width.

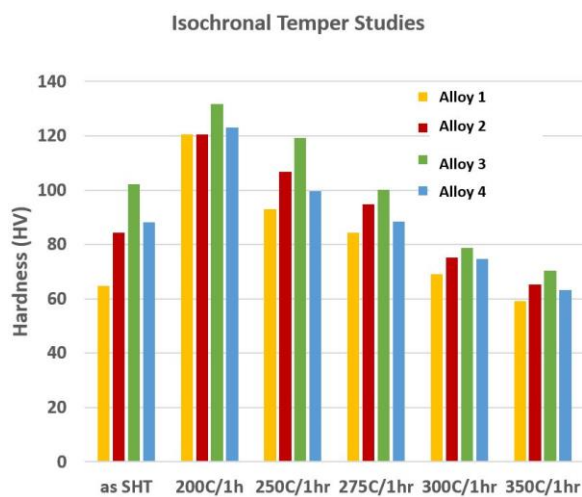


Figure 9. Isochronal hardness of four alloys solution heated treated, quenched, and aged.

At even greater temperatures (i.e., 300 and 350°C), the driving force for precipitation is too low and the number and size of precipitates are insufficient to have an impact on the hardness and strength of the material. In fact, the hardness is now less than the supersaturated solution of the solution heat-treated and quenched specimens.

Isothermal plots of four alloys held at 200 and 250°C are shown in Figure 10. The hardness of all alloys greatly deteriorates at 250°C.

Potentially viable concepts were cast into chilled plates for mechanical property tests. The chilled plates were cut up into tensile samples with three different values of secondary dendrite arm spacing (SDAS).

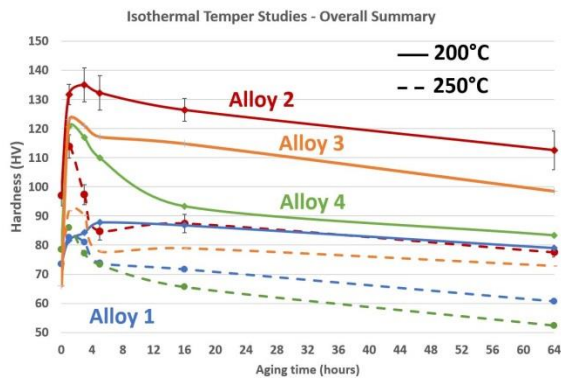


Figure 10. Isothermal hardness tests for four selected alloy samples at 200 and 250°C.

Each tensile testing data point represents an average of three tests at each SDAS. All high-temperature tests were performed on samples that first underwent 200 hours of conditioning at the test temperature. Figure 11 is a plot of tensile properties with temperature for the baseline A356 alloy and two cast alloy concepts. The plot is for a coarse SDAS microstructure to reflect the worst-case properties, in particular plastic elongation. Room temperature ultimate tensile strength is not difficult to achieve. However, the alloy with maximum tensile strength throughout the temperature range also has insufficient ductility. DOE also targets a maximum elongation of 20% at 300°C and all alloys fall well below this goal. However, this is not a key requirement and has very little, if any, impact on head performance or manufacturability. All alloys are still below the 300°C tensile strength requirement. The challenge going forward is to continue to raise the high-temperature tensile strength but, most critically, without the loss of room and lower temperature ductility. Our goal to achieve this is to incorporate elements into the concept structure that reduce diffusion and growth of the precipitate. In addition, research continues to identify elements and compounds that precipitate out separately and provide high-temperature strength without impacting low-temperature ductility.

Technology Transfer Path

In the final year of the project, when the final alloy and process has been established, a casting trial on production heads will be carried

out. This trial will measure tensile and fatigue properties, and evaluate castability in a head. This is the first step in evaluating the alloy for production.

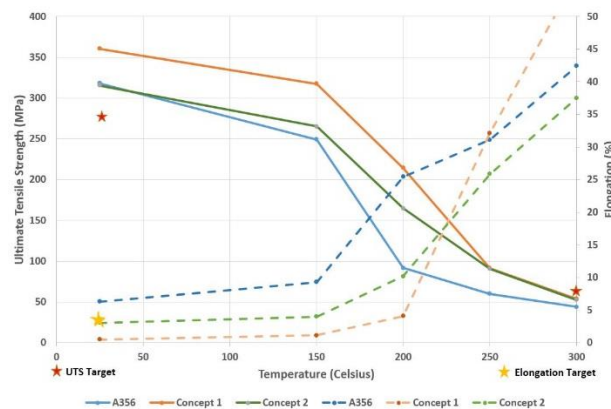


Figure 11. A comparison of tensile properties of baseline A356 alloy and cast concept alloys with a coarse SDAS microstructure.

Secondly, an evaluation of the recyclability will be carried out. It is essential that any alloy put into production will not adversely affect the aluminum recycling stream.

Thirdly, as required by the funding opportunity announcement and implemented into the second phase of the project, comprehensive cost models will be developed to include materials production, component casting, heat treatment, and machining costs for annual production runs up to 500,000 units of cylinder heads using the new alloy. A technology transfer and commercialization plan will be developed for the new alloy using the material properties and results of the cost model.

Once these steps have been completed, General Motors will evaluate and select what future head is the best first candidate for this new alloy. The head design will take into account the improved higher-temperature properties offered by this alloy. Prototype tooling will be made and additional casting trials will be carried out. These casting trials will collect material property data again, but heads will also undergo various bench tests and finally engine build and dyno-tests. General Motors will either select a supplier to conduct the trials or plan for production at one of our captured foundries. After patent protection has been

established, Tier one suppliers will be given full knowledge of how to produce the alloy and process the alloy for production purposes.

Conclusions

In FY 2014, General Motors and its partners developed a material requirement matrix to guide the development of a new high-temperature aluminum alloy. Through ICME, the team has identified eight alloy concepts that have a potential to contribute to the overall material property requirements for high-performance light-duty engine heads. Several concept alloys have been cast into either chemical button or test plate castings. The casting buttons and plates have been used to validate the current ICME model predictions, as well as used as input data for ICME model improvement. LEAP, isochronal hardness plots, isothermal hardness measurements, and tensile data have all been utilized for model validation. ICME methods such as CALPHAD, DFT, precipitation models, casting solidification models, and material property and durability models are all being utilized to identify the best characteristics of the alloy and to improve the high temperature strength of the developed alloy.

Current results indicate that achieving room temperature tensile strength has already been obtained with the current concepts. However, room temperature elongation falls well short of target for these higher strength alloys. Although the high-temperature targets have not been fully achieved, new alloy concepts have approached targeted strength properties. Global engine durability and global engine thermal cycle simulations reveal the critical importance of thermal conductivity and ductility in the material requirements for a head material.

Therefore, in 2015, research will focus on parameterizing and optimizing the alloy concepts and finding elements that will not only increase the high-temperature strength but also improve the room temperature ductility. Thermal conductivity will be modeled, measured and a preference to high thermal conductivity alloys will be determined. Validation by microscopy, casting experiments, and mechanical testing will continue.

Project 21656 – Cast Alloys for Engines

Agreement 27382 – ICME Guided Development of Advanced Cast Aluminum Alloys for Automotive Engine Applications

Melissa Hendra, Ford Contracts Manager
Ford Research and Advanced Engineering Laboratory
Dearborn, MI 48124
Phone (313) 594-4714; fax (313) 322-7162; email: mhendra@ford.com

DOE Technology Manager: Jerry L. Gibbs
Phone (202) 586-1182; fax: (202) 586-1600; e-mail: jerry.gibbs@ee.doe.gov
Ford Technical Advisor: Mei Li
Phone (313) 206-4219; e-mail: mli9@ford.com

Contractor: Ford Research and Advanced Engineering Laboratory, Dearborn, Michigan
Prime Contract No.: DE-EE0006020

Objectives

- To develop a new class of advanced, cost-competitive aluminum casting alloys, providing a 25% improvement in component strength relative to components made with A319 or A356 alloys, using sand and semi-permanent casting processes for high-performance engine applications.
- To demonstrate the power of integrated computational materials engineering (ICME) tools for accelerating development of new materials and processing techniques, as well as to identify the gaps in ICME capabilities.
- To develop comprehensive cost models to ensure that components manufactured with these new alloys do not exceed 110% of the cost using incumbent alloys A319 or A356.
- To develop a technology transfer and commercialization plan for deployment of these new alloys in automotive engine applications.

Approach

- Start the alloy design process with a baseline alloy in line with 356/319 alloys that have well quantified properties.
- Optimize the composition and heat treatment of the baseline alloy.
- Evaluate the heat treatment response and strengthening effect of some heat-resistance elements of interest in simple model alloys, particularly at high temperature (300°C).
- Combine the knowledge acquired from the baseline alloy and the simple model alloys together for the final alloy composition. Design a compromised heat treatment process to attain balanced strengthening from both the baseline composition and the novel alloying additions.

Accomplishments

- Identified several novel elements that could potentially address the challenge of high-temperature (i.e., 300°C) mechanical property degradation experienced by existing cast aluminum alloys.
- Successfully developed a promising Heat 15 alloy with balanced baseline composition and novel alloying additions, which is capable of reaching the U.S. Department of Energy's (DOE's) target on yield strength at 300°C, with the customized multi-step heat treatment process.

- Cost of alloy composition, casting condition, and heat treatment procedures have been taken into account throughout the alloy design process; therefore, the properties of Heat 15 alloy are directly applicable to production.

Future Direction

- Optimize the composition and heat treatment of Heat 15 alloy to meet all DOE requirement on yield strength at both room temperature and high temperature.
 - Quantitative in transmission electron microscopy (TEM) characterization of the precipitation process in optimized Heat 15 at various temperatures and times.
 - Develop yield strength model based on quantitative TEM results.
 - Evaluate the fatigue property of Heat 15 and compare with the baseline Heat 14 alloy by performing standard isothermal LCF and HCF, thermomechanical fatigue, and customized coupon-level thermal fatigue testing.
 - Investigate castability of Heat 15 alloy in component geometry via computational simulation.
-

Introduction

Recently legislated fuel economy standards require new U.S. passenger vehicles to achieve at least 34.1 mpg, on average, by model year 2016 and 58 mpg by 2030, which is up from 28.8 mpg today. Two major methods of achieving improved fuel economy in passenger vehicles are reducing the weight of the vehicle and developing high-performance engines. However, to increase engine efficiency, the maximum operation temperature of these components has increased from approximately 170°C in earlier engines to peak temperatures well above 200°C in recent engines. The increase in the operational temperatures requires a material with optimized properties in terms of tensile, creep, and fatigue strength. This program focuses on developing advanced cast aluminum alloys for automotive engine applications to meet these challenging requirements.

Several alloy compositions have been proposed in year 2013. These alloys, which are based on the commercial AS7GU alloy composition with the addition of some novel alloying additions, were cast and characterized microstructurally and mechanically. Some of the alloys showed very promising microstructure and high-temperature yield strength.

This year (i.e., 2014), more focus has been placed on understanding the strengthening mechanism of these novel alloying elements quantitatively, and applying that knowledge in designing an alloy and heat treatment that could potentially meet all the requirements proposed by DOE. Two groups of alloys were proposed and cast, Al-Si-X-Y based (X, Y being the novel alloying elements) and 319 based, to assist the investigation. Aging study of Al-Si-X-Y alloy clearly showed the strengthening effect of these elements, whereas detailed TEM characterization confirmed the precipitation of very fine particles with spherical morphology. Practical aging temperature and time for these novel precipitates was proposed based on these aging results. Heat 15, the latest alloy developed based on 319 alloy and proper level of these novel elements, showed high temperature yield strength higher than the DOE target, even after

the 100-hour pre-exposure time at the testing temperature (300°C).

Results

Alloys Proposed

In this project, 15 different alloys have been proposed to help us understand the effect of different alloying additions and types of microstructure. In the last year, Heat 1 through 7 alloys were proposed based on the commercial alloy ASGU. This year, Heat 8 through 13 alloys were proposed, which contain only Al, Si, and some novel elements of interests. These alloys were designed to isolate the strengthening effect of the added novel elements. Finally, Heat 14 and 15 alloys were proposed. These two alloys were based on the composition of 319 alloy. Heat 15 alloy has a certain level of novel alloying additions, while Heat 14 alloy does not.

Composition Control

Composition is one of the key factors that determine an alloy's overall properties. Therefore, controlling alloy composition is of critical importance in the manufacturing cycle, particularly for cast alloys for which post processing is somewhat limited. For our research on discovering novel elements that can enhance the performance of existing cast aluminum alloys, composition control is extremely important because the only way we can isolate the effects of these novel elements is by ensuring identical baseline composition and by accurately controlling the concentration of novel elements of interests in our casting. Last year, we proposed seven different alloy compositions (Heat 1 to Heat 7) and have gained valuable information regarding mechanical property and microstructure, but that knowledge was qualitatively in nature. This is because the concentration of certain alloying additions was outside the capability of our old in-house spectrometer. The compositional information we received from different outside sources showed different results. To eliminate this issue, a new optical emission spectrometry from Spectro was purchased this year and was calibrated, with a standard material covering all the major alloying elements for the range we are interested in (Figure 1). The bulk compositions of all the

alloys cast in this project are measured using this spectrometer; therefore, they are directly comparable.



Figure 1. In-house SPECTROMAXx spark optical emission spectroscopy metal analyzer.

Another critical control regarding composition is strontium (Sr). Sr is usually added to provide modification to the eutectic Si particle, which has a significant effect on the fatigue property of cast aluminum alloys. To ensure such an effect is taking place, 80 to 120 ppm Sr is necessary in the casting. However, the level of Sr tends to drop during the casting process, particularly at higher pouring temperature (750°C), because it is highly oxidative. In order to quantitatively understand how fast Sr burns out during casting and to ensure the Sr level of future casting is within the targeted concentration range, a Sr burn-out rate experiment was conducted, with 250 to 300 ppm Sr being added to one of the previously proposed alloys at 750°C. A spectrometer disk sample was taken every 30 minutes to monitor the Sr level within the melt. The result is shown in Figure 2, with two curves measured on two different dates.

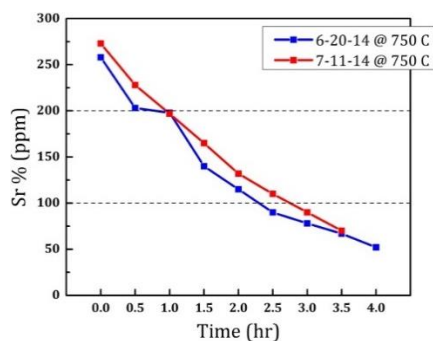


Figure 2. Levels of Sr in melt versus time at 750°C.

Both of these two curves show that the Sr level drops relatively faster at the beginning and the burn-out rate gradually slows down when the Sr level becomes lower. The window between 200 to 100 ppm Sr level is about 1.5 hours, which is consistent in both experiments. Based on this results, torpedo casting of future alloys are poured once the Sr level is at about 200 ppm and the Sr concentration is monitored and adjusted every hour throughout the casting process.

Cooling Rate Control

A production engine component has a range of secondary dendrite arm spacing (SDAS) and it is crucial to investigate the performance of the new alloys at relevant microstructures. The permanent mold that is currently used for casting torpedo samples provides a relatively fast cooling rate that generates a SDAS of about 15 μm . However, the more practical cooling rates commonly observed in the industrial engine block/head casting process generate a SDAS of about 25 μm . To ensure the microstructure and mechanical properties are representative of engine block/head materials, much slower cooling rates need to be achieved. To tackle this problem, a layer of coating was applied to the surface of the mold, with paint density, air pressure, and mold temperature set to optimal values (Figure 3). The cooling rate of the torpedo bar during solidification was monitored by inserting a thermocouple into the center of the torpedo bar cavity within the mold. It is evident from the cooling curves that the liquid aluminum cools much slower with a layer of coating on the surface of the mold (Figure 4). The center slice of the torpedo sample was sectioned and went through typical metallographic preparation procedures. Ten to twenty optical images were taken at appropriate magnification across the sample and 300 to 400 secondary dendrite arms were measured to ensure the value is statistically significant. The result of the latest coating trial shows that the SDAS is very close to our target value (i.e., $24 \pm 4 \mu\text{m}$) (Figure 5).



Figure 3. Cast iron mold for casting torpedo sample: (a) without coating and (b) with coating.

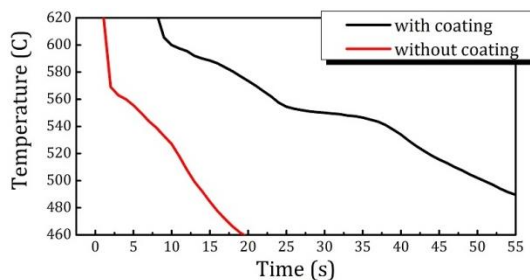


Figure 4. Cooling curves of torpedo bar during solidification.

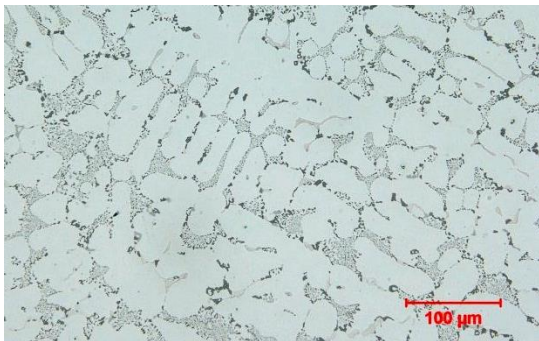


Figure 5. As-cast microstructure of a 319-type alloy showing the SDAS close to 25 μm after applying coating on the surface of the mold.

Aging Response of Heat 10

The biggest challenge in this project is to increase high temperature strength of existing cast aluminum alloys. Several novel elements have been added to the baseline composition, particularly for this purpose. Although both literature review and our previous results indicate that these elements might be beneficial, the pressing need at current stage is still to isolate and quantify the strengthening contribution of these novel elements.

Heat 8 through 13 alloys, which have different combinations and concentrations of novel elements were performed aging treatment at four different temperatures. According to literature, this temperature range was reported to be the most relevant to formation of heat resistance precipitates caused by addition of novel elements. Aging curves of Heat 10 are shown in this report as an example of other model alloys (Figure 6). Consistent with previous reports, a Rockwell E scale was used when measuring hardness. When aged at high temperatures, no clear aging response was observed in Heat 10 alloy. Instead the hardness keeps decreasing, possibly because the temperature is too high and precipitates form and coarsen very fast, which leads to the continuous drop in hardness. When the aging temperature is lowered, a much clearer aging behavior was observed. Higher peak hardness (HRE62) and a longer peak aging time (6 to 8 hours) was observed at the lowest aging temperature performed, T_{a1} , compared with the aging response at relative higher temperatures. It is likely that a much higher volume fraction and finer size of precipitates was formed at lower temperature, which might be related to a sudden decrease in solubility of added elements within the Al matrix at this temperature. These aging studies provide valuable information for the kinetics of these novel heat-resistant precipitates because no θ' or Q' precipitates are formed in these model alloys.

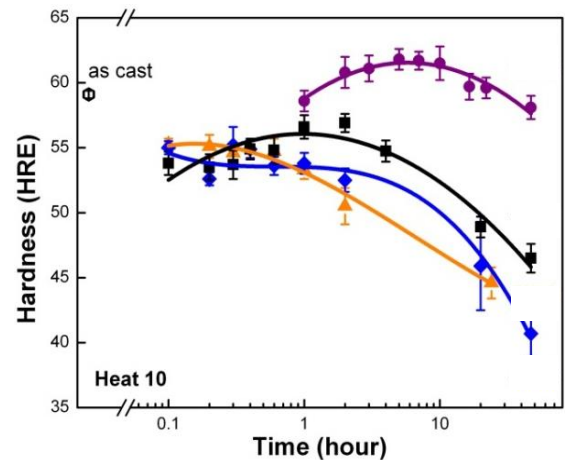


Figure 5. Aging response of Heat 10 alloy at various temperatures evaluated by Rockwell E hardness.

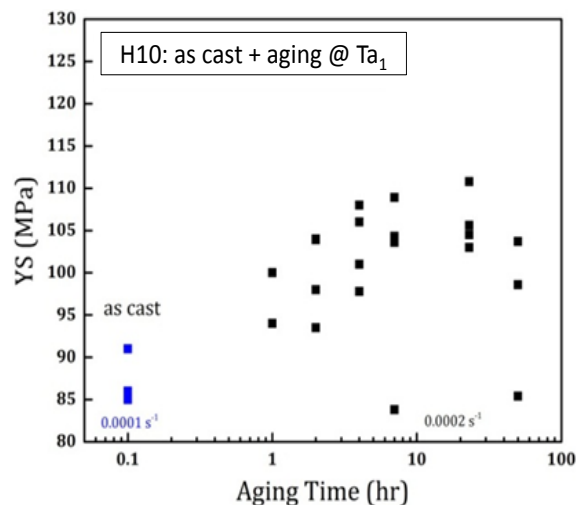


Figure 6. Aging response of Heat 10 alloy at 400°C, evaluated by room temperature yield strength.

To confirm the observed aging response, torpedo samples of Heat 10 were aged at T_{a1} for 0, 1, 2, 4, 7, 23, and 50 hours, followed by water quench with no prior solution treatment. As-aged samples were then machined into tensile bars and tested at room temperature at a quasi-static strain rate. Compared with the aging curve characterized with the Rockwell E hardness measurement, a much stronger aging response could be seen from the yield strength data (Figure 7). The yield strength is 88 MPa for the as-cast sample, which increases to 108 MPa at a peak aging time of 23 hours. Several interesting conclusions/hypotheses could be drawn here. First, Heat 10 is a quaternary alloy and contains only two novel elements as the main strengthening elements, besides the Al-Si baseline composition. The aging response confirmed that these elements indeed provide strengthening to the Al-Si baseline alloy and it is very likely due to precipitation strengthening. Secondly, these precipitates peak at ages of 23 hours, which is much more sluggish than conventional θ/Q' precipitates. This suggests that these new precipitates have very slow diffusion kinetics and could potentially be incorporated into traditional cast aluminum alloys as heat-resistant precipitates. Thirdly, the increase in yield strength from an as-cast condition to peak-aged condition (about 20 MPa) could be significant at 300°C, at which

temperature the conventional cast aluminum alloys (319/356) all have a yield strength below 45 MPa.

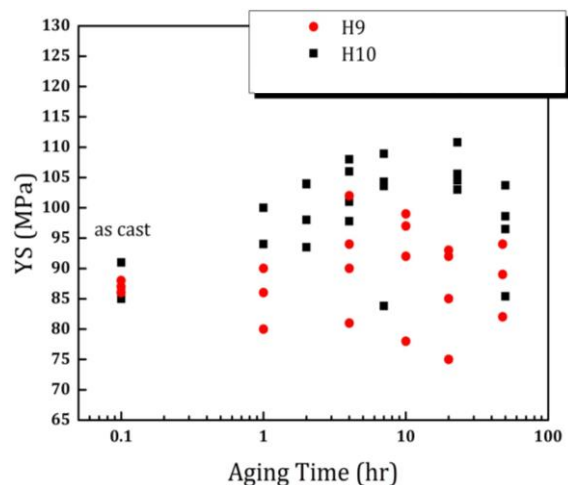


Figure 7. Comparison of 400°C aging curve of Heat 9 and Heat 10 alloy.

To understand how much of these elements is necessary in our alloy and to avoid unnecessary increase in cost, the same aging treatment was performed on Heat 9 alloy, which is similar to Heat 10 alloy but with a lower level of those novel elements. As-aged Heat 9 samples were tensile tested at room temperature and compared with Heat 10 samples in Figure 8. The result shows that at almost all aging conditions, Heat 10 exhibits higher yield strength than Heat 9, indicating the level of X and Y element in Heat 10 is likely to be more beneficial than Heat 9 (Figure 8).

Comparison Between Heat 14 and 15

The latest alloys proposed in this DOE project is Heat 14 and Heat 15. Heat 14 is based on 319 alloy, while Heat 15 is essentially Heat 14 alloy with some novel alloying elements that have been investigated throughout this project. The purpose of proposing these two alloys is to identify any beneficial effect of these novel elements in a commercial alloy, applying the newly designed heat treatment. The 319 alloy, which contains 3 wt% Cu, was chosen as the baseline alloy because Cu is known to provide better high-temperature strength.

When the as cast microstructures of these two alloys were examined under optical microscope, the difference was significant. To better reveal the difference, polished samples were electrolytically etched in the Barker's reagent (solution of 5 mL HBF₄ [48%] + 200 mL water, 20 V for 90 seconds) under polarized light. Heat 14 alloy without the novel alloying additions shows an equiaxed grain structure with grain size larger than 500 μm , consistent with our previous results on 319-based alloys (Figure 9(a)). However, Heat 15 shows a much finer grain size (about 70 μm) that is almost ten times smaller than Heat 14 (Figure 9(b)). When Heat 15 was examined under higher magnification, small particles with size on the order of 5 μm were observed in the center of Al dendrites as circled in Figure 9(c) and (d). The location of these particles indicates that these are primary phase that formed prior to the solidification of Al dendrites. It is likely that the formation of these uniformly and densely distributed primary particles provides effective nuclei for primary aluminum dendrite, leading to a much finer grain structure.

This result is very exciting for two reasons. First of all, a finer grain size means higher yield strength according to the Hall-Petch relationship. Second of all, a finer grain size also reduces the length scale across which macro-segregation can occur. This is critically important because the degree of segregation in cast alloys determines the temperature and duration of solution heat treatment. With a fine-grained microstructure, the traditional solution heat treatment could be potentially shortened, leading to significant energy savings. The tensile properties of Heat 14 and Heat 15 at both room temperature and 300°C are being tested as shown in Figure 10(a).

Both alloys were heat treated prior to tensile testing. When the close-up looks of the 300°C yield strength of these two alloys are compared (Figure 10(b)), the yield strength of Heat 15 (i.e., 48 MPa) is 25% higher than Heat 14 (i.e., 39 MPa), which is a significant improvement.

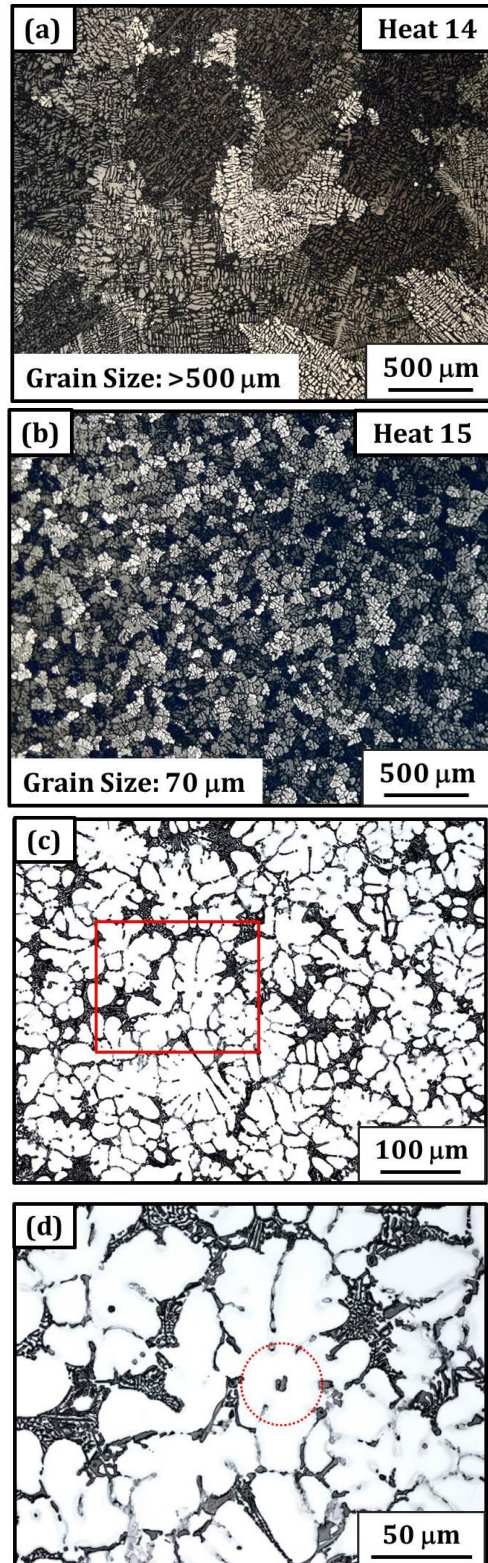


Figure 9. (a) Cast microstructure of Heat 14 with coarse grains; (b) cast microstructure of Heat 15 with fine grains; (c) cast microstructure of Heat 15 showing individual dendrites; (d) close-

up image of Heat 15 showing particles within the center of the dendrites serving as nuclei for Al dendrite formation during solidification.

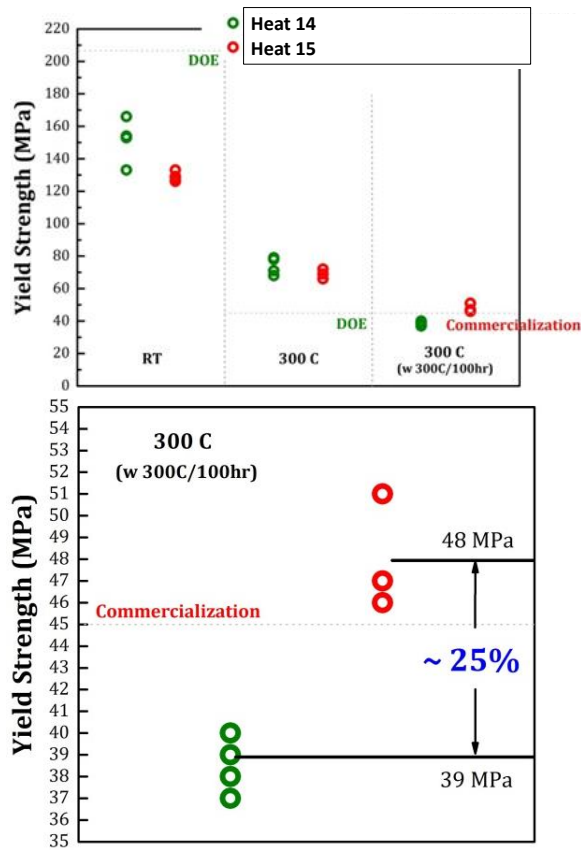


Figure 10. (a) Yield strength comparison of Heat 14 and Heat 15 at room temperature, 300°C, and 300°C with 100-hour pre-exposure and (b) close-up look at the difference between Heat 14 and 15 when tensile tested at 300°C with 100-hour pre-exposure.

Conclusions

The aging response study of Heat 10 (Al-Si-X-Y) has unambiguously confirmed that the novel alloying elements that have been investigated in this project indeed promote very fine precipitate, which could potentially strengthen the matrix at both room temperature and high temperature.

A 319-based alloy, Heat 15, was proposed, along with a novel multi-step heat treatment procedure, to take advantage of both the traditional θ'/Q' precipitates and the novel precipitates. Yield strength at 300°C of Heat 15 meets the DOE target, even after a 100-hour pre-exposure. Comparison between Heat 15 and Heat 14 suggests that the superior property of Heat 15 at high temperature is likely resulted from the novel alloying additions.

Project 21656 – Development of High-Strength Crankshafts

Agreement 27387 – ANL: Alloy Development for Rotating Components

John Hryn, D. Singh, and C. Chuang

Energy Systems Division

Argonne National Laboratory

9700 S. Cass Avenue

Argonne, IL 60439

Phone (630) 252-5894; fax (630) 252-5132; email: jhryn@anl.gov

DOE Technology Manager: Jerry L. Gibbs

Phone (202) 586-1182; fax: (202) 586-1600; e-mail: jerry.gibbs@ee.doe.gov

Argonne National Laboratory Technical Advisor: Dileep Singh

Phone (630) 252-5009; fax: (630) 252-2785; e-mail: dsingh@anl.gov

Contractor: Argonne National Laboratory, Argonne, Illinois

Prime Contract No.: DE-FOA-0000793

Objectives

- Overall program goal is to develop cast steel alloys and processing techniques that are tailored for high-performance crankshafts and achieve target as-cast properties of 800-MPa UTS and 615-MPa yield strength as a replacement for expensive forgings.
- As part of the project team, Argonne National Laboratory (ANL) will utilize advanced material characterization capabilities at the Advanced Photon Source to determine the internal casting quality of the samples and conduct innovative in situ measurements of phase evolution and damage nucleation during heating and cooling under various loading conditions. The goal aims to better understand the chemistry-structure-process relationships.

Approach

- Use high-energy tomography to assess the basic casting quality, including size and distribution of porosity and inclusions, of casting samples. Absorption and/or phase contrast micro-tomography will be used in conjunction with metallography to understand the three-dimensional (3D) structure (e.g., shape, cell size, interconnectivity, etc.) of the internal defects.
- Use in situ high-energy x-ray diffraction to study the phase evolution for the new compositions being developed and correlate it to the mechanical performance of the alloys. The experiments will involve heating the samples to a high temperature (1200 to 1500°C) in a ceramic mold and monitor the phases developed as the sample is cooled down at cooling rates similar to that in actual castings.
- Mechanical testing equipment available at the beam line will be used to conduct in situ mechanical property characterizations up to temperatures of 350°C.

Accomplishments

- Developed a procedure for the 3D characterization of morphologies of various phases in castings. The internal connectivity, porosity, shape, and size distributions in alloys can be investigated nondestructively. As preliminary effort, the procedure has been demonstrated on cast irons.

- Developed and tested apparatus for in situ high-temperature x-ray diffraction experiment. The system allows the characterization of phase evolution during the alloy solidification process.

Future Direction

- Utilize 3D tomography techniques to assess the basic casting quality, including size and distribution of porosity, inclusions, and phase structures of cast steel samples.
 - Conduct in situ phase evolution study of cast steel alloys and correlate it to the processing conditions to develop and optimize the cast alloys to meet the target properties.
-

Introduction

The demand for smaller and lower weight engine and power train components with improved efficiency to reduce fuel consumption, emissions, and costs for vehicle use, while maintaining or even increasing engine performance is increasing rapidly. Increasing engine power and efficiency requires higher operating cylinder pressures, resulting in increased loads on the crankshaft. For high-performance engines, the loads on the crankshaft are too high for today's cast materials and are required to be produced from more expensive forgings. Material and process developments are required for design and production of high-performance cast crankshafts that meet strength, fatigue, and other functional requirements in order to produce a high-efficiency engine that is both lightweight and cost-effective.

The objective of this project is to develop cast steel alloys and processing techniques that are tailored for high-performance crankshafts and achieve target as-cast properties of 800-MPa UTS and 615-MPa yield strength as a replacement for expensive forgings. Even more challenging, the cast material must achieve sufficient local fatigue properties to satisfy the durability requirements in today's high-performance gasoline and diesel engine applications that currently use forged crankshafts.

The project team consists of Caterpillar, Inc., General Motors, Northwestern University, University of Iowa, and ANL. The project team will focus on cast steel alloys and processes to take advantage of the higher stiffness, ductility, and high-cycle fatigue properties over other traditional cast crankshaft material choices. The team will tailor the alloy design and develop innovative processing methods to produce clean steel castings with refined microstructures and required soundness and hardenability. Utilizing the casting process and the stiffness advantage of steel will allow the weight reduction potential to be maximized without sacrificing performance. The technology developed should be able to produce high-performance crankshafts

at no more than 110% of the cost of current production low-performance cast units.

As part of the project team, ANL will utilize the Advanced Photon Source within the laboratories to quantify casting quality and conduct innovative in situ measurements of phase evolutions and damage nucleation during thermal and mechanical loading conditions to better understand the chemistry-structure-process relationships.

For the first year of the project, ANL focused on 3D tomography of casting quality and structure. In this task, x-ray tomography was used to assess the basic casting quality, including size and distribution of porosity and inclusions, of casting samples. Absorption and/or phase contrast micro-tomography was used in conjunction with metallography to understand the 3D structure (e.g., shape, cell size, interconnectivity, etc.) of the internal defects. Understanding of the 3D features of the microstructure (such as grain size and phase distribution) was also of interest.

The design and build of the required apparatus for the phase evolution studies is another major task. The objective of this part is to study the phase evolution for the new compositions being developed and correlate it to the mechanical performance of the alloys. A typical experiment will involve heating the samples to a high temperature (1200 to 1400°C) in a ceramic mold and monitor the phases developed as the sample is cooled down (at rates similar to actual castings). The technique allows capturing the phase evolution by using high-energy x-rays in the bulk as a function of time. Formation of precipitates (i.e., size, distributions, and locations) and voids can be followed as the sample is cooled down. Information generated will be critical in the alloy development and optimization of the controlled cooling process to achieve required structures.

Results

In the early stage of the project, while the alloy design was computer simulation phase, ANL's effort focused on development of the experimental apparatus for the tomography and

in situ phase evaluation studies. The primary activities included (1) validate x-ray tomography for 3D structure characterization of cast alloy, (2) design of environmental chamber to heat and hold the sample, which allows the in situ characterization by x-ray imaging and diffraction techniques simultaneously, (3) selection of crucible materials to hold the sample at both liquid and solid state, and (4) test the prototype system.

3D Tomography of Casting Quality and Structure

For the first year of the project, the ANL team developed the experimental and data analysis procedure to use high-energy x-ray tomography for non-destructive 3D structure characterization.

A commercial gray cast iron sample was characterized to validate the tomography technique on cast alloys. After tomography measurement, the same sample was mechanically sliced and polished; the region of interest on the polished surface was then selected under optical microscope (OM). To further validate that the nondestructive tomography measurement can provide the same information as from metallography, we went back to the tomography data and looked for the same features in the series of two-dimensional (2D) tomographic images. The results of the comparison are very encouraging.

The OM image of the feature is shown in the left of Figure 1 and the corresponding 2D tomographic image is shown on the right. The comparison in Figure 1 clearly shows that the tomography provides an almost identical image as under OM. The image from tomography is slightly blurred due to a lower resolution. Although the expected spatial resolution of the tomography for our setup is about 1 μm , the real resolution is estimated around 2 to 4 μm . It is not as sharp as the OM image, but is good enough to reveal the graphite morphology with acceptable details in gray cast iron.

The 3D model of the graphite particles was built subsequently from series of 2D images. Figure 2 shows the 3D graphite morphology near the slicing surface (in Figure 1). The

graphite structure within the volume can be observed clearly, and its connectivity and volume fraction can be calculated precisely.

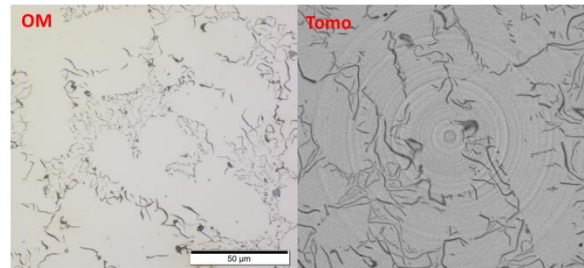


Figure 1. OM image of flake graphite on the mechanical polished surface (right) and the corresponding tomography image of the similar feature inside the same sample prior to mechanical slicing.

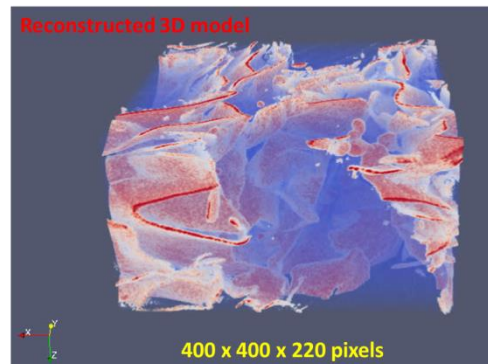


Figure 2. 3D reconstructed model of commercial gray cast iron.

With the 3D structure model, the geometrical analysis of the particles in the selected volume can be performed and the volume, surface area, and sphericity of each individual particle can be calculated. The particle distribution as a function of sphericity and the size distribution of the nodular graphite are presented in Figure 3. In the analysis, we define the nodular graphite as particle with its sphericity larger than 0.48. In principle, the sphericity of a perfect sphere is 1.0, the smaller the sphericity, the more deviation the shape of the particle has from a sphere. However, due to the size of the voxel and the resolution of the technique, the sphericity of a perfect sphere is only about 0.7. The criterion, 0.48, was determined empirically after manually reviewing several particles in 3D. Based on this number,

we found that 90+% of the particles belong to nodular graphite, and most of the nodular graphites are 10 to 20 μm in diameter. The statistical analysis of the particles shows the nodularity of this sample is about 30%. It can be seen that 3D analysis is required to determine the correct morphology, connectivity, and distribution of the characteristic features.

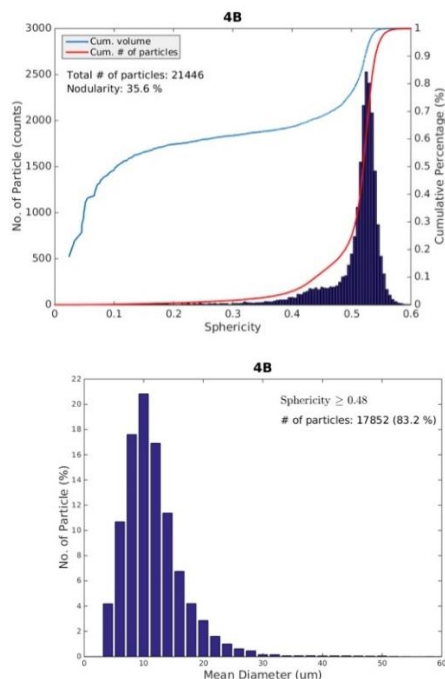


Figure 3. Quantitative analysis of the graphite morphology. The top is the particle distribution as a function of sphericity and the bottom is the size distribution of nodular graphite.

High-Temperature XRD Apparatus

In addition to the quantitative 3D analysis, the ANL team has also designed and tested several experimental apparatus this year for the in situ phase evaluation studies.

To conduct the phase evolution study, one typical experiment involves melting the sample and starting phase characterization during the solidification and cooling process. A sample holder needs to hold the sample at both liquid and solid state and the design needs to allow the synchrotron x-ray to go in and out of sample for structure characterization. A working design of the sample holder system is shown in Figure 4. The whole system contains a quartz tube and induction coil to heat the sample and an IR

camera to monitor the temperature. An argon source and a vacuum pump connect to the quartz tube. The purpose of the argon is to purge the system at the beginning and push the liquid iron into the necked quartz tube at high temperature.

A detailed design of the sample holder was presented in Figure 5. The design consists of two chambers connected by a smaller tube. The hourglass type design allows the sample to flow through the smaller tube when it is melted at high temperature. The time-dependent structure characterization can be conducted by synchrotron x-ray at the necked area in situ, while the sample cools from the high temperature as indicated in the figure. The proposed design ensures the cross section of the characterized area is within 2 mm, which is required for both tomography and diffraction techniques. The tomography tells information about the size, distribution, and morphology of the heterogeneous phases (e.g., precipitates, voids, oxide phases, etc.), while diffraction reveals the formation sequence of different phases.

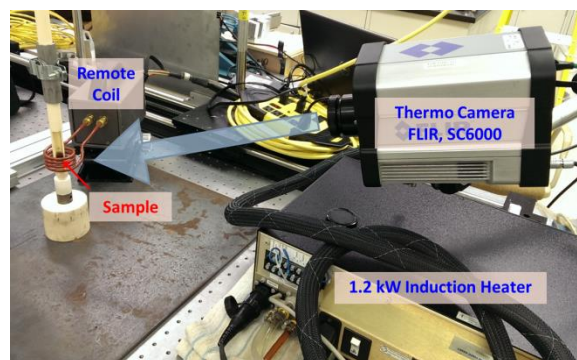


Figure 4. Schematic diagram of the holder for in situ heating experiment. The holder consists of a quartz tube, which is used to hold and melt the sample; Argon gas source; and a mechanical pump.

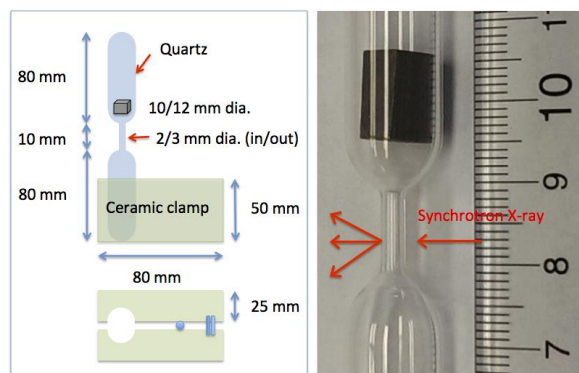


Figure 5. Schematic diagram of the hour-glass type sample holder. The holder consists of two chambers connected by a smaller tube. Once the sample at the top chamber is melted, the liquid will flow through the necked tube to the bottom chamber. The necked area allows structural characterization via synchrotron x-ray as indicated in the right figure.

For this design, a suitable sample holder to hold the sample at both liquid state and solid state is essential. The crucible (holder) needs to maintain its structural stability both microscopically and macroscopically within the temperature range (25 to 1400°C) and does not generate diffraction patterns that will interfere with the samples being characterized. Owing to the amorphous structure and transparency under both visible light and high-energy x-ray, we identified “fused silica” as the crucible/holder material.

Figure 6 shows the geometry of the in situ x-ray diffraction experiment. The sample, once it is melted, will flow through the necked area and the x-ray measurement will be done in this area. The right side of Figure 6 shows a picture of the real heating test. A furnace that can melt the sample in a timely manner and is small enough to be installed at the synchrotron facility is the key part of the experiment. Here, we choose induction heating to carry out the task. Induction heating is the process of heating an electrically conducting object (usually a metal) by electromagnetic induction, where eddy currents (also called Foucault currents) are generated within the metal and resistance leads to Joule heating of the metal. There are several advantages for using induction heating in the present because heating happens very fast

compared to gas and electric heating (1) fast heating: induction heating allows you to start up and shut down at any time; (2) fast start-up: furnaces contain large amounts of refractory materials that must be heated during start-up, resulting in large thermal experiment inertia (starting up induction heating furnaces is instantaneous, eliminating the problem of slow start-ups that gas and electric furnaces have); (3) energy efficiency: when not in use, the induction heating power supply can be turned off because restarting is rapid (with gas and electric furnaces, energy must be supplied continuously to maintain temperatures during delays in processing; also, induction heating heats only the sample itself, which will minimize the heat load to the surrounding instruments and environment); and (4) space saving: induction heating is a very compact way to get results, unlike the big and bulky gas and electric furnaces. This is especially important, because extra space is needed for diffraction and tomography detectors in the in situ synchrotron experiment.

Temperature measurement is another key part of the experiment. A high-precision thermo camera was used to monitor the temperature changes during melting and solidification.

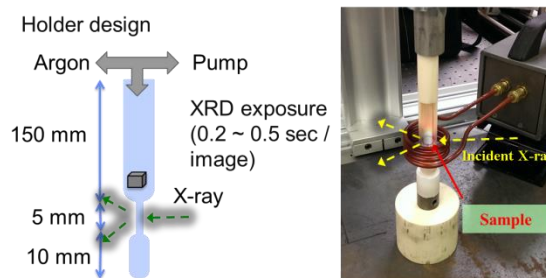


Figure 6. Schematic diagram of the experimental set-up (left) and its operation (right).

To prove the concept of the design, we used a 2.4-kW machine to conduct a heating experiment; 2.97 g of commercially available gray cast-iron was heated in a quartz tube and the corresponding temperature and power level was recorded (Figure 7). The result showed the coil can easily heat the sample to about 1000°C within about 30 seconds, while the environment (2 in. below the tube) remains cool (i.e., less than 50°C) during the whole process. In this test,

the sample was not completely melted due to surface oxidation and inadequate coil geometry. A subsequent test under vacuum shows the sample was completely melted, and by adjusting the power output of the furnace, the temperature of the sample can be controlled precisely.

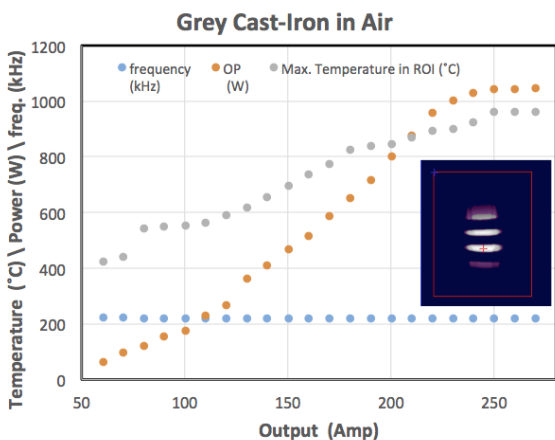


Figure 7. Heating curve of about 3 g of commercially available gray cast-iron in air.

Figure 8 shows the typical x-ray diffraction pattern obtained from the recent in situ melt experiment. Similar diffraction patterns were obtained as a function of cool-down temperature in a time resolved manner. These results are currently being analyzed to understand the nucleation and growth of the phases in gray cast iron. Similar experiments and protocols will be employed to conduct experiments on the cast steels for crankshaft application.

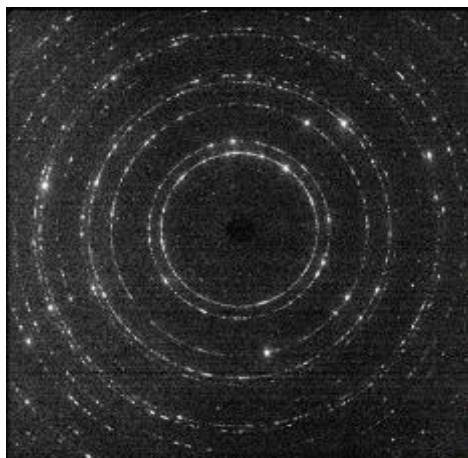


Figure 8. A typical 2D diffraction image from the experiment showing graphite and iron peaks.

Conclusions

The tomography analysis of a gray iron sample validated that x-ray tomography is indeed a powerful tool to characterize the internal microstructure of the cast alloy in a nondestructive way. The preliminary results show a different type of graphite morphologies in the tested sample. The comparison between scanning electron microscopy and tomography image show that the tomography reveals the morphology of graphite phases nondestructively and provide more information when compared to the traditional metallography technique.

The spatial resolution of the tomography is around 2 to 4 μm , which is a good fit for the cast iron system. Further volumetric analysis shows the graphite morphology can be nodular, round flake (CG), or a combination of both and it allows true 3D quantitative analysis.

The test apparatus to investigate in situ phase evolution was designed, built, and tested. Preliminary tests prove the feasibility of the design and integration of the system to the synchrotron beam line is also validated. Quartz showed to be a good candidate for the in situ synchrotron experiment. Several heating experiments were conducted to heat cast iron in air and in vacuum, respectively. An approximate 5-g sample in a vacuum-sealed tube can be melted completely. The capacity of the power supply, sample oxidation, and coil design are key factors affecting the result. The temperature of the sample can be measured accurately in real time by a thermo camera with proper calibration. The temperature of the sample is somewhat linearly proportional to the power output. Controlling the temperature by adjusting power output is recommended for the in situ XRD experiment. The thermo history can be monitored and recorded precisely by an IR thermo-camera. Data collection for several samples has been completed and is being analyzed.

Project 21656 – Cast Alloys for Engines

Agreement 27860 – Development of High-Performance Cast Crankshafts

Richard K. Huff

Caterpillar Inc.

14009 N. Old Galena Road

Mossville, IL 61552-7547

Phone (309) 494-7349; fax (309) 578-2764; email: huffrk@cat.com

DOE Technology Manager: Jerry L. Gibbs

Phone (202) 586-1182; fax: (202) 586-1600; e-mail: jerry.gibbs@ee.doe.gov

Contractor: Caterpillar Inc., Mossville, Illinois

Prime Contract No.: DE-EE0006428

Objectives

- To improve the power density of today's gas and diesel engines, material and process technologies will be developed that will enable the production of cast crankshafts that meet or exceed the performance of current state-of-the-art high performance forged crankshafts.
- Achieve minimum core material properties of 850-MPa tensile strength and 615-MPa yield strength. Material also must be able to meet the local ultra-high cycle fatigue properties required in a crankshaft.
- Identify a pathway to meet incremental cost targets of less than 110% of current production cast units.

Approach

- Use an integrated computational materials engineering (ICME) approach to computationally engineer new material compositions and manufacturing processes that improve performance of cast steel alloys.
- Integrate process-structure modeling techniques with finite element analyses by crankshaft designers to optimize crankshaft life-cycle cost and performance.
- Produce and characterize prototype melts iteratively for an alloy design within a stage-gate process to validate the alloy performance and provide feedback to material design and manufacturing process models.
- Use the advanced photon source at Argonne National Laboratory to conduct innovative in-situ measurements of phase evolutions and damage during heating and cooling under various loading conditions.
- Perform production and validation of prototype crankshafts using standard bench tests at Caterpillar and General Motors (GM). A full engine test is planned for the prototypes to ensure the crankshaft and con-rod bearing system will withstand the same severe overspeed conditions as the current baseline forging.

Accomplishments

- Defined common material requirements and validation procedures for Caterpillar and GM crankshafts.
- Identified and prioritized alloy, processing, and design concepts for investigation.

- Completed a test bar casting design for future Design of Experiments. Optimization of approximately a half dozen alloy concepts is in progress. Full characterization of an initial baseline alloy casting trial is underway.
- Investigating baseline castability of current crankshaft designs. Innovative methods for producing clean steel castings are also being investigated with casting process simulation models.

Future Direction

- Optimize compositions of the preliminary alloy concepts using the current ICME tools.
 - Procure sand mold pattern for the new test bar casting design and cast an initial alloy Design of Experiments. Fully characterize the microstructures and mechanical properties to down select the high-potential candidates.
 - Develop optimized crankshaft design concepts and processing methods for producing quality cast steel crankshafts.
 - Scale up laboratory experiments using concept crankshaft geometry to investigate high potential alloy concepts.
 - Develop plans and execute the evaluation of post-casting processing of scaled prototype crankshafts.
-

Introduction

Today, customers are demanding engine manufacturers produce engines with lower weight and improved efficiency to reduce fuel consumption, emissions, and costs associated with vehicle use, while maintaining or even increasing engine performance. Increasing the power density of the engine is a direct approach to achieving these objectives. However, increasing engine power and efficiency requires higher operating cylinder pressures, resulting in increased loads on the crankshaft. For higher-performance applications, the loads on the crankshaft are too high for today's cast materials and are required to be produced from more expensive steel forgings.

The current production split for cast ductile iron and forged steel crankshafts at GM is about 50/50. Caterpillar has a cast ductile iron crankshaft that is used in smaller 3.3L and 4.4L engines with lower power ratings. However, for higher power ratings and all other larger engines, only forged steel crankshafts are used. Enabling the use of cast crankshafts for high-performance engines will enable designers at GM and Caterpillar to optimize material use to develop lighter weight crankshafts while maintaining the torsional and bending stiffness requirements. Reducing the rotating mass of the crankshaft will enable further reduction in the engine block weight as it supports the crankshaft loads. Replacing current cast ductile iron crankshafts used in smaller engines with higher-strength castings will enable the power and efficiency of the engine to be increased. Thus, smaller more efficient engines may be able to replace larger engines, which could greatly reduce the petroleum usage and greenhouse gas emissions from automobiles and heavy-duty trucks and equipment.

The objectives of this project are to develop cast alloys and processing techniques that meet or exceed the properties achieved in today's high-performance forged crankshafts. The target properties of the new core material are at least 850 MPa tensile strength and 615 MPa (0.2% offset) yield strength with 12% elongation. Because of the high number of cycles and engine experiences over its lifetime, a more

challenging requirement is the cast material needing to achieve sufficient local fatigue properties to satisfy the durability requirements in today's high-performance gasoline and diesel engine applications. The materials and processes developed should be able to produce high-performance crankshafts at no more than 110% of the cost of current production cast units.

The project team will focus on development of cast steel alloys for application in crankshafts to take advantage of the higher stiffness over other potential material choices. The current alternative material for cast crankshafts (i.e., ductile iron) has a lower Young's Modulus than steel (typically 14% lower), which results in a significant drop in crankshaft stiffness if mitigating redesign (addition of more material) is not considered. The drop in stiffness leads to increased force transmission into the cylinder block, which can lead to not only structural implications, but increased noise levels. Using the casting process and the stiffness advantage of steel will allow the weight reduction potential to be maximized without sacrificing performance. The significant challenge in this project will be developing production methods for steel castings that can meet the performance and cost requirements.

The team will tailor the cast steel alloy design and develop innovative processing methods to produce clean steel castings, achieving a fine as-cast microstructure meeting required strength and fatigue properties. To minimize cost, designs will seek to eliminate the need for quenching and tempering, developing properties as-cast with controlled cooling or normalizing and controlled air cooling. New filling, feeding, and molding techniques will be developed to achieve the desired liquid metal flow and solidification behavior, resulting in a fine microstructure and minimal porosity and inclusions in the cast steel.

The project team will use an ICME approach to design new alloys and processes, rather than using only traditional trial-and-error methods, which has been proven to accelerate alloy development time. The multi-disciplinary effort will integrate finite element analyses by

engine designers and geometry-specific casting simulations with existing materials models to optimize crankshaft cost and performance. Both Caterpillar and GM have developed extensive integrated modeling infrastructures for advanced casting development. Figure 1 shows the use of the Virtual Cast Development Program for engine block casting development. The Virtual Cast Development Program consists of integrated state-of-the-art modeling and simulation methodologies for cast components, starting from computational alloy and casting design, through casting and heat treatment process modeling, multi-scale defect and microstructure simulation, and culminating in casting property and durability prediction. Caterpillar had similar models for application to cast steel components, from alloy design and casting process optimization to component life prediction considering local microstructures, defects, and residual stresses.

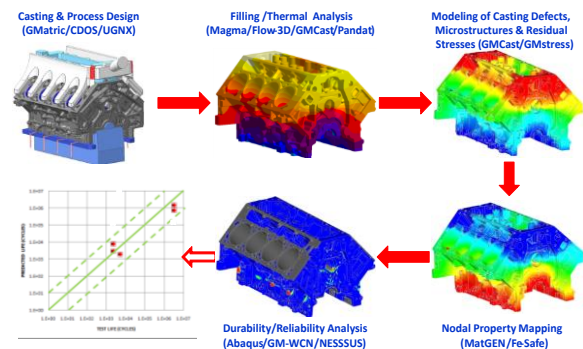


Figure 1. The Virtual Cast Development Program process flow from the casting design through process and microstructure simulation to nodal property and structure performance prediction for a complex sand casting.

Northwestern will apply its Integrated Computational Materials Design (iCMD) toolset (see Figure 2), which is a core modeling software system that integrates proprietary and commercial mechanistic modeling tools to facilitate rapid design and development of new materials and has been demonstrated on many novel steels. For solidification and solid-state transformation modeling, the iCMD platform includes the proprietary multi-component multi-particle precipitation code, PrecipiCalc™, which draws upon calculations from CALPHAD

software tools such as Thermo-Calc® and DICTRA for thermodynamic and diffusion information.

The University of Iowa has developed advanced casting process simulation models for calculating porosity and inclusion formation in steel castings. These models quantitatively predict the size of the defects that are then mapped into fatigue models to predict the effect on the life of the casting. These approaches will be used to optimize the casting process design and determine the location-specific defect allowables in the crankshaft.

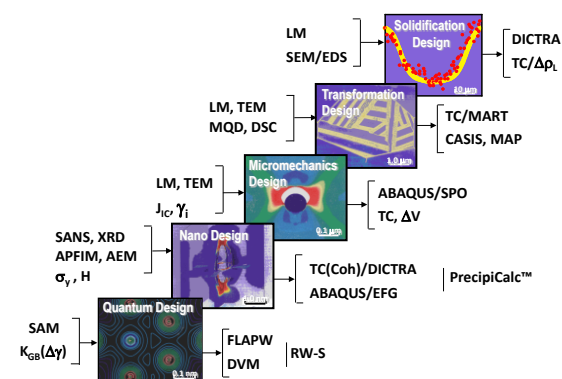


Figure 2. Hierarchy of design models supporting computational materials design. Acronyms on the right side are models and software platforms. Acronyms on the left are instrumentation employed for calibration and validation.

Prototype melts will be produced and characterized iteratively for an alloy design within a stage-gate process. Standard characterization and material testing will be done by Caterpillar and GM to validate the alloy performance against design targets and provide feedback to material design and manufacturing process models. Additionally, the project team will use the advanced photon source at Argonne National Laboratory to quantify casting quality and conduct innovative in-situ measurements of phase evolutions and damage nucleation during thermal and mechanical loading conditions to better understand chemistry-structure-process relationships.

Prototype crankshafts will be produced using the high potential material and processing concepts. Additional manufacturing processes

required to resist cyclical bending and torsional stresses, especially in the concentrated stress regions like the bearing journal fillets and oil drill holes, will then be investigated. Instilling compressive residual stresses into the part are potential methods for mitigating stresses and reducing potential material development risks.

Caterpillar and GM will develop optimized crankshaft designs using the final material and manufacturing processing path. Prototype crankshafts of the final design will be produced and validated using laboratory bending and torsion tests. A full engine test is planned on a running engine, with periodic measurements to determine durability and reliability. The on-engine test will also qualify that the crankshaft and con-rod bearing system will withstand severe overspeed conditions. Bearing temperatures and pressures will be monitored and compared to specifications.

Results

A preliminary casting trial was conducted using a modified SAE 15V22 steel alloy. Weld plates with dimensions of 184 × 305 × 34 mm were cast as shown in Figure 3. Figure 3(b) shows the thermocouple locations used in the simulations in order to extract the cooling rates in the plates during solidification and heat treatment. A normalization heat treatment was used: austenization at 950°C for 1 hour, followed by either a still air cool or fan cool to room temperature. The simulation indicated that the cooling rate at all locations around 700°C is about 0.035°C/s during solidification, while cooling rate during normalization depends on location as follows: corner (TC-2): about 0.50°C/s, edge (TC-1, TC-5, TC-6): about 0.40°C/s, and center (TC-4): about 0.30°C/s.

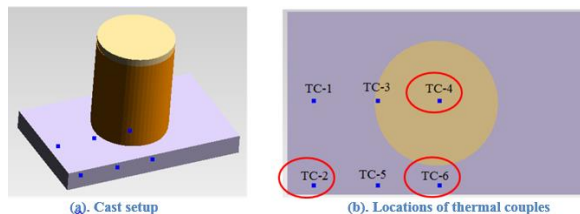


Figure 3. Cast setup of weld plate with dimension of 184 × 305 × 34 mm. The marks are locations of virtual thermocouples set in the simulation.

Tensile specimens were taken from the edge of the plates (TC-5/6 location) and Charpy specimens were taken from the corner of the plates (Figure 4).



Figure 4. Weld plate cast with modified SAE 15V22 with test sample cut locations marked.

The mechanical test results are listed in Table 1. Using the cooling rates given above, the prediction of the microstructure phases and mechanical properties with JMatPro are presented in Table 2.

Table 1. Mechanical properties of weld plate cast with modified SAE 15V22.

IE1667mod	1A	1B	2A	2B
Solution at 950°C	Normalization with air-cool	Normalization with fan-cool	2x Normalization with air-cool	2x Normalization with fan-cool
Tensile, MPa	853, 784	839, 801	833, 760	855, 800
Yield, MPa	581, 582	577, 586	575, 570	585, 591
Elongation, %	3, 2	3, 1.3	3.2, 2.1	3.1, 2.2
RA	5, 5	5, 4	6, 4	4, 4
Charpy-V at room temp	11.8, 10.9, 10.9	11.5, 10.6, 11.8	15.1, 12.9, 16.4	13.7, 13.6, 12.6
HRC surface	26, 27, 27	27.5, 28, 27.5	26.5, 26.5, 26.5	28, 27.5, 27.5

Table 2. Comparison of different predictions with experiments of mechanical properties of weld plate cast with modified SAE 15V22.

Location	Cooling Rate (around 700°C)	Phases %		Properties after Normalization		
		Bainite	Pearlite	YS (Mpa)	UTS (Mpa)	HRC
TC-2: Corner	0.5°C	99	1	663	911	27.7
TC-6: Side	0.4°C	98	2	654	901	27.2
TC-4: Center	0.3°C	95	4	643	888	26.5

A comparison of the predicted values at location TC-6 with the measured values indicates that the predictions are higher by about 75 MPa. The hardness predictions matched exactly with the measured values. It was very encouraging that the measured strength values were very close to target properties. However, the elongation values were quite low, around 2% on average, compared to the target of 12%. The low measured elongation values could be related to material defects, which could also explain the

actual strengths being lower than the predicted strengths. The measured Charpy values were also lower than desired, which is an indicator of the presence of brittle phases or material defects. The Series 2 samples in Table went through a double normalize process to determine if any microstructure refinement and improvement in properties could be achieved. As can be seen in the data, no improvement was found for this alloy.

Cast and heat-treated samples were also sent to Northwestern for a more in-depth analysis of the microstructures to better understand the structure-property relations and determine mechanisms for improving toughness. Polished unetched samples are shown at various scales in Figures 5 and 6 for the material in the as-cast, normalized, and air-cooled states, respectively. In the polished samples it is clear that there are many small defects (i.e., 10 to 20 μm) finely dispersed throughout the material. In the normalized material (Figure 6), light brown rings have formed around the defects after the material was normalized. These light brown areas likely formed as either a result of diffusion from the inclusions into the matrix or could possibly be rust formed from the polishing liquid. The source of the inclusions is unclear at this time; it may have been dirty metal or molds or the inclusions may have formed due to a poor filling method resulting in reoxidation artifacts.

Because the casting process was not observed for this trial, it is not possible to know if there was something improper with the process (such as deoxidation or problems with the pouring practice). Because these defects quite possibly could be the reason for the low elongation and Charpy values, further analysis of these defects will be performed. Northwestern will analyze these defects with SEM/EDX to identify the composition of the defects and the segregation of the elements around the defects in the as-cast and normalized condition.

The material samples were also etched to study the microstructural phases present after various processing steps. Figure 7 shows etched samples of the material in the as-cast state at two different magnification levels. These are quite interesting images, with white areas uniformly

distributes throughout the structure. These white areas were thought to be ferrite, but it has been questioned whether they are untransformed austenite. The dark areas are pearlite and the bluish areas are likely bainite. Deeper investigation is still necessary to truly understand the solidification and solid-state transformation of this alloy and the resulting phases that form.

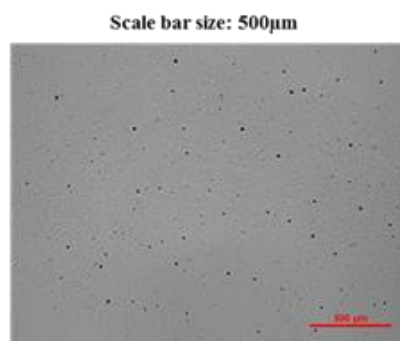


Figure 5. Polished sample from as-cast material. Many small defects are finely dispersed throughout the material.

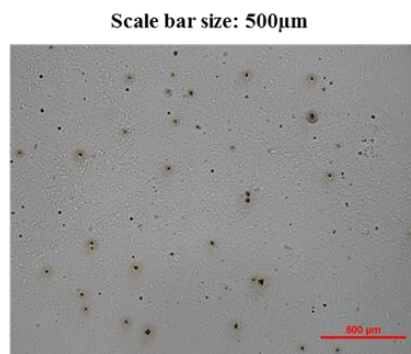


Figure 6. Polished sample from Series 1A, normalized and air-cooled material. A light brown ring has formed around the finely dispersed defects after normalization.

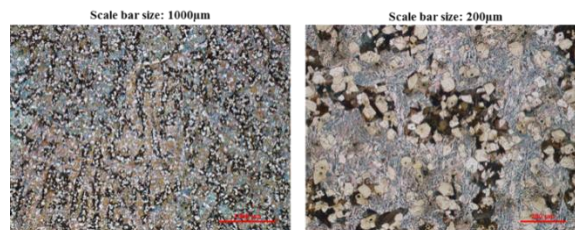


Figure 7. Example of the cast structure from an as-cast material sample.

Figure 8 shows the structure after normalization and cooling in still air at two different magnification levels. The image on the left in Figure 8 reveals the dendritic structure. It appears the structure has transformed to bainite, agreeing with the previous analysis and the modeling predictions in Table 2.

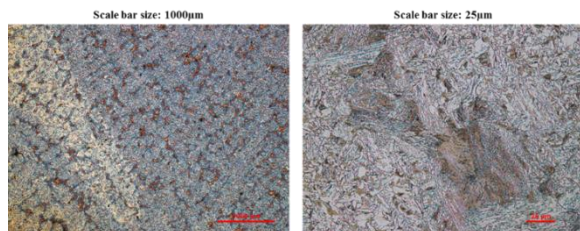


Figure 8. Etched sample from Series 1A, normalized and air cooled.

The plate casting used for the preliminary alloy trial discussed above has a large riser in the middle of the plate (Figure 3). Because the plate is not very thick, test specimens cannot be taken from regions under the riser, because they would be too close to the riser. The large riser will lead to significant under riser segregation, which is not desirable for evaluating different alloy concepts. Thus, the team focused on developing a new test casting design to produce samples in support of the alloy development effort. A key requirement for the test casting is to have sections with varying cooling rates during solidification and heat treatment that are representative of the range of cooling rates that an actual crankshaft would experience. Calculated cooling rates in a small Caterpillar crankshaft ranged from 0.5 to 2.5°C/s during solidification and were around 0.02°C/S at the solid-state transformation temperature during in-mold cooling. After normalization, the cooling rates were between 0.3 and 0.4°C/s at the solid-state transformation temperature during air cooling. Another key requirement is to have a good bottom filling process with controlled velocity to reduce the formation of reoxidation defects and produce high-quality material. Also, the ability to use a filter is preferred to improve cleanliness and to further control the liquid velocities during filling.

After several design revisions and simulations, a final design is selected as shown in Figure 9. The test casting consists of a 1-in.,

2-in., and 3-in. test bar. A large draft is applied to each bar to promote directional solidification toward the open top risers. A tapered runner is designed to flow under the test bars to promote uniform bottom filling. At the end of the runner, a well and thin vent tube were added in order to trap the initial liquid in the mold and enable the liquid metal to more easily displace the air in the mold. Sand cast simulations were then carried out using the modified SAE 15V22 material and the property database developed for this alloy. Varying carbon contents of 0.24%C, 0.30%C, and 0.40%C were simulated to test the robustness of the design for producing test bars without gross macro-porosity defects. A pouring temperature of 1600°C was used with a pressure boundary condition of 30 mBar, set at the inlet to simulate the head height expected in a typical gravity pour filling processes. The feeding effectivity was set to cut-off feeding in the mushy zone at 50% solid fraction.

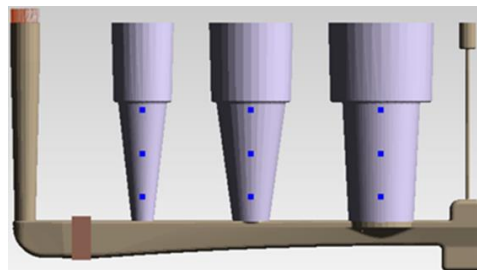


Figure 9. Geometry of the final test casting design.

The simulated filling sequence at different times is presented in Figure 10 and the predicted fill time is 9.4 seconds. It shows quite smooth filling, except for some very minor liquid splashing during the early filling period. In this design, any entrained gas or oxides formed during the early filling due to the splashing should easily float out to the top risers. The liquid fraction evolution over time is shown in Figure 11. From these images, it can be seen that there is directional solidification toward the top risers, except for a weak indication to form an isolated mushy region at the bottom 2-in. bar.

The porosity prediction presented in Figure 12 indicates all the risers pipe effectively and there is no gross shrinkage in the actual test bars. A very small spot of porosity was predicted

at the bottom of the 2-in. bar, but this is far from the gage region of the test specimens to be extracted from these bars.

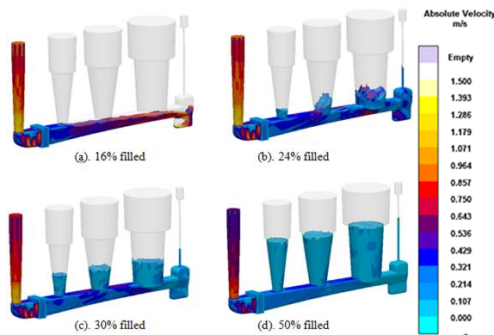


Figure 10. Liquid metal velocities at various stages during the filling process are shown. The filling in uniform lamellar flow with velocities is mainly lower than the 1-m/s threshold for the optimal filling process.

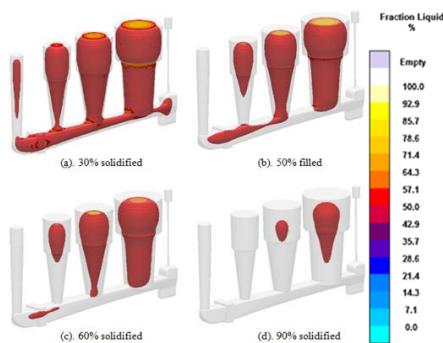


Figure 11. Evolution of liquid fraction (shown regions above 50%) during solidification.

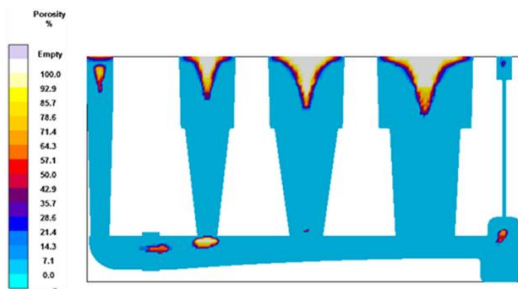


Figure 12. Predicted porosity in the test casting after solidification is complete. The riser pipe nicely and yield sound (porosity free) test bars.

The Niyama value in all three bars is above the critical value for the gross microporosity of $0.7 [C s]^{0.5}/mm$, except for a small spot at the bottom of the 1-in. bar (Figure 13).

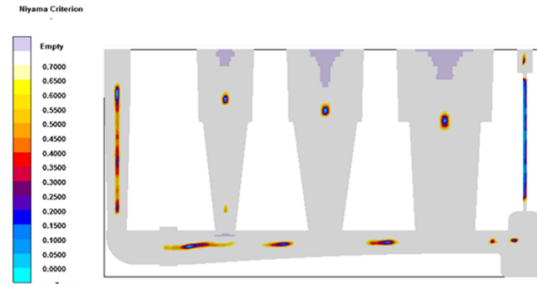


Figure 13. Niyama criterion, indicating areas of potential micro-shrinkage.

Cooling rates were calculated at around $704^{\circ}C$ at the center of each bar. During in-mold cooling after solidification, the cooling rates varied from 0.03 to $0.04^{\circ}C/s$, while they ranged from $0.29^{\circ}C$ in the 3-in. bar to $0.45^{\circ}C$ in the 1-in. bar during air cooling after normalization. These values represent the predicted cooling rates at different locations in the Caterpillar and GM crankshafts previously analyzed.

The project team investigated the castability of multiple Caterpillar and GM crankshaft designs. These crankshafts consisted of both current forged and cast ductile iron crankshafts. Each crankshaft was first simulated without gating and risers, which is termed natural solidification. The natural solidification results were used as a baseline and compared to new processing concepts. At this stage of the project, the processing concepts explored were limited to riser and gating concepts, casting orientation, and filling methods. The goal was to identify the challenges and feed that information to designers to develop crankshaft design concepts more suitable as a steel casting. The identified challenges also serve as a basis for prioritizing focus areas for new process technology development specific to crankshafts.

One of the cases studied was casting a small Caterpillar crankshaft in a horizontal casting orientation using the modified SAE 15V22 steel alloy. Simulations were conducted in MAGMA5 for several riser and gating configurations, with the objective of minimizing the total volume fraction of porosity in the crankshaft. The best results of several configurations studied were obtained using five top risers and bottom gating through one end as shown Figure 14. A low volume of porosity in the crankshaft was

achieved for this configuration (Figure 15). Figure 15(b) shows that most of the porosity in the crankshaft is toward the center of the journals at the surface of the cores used to cast the journals hollow. This is encouraging because the shape of the cores could be optimized to remove the hotspots and improve the directional solidification toward the risers.

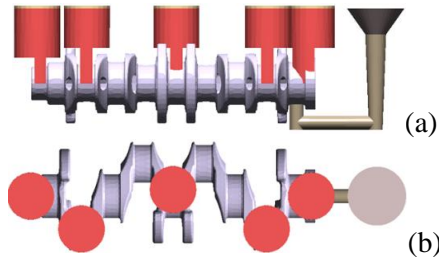


Figure 14. (a) A side view of the Caterpillar crankshaft with three risers on the main journals and two risers on the rod journals. Red indicates a riser, grey is the crankshaft, and the gating is brown; and (b) a top view of the Caterpillar crankshaft.

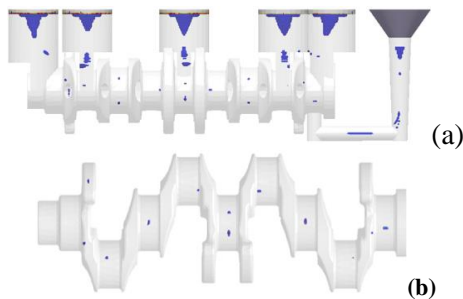


Figure 15. (a) A transparent side view of the Caterpillar crankshaft with five risers. The blue indicates porosity locations within the crankshaft and risers; and (b) a transparent top view with the risers removed so the porosity could be more easily observed.

The team also investigated vertical orientation casting processes for several current crankshaft designs. For vertical casting orientation, both gravity pouring and counter-gravity filling processes were examined. The counter-gravity process draws the liquid metal up into the mold cavity using a vacuum, which provides excellent flow control resulting in a lamellar filling process. This is especially important for casting in the vertical orientation as the metal has to fall a long distance using

gravity pouring techniques, leading very high filling velocities and creating excessive turbulence and splashing. An example of the vertical casting studies is demonstrated on a GM small gas engine crankshaft. A new casting technique was simulated in which the crankshaft is rotated 180 degrees after counter-gravity filling is complete. Figure 16(a) shows the casting in a vertical orientation, with the inlet at the bottom and the riser at the top. This is a typical bottom fill casting process. Figure 16(b) shows the configuration where the riser is at the bottom and the casting is filled through an inlet at the bottom of the riser. After filling is complete, the casting is rotated 180 degrees so that the riser is at the top (Figure 16(a)).

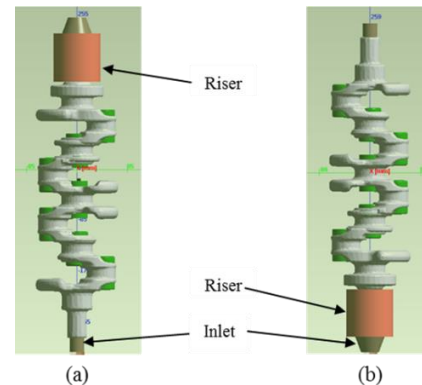


Figure 16. (a) Geometry of the vertically cast GM crankshaft that does not rotate after filling; and (b) geometry of the vertically cast GM small gas engine crankshaft that rotates 180 degrees after filling. The geometry shown is before rotation, after rotation the riser will be on top of the casting as in (a).

The temperature contours in Figure 17 show that when the casting is rotated after filling, the riser has a higher temperature than the rest of the casting. The riser in the casting that was not rotated is at a lower temperature than the casting, which one would expect would lower its feeding efficiency.

Comparing the porosity in the casting, it can be seen in Figure 18 that the porosity in the casting with rotation is slightly different than the case without rotation. There may be less porosity in the top half of the casting for the rotated case. However, due to the complex geometry, the single top riser cannot feed the

entire casting and the total volume fraction of porosity is not significantly improved.

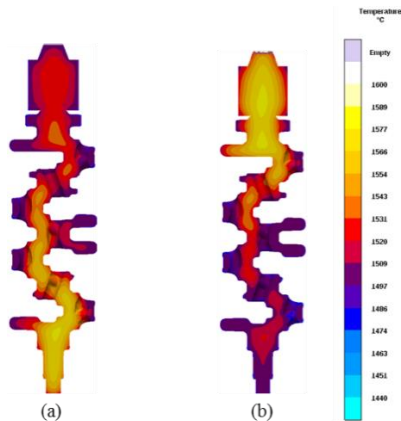


Figure 17. Temperature contour at the center of the vertically cast GM crankshaft: (a) no rotation after filling and (b) 180-degree rotation after bottom filling through the riser.

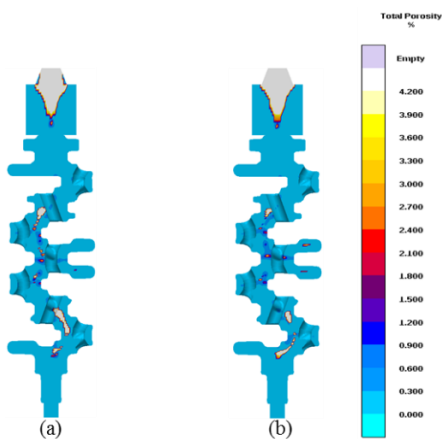


Figure 18. (a) Porosity contour of the vertically cast GM crankshaft that does not rotate after filling (cut to show the center of the casting) and (b) porosity contour of the vertically cast GM crankshaft that rotates 180 degrees after filling (cut to show the center of the casting).

Summary and Next Steps

This is a new project that began in late March. In this limited time, encouraging results have been achieved in a preliminary alloy casting trial. A test casting design has been completed for use in future alloy development experiments. Several virtual casting process studies have been conducted and the team is identifying promising paths forward to successfully cast steel crankshafts. Design features are being identified that can improve the castability for steel alloys.

In Fiscal Year 2015, the team will continue to utilize ICME modeling to optimize several alloy concepts the team has identified. A pattern will be procured for the new test bar casting and samples of the optimized alloy concepts will be cast. Microstructure characterization and mechanical properties will be measured from the cast samples. High-potential alloys will be selected from this initial screening for further optimization. Casting process developments will continue using the high-potential alloys and optimized crankshaft design concepts, considering the solidification behavior of these high-potential alloys. The team will begin looking for capabilities and sources for casting prototype crankshafts using the new processing concepts. The team will also begin looking at post-casting processing and evaluating the material response to further down select high-potential alloy concepts.

Project 21656 – Cast Alloys for Engines

Agreement 27926 – High-Performance Cast Aluminum Alloys for Next Generation Passenger Vehicle Engines (Project Number CEVT211)

Amit Shyam, Shibayan Roy, Larry Allard, Dongwon Shin, Adrian Sabau, Ryan Cooper, G. Muralidharan, Wallace Porter, and Thomas Watkins*

**Oak Ridge National Laboratory*

1 Bethel Valley Road

Oak Ridge, TN 37831-6068

Phone (865) 241-4841; fax (865) 574-6098; email: shyama@ornl.gov

Lin Zhang

Chrysler Motors, LLC

Jose Talamantes and Andres Rodrigues

Nemak, S.A.

DOE Technology Manager: Jerry L. Gibbs

Phone (202) 586-1182; fax: (202) 586-1600; e-mail: jerry.gibbs@ee.doe.gov

Technical Advisor: J. Allen Haynes

Phone (865) 576-2894; fax: (865) 574-4913; e-mail: haynesa@ornl.gov

Contractor: Oak Ridge National Laboratory, Oak Ridge, Tennessee

Prime Contract No.: DE-AC05-00OR22725

Objectives

- To develop high-performance cast aluminum alloys with improved castability, high-temperature strength, and fatigue performance compared to industry standard 319 and 356 baseline alloys. Engine cylinder heads cast with the new alloys will have a minimum of 25% strength improvement compared to those cast from the baseline alloys. The cost of engine cylinder heads manufactured by the new alloys will be less than 110% of heads manufactured by 319 or 356. The developed alloys will enable an increase in maximum component operating temperature by about 50°C.
- To evaluate the adequacy of existing integrated computational materials engineering (ICME) models and codes for the prediction of properties and development of cast aluminum alloys. A gap analysis report for existing ICME codes for cast aluminum alloy development will be generated.

Approach

- Develop microstructure-property maps for baseline compositions.
- Predictive modeling and ICME approach for alloy development and material and component property prediction.
- Casting and mechanical property measurements for select compositions.
- Components cast for materials that meet cost and property requirements.
- Engine testing for components.
- Cost analysis for production of a large number (i.e., hundreds of thousands) of components.
- Commercialization plan.

Accomplishments

- The evaluation of microstructural, tensile, thermal, and mechanical properties of baseline 319 and 356 type cast alloys was completed.
- The microstructural, tensile, thermal, and mechanical properties of an Al-5Cu type alloy were characterized.
- Microstructural coarsening was identified as a significant hurdle for the design of high-temperature aluminum alloys.
- Alloy design paths were identified based on characterization of the baseline and other Al-Cu alloys.
- The ICME modeling roadmap for the present effort was established.
- Predictive models for several properties (such as solidification porosity and fatigue limit) measurement were established.

Future Direction

- The alloy system for further development will be identified.
 - ICME models for alloy development will be implemented and the gaps associated with the predictive models will be identified.
 - Casting and characterization of new alloys will be the focus of Fiscal Year (FY) 2015.
-

Introduction

The cast aluminum alloys that are standard across the automotive industry, such as 319 and 356 aluminum, have now been available for several decades. The design and implementation of higher-efficiency passenger automotive engines is currently limited by the absence of economical lightweight materials with improved castability, high-temperature strength, and fatigue performance. The next generation of lightweight alloys must allow a significant reduction in the total weight of automobiles while still maintaining vehicle performance and safety. The electrification of transportation vehicles has accorded an additional emphasis on lightweighting because of the additional weight of power systems (such as batteries).

Development of new cast aluminum alloys that allow improved performance will be dictated, to a large extent, by the ability to manipulate and enhance the desirable features of microstructural constituents. However, the alloy system is too complex to undertake this development process by trial and error. Moreover, the trial and error alloy development approach is inefficient and expensive in the long run. In this regard, predictive modeling and ICME provide powerful tools to accelerate development and deployment of new cast aluminum alloys. In the present project, we plan ICME-based iterative design and development of new cast aluminum alloys with improved performance characteristics compared to industry standard 319/356 alloys. The new cast aluminum alloys will represent a significant opportunity for the automotive industry to increase engine and vehicle efficiency.

Results

Cast and heat-treated aluminum alloy materials were received from NemaK S.A. The following five alloys were cast and machined in the form of blocks (about 1-in. x 1-in. x 7 in.) from an area in a wedge casting with secondary dendrite arm spacing of about 30 μm :

- 319 – T7
- 356 – T6
- A356 – T6

- A356 + 0.5 Cu – T6
- 206 – T6.

Two categories of tasks were performed in FY 2014, namely (1) characterization of baseline aluminum alloys and (2) implementation of predictive ICME models for alloy development and materials property prediction. These are detailed in the following sections.

Characterization of Baseline Alloys

Specimens were prepared for mechanical, microstructural, and thermal property characterization of these baseline alloys. Mechanical property characterization included tensile behavior of the alloys at room and elevated temperature (up to 300°C) for aged specimens. The specimens for high-temperature mechanical testing had an additional preconditioning treatment performed on them, which consisted of a 200-hour treatment at the testing temperature. The tensile properties of the alloys were characterized at 20, 200, 250, and 300°C. The ultimate tensile strength variation with temperature for the baseline 3xx series alloys are compared in Figure 1. The minimum target room temperature (blue) and 300°C (red) properties for these alloys are also included in Figure 1. It is observed that several alloys meet the minimum target at room temperature, but none of the alloys meet the minimum target at 300°C. Therefore, development of cast aluminum alloys, with the desired high temperature strength, is the most demanding challenge in the present project.

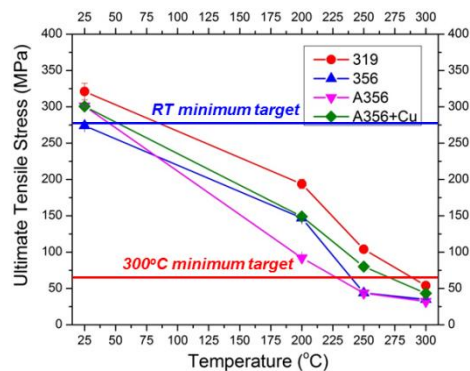


Figure 1. The ultimate tensile strength variation with temperature for baseline 3xx aluminum alloys.

The true stress-strain curves of the alloys at 20 and 250°C are compared in Figure 2. All alloys displayed a distinctive change to softening behavior at the higher temperature compared to hardening alone at room temperature. The change in hardening characteristics of all alloys was examined in detail and also related to the change in fracture surface characteristics. As shown in Figure 1, the yield and ultimate tensile strength of the alloys decreased significantly due to an increase in temperature.

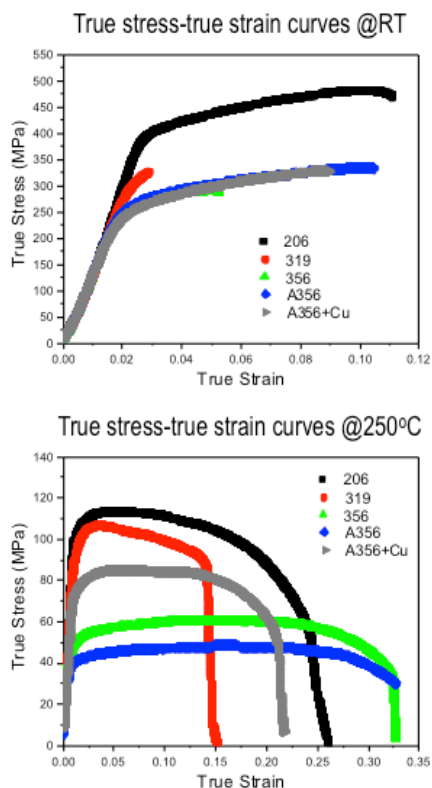


Figure 2. The true stress-strain curves of the five supplied cast aluminum alloys at 20 and 250°C.

The thermal conductivity of the baseline alloys was measured by measuring the thermal diffusivity, specific heat, and thermal expansion of the baseline alloys. Thermal conductivity is the product of thermal diffusivity (measured by the laser flash technique), specific heat, and density of the material. In order to measure the density at elevated temperature, the thermal expansion needs to be measured. High thermal conductivity is an important requirement of engine cylinder head applications. The effect of

temperature on the thermal conductivity of baseline 3xx series aluminum alloys is shown in Figure 3. It is observed that the 319 alloy has a lower thermal conductivity than 356 type alloys at all temperatures.

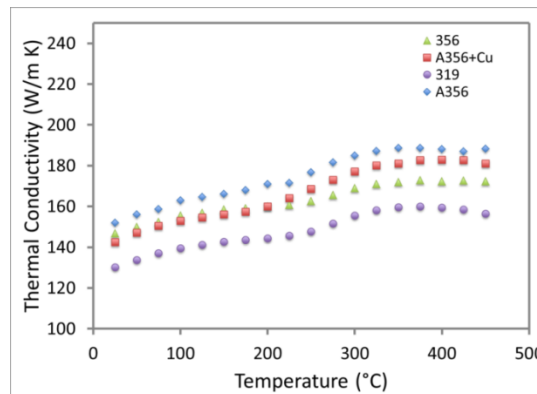


Figure 3. Thermal conductivity of baseline 3xx series aluminum alloys up to 450°C.

Detailed microstructural characterization was performed on the received alloys. An example of the type of microstructural characterization (optical and energy dispersive spectroscopy [EDS] in a scanning electron microscope [SEM]) on 319 aluminum alloy is shown in Figure 4. Figure 4a includes the backscattered SEM image, along with the color coded elemental image maps for two different regions in this alloy. The presence of various intermetallic precipitates that are key to the castability and fatigue characteristics of the material is noted in Figure 4a. EDS analysis, along with a literature review, revealed the composition of the large-scale precipitates present in 319 aluminum (Figures 4a and b). In addition, the SEM image in Figure 4b reveals the other microstructural features associated with 319 cast aluminum alloys, including secondary dendrite arm spacing, microporosity, the eutectic silicon, and larger β -Al₃FeSi type precipitates (with or without Mn, which determines their morphology). The porosity distribution and, in particular, the largest pores in the distribution are responsible for initiation of fatigue cracks in the microstructure of 319 alloy being investigated. The objective of the microstructural characterization was to establish microstructure-property relationships for the received alloys (in the as-aged condition).

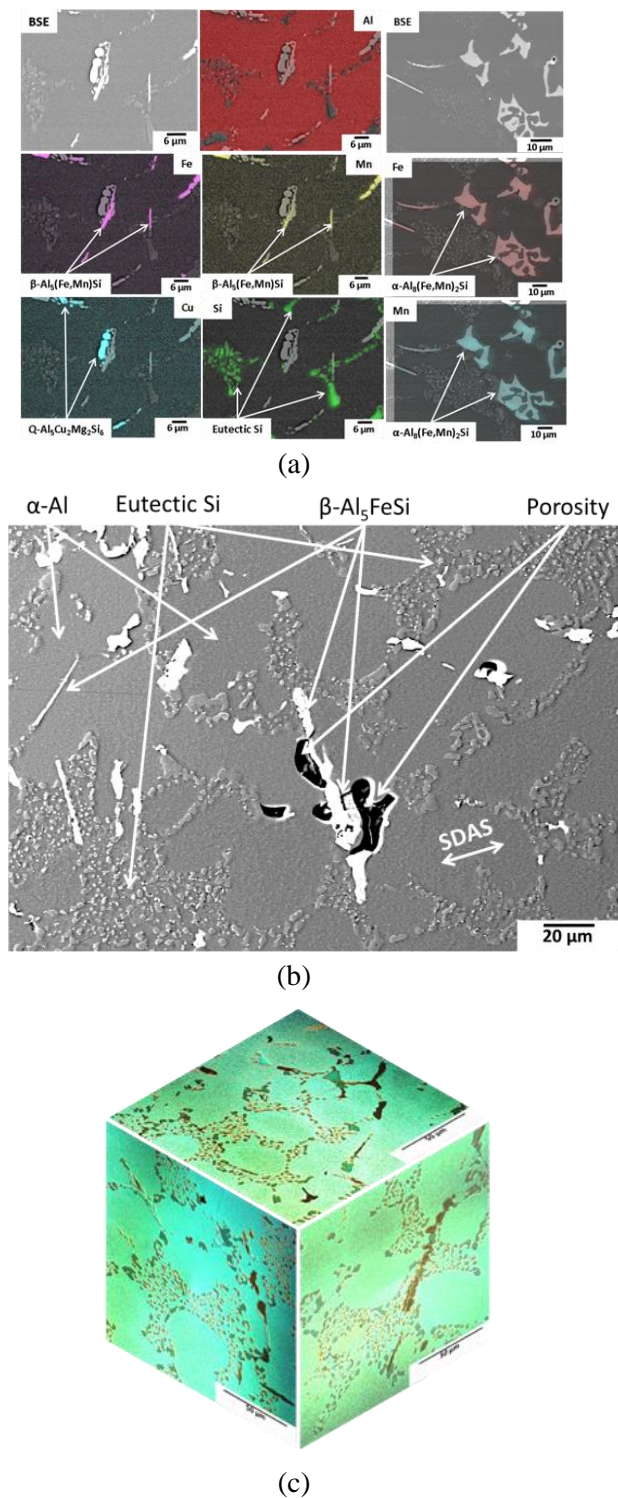


Figure 4. Example of microstructure characterization for 319-T7 cast aluminum (see text).

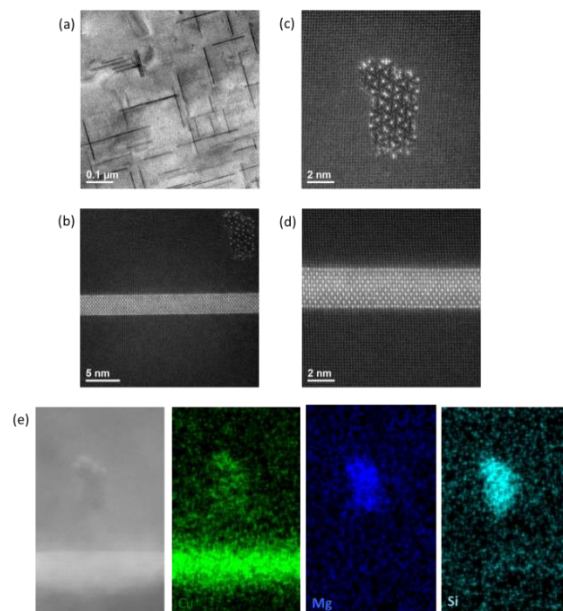


Figure 5. HRTEM images of 319-T7 alloy. (a) Bright field image of nanoscale strengthening precipitates. (b) Dark field image of two different types of nanoscale precipitates in 319-T7, with an irregular shape shown magnified in (c) and a plate shape shown in (d). (e) Shows the chemical analysis in the transmission electron microscope (TEM) EDS mode for these same two precipitates.

A summary of high-resolution TEM images for 319-T7 aluminum, as observed in aberration-corrected electron microscopy, is shown in Figure 5. A bright field image that shows the fine distribution of Al-Cu type precipitates is shown in Figure 5(a). These precipitates appear dark in the bright field image. A single plate-like precipitate appears bright in the dark field image in the $\langle 001 \rangle$ zone axis shown in Figure 5(b). The plate-like precipitate appears in the middle of the image in Figure 5(b), whereas another fine precipitate is in the top right of this image. The latter precipitate is not coherent with the matrix and a further magnified image of this precipitate with atomic columns resolved is shown in Figure 5(c). A heavy atomic number element (likely copper) decorates this precipitate in a hexagonal pattern. The plate like precipitate was also observed at a higher magnification and is shown in Figure 5(d). This precipitate was observed to remain relatively coherent with the

α -aluminum matrix. EDS chemical analysis in a TEM (Figure 5(e)) reveals that the plate-like precipitate is Al-Cu type and the d-spacing indicates that it is likely the θ' (Al_2Cu) phase with detectable amounts of Si and Mg. The precipitate in Figure 5(c) was revealed to be an Al-Cu-Mg-Si-type precipitate by TEM-EDS analysis and is likely the well reported Q phase (also observed at a microscopic scale in Figure 4(a)). The above analysis provides unprecedented access to the details of the structure and chemistry of the nanoscale strengthening precipitates in the 3xx series of aluminum alloys.

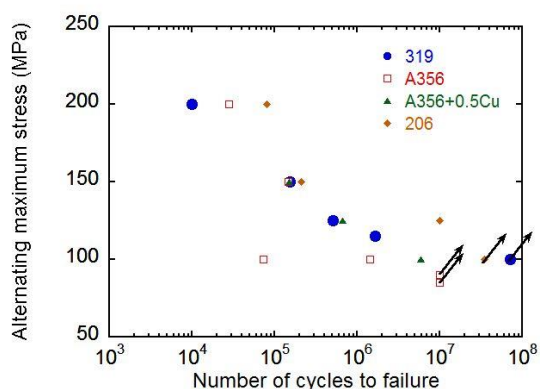


Figure 6. High-cycle fatigue behavior of baseline cast aluminum alloys at room temperature.

High-cycle fatigue testing was performed on the baseline alloys. A comparison of the high-cycle fatigue behavior of three 3xx series and 206 cast aluminum alloys is shown in Figure 6. The 3xx series alloys materials show a fatigue limit in the range 85 to 100 MPa, which is consistent with the values reported in literature. The 206 alloy displayed a higher fatigue limit in the range of 100 to 120 MPa, consistent with its higher strength at room temperature.

The baseline alloy characterization led to the following important conclusion about the studied alloys: *the most important attribute of the aluminum alloys for use at elevated temperature is their microstructural stability at temperatures above 200°C*. To study this, the effect of preconditioning treatment temperature on the room temperature Vickers hardness value

of the alloys was investigated (Figure 7). It is observed that the hardness value decreases by a significant amount as a result of 300°C preconditioning treatment. Microstructural observations confirmed that this decrease could be largely attributed to coarsening of the strengthening precipitates at 300°C (fine, light-colored precipitates in Figure 7 for 319 alloy). The same precipitates are fine enough to not be observed in a SEM in the as-aged condition; therefore, they were characterized by high-resolution TEM (Figure 5).

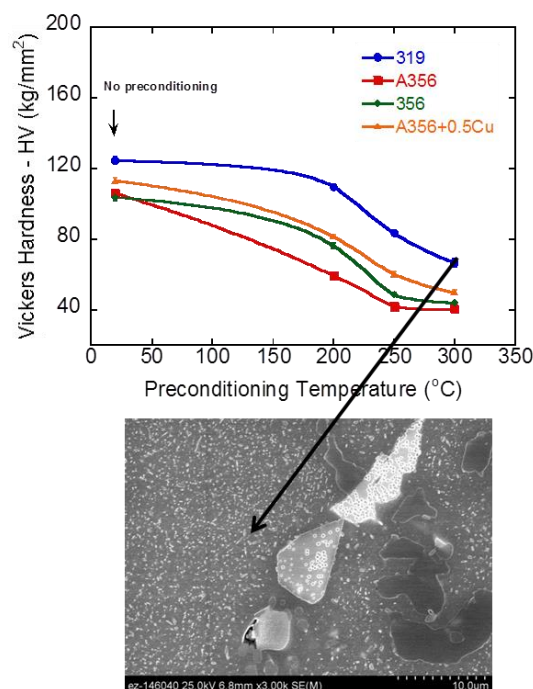


Figure 7. The effect of preconditioning (200-hour treatment) temperature on the room temperature Vickers hardness of 3xx series alloys. The SEM image on the right corresponds to a 319-T7 specimen preconditioned at 300°C.

Predictive Models for Property Prediction

As noted earlier, one of the objectives of this project is to evaluate the adequacy of ICME models toward alloy development and materials property prediction. Models and tools will be evaluated for predictive capabilities and ability to bridge scales. The latter is important because, for the ICME evaluations, key microstructural scales need to be defined for prediction of different properties. For example, for the fatigue

limit prediction, the key microstructural scale is the mesoscale, where the largest pores form and initiate cracks during cyclic loading.

A probabilistic model for the prediction of fatigue limit in 319 aluminum alloys was implemented in this project in the reporting period. This model is presented as an example of the ICME modeling for properties undertaken in the present project and is summarized below.

We produced a weakest link prediction of fatigue strength based on the distribution of pore size and location. We adopted the framework previously implemented by Zhu et al.

(*Metallurgical and Materials Transactions A*, May 2007, Volume 38, Issue 5, pp 1111-1122). First, we generated a log normal distribution of pore sizes in a gage volume that corresponded to a typical fatigue specimen, with a uniformly random distribution of pore locations within a volume. The result of this procedure is illustrated in Figure 8. A virtual fatigue staircase testing procedure was applied on this gage volume and was based on a failure/run out result; the procedure was repeated 1,900 times with a new microstructure corresponding to each simulated fatigue test.

The results of the Monte Carlo simulation are now discussed. The experimentally measured mean fatigue strength and standard deviation is measured to be $\sigma_0 = 85 \pm 8.5$ MPa (Zhu et al. 2007). For the simulation parameters applied, the developed model predicted a mean fatigue strength of $\sigma_0 = 83 \pm 8.9$ MPa. This result is statistically close to the experimental results. The initiating pore size is also very similar to the experimentally observed initiating pore size (Figure 9). Increasing the number of samples from 1,900 to 19,000 in the Monte Carlo simulation resulted in the same distribution of initiating pore sizes and fatigue strength measure, leading us to believe that convergence has been adequately achieved in this simulation.

The significance of this method is in the predictive capability for the mean fatigue strength and initiating pore sizes. Viewed another way, this method allows us to computationally perform a large number of fatigue tests if the pore size distribution of a new

alloy is known. Such large experimental test schedules will be prohibitively expensive and time consuming.

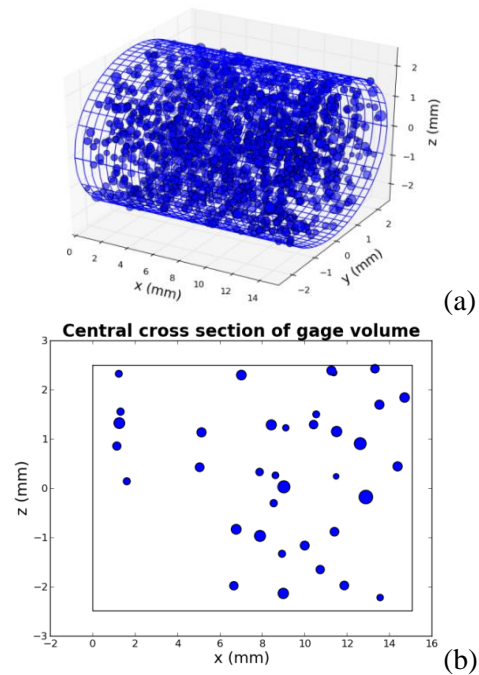


Figure 8. (a) Lognormal porosity distribution simulated in a gage volume of a fatigue specimen and (b) shows a central cross section of the gage volume in (a). The size of the pore diameters have been magnified 1,000 times for visualization.

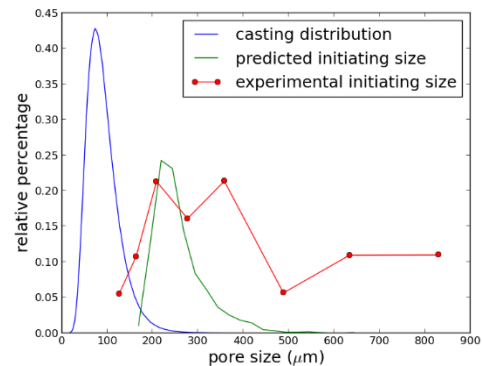


Figure 9. Input pore distribution in blue, pore sizes predicted to initiate failure in green, and experimentally observed initiating pore size in red marked at data points with circles. The predicted and measured initiating size distributions coincide with reasonable accuracy.

The limiting factor to this method is quantification of the pore size distribution. To date, it is computationally difficult to predict the pore size distribution within a given casting system. The process is also quite difficult experimentally and requires assumptions to scale the 2D cross sections into a 3D volume or a tedious experiment to perform a full 3D reconstruction of a representative microstructural volume.

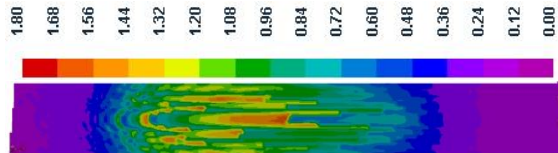


Figure 10. Microporosity prediction results for a plate casting of 319 alloy.

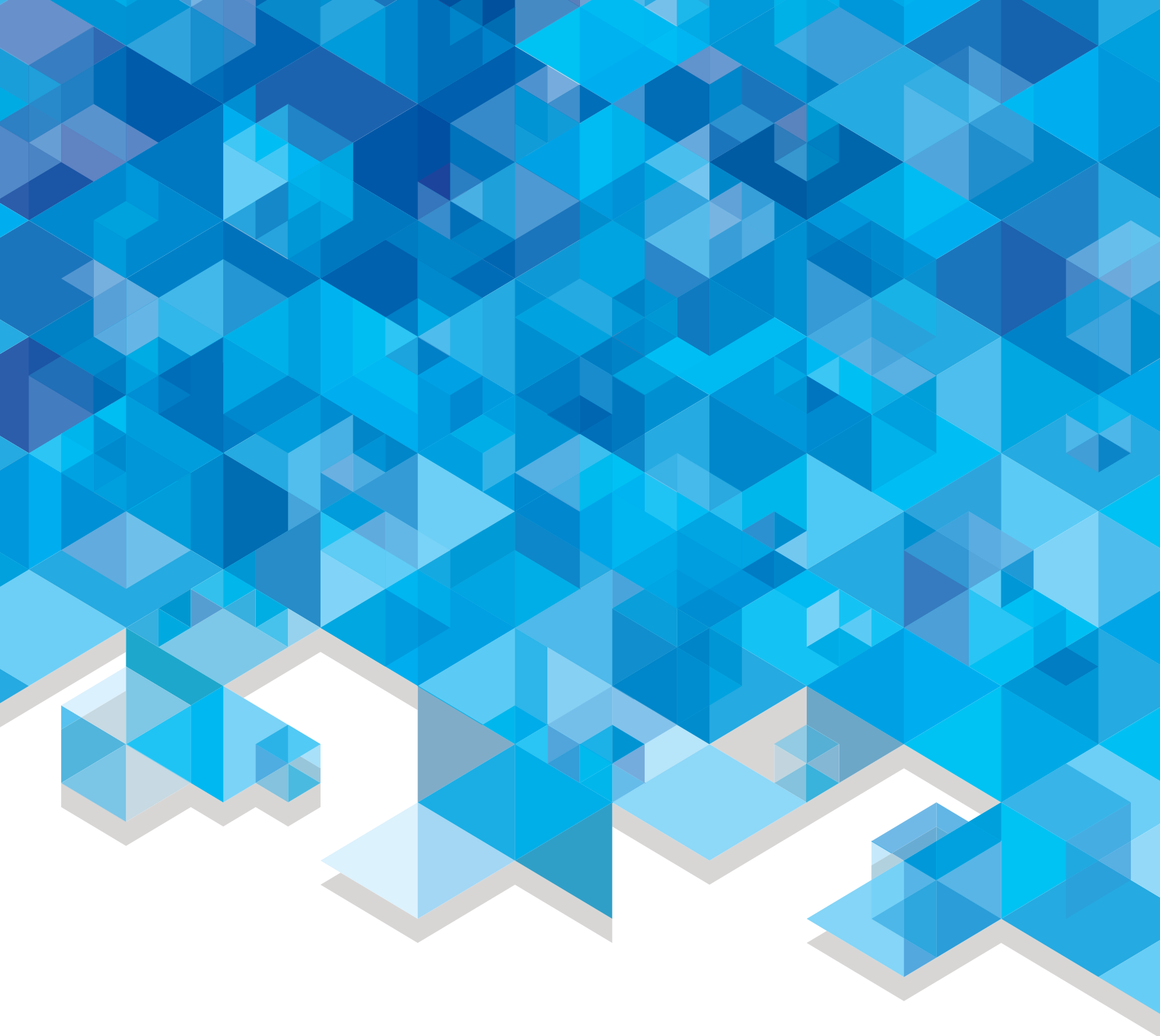
Progress was made toward implementation of a predictive model for pore-size distributions. Numerical simulation results were performed for the section of a plate casting with cast iron chills. The plate dimensions were 14 x 22.9 x 3.2 cm. ProCAST software was used in this study for metal casting simulations. The results for microporosity distribution for 319 alloy are summarized in Figure 10. For 319, with an initial hydrogen content of 0.1 cc/100 g, the length of the high-porosity region and the maximum microporosity value were found to be the largest compared to other 3xx alloys (simulations not shown).

This is expected because shrinkage demand in the last stages of solidification is highest for 319. The calculated high-porosity region for the 319 alloy can be seen in Figure 10. In FY 2015, a model for the pore size distribution will be implemented and linked to the fatigue limit model to simulate the fatigue and strength of cast aluminum alloys, based on newly developed compositions.

Conclusions

The microstructure, mechanical, and thermal property characterization of a series of baseline aluminum alloys was completed. The structure of the fine strengthening precipitates in these alloys was studied at an unprecedented resolution with HRTEM microscopy. It was observed that the most deficient feature of these alloys at temperatures greater than 200°C was significant coarsening of the strengthening precipitates that led to a loss in strength.

ICME-based models for some selected properties were implemented. The ICME modeling and related alloy development will be the focus of activities in the upcoming year.



U.S. DEPARTMENT OF
ENERGY

Energy Efficiency &
Renewable Energy

For more information, visit: energy.gov/eere

DOE/EE-1217 • May 2015